Australian National University

In situ photopolymerization approach to polymer composite materials

Xiaotong Peng

November 2024

A thesis submitted for the degree of Doctor of Philosophy of
The Australia*n* National University

Declaration

I declare that this thesis, titled "In situ Photopolymerization Approach to Polymer Composite Materials," contains no material that has been accepted for the award of any other degree or diploma at any university. To the best of my knowledge, it contains no material previously published or written by another person, except where proper reference has been made in the text. All work presented in this thesis was conducted at the Research School of Chemistry, The Australian National University, during the period of my Ph.D. studies from 2020 to 2024.

Xiaotong Peng

November 2024

Acknowledgements

First and foremost, I would like to express my profound gratitude to my primary supervisor, Professor Pu Xiao, whose mentorship, encouragement, and expertise have been a constant source of inspiration throughout my PhD journey. His insightful guidance, patience, and dedication to my development as a researcher have shaped not only this thesis but also my academic and personal growth. Prof. Xiao has been instrumental in refining my research approach, fostering my critical thinking skills, and encouraging me to pursue new ideas with confidence. His unwavering support, even during challenging times, has made an immeasurable difference, and for that, I am deeply grateful.

I would also like to extend my heartfelt thanks to my panel members: Professor Liu Yun, Professor Michelle Coote, and Professor Nick Cox. Their constructive feedback, valuable discussions, and expertise have greatly enriched this work and contributed to its development.

I am sincerely grateful to all the collaborators who have generously offered their expertise and resources during my research. Their contributions have been invaluable to the progress and success of this thesis.

Finally, I am deeply thankful to my family and friends, who have stood by me throughout this journey. Their constant support, understanding, and encouragement have been a source of strength and inspiration, helping me stay focused and motivated every step of the way.

To each of you, thank you for making this accomplishment possible.

This research is supported by University Research Scholarship (International), Australian National University.

Abstract

This thesis explores the development of high-performance polymer nanocomposites through photopolymerization, a technique that has gained significant attention due to its rapid, energy-efficient, and environmentally friendly nature. Photopolymerization offers unique advantages over conventional methods by enabling solvent-free, spatially controlled polymerization at ambient temperatures using light. This precision and adaptability are particularly valuable for fabricating nanocomposite materials, where achieving uniform dispersion of nanofillers is crucial to optimizing properties. By incorporating functionalized nanomaterials, photopolymerization facilitates the formation of polymer networks with enhanced mechanical, optical, and functional attributes, making it a preferred approach for creating materials tailored to specific industrial, biomedical, and environmental applications. Each chapter in this thesis presents a distinct photopolymerization strategy to integrate dual-role nanomaterials that function as both photoinitiators and reinforcing agents, yielding composites with enhanced stability, functionality, and potential for scalable production.

Chapter 1 provides a comprehensive review of the latest advances in photopolymerization techniques for fabricating polymer composites with functionalized nanofillers. It emphasizes the significance of selecting suitable monomers and nanofillers, modifying filler surfaces, and optimizing interfacial interactions to improve material properties. This chapter highlights key applications in sensors, gas separation, and biomedical fields, establishing a foundation for subsequent experimental work.

Chapter 2 details the synthesis of triazine-coated silica nanoparticles (Si-triazine NPs), which act as both photoinitiators and reinforcing agents under LED (410 nm)

irradiation. These nanoparticles effectively initiate free radical polymerization of trimethylolpropane triacrylate (TMPTA) while enhancing mechanical strength and reducing shrinkage in the polymer matrix. The study further evaluates the impact of different Si-triazine NP concentrations on photopolymerization kinetics, highlighting optimal formulations for improved migration stability and mechanical integrity.

Chapter 3 investigates the dual-role potential of $CsPbBr_3$ quantum dots (QDs) as photoinitiators and emitters within polymer composites for optoelectronic applications. By combining the QDs with diphenyliodonium hexafluorophosphate (Iod) or ethyl 4-(dimethylamino) benzoate (EDB), the study enhances photoinitiation efficiency, achieving composites with superior photoluminescence and long-term stability. The research demonstrates that Iod as an additive significantly improves photoinitiation, enhancing the composite's performance in luminescent displays and lighting.

Chapter 4 introduces a novel approach to create polymer/MOF (metal-organic framework) composites by functionalizing UiO-66 MOFs with visible-light-sensitive photoinitiators, *N*-(1-pyrenyl)glycine (NPYG) and triazine. These modified MOFs enable rapid, thick curing under LED light, improving structural stability. UiO-66-NPYG composites demonstrate potential for high-resolution 3D printing, while UiO-66-Tz composites exhibit selective cationic dye absorption, showing promise for water purification applications.

Chapter 5 explores a hybrid system of TiO_2 and carboxylated nanodiamonds (NDs) in zwitterionic hydrogels derived from 2-(N-3-Sulfopropyl-N,N-dimethyl ammonium)ethyl methacrylate (SBMA). This system enhances both the mechanical strength and anti-fouling properties of SBMA hydrogels, with TiO_2/ND acting as a

photoinitiator and reinforcing agent. The hydrogels demonstrate increased electron-hole separation efficiency, enabling enhanced photopolymerization and potential moisture-sensing applications.

Together, these chapters present innovative, sustainable photopolymerization methodologies for producing multifunctional nanocomposites, advancing their utility across industrial, environmental, and biomedical applications.

Table of Contents

List of Tables

List of Figures

Chapter 1 Literature Review

1.1. Statement of contribution

I declare that the literature review presented in this chapter are the original work I wrote as part of my Ph.D. program at the Australian National University. As the primary author, I was responsible for drafting the initial manuscript, under the guidance of my primary supervisor, Prof. Pu Xiao.

1.2. Publication status

The published review titled “Photopolymerization Approach to Advanced Polymer Composites: Integration of Surface-Modified Nanofillers for Enhanced Properties” is reproduced in this chapter with permission[1] from Wiley-VCH GmbH, © 2024. This manuscript was published in the journal **Advanced Materials** in 2024. The citation for the published work is:

Peng, X.; Zhang, J.; Xiao, P. Photopolymerization approach to advanced polymer composites: Integration of Surface-Modified Nanofillers for enhanced properties. ***Advanced Materials,* 2024**, *36* (33). https://doi.org/10.1002/adma.202400178.

1.3. Abstract

The incorporation of functionalized nanofillers into polymers has been the subject of much research in recent years due to the unique properties they can impart to the resulting materials. One promising method for preparing such polymer composites is through the use of photopolymerization, which allows for the rapid polymerization of monomers in the presence of nanofillers under light irradiation. This paper reviews recent developments in preparing functional polymer composites that contain functionalized nanofillers using the

photopolymerization approach. It highlights several important factors that must be considered when using photopolymerization to fabricate functional composites, including the selection of monomers and nanofillers, the modification of nanofillers, and the interfacial interactions between nanofillers and polymer matrix since these closely relate to the final properties of the polymer composites. The paper also discusses some of the key applications of the functional composites prepared through photopolymerization, including the fabrication of materials for use in sensors, gas separation, purification, optical devices, and biomedical applications. Overall, the review can provide insight into the relationship between the interfacial interaction and the modifications, thereby inspiring new ideas on modifications of broad types of nanofillers in preparing high-performance materials that are applicable in multidiscipline.

1.4. Introduction

Polymers and nanoscale reinforcement materials have been long aware of their unique properties. The former is easy to process, lightweight, flexible, and versatile for material design, whereas the latter can possess unique optical, electrical, catalytic, magnetic, superior thermal, and mechanical properties.[2-12] Nevertheless, the individual of them lacks advantages over each other, which limits their potential applications.[13, 14] A new class of materials known as polymer nanocomposites has been developed to expand the applications. Polymer nanocomposite materials consist of nanoscale, noncontinuous reinforcements, and continuous polymer matrix phases. Combining reinforcement and matrix produces polymer nanocomposites with combinational properties and are now found in applications such as electronics, photocatalysis, drug delivery, energy storage,

wastewater treatment, optical devices, and carbon capture.[15-35] In general, polymer nanocomposites can be prepared by melt blending, [36] solution mixing,[35, 37] or in situ polymerization by heat or light.[38] As a matter of fact, the first two options are usually adopted by the industry due to their ease of use and economic viability.[39] Even so, these processes are usually highly time-consuming and require high temperatures and toxic organic solutions,[40, 41] which are against green chemistry and require further research and development. Alternatively, in situ polymerization can be advantageous in terms of solving the issues.[42] Compared to thermal polymerization, photopolymerization, which allows rapid reactions under energy-saved mild conditions and provides spatial-temporal control over reaction, has been well adopted since twenty century.[43-46] In this technique, photoinitiator is one of the key components responsible for the initiation of monomers. While most of the commercially available photoinitiators reactive under the ultraviolet (UV) range,[47, 48] many researches have been focused on developing novel photoinitiators that can work under the longer wavelengths of light to ensure safety and be able to activate multiple monomer systems to expand the possible applications.[23, 48-82] The increasing maturity of photopolymerization technology has sparked a growing interest in using it to produce functional polymer nanocomposite materials.

A significant aspect related to the properties of nanocomposites is how well the nanomaterials are dispersed in polymers, which largely determines how strong they are. Due to the strong interparticle interactions and the weak interfacial interactions between nanofillers and polymers, aggregation and phase separation are often observed, degrading the properties of nanocomposites significantly.[83] Consequently, obtaining polymer composites with high nanofiller loading is difficult to achieve, especially with the widely used melt-blending or solution-mixing techniques. A new approach called “P&F” has been proposed by iteratively pressing and folding to achieve up to 74 vol% loading with good

dispersion.[84] Yet, this has still been limited due to the high temperatures and the long processing times. To achieve better dispersion, researchers have also attempted to modify the surfaces of nanomaterials to improve their dispersion.[85, 86] Most typically, polymer surfactants or other molecules that are capable of providing repulsion between nanomaterials are usually selected.[87] Despite the possibility of improving filler dispersion, the lack of interactions between the nanofillers and the matrix may still cause the nanofillers to separate from the matrix or migrate out into the environment. As a result, many studies have focused on developing nanofillers with reactive groups that could physically or chemically link with the matrix during the manufacturing processes.[86, 88-91] Since photoinitiators and monomers are the key components required in photopolymerization, they became the potential candidates to be considered in nanofiller modifications. Modifications of nanofillers with cross-linkable fragments or photoinitiating fragments significantly enhance the dispersity, improve the polymer/nanofillers interactions, and reduce the tendency of photoinitiators/nanofillers migration.[92, 93] However, the relationship between interfacial interaction and nanofiller modification, as well as the effects of different types of nanofiller modification on the properties of final polymer composites and their potential applications are rarely summarized or discussed.

Therefore, this review summarizes works in preparing functional polymer nanocomposites with in situ photopolymerization technique. Since there have been plenty of great books or reviews focused on the selection of monomers,[94-101] we will only give a brief overview of this in the first section. We then focus on discussing the selection of different modified nanofillers, the interactions between the polymer and the nanofillers, which reflect different properties of the polymer nanocomposites, and the current applications. Our review can provide helpful guidance for researchers in the areas of chemistry and materials science regarding the design and selection of appropriate nanofillers to fabricate polymer

nanocomposite materials with better performance via a simple photopolymerization approach.

1.5. Overview of the selections of photopolymers in preparing polymer composite

Polymer composites are synthesized by integrating functional nanofillers into a photopolymerizable resin system, followed by light-induced polymerization to form a crosslinked network. Depending on the polymerization mechanism, four major types of monomers are well adopted in photopolymerization: free radical polymerization of (meth)acrylate systems or thiol-ene/nye systems and cationic polymerization of epoxies or vinyl ethers. In brief, free radical photopolymerization involves the generation of radicals upon light activation of a photoinitiator, which subsequently initiates chain-growth polymerization. In contrast, cationic photopolymerization operates via a cationic chain-growth mechanism, initiated by photogenerated acid species. Furthermore, thiol-ene photopolymerization is a hybrid approach that follows a step-growth mechanism.[96, 102, 103] Even though cationic polymerization exhibits advantages such as insensitive to oxygen inhibition, substantial dark polymerization, and reduced volume shrinkage compared to free radical polymerization,[104, 105] free radical photopolymerization still dominates the research of polymer nanocomposites since they react rapidly, are insensitive to trace impurities, and tolerate wide functionalities.[106, 107] Besides, diluents are usually incorporated to reduce the viscosity since the introduction of nanofillers increases viscosity, thereby affecting the fabrication process. Alternatively, monomer blends (e.g., acrylates and epoxies) has also been a selection to enhance the mechanical properties of the corresponding polymer nanocomposites.[108] Most importantly, the selection of photocurable resins should be determined by the intended applications, as well as the compatibility of the nanofillers with

the resins. For instance, to yield polymer nanocomposites with improved transparency, polymer/nanofillers with similar refractive indexes are usually considered the ideal combinations (e.g., acrylate-based resin and silica nanofillers).[109] In summary, selecting the appropriate photopolymer is critical to creating high-quality polymer composites with the desired properties. The selection process must take into account several key parameters, including reactivity, viscosity, shrinkage, and compatibility with the reinforcement materials. Through careful consideration of these parameters, it is possible to create polymer composites with optimized properties for specific applications.

1.6. Selection and development of functional/modified nanofillers for polymer composites and their achieved properties

As part of the polymer nanocomposites, nanofillers significantly affect the resulting properties and their potential applications. Here, some commonly used nanofillers, their properties and potential applications are summarized in Table 1.1. Specifically, the effect of different nanofillers on polymer composites' properties will be discussed in the following section in the order of mechanical, optical, environmental-related, and electrical properties. Moreover, the details on the modifications of different nanofillers and the approach to the corresponding polymer nanocomposites via photopolymerization will also be discussed. It should be noted that some nanofillers without functionalization have also been included in certain sections. This is because they are involved in photopolymerization reactions, acting as photoinitiators or photosensitizers.

Table 1. 1. Types of nanofillers and their properties and potential applications.

Nanofillers	Properties	Applications	References
Carbon-based materials (graphene, graphene oxides,	High aspect ratio, excellent mechanical properties, electrical conductivity, high	Sensors, biomedical devices, conductive composites, water	110-112

carbon nanotubes)	surface area	purification	
Silica nanoparticles	High surface area, good mechanical properties, biocompatibility	Optical coatings, biomedical devices	113-116
Clays and Minerals	High surface area, layered structure, good mechanical properties, barrier properties	Reinforcing fillers	117-119
Metal-organic-frameworks	High surface area, tunable pore size and surface chemistry, structural versatility	Gas storage, catalysis, sensing	120-123
Cellulose	Renewable, biodegradable, high mechanical strength, low thermal expansion	Biomedical applications	124-129
Chitin and chitosan	Biodegradable, abundant, non-toxic, biocompatible	Wound healing, drug delivery, tissue engineering	130-133
Perovskites	High luminescence, piezoelectric, ferroelectric	Photovoltaics, light-emitting devices, sensing	134-136
Ionic liquids	Low volatility, wide electrochemical window, tunable properties	Electrochemical devices, catalysis, separations	137-140

1.7. Mechanical property

1.7.1. Silica oxides

Silica nanoparticles have been widely selected over other inorganic nanofillers (e.g., titanium dioxide[45], aluminum oxides[141], gold[142], silver[7], etc.) owing to their easily functionalizable surface, high biocompatibility, controllable sizes, and rich textural properties. Recently, many efforts have been made to graft commercially available photoinitiators onto the surface of silica nanoparticles (Si NPs). [92, 143-145] This can increase the dispersity of nanoparticles in the polymer matrix and decrease the migration tendency of photoinitiators after photopolymerization. As a matter of fact, the migration issue is highly assessed in the food packaging industry because any left-over photoinitiators that migrate out could cause health problems.[93, 146, 147] For instance, a commonly used type II photoinitiator, 2-chlorothioxanthone (CTX), has been grafted onto silica NPs and the

modified NPs are subsequently used to initiate the polymerization of epoxy acrylate resin under the light from a Hg-Xe lamp with a light intensity of 80 mW/cm^2.[145] As expected, good dispersion and low migration were achieved, and an improved tensile strength (from 66 MPa to 84 MPa) and elongation at break (from 7.6% to 9.7%) were observed compared to the polymer prepared by free CTX. Nevertheless, only 3 wt% of functionalized silica NPs were incorporated. A question remains whether the good dispersion is due to the functionalization or low loading of silica NPs. Alternatively, two type I photointiators, trialkoxysilyl-functionalized bis(acyl)phosphane oxide (TEMSI2-BAPO) or 1-[4-(2-(3-triethoxysilanylpropylcarbamoyloxy)ethoxy)phenyl]-2-hydroxy-2-methyl-1-propane-1-one (TESI-IC2959) were immobilized onto the silica NPs.[92] They can successfully initiate thiol-ene photopolymerization with a high-pressure Hg lamp with a wavelength ranging from 250 nm to 470 nm. Notably, a low migration of residue photoinitiators from the corresponding composites was achieved. This work has been focused on comparing two different functionalization routes while lacking an investigation of the properties of the as-prepared nanocomposites. Furthermore, one major drawback of this approach was that a relatively large amount of organic solvent was used to allow the fair distribution of silica NPs. This took away the advantage of photopolymerization (solventless). Similarly, another type I photoinitiator, ethyl(2,4,6-trimethylbenzoyl) phenylphosphinate (Irgacure TPO-L), bearing trialkoxysilyl units were functionalized onto Silica NPs and mixed with acrylic monomers to form nanocomposite under a high-pressure Hg lamp with wavelength range from 250 nm to 470 nm.[144] Silica NPs were distributed evenly into the polymer matrix owing to the addition of organic solvent, and patterned polymerization was possible with the photomask. Despite the successful synthesis of the photoinitiating silica NPs, using UV light and organic solvents for polymerization in the studies mentioned above is unfavorable since it may raise health issues.[148] To tackle this problem, our group has grafted a blue light-sensitive

photoinitiator, 4-(2-(4,6-bis(trichloromethyl)-1,3,5-triazin-2-yl)vinyl)phenyl (3-(triethoxysilyl)propyl)carbamate (silylated triazine) onto the silica nanoparticles as shown in Figure 1.1 (a), which were found to work in dual functions.[143] Specifically, being a photoinitiator, the modified silica nanoparticles could successfully initiate free radical polymerization with up to 69% conversion within 5 minutes; being fillers, the flexural modulus of the as-prepared composites could be improved from 43 MPa to 286 MPa as shown in Figure 1.1 (b). Notably, the dispersion of nanoparticles in the matrix was significantly enhanced, and the as-prepared nanocomposites showed minor photoinitiator migration when immersed in the organic solvent.[143] Nevertheless, the high loading of Si NPs is still limited. The flexural modulus started to decrease when 20 wt% of functionalized Si NPs were added.

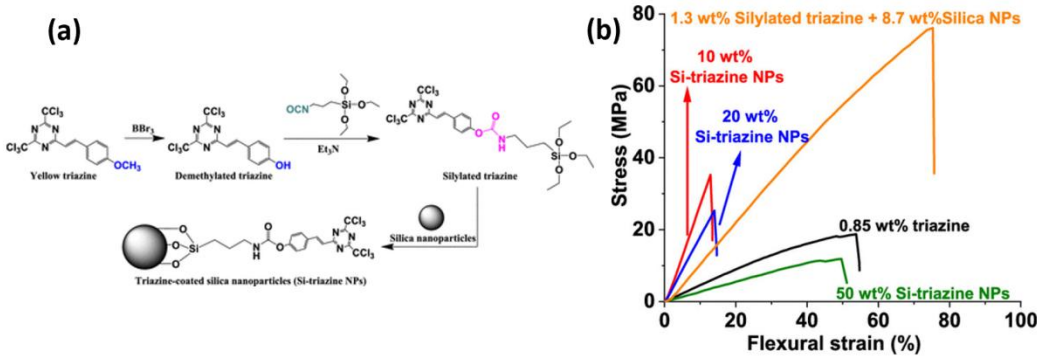

Figure 1. 1. (a) Synthetic procedure to obtain triazine-coated silica nanoparticles (Si-triazine NPs); (b) Stress–strain curves in a three-point bending test of the photocured samples prepared from the photopolymerization of TMPTA initiated by 0.85 wt % triazine (molar concentration: 19.1 μmol/g), 1.3 wt % Silylated triazine + 8.7 wt % Silica NPs (molar concentration of triazine moieties: 19.1 μmol/g), 10 wt % (molar concentration of triazine moieties: 19.1 μmol/g), 20 wt % (38.2 μmol/g), or 50 wt % (95.4 μmol/g) Si-triazine NPs.[143] Copyright 2021. Reproduced with permission from American Chemical Society.

To achieve a high loading, an alternative way is to modify the surface of Si NPs with polymerizable groups. In one research, 3-methacryloxypropyl trimethoxysilane (MPS) has been used to modify the surface of Si NPs (MPS-Si NPs).[149] To ensure the compatibility between nanofillers and matrix, a methacrylate-terminated polyether polyol(polyether-MA)

was synthesized as the photocurable resin. With the combination of a diluent, isobornyl methyacrylate (IBOMA) and a photoinitiator, Irgacure 819, the resulting elastomer composites were investigated and 3D printed with 405 nm light irradiation. In the prepolymer system, the addition of 20 wt% of MPS-Si NPs was found to have an average hydrodynamic size of 154 nm compared to the pristine Si NPs (432 nm), which confirmed the exceptional dispersity of MPS-Si NPs in the polymer matrix. Moreover, the high loading did not induce severe light scattering. In fact, it resulted in a greater photocuring depth compared to those with 0 or 10 wt% MPS-Si NPs. This was explained by the additional nucleation sites for polymerization when a good dispersibility of nanofiller was achieved. The extraordinary dispersity also reflected a significant improvement in mechanical properties. The tensile strength and hardness were increased by 88% and 52% from 3.29 to 6.18 MPa and 48.6 to 74.0, respectively. In the meantime, the insignificant effect of light scattering allowed the 3D printability of these mixtures. As illustrated in Figure 1.2, a gripper that showed high robustness and durability can be successfully 3D printed out and therefore can be potentially used in soft actuator applications.

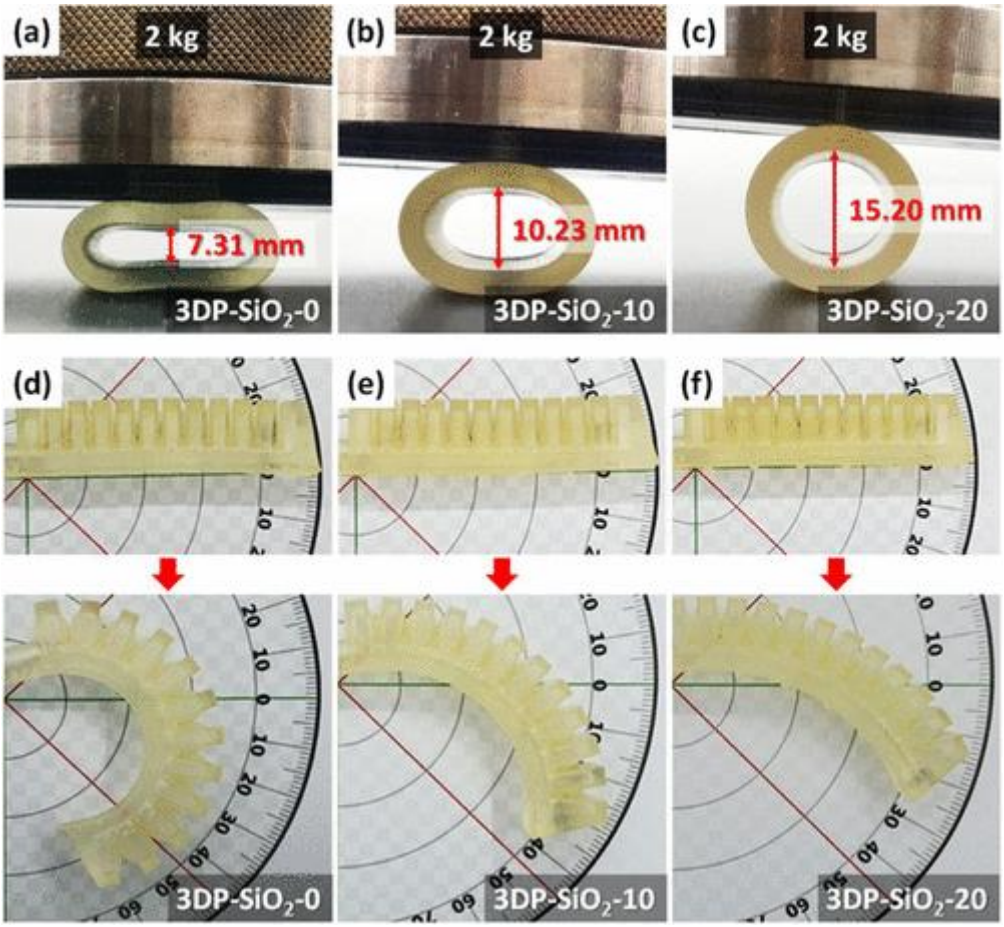

Figure 1. 2. Compression test of a 3D-printed hollow cylinder with different contents of SiO_2 NPs: (a) 3DP-SiO_2-0, (b) 3DP-SiO_2-10, and (c) 3DP-SiO_2-20. The weight of the stainless-steel plates on top of the hollow cylinder was 2 kg. Pneumatic actuation of 3D-printed grippers with different amounts of SiO_2 NPs content before and after pressurization at 150 kPa: (d) 3DP-SiO_2-0, (e) 3DP-SiO_2-10, and (f) 3DP-SiO_2-20.[149] Copyright 2020. Reproduced with permission from American Chemical Society.

In another research, a series of oligomers with different lengths and degrees of functionality were studied to reveal their effects on the properties of the resulting polymer composite.[150] In brief, three epoxy oligomers with the molecular weight of 1075, 4000, and 6100 g/mol reacted with isocyanatoethyl methacrylate (IEM) to different extents (either 10% or 100% OH groups reacted with the IEM) to achieve various methacrylate functionality along the chains as shown in Figure 1.3 (a). The oligomers with various lengths and methacrylate functionality were then grafted onto the Si NPs surfaces as illustrated in Figure 1.3 (b). The photopolymerization was carried on with a dental curing light irradiation

(IQ2, Caulk, Dentsply) with a maximum output of 465 nm. Irradiation of a mixture of dental resin (mixture of (2,2-Bis[4-(2-hydroxy-3-methacryloyloxypropyl-oxy)phenyl]propane (BisGMA) and triethylene glycol dimethacrylate (TEGDMA) in 70:30 mass ratio), modified Si NPs, camphorquinone and ethyl 4-N,N-dimethylaminobenzoate yielded the corresponding polymer-based dental restoratives. Specifically, a pronounced shrinkage reduction was observed when incorporating modified Si NPs with a longer chain and lower methacrylate functionality. This was ascribed to the increased mobility of the compliant interface between the fillers and polymer matrix, reducing the accumulated interfacial stress. A high loading of modified Si NPs (up to 30 wt%) can be achieved because of the improved interface, and the shrinkage was reduced by 30% compared to conventional dental materials.

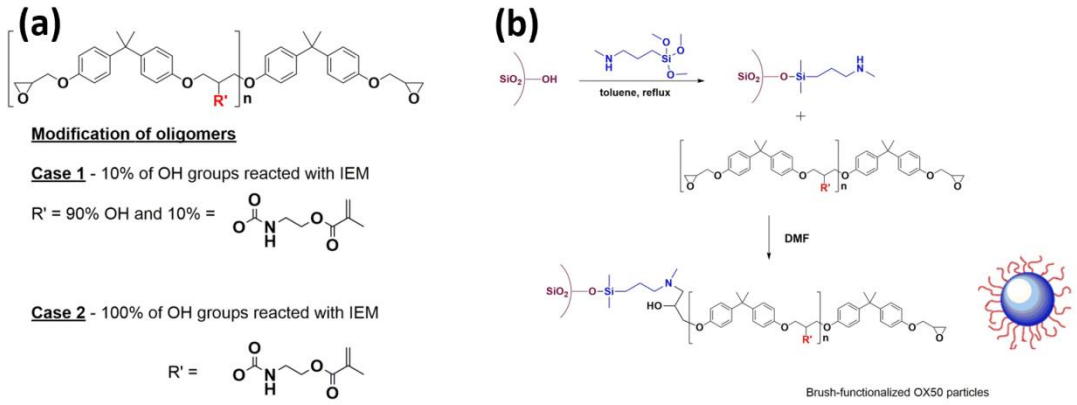

Figure 1. 3 (a) Structure of epoxy oligomer series used to modify the OX50 surface where n varies from 2 to 20. Modification of oligomers – Case 1 – Low methacrylate group concentration on oligomer backbone – 10 % of OH groups are reacted with IEM, leaving 90 % OH groups unmodified. Case 2 – High methacrylate group concentration on oligomer backbone – all OH groups are reacted with IEM; (b) Attachment of oligomers to silica particle surface – OX50 particles were silanized in dry conditions with MAPTS. MAPTS was further reacted with modified epoxy oligomers to yield particles with oligomers on the surface.[150] Copyright 2021. Reproduced with permission from Elsevier.

Besides methacrylate moiety, others also investigated the effect of the modification with vinyl groups on the properties of the corresponding polymer composites. For instance, Si NPs were first modified with methacrylate (MA-Si NPs) and vinyl groups (V-Si NPs), respectively. Then the photocurable Si NPs were incorporated into poly(ethylene glycol) diacrylate (PEGDA) in the presence of 2-dimethoxy-2-phenylacetophenone (DMPA) under

irradiation with a MelodySusie UV Gel Nail Polish Dryer UV light (Model DR-301C) at 365 nm.[151] The introduction of MA-Si NPs and V-Si NPs increased Young's modulus and ultimate compressive stress of the corresponding composite materials. But interestingly, the relationship between Si NPs loading and the maximum mechanical property differed for MA-Si NPs and V-Si NPs. In short, a higher loading of V-Si NPs (10.7 wt%) was required to reach its maximum mechanical properties (~240 MPa of Young's modulus and ~56 MPa of compressive stress). In comparison, 7.4 wt% of MA-Si NPs can achieve composite materials with similar mechanical properties, and further increased loading resulted in increased mechanical properties (~340 MPa of Young's modulus and ~60 MPa of compressive stress). This could be due to the shorter molecular crosslink between the nanofillers. Moreover, well-dispersed MA-Si NPs and an agglomeration of V-Si NPs were found when blending into the matrix system. It indicated the importance of the selection of modified groups which impacts the final composite properties, and the functional groups with similar chemistries to the matrix should be considered.

While Si NPs have been mostly investigated for surface modification, one group also explored the feasibility of another type of silica-based nanomaterial, polyhedral oligomeric silsesquioxanes (POSS), which are the smallest hybrid silica particles (1–3 nm) with well-defined structures.[152] The POSS was functionalized with a polymerizable vinyl group (V-POSS), and then mixed with acrylic acid (AA), ionic liquid, 1-Ethyl-3-methylimidazolium diethylphosphate ($EMIM(EtO)_2PO_2$) and photoinitiator, 1-hydroxycyclohexyl phenyl ketone, followed by photopolymerization under 365 nm irradiation to achieve the dual crosslinked inongel.[152] The combination of the multifunctional chemical crosslinking provided by V-POSS and the reversible hydrogen bonding provided by AA yielded the composites with superior mechanical flexibility (stretchability up to 7000%), self-adhesiveness, and outstanding self-healability. Moreover, the prepared inogel was 3D printed as a strain

sensor, which showed good stability, high gauge factor (1.52–3.93), wide sensing range (1%-1200%), and excellent durability (10,000 cycles). Therefore, it was then assembled as a wearable sensor as depicted in Figure 1.4. Surprisingly, human motion recognition can be achieved, and it can also act as human–machine interface to control the mechanical hand under extreme temperature. Due to the outstanding outcomes, this study provides guidance for the fabrication of intelligent electronics.

Figure 1. 4.The real-time wireless human–machine interface control system. a-c) Schematic of the system. The response of ionogel based sensor from hand motion is first real-time captured and converted to the digital signal, and then the data is real-time wireless transferred to a mechanical hand. d-f) Human hand gesture recognition and mechanical hand real-time response and reconstruction. g) and h) Human-machine Interface under −60 °C and 150 °C.[152] Copyright 2022. Reproduced with permission from Elsevier.

1.7.2. Clay and minerals

In addition to the commonly used Si NPs, clay and minerals are another group of materials that are usually used to tailor the mechanical properties of polymer nanocomposites. This section will summarize and discuss the functionalization of clay and minerals such as halloysite, boehmite, hydroxyapatite, and montmorillonite. Specifically, the structures of the discussed clays and minerals are illustrated in Figure 1.5.

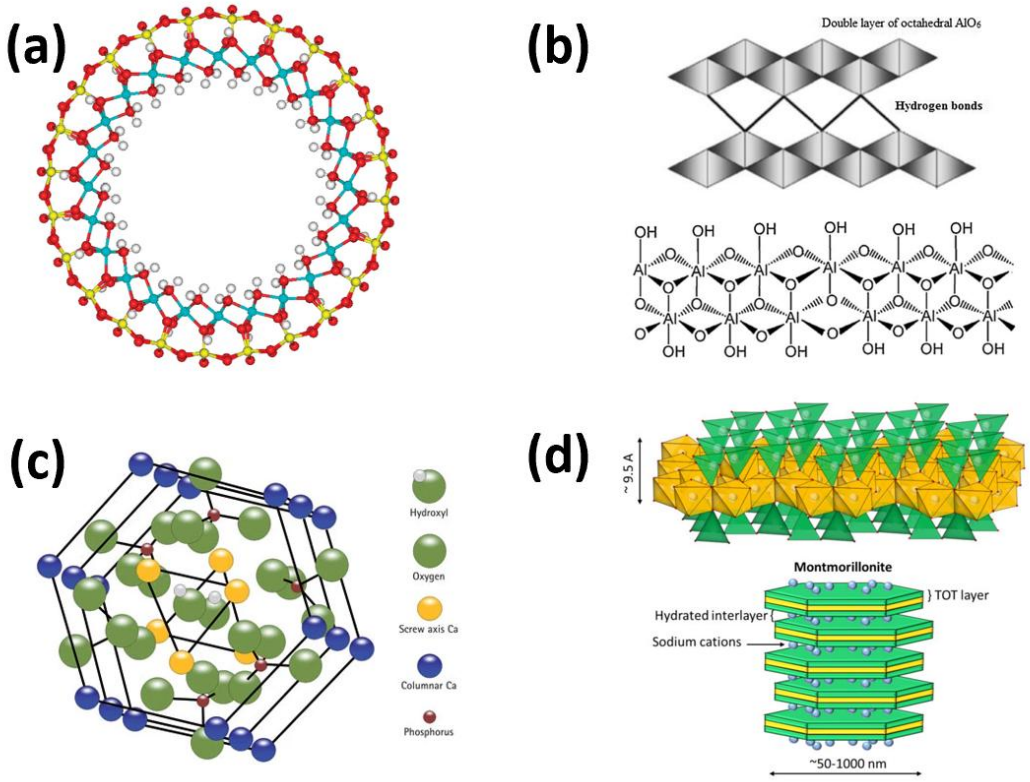

Figure 1. 5. Structures of (a) halloysite nanotube (White atoms are H, red O, grey Al, and yellow Si)[153]; (b) boehmite[154]; (c) hydroxyapatite[155]; and (d) montmorillonite. (The green sheet indicates a tetrahedral silica layer (T), the yellow sheet indicates an octahedral alumina layer (O), and the blue spheres represent sodium cations)[156] Copyright 2010 and 2021. Reproduced with permission from American Chemical Society and Elsevier.

Halloysite (HNT) is a silica-alumina nanoclay with a tubular structure that is usually used as an alternative to carbon nanotubes (CNTs) due to their lower cost and natural availability.[157] Furthermore, their biocompatibility, high functionality, and mechanical properties also make them suitable nanofillers for the mechanical enhancement of composite materials. As

shown in Figure 1.6, halloysites were modified with polymerizable groups, 3-(trimethoxysilyl) propyl methacrylate (MAPTS),[158] vinyltriethoxysilane (VTES),[159] and 3-(glycidyloxypropyl)trimethoxysilane (GPTS).[160]

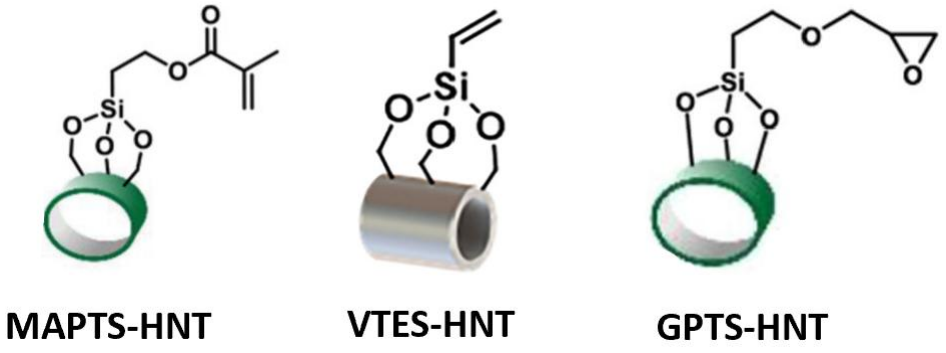

Figure 1. 6. structures of modified halloysites.[158-160] Copyright 2020, 2022 and 2021(ref 69-71). Reproduced with permission from Wiley-VCH GmbH, Society of Plastics Engineers and Elsevier.

For the MAPTS-HNT and VTES-HNT, they were photopolymerized in a merry-go-round photoreactor equipped with 16 UV lamps (Philips 8 W/06 emitting at 300–400 nm wavelengths) with the mixture of Bis-GMA/TEGDMA contained DMPA as the photoinitiator. In contrast, the GTPS-HNT was photopolymerized in the same irradiation setup, but an alternative mixture of bisphenol A diglycidyl ether (BADGE) and trimethylolpropane triglycidyl ether (TTE) which contained benzophenone and diphenyliodonium hexafluorophosphate (Iod) as the photoinitiating system. The monomers were selected based on their compatibility with the modified HNT. Interestingly, in all three approaches, 4 wt% of modified-HNT was found to be the optimal loading amount in producing composites with maximum mechanical properties. Specifically, the tensile strength and elastic modulus (59.13 MPa and 782.27 MPa, respectively) of MAPTS-HNT-containing composites were 5 times and 33 times higher than the neat thermoset (11.54 MPa and 23.97 MPa, respectively). However, with the same matrix, composites containing VTES-HNT only showed 4.9 times higher tensile modulus (27.26 MPa) and 1.5 times higher elastic modulus

(28.36 MPa) compared to the neat thermoset (5.51 MPa and 18.47 MPa, respectively). This was probably due to the better compatibility of methacrylate-HNT with the matrix compared to vinyl-HNT. It is worth noting that, even though the addition of 4 wt% of modified-HNT resulted in significant enhancement of mechanical properties, a mixed morphology of agglomerate and non-agglomerate was still present. Therefore, further consideration and improvement are needed for the modification and selection of polymer.

Similar to halloysite, montmorillonite is also a silica-alumina nanoclay but usually exists in a laminate structure. To achieve specific properties, exfoliation of these laminated nanoclays becomes important. Montmorillonite was modified with three different polymerizable groups, which were tetradecyl-2 methacryloyloxy(ethyl)dimethylammonium bromide (C14MA), undecylmethacryloyloxytrimethylammonium bromide (PM1), and tetradecyltrimethylolbis(3-mercaptopropionate)dimethylammonium bromide (PSH2).[161] Specifically, the C14MA-organoclay contained methacrylate groups close to the clay surface, while PM1-organoclay contained methacrylate groups that were further away from the clay surface. Alternatively, PSH2-organoclay contained thiol groups. To achieve photopolymerization, DMPA was used as the photoinitiator and the prepared mixtures (modified organoclay with 1,6-hexanediol diacrylate (HDDA)) were irradiated with 365 nm light (3 mW/cm^2). Interestingly, C14MA-organoclays showed an intercalated morphology in HDDA, while PM1-organoclays were exfoliated instead. This was ascribed to the different positions of the methacrylate groups, where C14MA-organoclays that had methacrylate groups closer to the clay surface experienced more steric hindrance during photopolymerization. In contrast, PM1-organoclays had more accessible methacrylate groups and were readily exfoliated even before photopolymerization. Even though they showed different morphology, the mechanical performance was similar, resulting in a 30-35% increase in storage modulus (~530 MPa and ~540 MPa for C14MA organoclay composite and PM1-organoclay

composite respectively, compared to ~400 MPa of neat polymer). On the other hand, PSH2-organoclay, which contained thiol groups, showed enhanced exfoliation due to the reaction of thiol and acrylate. Therefore, it resulted in a more remarkable improvement of mechanical properties where the storage modulus was almost double (~700 MPa) of the neat polymer (~400 MPa).

While most modification focuses on methacrylate, vinyl, and epoxy groups, acrylate groups are seldom selected. It has been reported that boehmite nanowires modified with acrylate groups were found to have greater mechanical properties than those modified with methacrylate groups.[162] In detail, boehmite wires were modified with β-carboxyethyl acrylate (β-CEA) and photopolymerized with HDDA in the presence of bis-(2,4,6-trimethylbenzoyl) phenylphosphine oxide. Surprisingly, up to 12 wt% of β-CEA-boehmite could be incorporated, resulting in 53.2% higher (87.1 MPa) flexural strength compared to the neat resin (56.8 MPa). However, only 6 wt% methacrylate-boehmite could be incorporated, and the resulting flexural strength only increased by 26.7%. This significant difference was due to the different grafting efficiency of β-CEA and methacrylate groups. During the modification step, the boehmite-water mixture was weak acidic, and the methacrylate groups MAPTS used for functionalization tended to self-condense, therefore limiting the grafting amount. In contrast, the reaction between β-CEA and boehmite was promoted under acidic conditions. As a result, β-CEA-boehmites were better dispersed in HDDA and reflected a significant mechanical enhancement. Moreover, the β-CEA-boehmite showed versatile reactivity in various monomer systems, including PEGDA and Bis-GMA/TEGDMA. Therefore, they were highly feasible in 3D printing.

In addition to silica/alumina-based clay, calcium-based minerals are also of great interest, especially the hydroxyapatites (HAs), which form the mineral phase of bones.[163] A group fabricated polymer composites containing hydroxyapatites that had osteogenesis

potential.[164] To avoid aggregation, nano HAs were functionalized with hydroxyethyl methacrylate (nHAMA) and photocrosslinked under a UV lamp (wavelength of 365 nm and intensity of 5 mW/cm^2, Analytikjena, Germany) with tri-block poly (lactide-*co*-propylene glycol-*co*-lactide) dimethacrylate (P_mL_nDMA, m and n respectively represent the unit length of propylene glycol and lactide) in the presence of Irgacure 819.[164] The modification allowed exceptional dispersity where loading of 50 wt% nHAMA could be achieved. The improved interfacial bonding between P_mL_nDMA and nHAMA, therefore, resulted in a 10-and 9-fold increase in tensile modulus (157 MPa) and compressive modulus (362 MPa) respectively, compared to the neat resin (16 and 43 MPa, respectively). The photocured composites allowed the encapsulation of heat-labile molecules and a long-term release over 60 days. In addition, they also showed good biocompatibility and oestrogenic potential (Figure 1.7), which can be potentially used for bone grafts.

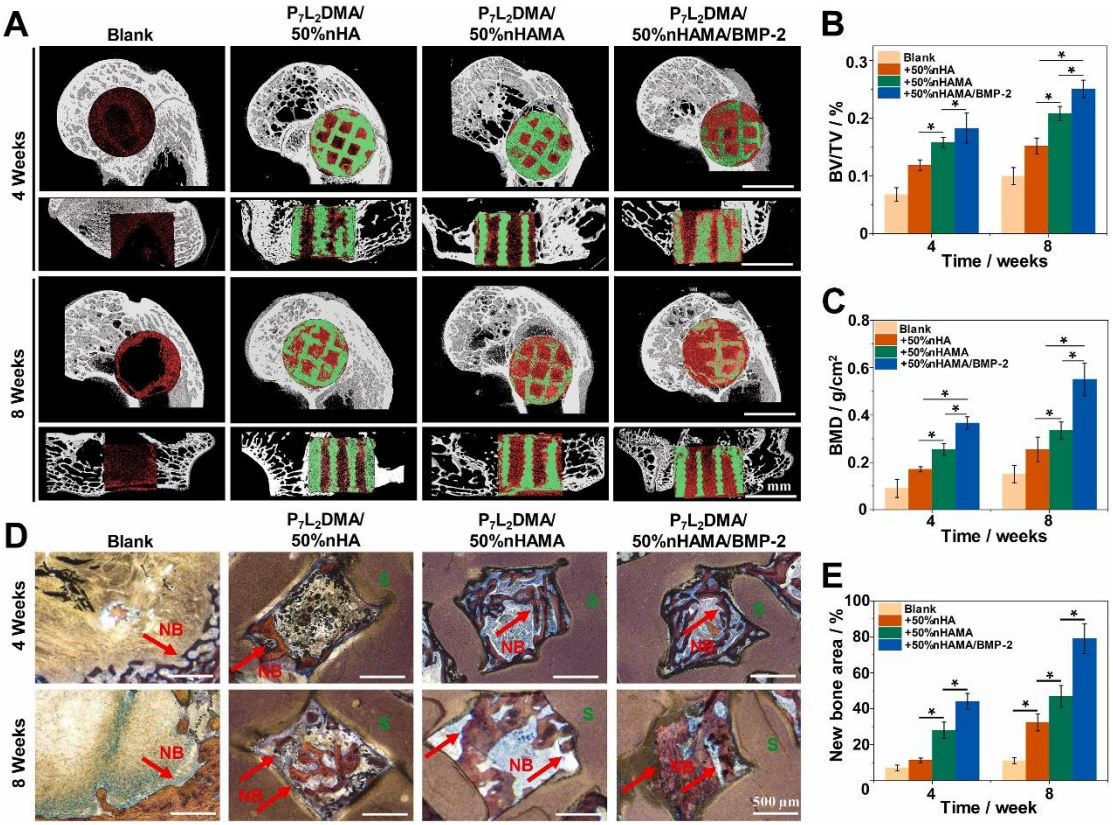

Figure 1. 7. Micro-CT evaluation and histomorphological observation of the *in vivo* bone regeneration in a rabbit femoral condyle defect model. The femoral condyle defects were

implanted with P_7L_2DMA/50%nHA, P_7L_2DMA/50%nHAMA and P_7L_2DMA/50%nHAMA/BMP-2 scaffolds, and the rabbits with no scaffold implantation served as blank control. (A) 3D reconstructed micro-CT images of different groups showing the influences of different samples on the new bone formation after implantation for 4 and 8 weeks. The red color indicated the new bone tissues and green color represents the scaffolds. Quantitative statistic of (B) BV/TV and (C) BMD of the newly formed bone at week 4 and 8. BV/TV: bone volume/total volume; BMD: bone mineral density. (D) Representative images of Van Gieson's staining showing the osseointegration of scaffolds with the new bones. S represented implanted scaffolds and NB indicated new bone tissues. The red-stained areas indicated by the arrows refer to the ossein. (E) Quantitative analysis of the new bone area in the defects. Data are presented as mean ± SD and analyzed by one-way ANOVA (n = 6 for each group, *p < 0.05).[164] Copyright 2020. Reproduced with permission from Elsevier.

1.7.3. Carbon-based nanomaterials

Carbon nanomaterials are well known for their superior mechanical properties. In this section, three types of carbon-based nanomaterials, *i.e.* graphene oxides, graphene nanosheets, and carbon nanotubes, will be discussed. The structures of three types of carbon-based nanomaterials are depicted in Figure 1.8.

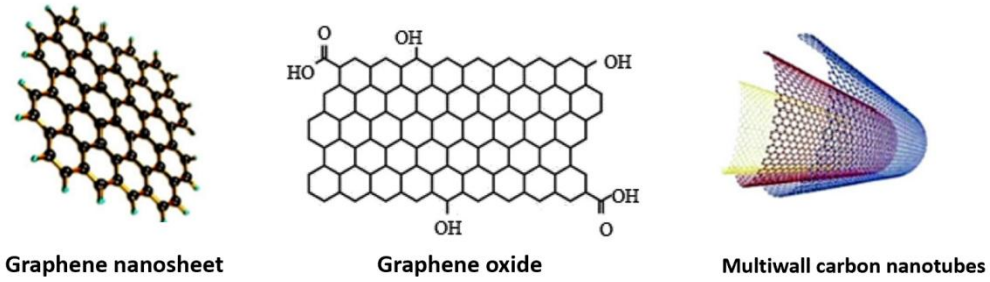

Figure 1. 8. structures of carbon-based nanomaterials.[165] Copyright 2020. Reproduced with permission from Elsevier.

1.7.3.1. Graphene oxides and graphene nanosheets

Similar to other inorganic nanomaterials, graphene oxides (GOs) suffer from severe aggregation when directly mixing into a polymer matrix which significantly affects the mechanical properties. Therefore, a strong matrix-filler interaction is required to allow successful load transmission when an external force is applied. Just like the majority type of

modification, GOs were modified with acryloyl chloride (fGO) and mixed with a methacrylate-based resin (MA) to form the 3D printing prepolymer.[166] With irradiation of 405 nm light (Formlabs), MA-fGO nanocomposites could be successfully 3D printed. At the optimal loading of 0.2 wt% fGO, the MA-fGO nanocomposites exhibited a 46% increase in ultimate strength (from 40 MPa to 60 MPa), 66% increase in ductility (from 3.5% to 6%), and 186% increase in toughness (from ~75 MPa $m^{1/2}$ to ~210 MPa $m^{1/2}$) compared to the neat MA. With the superior mechanical properties achieved, the fGO was viable in drone parts manufacturing as shown in Figure 1.9.

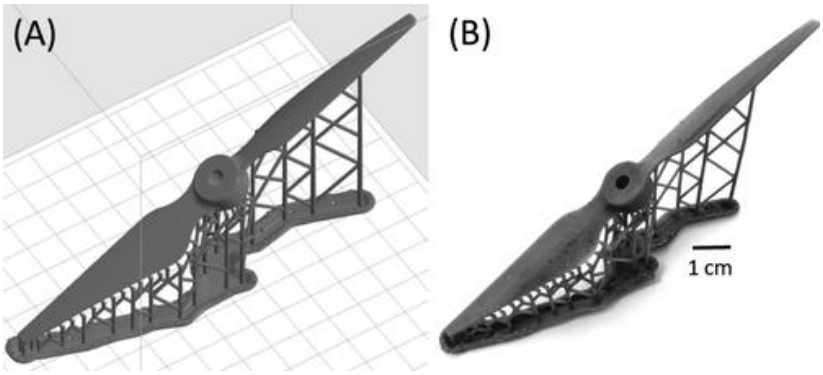

Figure 1. 9. Images showing the drone blade (A) .STL file object and (B) 3D-printed fGO nanocomposite suitable for a drone manufacturing application.[166] Copyright 2019. Reproduced with permission from American Chemical Society.

In another study, GOs were functionalized with a sniff base, *N*-(3-triethoxysilylpropyl)propan-2-imine (ITES).[167] The detailed synthesis steps are depicted in below Figure 1.10. Notably, three GOs with different functionalization levels (ratio of NH_2/NH^{3+} groups), i.e. AGOL, AGOM, and AGOH were obtained (L, M, and H stand for low, medium, and high). They were blended with commercially available methacrylate-based resin containing photoinitiators and subjected to further characterizations and 3D printing. Specifically, the necessary loading of functionalized GO to achieve superior mechanical properties was only 0.01 wt%. AGOL, which had low grafting density resulted in the production of a ductile composite; while AGOH, with high grafting density, produced a brittle

composite. The toughness also followed the same trend, which AGOH being the lowest (24 MPa), followed by AGOM (342 MPa), and the toughest AGOL (562 MPa). In addition, AGOM and AGOH, with higher grafting density compared to AGOL showed a more exfoliated morphology.

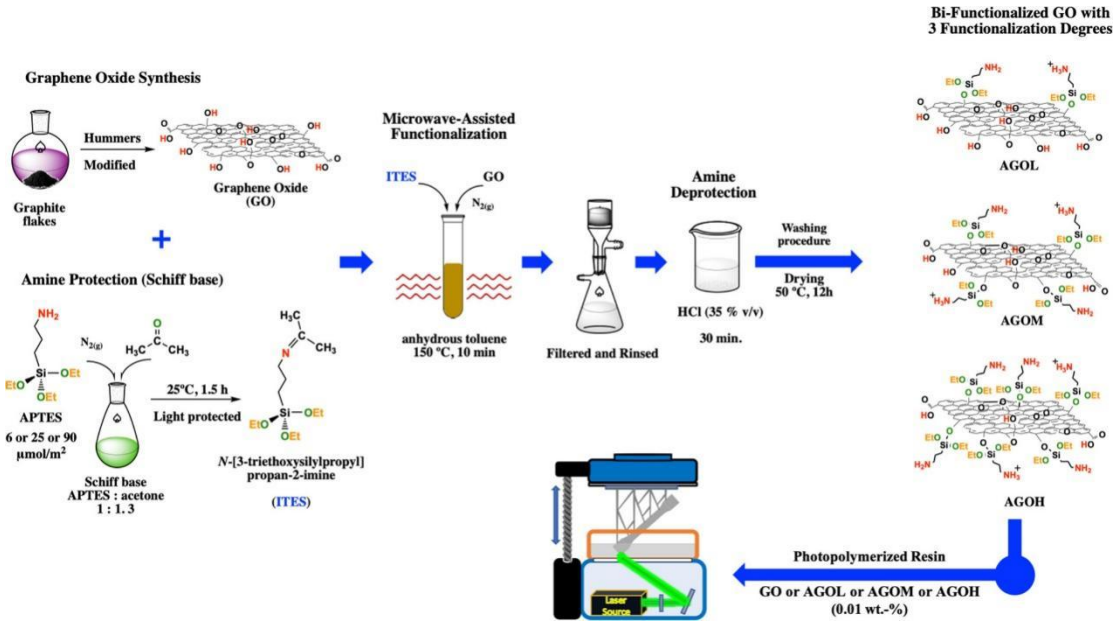

Figure 1. 10. Surface bifunctionalization of GO with NH2/NH3+ at different functionalization levels and their use to achieve stereolithographic 3D-printed nanocomposites with tuned toughness.[167] Copyright 2020. Reproduced with permission from American Chemical Society.

Since thiol-ene photopolymerization yields final products with low shrinkage and uniform structure, a thiol compound, 3-mercaptopropyl trimethoxysilane was used to modify graphene nanosheets (FGNSs) as shown in Figure 1.11.[168] FGNSs were then photopolymerized with triallyl isocyanurate (TAIC) by adding 2-hydroxy-2-methyl-1-phenyl-1-propanone (Darocur 1173) as the photoinitiator. While the unfunctionalized GNSs were stacked in the polymer matrix, FGNSs were exfoliated and finely dispersed. The strong interfacial adhesion and high stiffness of graphene endowed the corresponding composites with up to 138% enhancement in storage modulus (From ~1500 MPa to 3500 MPa).

Moreover, they also exhibited enhanced thermal stability due to the barrier effect of lamellar structure.

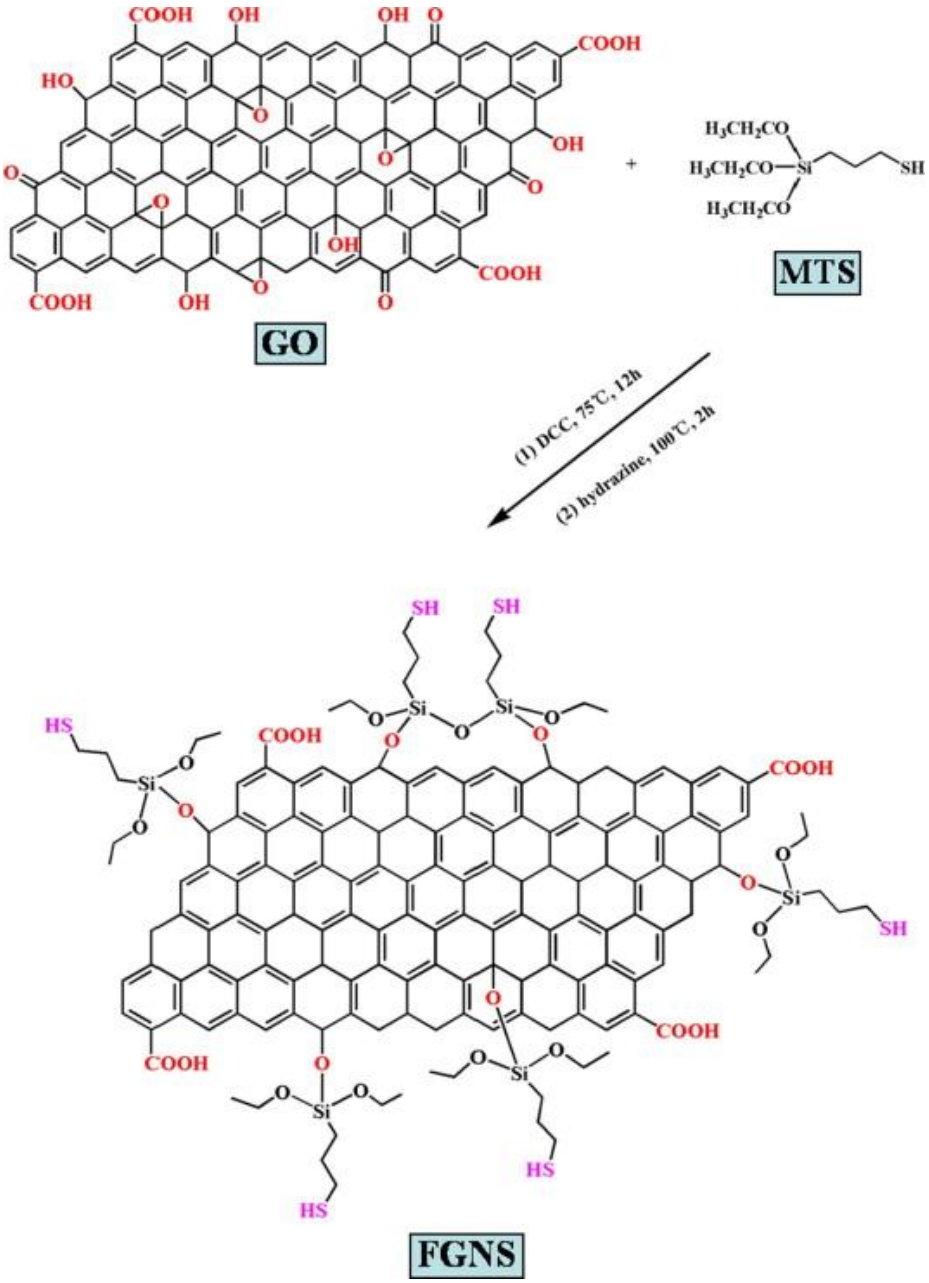

Figure 1. 11. Schematic illustration of the synthetic route of functionalized graphene nanosheets.[168] Copyright 2013. Reproduced with permission from Elsevier

Besides polymerizable groups, magnetic Fe_3O_4 was also considered a promising functionalization group on the GNSs (f-GNSs).[169] Upon irradiation with LED lamps at 385 nm, the mixture of f-GNSs, aliphatic urethane diacrylate, 2-hydroxyethyl methacrylate

(HEMA) and isobornyl acrylate (IBOA) was photopolymerized with the addition of bis (2,4,6-trimethyl benzoyl) phenylphosphine oxide. Since the modification yielded magnetic f-GNSs, the orientation of f-GNSs in the polymer matrix was then controlled by placing magnets below the prepolymer prior to the irradiation. Interestingly, the composite films with f-GNSs oriented in the horizontal alignment displayed superior tensile and barrier properties (i.e., water vapor transmission rate (WVTR) of only 0.89 g-mm/m^2/day) than the materials with random-dispersed f-GNSs (1.87 g-mm/m^2/day) or f-GNSs oriented in vertical alignment (5.57 g-mm/m^2/day). Therefore, the encapsulation of the horizontal-oriented f-GNSs composites greatly extended the lifetime of organic photovoltaic (OPV) cells, which made them highly applicable in producing stable photovoltaic devices.

1.7.3.2. Multiwall carbon nanotubes (MWCNTs)

Apart from two-dimension graphene, three-dimension MWCNTs are also widely selected as nanofillers in producing composite materials. MWCNTs were functionalized with poly(ethylene glycol) methacrylate (PEGMA).[170] Unlike most studies where only one type of nanofillers was used, this work used both the PEGMA-MWCNTs and Si NPs to enhance the corresponding composites' properties. In brief, the prepolymer contained the following: epoxy acrylate LR 8992 and poly(dimethyl siloxane-urethane methacrylate) (PDMS-U methacrylate) as reactive oligomers, HDDA and nonbornyl acrylate as crosslinkers, N-vinyl pyrrolidone (NVP) as a reactive diluent, and PEGMA-MWCNTs, sol–gel precursor, and hydrophobic nanosilica as nanofillers. The prepolymer was photocured under UV irradiation in the presence of Irgacure 184. Interestingly, when only PEGMA-MWCNTs were added, phase-separated morphology was observed, probably due to the micro-micellization of the hydrophilic and hydrophobic chain. Agglomeration was observed when the sol-gel precursor was added. In this case, the hydrophobic silica acted as a reinforcer to overcome

the phase separation. Overall, the modulus of the composite increased from 245 MPa to 318 MPa after the addition of PEGMA-MWCNTs and silica. Even though the mechanical property did not increase to a great extent, this study demonstrated the synergetic effect of multiple nanofillers on the final composite properties.

Unlike most modifications that focused on polymerizable groups or photoinitiators, one selected polydopamine (PDA) as a functional group.[171] As shown in Figure 1.12, MWCNTs were modified with PDA via surface oxidative polymerization (PDA/MWCNTs) and subsequently photopolymerized with 3,4-Epoxycyclo hexylmethyl-3′,4′-epoxycyclohexane carboxylate (ECC) in the presence of diphenyliodonium hexafluorophosphate (Iod) and N-vinylcarbazole (NVK). Surprisingly, PDA/MWCNTs showed dual roles, which can not only act as mechanical reinforcement but also act as photosensitizer/co-initiator in accelerating polymerization rate. Specifically, the conversion was improved from 28% to 69% compared to the system containing a commercial photoinitiator (Irgacure 819). This was ascribed to the synergy between MWCNTs and PDA where MWCNTs act as an electron sink to prevent charge recombination, thereby leaving more reactive species in the system to achieve higher final conversion. Furthermore, the PDA component was highly compatible with multiple surfaces, and the PDA/MWCNTs were therefore highly applicable in coating, adhesive and 3D printing.

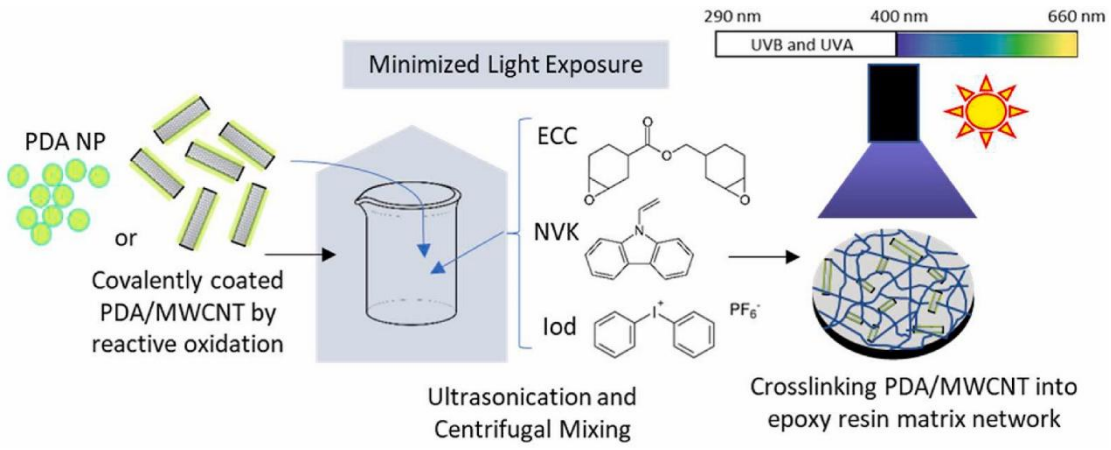

Figure 1. 12. Process Methodology: PDA and MWCNT nanohybrids as photosensitizer/co-initiator.[171] Copyright 2022. Reproduced with permission from Elsevier

1.7.4. Bio-based nanomaterials

1.7.4.1. Nanocellulose

The abundance and renewable nature of nanocellulose make them suitable nanofillers in preparing biocompatible composites. To achieve high bio-based composites, the functionalization has not been limited to photoinitiators[172] and polymerizable groups,[173] but also fatty acids [174] and plant polymers.[175] In the case of photoinitiator modification, celluloses were grafted with bis(acyl)phosphate oxide (BAPO) to yield the photoinitiating cellulose nanocrystals (BAPO-CNCs).[172] Importantly, high grafting density with up to 2100 BAPO units in each CNC was achieved, resulting in a much shorter gelation time of poly(ethylene glycol) methyl ether methacrylate (PEGMEM) compared to the systems contained either BAPO or BAPO/unmodified CNCs. This was extremely important, especially in 3D printing, where high fidelity and resolution can be achieved. The functionalization of BAPO provided crosslinking sites between CNCs and PEGMEM, which a higher gel content (>80%) could be achieved compared to the one with BAPO (16%) or BAPO/unmodified CNCs (22%). The high gel content reflected an extraordinary swelling ratio of up to 1100% (Figure 1.13) and doubled Young's modulus (from 130 MPa to 270 MPa). Such efficient photoinitiating CNCs were therefore highly applicable in 3D printing.

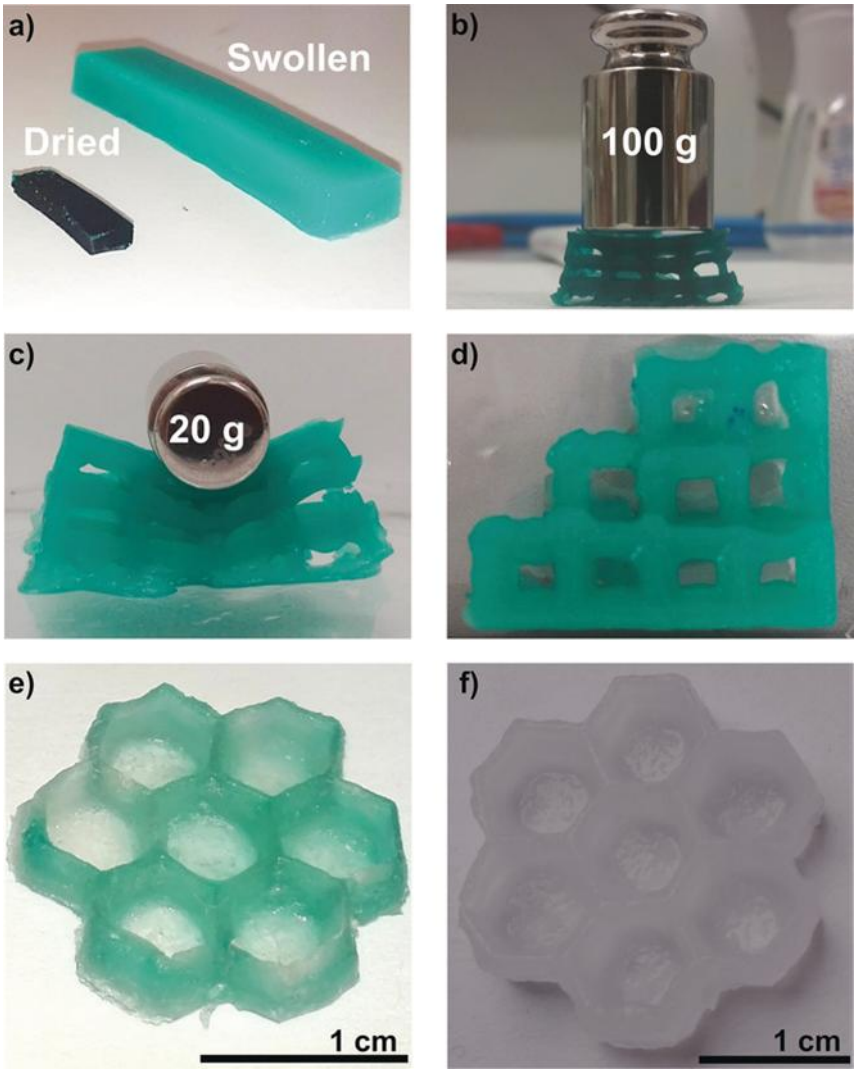

Figure 1. 13. a) Flat specimen from III. b) A dried cubic-lattice structure from III. c) The same structure after swelling for 1 h. d) The maintained structure after removing the 20 g weight. e) A hexagonal structure from IV. f) The swollen structure after repeating three times the drying and swelling procedure. The green dye, which was used to adjust the optical density during 3D printing, was washed out by re-dissolving in water.[172] Copyright 2018. Reproduced with permission from John Wiley and Sons.

In the case of polymerizable group modifications, CNCs were functionalized with acryloyl chloride (fCNCs) and subsequently photopolymerized with an elastic polymer (EP, Formlabs, US) containing methacrylate monomer, oligomer, and photoinitiating systems.[173] Interestingly, a lower loading of fCNCs (0.2-0.4 wt%) did not result in mechanical improvement, while a loading of 0.5 wt% resulted in 30% mechanical improvement (from ~1300 kPa to ~1700 kPa). Further increase of loading (0.6 – 1 wt%) again degraded the

mechanical properties. The optimal amount of fCNCs allowed the formation of a strong primary network where stress was transferred effectively. At much lower loading (0.2 wt%), the matrix reached its strain before transfer to the reinforced fCNCs, while above the percolation threshold, the matrix fraction decreased and became insufficient to support both primary and secondary networks. Nevertheless, with the optimal loading (0.5 wt%), ductility (from 25% to 38%), tensile strength (from ~1300 kPa to ~1700 kPa) and toughness (from 72 J-m^{-3} to 144 J-m^{-3}) have been increased by 50%, 30% and 100%, respectively. In addition, complex structures as shown in Figure 1.14 could be easily printed with the investigated formulas, suggesting the potential in various industrial applications such as 3D printing of an air-purifying respirator and prostheses.

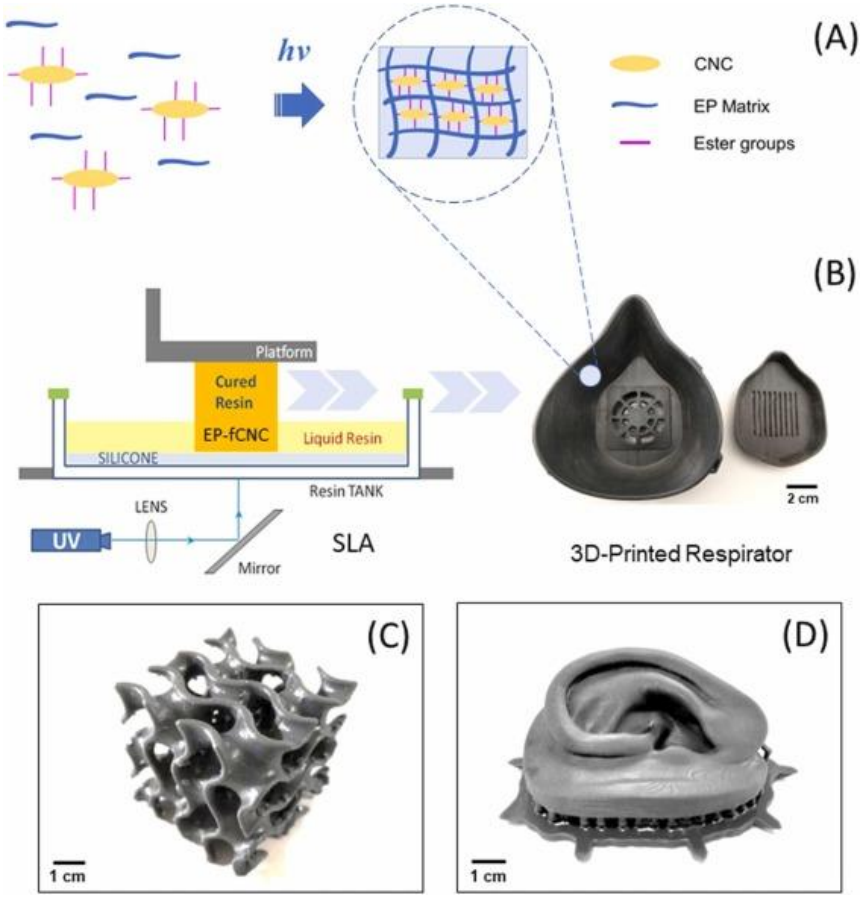

Figure 1. 14. (A) Photopolymerization of elastomeric matrix (EP), adsorbing on the surface of CNC through covalent bonding with the ester moieties in situ (B) 3D printing of complex structures via SLA such as air-purifying respirator, (C) gyroid cube, and (D) human ear construct using EP-fCNC thermosetting elastomeric nanocomposite material developed in

this study, demonstrating high degree of 3D printing flexibility, stability, and repeatability potentially suitable for various industrial applications.[173] Copyright 2022. Reproduced with permission from Elsevier.

Alternative to short polymer modification, long polymer modification and their effects have also been accessed. Compared to other studies, the lignin-coated CNCs (L-CNCs), however, only showed a minor increase in tensile strength (from ~35 MPa to ~37 MPa) for the photocured L-CNCs/methacrylate composites when an optimal amount (0.5 wt%) was added.[175] The insufficient interaction between L-CNCs and the matrix was responsible for the poor mechanical properties. On the other hand, CNCs modified with fatty acid extracted from safflowers oil (SOFA) behaved differently from the L-CNCs.[174] The modification considered the compatibility of modified groups and photocured matrix. Since the matrix (eResin-PLA photopolymerresin (RPLA)) was hydrophobic, the modification was therefore focused on the hydrophobization of CNCs. The excellent compatibility resulted in greater dispersity compared to other modified CNCs, and subsequently increased the maximum possible loading of SOFA-CNCs to 5 wt%. This was hardly achieved in other studies where CNC modification was also performed with a maximum loading of 1 wt%.[173, 175] Besides, the transparent natural of SOFA-CNCs also facilitated the photopolymerization compared to those using carbon-based nanofillers (graphene, carbon nanotubes, etc.). Overall, the high transparency, excellent compatibility, mechanical reinforced properties, and high bio-based content of SOFA-CNCs made them suitable for the preparation of environmentally sustainable composites via 3D printing.

1.7.4.2. Chitins and chitosan

Chitins, which have a structure similar to cellulose, are more hydrophobic in nature due to the presence of acetyl groups compared to hydroxy groups in celluloses. Similar to one of

the previous work, where chitins (CNCs) were modified with acryloyl chloride (fCNCs)[173], chitin nanowhiskers (pCNWs) were also modified with acryloyl chloride.[176] However, they exhibited slightly different mechanical performance compared to fCNCs. With the same optimal loading of 0.5 wt% of CNCs, pCNWs showed a greater extent of mechanical reinforcement (from 35 MPa to 65 MPa, ~78% increase in tensile strength) after photopolymerization into the corresponding nanocomposites compared to fCNCs nanocomposites (from ~1300 kPa to ~1700 kPa, 30% increase in tensile strength). This was probably due to the more hydrophobic nature of pCNWs which increased the compatibility between nanofillers and matrix, thereby facilitating mechanical reinforcement. The importance of the compatibility of fillers with the matrix was also reflected in another chitin-modified study. Two modified chitins with different hydrophobicity were synthesized.[177] One was modified with methacrylic anhydride (ChNC-MA) and the other with decanoyl chloride (ChNC-C10). Photopolymerization was carried out using resin containing ethoxylated bisphenol A dimethacrylate (Bis-EMA), TEGDMA, HEMA, and the photoinitiator (camphorquinone/ethyl 4-(dimethylamino)benzoate). Noticeably, aggregation was found in the ChNC-MA incorporated composites, while ChNC-C10 was found to disperse better. This was ascribed to the shorter chain length and lower substitution in ChNC-MA, making them more hydrophilic than ChNC-C10, therefore, less compatible with the hydrophobic matrix. As a consequence, the resin was better reinforced by ChNC-C10, with higher flexural strength and hardness achieved compared to the neat resin.

The hydrophobic nature of chitins limits their potential applications. Therefore, their derivative, chitosan, with increased hydrophilicity, is usually selected.[178] Owing to the excellent biocompatibility, biodegradability, and antibacterial ability of chitosan[179], it is usually prepared into hydrogels for wound dressing and tissue engineering.[180, 181] To achieve fast curing at physiological temperature and spatial temporal control of hydrogels,

the photopolymerization approach is always preferred. An interesting highlight has summarized the various modifications of chitosan such that they could be photocrosslinked into functional hydrogels.[182] Nevertheless, the hydrogels prepared by only chitosan usually lack promising mechanical properties.[183] Consequently, designing corresponding composite materials is intriguing to enhance mechanical properties and expand potential applications. Here, one of the groups synthesized maleilated chitosan (MCS) and photopolymerized with methacrylated silk fibroin micro/nanoparticles (MSF) in the presence of D-2959 photoinitiator under irradiation of Omnicure series 1000 UV light as shown in Figure 1.15.[184] Interestingly, the increase concentration of MSF (from 0% to 0.1%) resulted in a decrease in equilibrium water uptake of the corresponding composite hydrogels (from 13.49 g/g to 8.79 g/g). This was mainly due to the increased crosslinking density in the hydrogel system. Nevertheless, it also increased compressive modulus from 0.06 MPa to 0.32 MPa. Besides, the in vivo cytotoxic evaluation revealed the biocompatibility of this MCS/MSF composite hydrogel, which was therefore highly applicable to be used as cartilage repair materials.

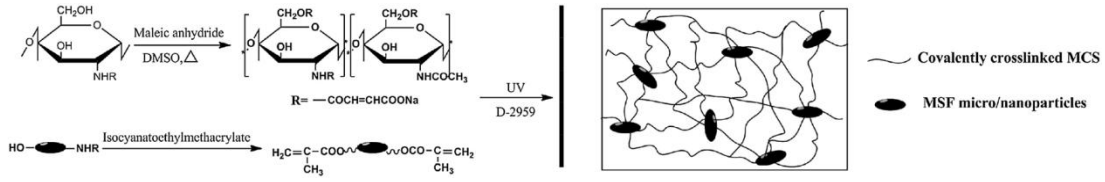

Figure 1. 15. Reaction schematic of MCS/MSF micro/nanocomposite hydrogels.[184] Copyright 2017. Reproduced with permission from Elsevier.

In an alternative study, chitosan-based nanofiber with micrometer pore size could be achieved via electrospinning followed by photopolymerization with poly(vinyl alcohol) mats (PVA).[133] In brief, chitosan was modified with photocrosslinkable methacrylate group (ethylene glycol arylate methacrylate (EGAMA)) through Michael addition reaction as depicted in Figure 1.16. The methacrylated chitosan (MACS) was mixed with D-2959 photoinitiator and PVA solution in a different ratio, electrospun into nanofibers, and

subsequently photopolymerized under the irradiation of Hg lamp. PVA was removed after that, leaving chitosan nanofibers with micrometer pores. Specifically, the addition of PVA (50 wt%) enhanced the electrospinnability by increasing the viscosity (from 0.6 to 1.14 Pa S) and reducing the electrical conductivity (from ~4.5 mS/cm to ~2 mS/cm) of the solution blend. Moreover, the tensile strength was also improved from 2.36 MPa to 3.37 MPa. The highly micro-porous structure was shown to facilitate cellular migration, making it highly applicable in tissue engineering.

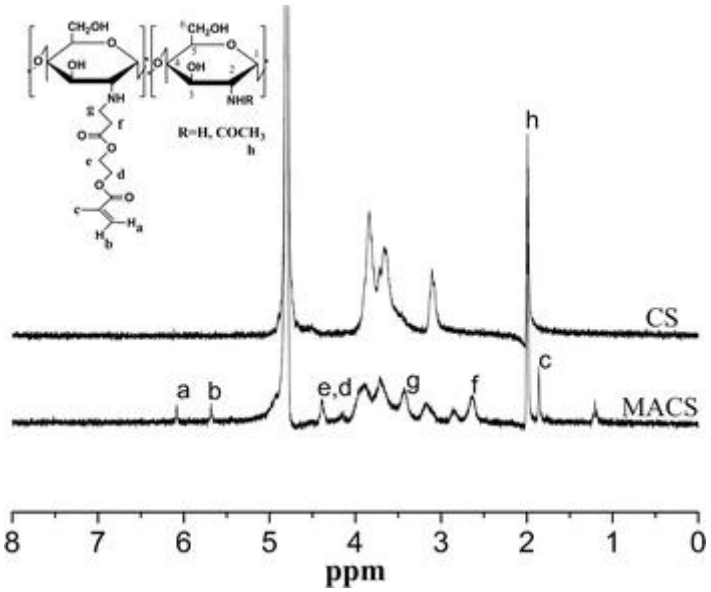

Figure 1. 16. structure of methacrylated chitosan (MACS) and its ^{1}H NMR spectra.[133] Copyright 2017. Reproduced with permission from Springer Science Business Media B.V.

1.8. Optical property

1.8.1. Halide perovskite quantum dots (QDs)

Halide perovskites have drawn a lot of attention for photovoltaic applications, making light-emitting diodes, X-ray detectors, and memory devices.[185-188] The inherent direct bandgaps, high absorption, and long exciton diffusion length offer them excellent optoelectronic properties, and the simple and accessible synthesis steps make them of interest in industries.[189, 190] The outstanding optoelectronic properties of halide perovskite QDs give a clue that they may demonstrate the potential to act as photoinitiators. $CsPbBr_3$ nanocrystals

(NCs) solution was mixed with styrene and irradiated with white light to achieve a polymer composite film with ~44% photoluminescence quantum yield (PLQY).[191] Specifically, the interaction between olefin's (styrene) filled π orbitals and an electron-deficient Pb was responsible for the photoinitiating ability of $CsPbBr_3$ NCs. Moreover, the degree of dispersity of $CsPbBr_3$ NCs was increased as the irradiation time increased since the longer polystyrene chains were polymerized on the surface of $CsPbBr_3$ NCs. After investigating the photoinitiating ability of $CsPbBr_3$ NCs, a red-emitting nanocomposite film containing $CsPbBr_{1.2}I_{1.8}$ NCs was prepared in a similar fashion. As such, by combining the two prepared green and red emitting composite films with a blue photoexciation LED as illustrated in Figure 1.17, a white light-emitting down conversion device that can be potentially used for color display was fabricated.

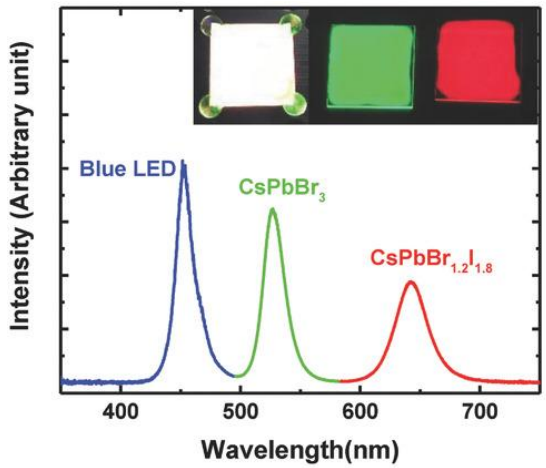

Figure 1. 17. Spectral characteristics and inset image of red and green-emitting perovskite–polystyrene nanocomposite films and their combination with a blue LED to form a white light-emitting downconversion device.[191] Copyright 2018. Reproduced with permission from John Wiley and Sons.

While a long irradiation time (14 h) was required in the previous study to allow polymerization, another work treated the $CsPbI_3$ NCs with a series of photoinitiators (triphenylphosphine (TPP), diphenyl (2,4,6- trimethylbenzoyl) phosphine oxide (TPO), DMPA, 1-hydroxycyclohexyl phenyl ketone (HPK) and 2-hydroxy-2-methyl-1-

phenylpropan-1-one (HMPO)) and photopolymerized in an acrylate monomer to prepare photoluminescence nanocomposite film in much shorter irradiation time.[192] Surprisingly, only the composite film contained TPP-treated $CsPbI_3$ NCs showed 88% of PLQY after photopolymerization, while the rest of the other photoinitiators-treated $CsPbI_3$ NCs composite films showed a drastic decrease in PLQYs (7.7%-26%). The interaction between $CsPbI_3$ NCs and TPP improved the photostability of the films, which was probably due to the ability of TPP to consume oxygen. With less oxygen present in the system, the $CsPbI_3$ NCs were prevented from photo-oxidation and therefore retained their photoluminescence properties even after polymerization. Enlighted with the excellent photoluminescence properties of the TPP-treated $CsPbI_3$ NCs, they were coated onto the polymethyl methacrylate (PMMA) to prepare a luminescent solar concentrator (LSCs). Impressively, an optical conversion efficiency of 3.1 % and optical quantum efficiency of 36 % were achieved as depicted in Figure 1.18.

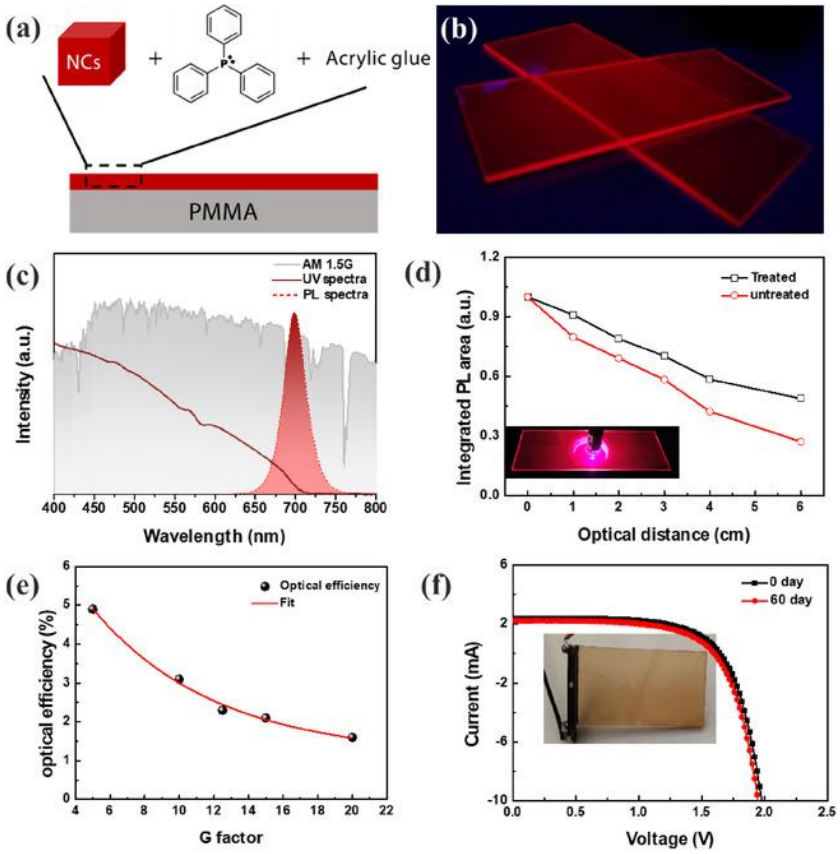

Figure 1. 18. a) Preparation of the thin-film LSCs using the doctor-blade method. b) Photograph of a 5×15 cm CsPbI3 NCs-based LSC under ultraviolet light. c) AM 1.5 G spectrum, UV/Vis absorption, and PL emission spectra of CsPbI3 NCs-based LSCs. d) Integrated PL emission of the untreated and TPP-treated LSCs at different optical paths. e) The optical efficiency of the LSCs coupled with silicon cell as a function of geometric factor (G factor). f) The I–V curves of the Si solar cell coupled with the edges of an LSC before and after storage for 2 months in ambient air.[192] Copyright 2020. Reproduced with permission from John Wiley and Sons.

Considering the photoinitiating potential of halide perovskites and the interaction with photoinitiators, our group has used $CsPbBr_3$ QDs as photoinitiators, with the aid of two different additives (Iod or ethyl 4-(dimethylamino) benzoate (EDB)) to achieve the corresponding photoluminescent composites with high stability.[193] It was found that $CsPbBr_3$ QDs could successfully initiate polymerization of thiol-ene system (triethyleneglycol divinyl ether (DVE-3) and pentaerythritol tetrakis(3-mercaptopropionate) (Tetrathiol)) under irradiation with 410 nm and 530 nm lights. The addition of Iod or EDB improved the photoinitiation ability of $CsPbBr_3$ QDs thereby increasing the polymerization rate and final conversion. However, when interacting with Iod, the CsPbBr3 QDs were significantly quenched, leaving the polymerized composites with minor photoluminescence. Alternatively, the interaction with EDB slightly quenched the $CsPbBr_3$ QDs and the corresponding composites showed long-term photoluminescence under elevated temperature or oxygen plasma environment as shown in Figure 1.19.

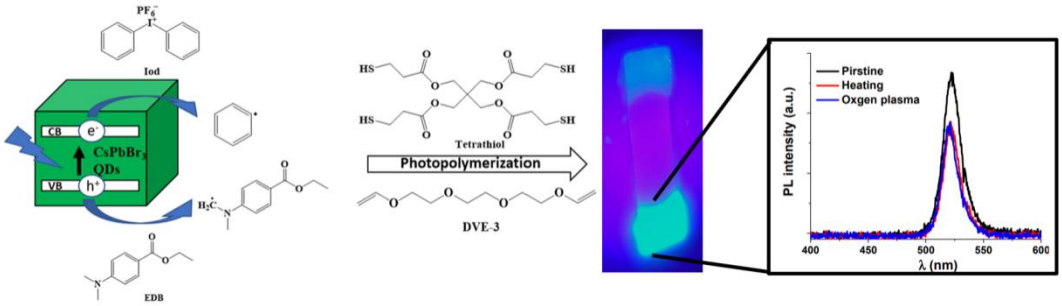

Figure 1. 19. Schematic Illustration of $CsPbBr_3$ QDs and Iod or EDB-induced thiol-ene photopolymerization under Light Irradiation. Photocured DVE-3/tetrathiol samples achieved (1:1 ene/thiol in functionality) in the presence of $CsPbBr_3$ QDs/Iod (up) and $CsPbBr_3$ QDs/EDB (down) ($CsPbBr_3$: 0.5 wt %; Iod: 0.5 wt %; EDB: 0.5 wt %) upon

exposure to LED@410 nm (110 mW cm^{-2}).[193] Copyright 2023. Reproduced with permission from American Chemical Society.

1.8.2. Boehmites and montmorillonites

As well known, the aggregation of inorganic nanofillers in a polymer matrix resulted in a light-scattering system, thereby limiting the production of highly transparent materials that are required in many optical applications. Therefore, surface modification of nanofillers to increase compatibility became the key solution. In one of the studies, two types of organo-modified boehmites illustrated in Figure 1.20 (one with *p*-toluenesulfonic acid (OS1), the other with C10-C13 alkylbenzenesulfonic acid (OS2)) were photopolymerized with 3,4-epoxycyclohexylmethyl-3′,4′-epoxycyclohexanecarboxylate in the presence of UVI 6976 under irradiation of Fusion lamp.[194] Unavoidably, the addition of two modified boehmites reduced the light transmittance. However, OS2-boehmite was found to induce a larger cluster in the matrix, resulting in a further decrease in light transmittance (reduced from 85% to 29%). The OS1-boehmite, on the other hand, was better dispersed, and the light transmittance of the corresponding composites could be retained at 64%. It again indicated the importance of understanding the chemistry between modified groups and matrix in order to correctly modify nanofillers with enhanced properties.

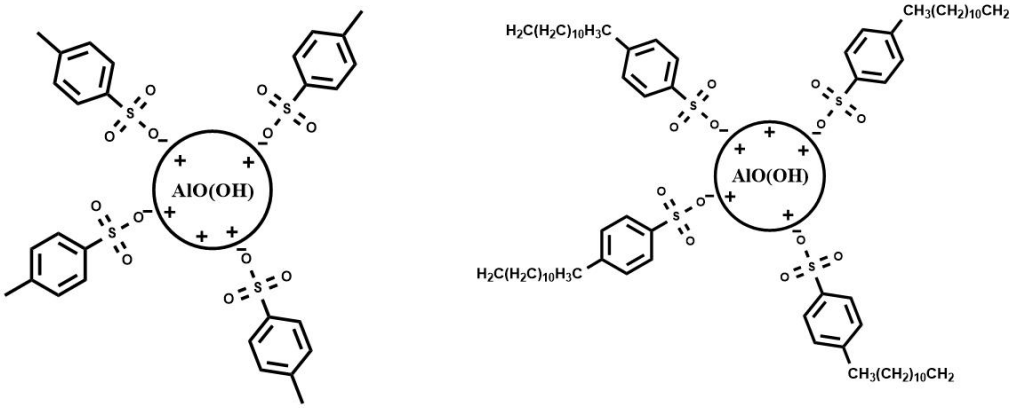

OS1-Boehmite **OS2-Boehmite**

Figure 1. 20. Structures of organo-modified boehmites.

In an alternative study, two nanocomposite coatings containing different photoinitiator-modified montmorillonites resulted in different optical properties.[195] In brief, the montmorillonites were functionalized with either Irgacure 2959 (PI-1-MMT) or benzophenone derivative (PI-2-MMT) and subsequently photopolymerized with urethane dimethacrylates. Specifically, the different chemistry of the two modifiers endowed the corresponding composites with different morphology. The PI-1-MMT composite appeared to be more intercalated, while PI-2-MMT appeared to be more exfoliated. In addition, PI-2-MMT composites showed a UV-shielding feature compared to PI-1-MMT composites owing to the UV light absorption nature of the benzophenone core, highlighting the great potential ofPI-2-MMT to be used for UV shielding materials.

1.9. Environment-related applications

1.9.1. Metal organic frameworks (MOFs)

To expand the structural diversity, a class of compounds with metal ions coordinated with organic linkers and metal-organic frameworks (MOFs) has brought wide attention. The outstanding porosity, internal surface area, and versatile synthetic tunability make them highly feasible, especially in environmental protection applications such as energy storage, wastewater treatment, and gas separation.[196, 197] Similar to other inorganic fillers, MOFs also suffer from aggregation issues. Typically, the modifications were done by functionalizing the organic linkers with polymerizable groups. Zirconium-based MOFs were functionalized with methacrylamide groups (UiO-66-NH-Met) and photopolymerized in the blend of butyl methacrylate (BMA) and phenylbis(2,4,6-trimethylbenzoyl)phosphine oxide (photoinitiator) to prepare a stand-alone membrane.[198] Compared to the unmodified MOFs,

UiO-66-NH-Met was found uniformly dispersed in the membrane owing to the improved chemical and physical interaction between MOFs and polymers. The corresponding membrane was then tested for pollutant separation. Surprisingly, it removed 80% heavy metal (Cr^{VI} ions) from the wastewater with a maximum separation capacity of 8 mg/g for only one cycle. This is much higher than the one with active carbon (4.3 mg/g) or unmodified MOFs (5 mg/g) membrane as depicted in Figure 1.21. As a result, this MOF-membrane was highly applicable in wastewater treatment.

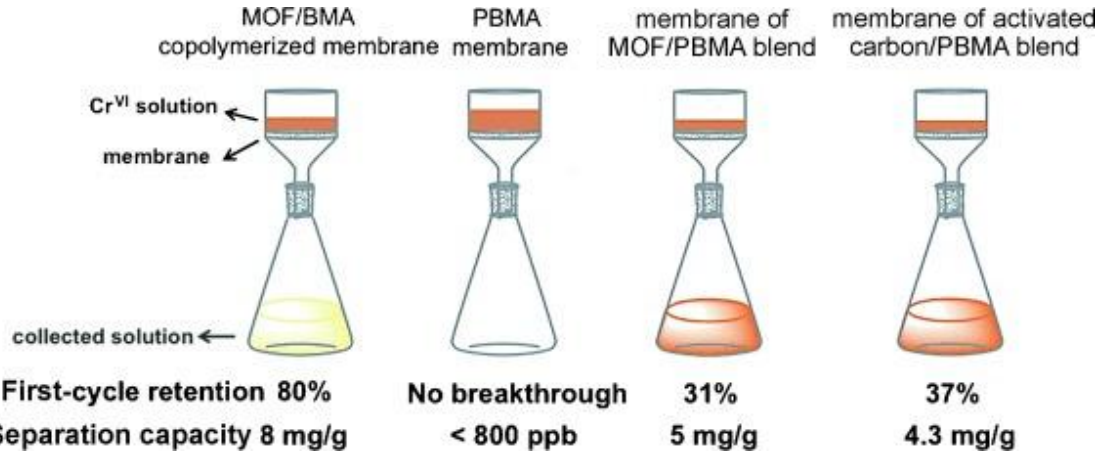

Figure 1. 21. Separation capacity for CrVI ions of a MOF/BMA copolymer membrane, a PBMA membrane, a membrane of a MOF/PBMA blend, and a membrane of an activated carbon/PBMA blend (unadjusted pH value, initial concentration and volume of K2Cr2O7 solution: 10 mg L−1×10 mL, performed in triplicate).[198] Copyright 2015. Reproduced with permission from John Wiley and Sons.

In an alternative study, vinyl-functionalized UiO-66-CH=CH_2 MOFs were synthesized using 2-vinyl-1,4-dicarboxylic acid as organic linkers.[199] They were then introduced into a monomer blend containing tetrathiol and 2,2-(ethylenedioxy)diethanethiol (EDDT)); poly(ethylene glycol) divinyl ether (PEO-250) and DMPA, followed by photopolymerization with super pressure Hg lamp (Lumatec Superlite SUV-DC-P, 315 <λ< 390 nm). Importantly, PEO-250 was selected since it showed affinity to CO_2 through strong dipole–quadrupole interaction. As expected, UiO-66-CH=CH_2 MOFs were well spread in the polymer, which was ascribed to the formation of the thioether linkage. The adhesion between MOFs and

polymer was improved, eliminating the potential interfacial defects. Thus a high loading of up to 60 wt% of UiO-66-CH=CH_2 MOFs could be incorporated. Moreover, the corresponding composites also achieved an 800% and 130% increase in Young's modulus (from 6 MPa to 59 MPa) and ultimate elongation (from 15% to 20%). In contrast, the unmodified MOFs suffered from severe aggregation, even with a relatively low loading of 20 wt%. Finally, the prepared membrane was tested for the potential for gas separation. Specifically, an increase in gas permeability was observed in UiO-66-CH=CH_2 MOFs composites compared to the pristine polymer. Following the previous work, dual-functionalized MOFs nanoparticles with core/shell morphology were further synthesized, as illustrated in Figure 1.22. In this case, MOFs contained 10% of polymerizable vinyl groups on the shell, while the cores contained either NO_2 group (UiO-66-NO_2) or naphthalene groups (UiO-66-Naph).[200] For photopolymerization, the same thiol-ene system and photoinitiators were used as in the previous work. Overall, the UiO-66-NO_2 membrane exhibited the highest CO_2 permeability and solubility when the loading concentration was 30 wt%. This was due to the strong absorption sites provided by the polar NO_2 groups. In addition, all the MOFs membrane presented a modest CO_2/CH_4 separation factor. The results together confirmed the potential of the composite membrane for gas separation application.

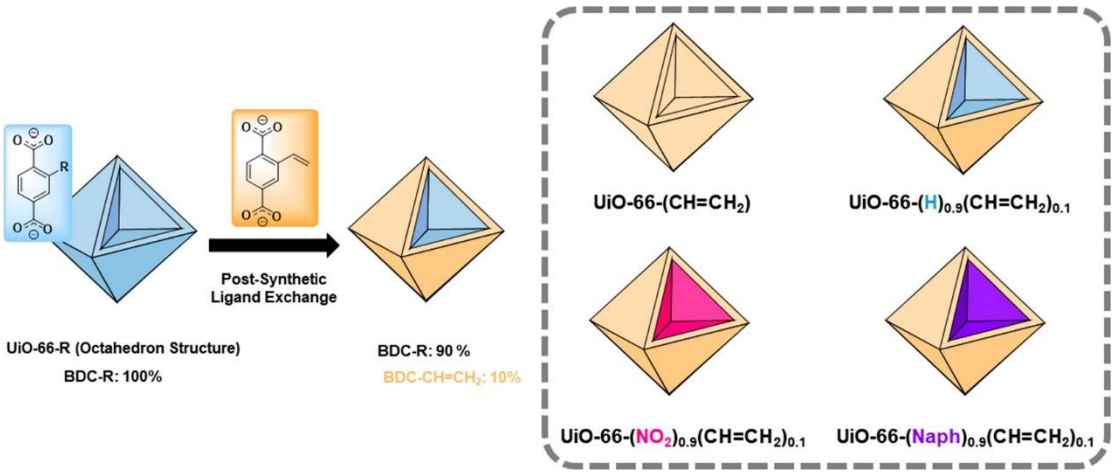

Figure 1. 22. Core/shell MOFs synthesized through PSE with vinyl functionality.[200] Copyright 2020. Reproduced with permission from American Chemical Society.

1.9.2. Ionic liquid and graphene oxides

Likewise, ionic liquids (ILs) have also been considered for carbon capture due to their selectivity of CO_2 over other gases (e.g., N_2, CH_4, and H_2). The first dual functionalizable ILs (1-Vinyl-3-butylimidazolium 1-[3-(Methacryloyloxy)propylsulfonyl]-(p-toluene-sulfonyl)imide (DIL)) were synthesized and subsequently photopolymerized with non-polymerizable IL ([C_4mim][Tf_2N]) and PEGDA in the presence of DMPA.[201] The structures and fabrication scheme are shown in Figure 1.23. The photocured poly(IL)-IL composite membranes were found to have good integrity with no free IL leaking out and high thermal stability. With the increased content of free IL, the membranes exhibited increased permeability for all gases. This was due to the changes in interchain spacing and chain flexibility, thereby creating more diffusive pathways for gas permeation. Additionally, the strong affinity between ionic liquid and CO_2 governed the high permselectivities of CO_2 over CH_2, N_2 and H_2 with the selectivity of 85.1, 68.1, and 3.5 respectively. Overall, this DIL was highly feasible for the preparation of gas separation membranes in industries.

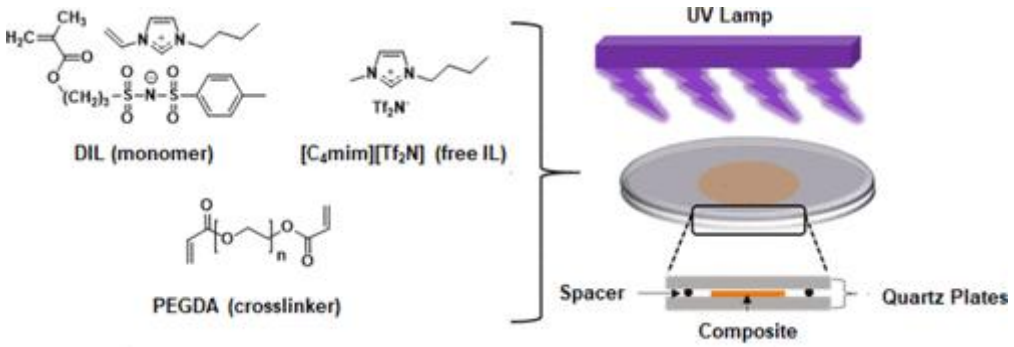

Figure 1. 23. Illustration of the poly(IL)-IL membrane composition membranes with PEGDA network.[201] Copyright 2020. Reproduced with permission from American Chemical Society.

Typically, graphene oxides (GOs) are widely used in mechanical reinforced applications or electronics. Interestingly, GOs were used to prepare functional hydrogels for wastewater treatment.[202] Briefly, GOs were modified with thiols (GO-SH), and then photopolymerized with poly(ethylene glycol) diacrylate (PEGDA) under irradiation of LUYOR-3405 UV lamp at 365 nm. With the increased addition of GO-SH, the pore volume and average pore diameter of the GO-SH/PEG composite hydrogels were larger than that of the pristine PEG hydrogel. The absorption ability of GO-SH/PEG composite hydrogels to three organic dyes (Congo red (CR), Rhodamine B (RhB), and methylene blue (MB)) was then evaluated. As expected, a hydrogel with the most concentrated GO-SH showed the greatest absorption ability towards the three dyes as shown in Figure 1.24. This was mainly due to its highest specific surface areas, allowing increased adsorbent activity points and more contact between dyes and activity points. Based on the excellent absorption properties of the GO-SH/PEG hydrogel, they were highly applicable for wastewater treatment.

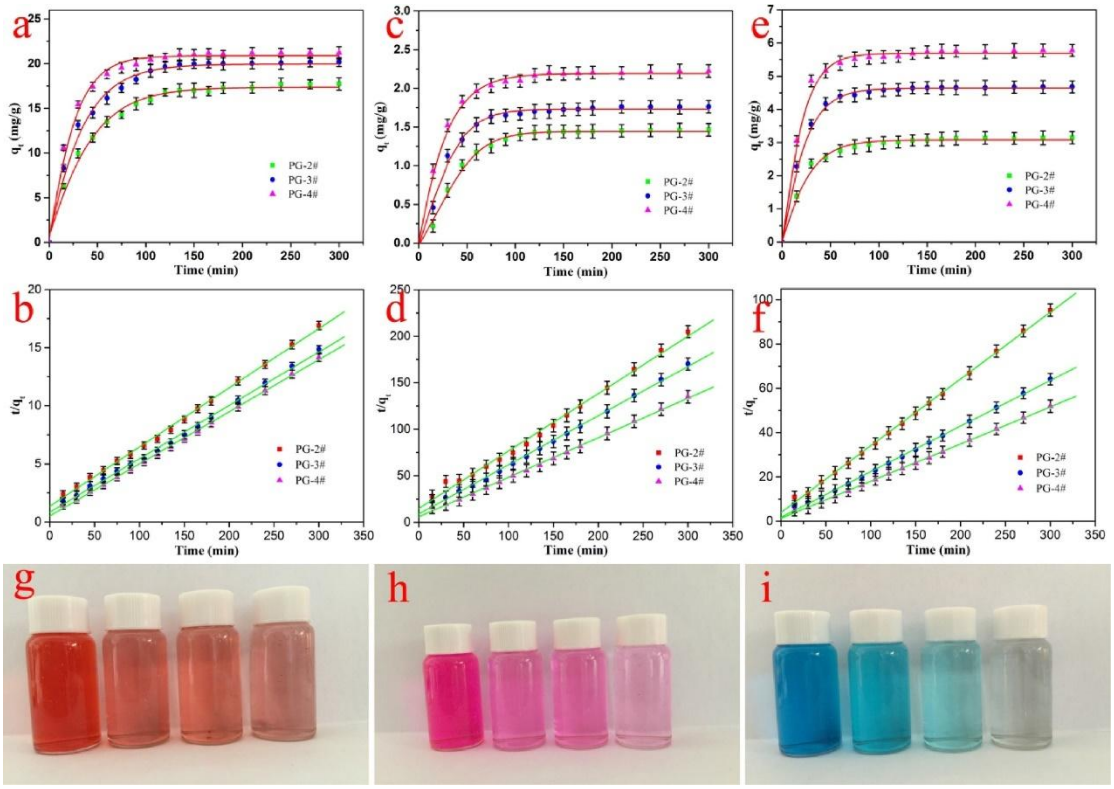

Figure 1. 24. Adsorption kinetics curves of as-prepared composite hydrogels (PG-2#, PG-3#, and PG-4#) on CR (a, b), RhB (c, d), and MB (e, f) at 298 K. Pictures (g, CR; h, RhB; i, MB) showed the dye solutions at different adsorption time intervals (0, 50, 100, and 280 min).[202] Copyright 2017. Reproduced with permission from Elsevier B.V.

1.10. Electric property

1.10.1. Carbon-based materials

Graphene is one of the most conductive materials, with conductivity values up to 1,000 times greater than copper. This makes it an excellent candidate for use in a wide range of electrical and electronic applications, such as batteries, capacitors, solar cells, and sensors.[203-205] Nevertheless, the high surface energy of graphene can lead to poor interfacial adhesion with the polymer matrix resulting in severe aggregation, which degrades the properties. As such, functionalization of gold nanoparticles onto graphene sheets (GNSs) was proposed and the corresponding composites were prepared via photopolymerization under a Fusion lamp by using 3,4-epoxycyclohexylmethyl-3',4'-epoxycyclohexyl carboxylate and triphenylsulfonium hexafluoroantimonate as polymerizable resin and photoinitiator, respectively.[206] The TEM revealed a homogeneous distribution of Au-GNSs in the polymer matrix. Furthermore, the charge transfer between gold and GNSs facilitated the increase in conductivity. Specifically, the conductivity was improved by four orders of magnitude from 10^{-6} S/m to 10^{-2} S/m. In an alternative study, a photoinitiator (benzophenone, BP) was used for modification. Unlike the commonly used chemical procedure, BP was functionalized onto the graphene oxides (BP-GOs) via UV irradiation as shown in Figure 1.25.[207] The BP-GOs were then used as fillers and photoinitiators in fabricating composites via photopolymerization in PEGMA or perfluoro butyl acrylate (PFBA). Specifically, more aggregates were found when polymerized in PFBA compared to PEGMA, possibly due to the increased hydrophobicity of perfluoro

chains. The conductivity measurements were then evaluated. Surprisingly, the BP-GOs were found to have a bulk conductivity that was two orders of magnitude higher compared to the pristine GOs. During the BP UV functionalization step, they also reduced the GOs, resulting in increased electrical conductivity. Nevertheless, a moderate electric conductivity was achieved (1.5 S/cm) for the prepared BP-GOs composites.

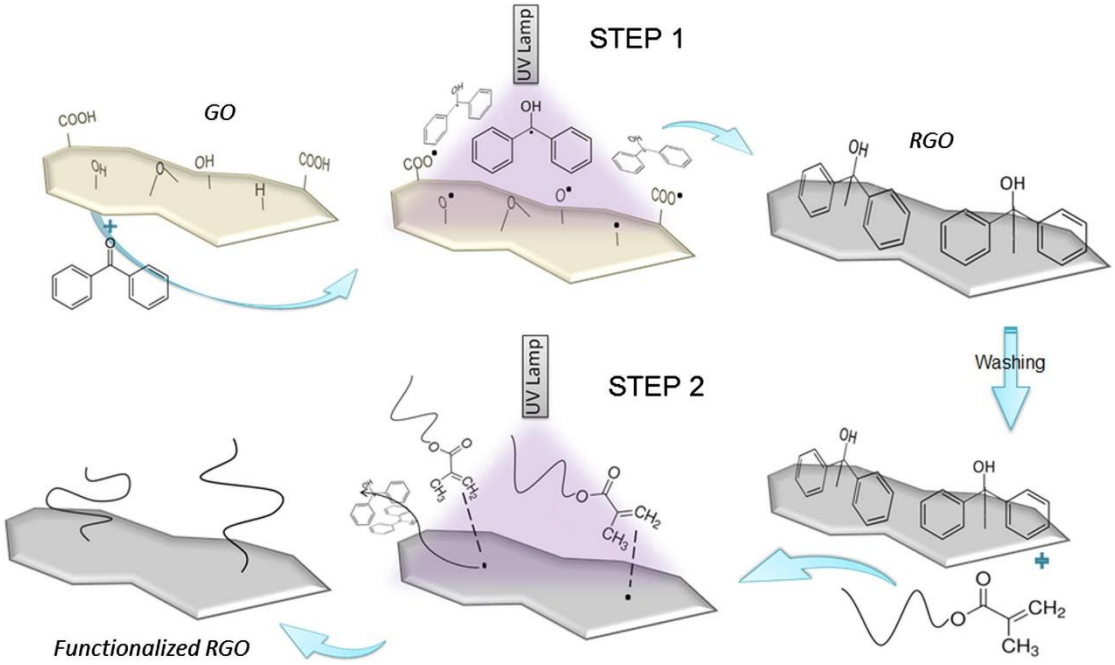

Figure 1. 25. Scheme of the two steps functionalization reaction.[207] Copyright 2014. Reproduced with permission from Elsevier.

1.10.2. MOFs and $BaTiO_3$

In addition to the important application of separation and purification, MOFs could also be applied to the design of high-performance Li-ion batteries. UiO-66-NH_2 MOFs were decorated with polycaprolactone (PCL), together with PEGDA, boronic ester monomer (BEM), lithium salt, and 1-hydroxycyclohexyl phenyl ketone, and then photopolymerized to yield the corresponding electrolyte composite.[208] Specifically, the modification improved the dispersity of MOFs in the matrix and the formation of a crosslinked network suppressed the formation of lithium-dendrites, leaving the electrolyte with a wide electrochemical window of

5.29 V and a high lithium-ion transference number of 0.59. Furthermore, the excellent long-cycling and rate performance indicated the high potential of the studied modified MOFs in high-performance Li-ion battery fabrication.

Other than MOFs, $BaTiO_3$, a perovskite material has drawn a lot of attention for electrical devices due to its unique ferroelectric properties. One of the groups was therefore selected for the fabrication of a pressure sensor.[209] In brief, $BaTiO_3$ nanoparticles were functionalized with 3,4-dihydroxyhydrocinnamic acid (HCA-$BaTiO_3$) to achieve good dispersion in an aqueous solution. Blending with polyvinylpyrrolidone (PVP), a copolymer of HEMA and acrylonitrile (AN) (HEMA-co-AN), ethylene glycol dimethacrylate (EGDMA), and DMPA followed by photocuring with the Blackray B100-AP UV lamp, a HCA-$BaTiO_3$/inogel composite was synthesized. With the incorporation of HCA-$BaTiO_3$ nanoparticles, the composite exhibited improved electromechanical properties, which could sense 5 kPa pressure and respond with up to 8 mV while the pristine inogel only responded with 3.5 mV. The electrochemical responses of pristine inogel and HCA--$BaTiO_3$/inogel composite are depicted in Figure 1.26. In addition, when the loading direction was opposite, the HCA-$BaTiO_3$/inogel composite responded with only 3 mV. The combination of the piezoelectric effect and anisotropy response of HCA-$BaTiO_3$/inogel composite made it feasible to be used as a discriminative pressure sensor.

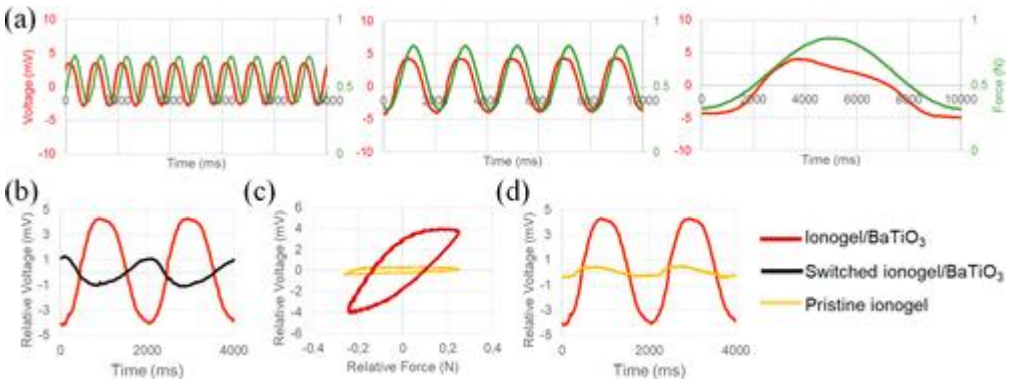

Figure 1. 26. (a) IG/BAT-Nc response at 0.1 (left), 0.5 (middle), and 1 Hz (right). (b) Anisotropic response of the IG/BAT-Nc at 0.5 Hz, observed by flipping the sample with respect to the normal force direction (c) Hysteresis loop of pristine ionogel and IG/BAT-Nc,

the latter showing the typical ferroelectric behavior. (d). Pristine ionogel and IG/BAT-Nc response at 0.5 Hz.[209] Copyright 2019. Reproduced with permission from American Chemical Society.

1.11. Conclusion and future perspectives

The use of photopolymerization for fabricating functional polymer composites containing functionalized nanofillers is a rapidly growing area of research with significant potential across various applications, including biomedical devices, environmental sensing, and optoelectronic materials. However, despite the advantages of photopolymerization—such as rapid curing, solvent-free processing, and precise spatial control—several challenges remain in achieving optimal nanofiller dispersion, strong interfacial adhesion, and efficient light penetration in highly loaded nanocomposites.

A key issue in photopolymerized nanocomposites is the aggregation of nanofillers, which can deteriorate the mechanical, optical, and electrical properties of the final materials. Therefore, surface modification strategies have been widely adopted to enhance compatibility between nanofillers and the polymer matrix, leading to improved interfacial interactions and dispersion stability. However, the relationship between nanofiller modification and the final composite properties is highly complex, as it depends on multiple factors, including:

- Chemical nature of the nanofillers (organic, inorganic, hybrid structures)
- Type of surface modification (covalent grafting, non-covalent interactions, functional coatings)
- Processing conditions (light intensity, polymerization kinetics, crosslinking density)
- Polymer matrix properties (hydrophobicity, glass transition temperature, flexibility)

Thus, a systematic approach is required to optimize nanofiller modifications for specific applications, ensuring that the resulting composites exhibit the desired mechanical, optical, and functional characteristics. Despite recent advancements, several challenges persist in the fabrication of functional polymer composites using photopolymerization, particularly when integrating nanofillers as photoinitiators and reinforcing agents. Some of the key challenges include:

- Optimizing Nanofiller Dispersion in Polymer Matrices

Achieving uniform distribution of nanofillers remains a challenge, particularly for highly loaded composites.

Developing advanced functionalization techniques to improve dispersibility without compromising photoinitiation efficiency.

- Enhancing Interfacial Adhesion Between Nanofillers and Polymer Matrices

Strong interfacial interactions are essential for mechanical reinforcement and functional performance.

Exploring novel coupling agents or multi-functional surface modifications to improve adhesion.

- Transitioning Photopolymerization from UV to Visible or Near-Infrared (NIR) Wavelengths

Many traditional photoinitiators require UV light, which limits biomedical and large-scale manufacturing applications.

Investigating visible-light-sensitive photoinitiators and hybrid nanomaterials to enable efficient polymerization under mild conditions.

- Addressing Light Penetration Issues in Highly Loaded Nanocomposites

The incorporation of high nanofiller concentrations can lead to light scattering and absorption, reducing polymerization depth.

Developing strategies for improving light transmission through tailored nanofiller refractive index matching and multi-stage curing approaches.

- Balancing Mechanical Performance and Functional Properties

Achieving a balance between mechanical robustness, flexibility, and conductivity in different composite systems.

Exploring synergistic effects of hybrid nanofillers to simultaneously improve multiple properties (e.g., toughness and conductivity).

In conclusion, the development of functional polymer composites using photopolymerization and functionalized nanofillers represents an exciting and rapidly evolving research area with vast technological implications. By addressing nanofiller dispersion, interfacial adhesion, photoinitiation efficiency, and functional integration, this thesis provides innovative material solutions tailored for biomedical, environmental, and industrial applications. The findings presented here pave the way for next generation photopolymerized materials with enhanced performance, versatility, and scalability, setting a foundation for future advancements in smart and sustainable nanocomposite technology.

1.12. Objective and thesis outline

This thesis aims to explore the development of functional polymer nanocomposites through photopolymerization, with a particular focus on integrating functionalized nanomaterials as both photoinitiators and reinforcing agents. The research seeks to address the limitations of traditional polymerization methods, leveraging photopolymerization's rapid, solvent-free curing under light exposure, which provides precise spatial and temporal control over polymer formation. By systematically investigating various nanomaterials and surface modifications, this work aims to enhance the mechanical, optical, and functional properties of polymer nanocomposites, with potential applications in biomedical devices, environmental sensing, and optoelectronic materials.

A key theme of this thesis is the progressive exploration of different classes of photoinitiators and their dual role as functional fillers in polymer nanocomposites. Each chapter builds upon the previous one by introducing new materials, improving photoinitiation strategies, and expanding the functional applications of the developed composites. The following structured approach was adopted in this research:

Chapter 2: The study begins by introducing a fully organic photoinitiator system, where triazine-coated silica nanoparticles (Si-triazine NPs) serve as both visible-light-sensitive photoinitiators and mechanical reinforcements. These nanoparticles efficiently initiate free radical polymerization under 410 nm LED irradiation while simultaneously improving the mechanical integrity and stability of the resulting polymer composites. This chapter establishes a fundamental approach to modifying nanomaterials for dual-function applications.

Chapter 3: Building upon the concept of dual-function photoinitiators, this chapter explores all-inorganic cesium lead bromide quantum dots ($CsPbBr_3$ QDs) as both photoinitiators and

luminescent emitters. The transition from Si-triazine NPs to $CsPbBr_3$ QDs introduces a new functionality—optoelectronic properties—while further optimizing photopolymerization efficiency through the addition of co-initiators (iodonium salt and ethyl 4-(dimethylamino) benzoate, EDB). The resulting nanocomposites demonstrate exceptional photoluminescence and stability, highlighting their potential for luminescent displays and lighting applications.

Chapter 4: The research then shifts to hybrid organic-inorganic systems by investigating UiO-66 metal-organic frameworks (MOFs) modified with visible-light-sensitive photoinitiators (NPYG and triazine). The transition from quantum dots to MOFs represents an effort to expand photopolymerization strategies beyond conventional photoinitiators, incorporating tunable porosity and selective adsorption properties. These composites not only exhibit strong photoinitiation capabilities but also enable high-resolution 3D printing and selective dye absorption, broadening the potential applications of photopolymer/MOF materials in advanced manufacturing and environmental remediation.

Chapter 5: The final experimental chapter builds upon the previous findings by integrating a hybrid inorganic system, combining TiO_2 and carboxylated nanodiamonds (NDs) to develop mechanically robust and electrically conductive zwitterionic hydrogels. This marks a significant transition from rigid nanocomposite materials to soft, responsive hydrogels, which leverage hybrid photocatalytic and radical-generation mechanisms to achieve enhanced mechanical properties, ionic conductivity, and moisture-sensing capabilities. The insights gained in this chapter reinforce the versatility of photopolymerization in different material systems, from rigid composites to functional hydrogels.

Overall, this thesis demonstrates a progressive exploration of diverse photoinitiating systems, advancing from fully organic (Si-triazine NPs) to all-inorganic ($CsPbBr_3$ QDs),

hybrid organic-inorganic (UiO-66 MOFs), and fully inorganic hybrid systems (TiO_2/carboxylated NDs). Each chapter builds upon the previous one by introducing new functionalities, optimizing photopolymerization conditions, and expanding the range of applications, ultimately showcasing the broad potential of photopolymerized nanocomposites in industrial, biomedical, and environmental applications.

1.13. Reference

1. Peng, X.; Zhang, J.; Xiao, P., Photopolymerization Approach to Advanced Polymer Composites: Integration of Surface-Modified Nanofillers for Enhanced Properties. *Advanced Materials* **2024,** 36, 2400178.
2. Brinson, H. F.; Brinson, L. C., Characteristics, Applications and Properties of Polymers. In *Polymer Engineering Science and Viscoelasticity: An Introduction*, Brinson, H. F.; Brinson, L. C., Eds. Springer US: Boston, MA, 2008; pp 55-97.
3. Balani, K.; Verma, V.; Agarwal, A.; Narayan, R., Physical, Thermal, and Mechanical Properties of Polymers. In *Biosurfaces* 2014; pp 329-344.
4. Chandra, A.; Turng, L.-S.; Gopalan, P.; Rowell, R. M.; Gong, S., Study of Utilizing Thin Polymer Surface Coating on the Nanoparticles for Melt Compounding of Polycarbonate/Alumina Nanocomposites and Their Optical Properties. *Composites Science and Technology* **2008,** 68, 768-776.
5. Fan, J.; Shi, Z.; Tian, M.; Wang, J.; Yin, J., Unzipped Multiwalled Carbon Nanotube Oxide/Multiwalled Carbon Nanotube Hybrids for Polymer Reinforcement. *ACS Applied Materials & Interfaces* **2012,** 4, 5956-5965.
6. Fei, T.; Yi, H.-J.; Zboray, R.; Yan, X.-Q.; Song, S.-S.; Ren, L.; Guo, H.; Jiang, Y., Bioinspired Enzymatic Mineralization Incorporates Caco3 Mesocrystals in Wood for Surface Reinforcement and Flame-Retardancy. *ACS Sustainable Chemistry & Engineering* **2022,** 10, 16118-16124.
7. Jiang, H.; Moon, K.-s.; Li, Y.; Wong, C. P., Surface Functionalized Silver Nanoparticles for Ultrahigh Conductive Polymer Composites. *Chemistry of Materials* **2006,** 18, 2969-2973.
8. Kerni, L.; Singh, S.; Patnaik, A.; Kumar, N., A Review on Natural Fiber Reinforced Composites. *Materials Today: Proceedings* **2020,** 28, 1616-1621.
9. Shimizu, T.; Ding, W.; Kameta, N., Soft-Matter Nanotubes: A Platform for Diverse Functions and Applications. *Chemical reviews* **2020,** 120, 2347-2407.
10. Wang, Z.; Chen, H.; Wang, Y.; Chen, J.; Arnould, M. A.; Hu, B.; Popovs, I.; Mahurin, S. M.; Dai, S., Polymer-Grafted Porous Silica Nanoparticles with Enhanced Co2 Permeability and Mechanical Performance. *ACS Applied Materials & Interfaces* **2021,** 13, 27411-27418.
11. Ziolo, R. F.; Giannelis, E. P.; Weinstein, B. A.; O'Horo, M. P.; Ganguly, B. N.; Mehrotra, V.; Russell, M. W.; Huffman, D. R., Matrix-Mediated Synthesis of Nanocrystalline Γ-Fe2o3: A New Optically Transparent Magnetic Material. *Science* **1992,** 257, 219-223.
12. Yan, J.; Huang, Y.; Liu, X.; Zhao, X.; Li, T.; Zhao, Y.; Liu, P., Polypyrrole-Based Composite Materials for Electromagnetic Wave Absorption. *Polymer Reviews* **2021,** 61, 646-687.
13. Park, S.-J.; Seo, M.-K., Chapter 7 - Types of Composites. In *Interface Science and Technology*, Park, S.-J.; Seo, M.-K., Eds. Elsevier: 2011; Vol. 18, pp 501-629.
14. Ramakrishna, S.; Mayer, J.; Wintermantel, E.; Leong, K. W., Biomedical Applications of Polymer-Composite Materials: A Review. *Composites Science and Technology* **2001,** 61, 1189-1224.
15. Mourdikoudis, S.; Kostopoulou, A.; LaGrow, A. P., Magnetic Nanoparticle Composites: Synergistic Effects and Applications. *Advanced Science* **2021,** 8, 2004951.
16. Jitputti, J.; Rattanavoravipa, T.; Chuangchote, S.; Pavasupree, S.; Suzuki, Y.; Yoshikawa, S., Low Temperature Hydrothermal Synthesis of Monodispersed Flower-Like Titanate Nanosheets. *Catalysis Communications* **2009,** 10, 378-382.
17. Parodi, A.; Evangelopoulos, M.; Arrighetti, N.; Cevenini, A.; Livingston, M.; Khaled, S. Z.; Brown, B. S.; Yazdi, I. K.; Paradiso, F.; Campa-Carranza, J. N.; De Vita, A.; Taraballi, F.; Tasciotti, E., Endosomal Escape of Polymer-Coated Silica Nanoparticles in Endothelial Cells. *Small* **2020,** 16, 1907693.
18. Nalone, L. A.; Amaral, R. G.; de Lima Oliveira, D. M.; Andrade, L. R.; de Hollanda, L. M.; da Silva, C. F.; Souto, E. B.; Severino, P., 15 - Applications of Nanocomposite Materials in the Delivery of Anticancer Drugs. In *Applications of Nanocomposite Materials in Drug Delivery*, Inamuddin; Asiri, A. M.; Mohammad, A., Eds. Woodhead Publishing: 2018; pp 339-352.

19. Yang, C.; Wei, H.; Guan, L.; Guo, J.; Wang, Y.; Yan, X.; Zhang, X.; Wei, S.; Guo, Z., Polymer Nanocomposites for Energy Storage, Energy Saving, and Anticorrosion. *Journal of Materials Chemistry A* **2015,** 3, 14929-14941.
20. Khodakarami, M.; Bagheri, M., Recent Advances in Synthesis and Application of Polymer Nanocomposites for Water and Wastewater Treatment. *Journal of Cleaner Production* **2021,** 296, 126404.
21. Ji, Y.; Zhang, M.; Guan, K.; Zhao, J.; Liu, G.; Jin, W., High-Performance Co2 Capture through Polymer-Based Ultrathin Membranes. *Advanced Functional Materials* **2019,** 29, 1900735.
22. Li, S.; Dong, Q.; Peng, X.; Chen, Y.; Yang, H.; Xu, W.; Zhao, Y.; Xiao, P.; Zhou, Y., Self-Healing Hyaluronic Acid Nanocomposite Hydrogels with Platelet-Rich Plasma Impregnated for Skin Regeneration. *ACS Nano* **2022,** 16, 11346-11359.
23. Li, J.; Liu, J.; Huo, W.; Yu, J.; Liu, X.; Haslinger, M. J.; Muehlberger, M.; Kulha, P.; Huang, X., Micro and Nano Materials and Processing Techniques for Printed Biodegradable Electronics. *Materials Today Nano* **2022,** 18, 100201.
24. Li, S.; Pei, M.; Wan, T.; Yang, H.; Gu, S.; Tao, Y.; Liu, X.; Zhou, Y.; Xu, W.; Xiao, P., Self-Healing Hyaluronic Acid Hydrogels Based on Dynamic Schiff Base Linkages as Biomaterials. *Carbohydr. Polym.* **2020,** 250, 116922.
25. Liu, S.; Ding, Z.; Zhu, H.; Gree, S.; Xiao, P.; Xu, Y.; Lalevée, J., Near-Infrared light/Thermal Dual-Responsive Epoxy-Based Polydiacetylene Composite for 3d Printing. *Adv. Mater. Interfaces* **2021,** 8, 2101481.
26. Xu, Y.; Ding, Z.; Zhu, H.; Zhang, Y.; Knopf, S.; Xiao, P.; Lalevée, J., Preparation of Iron Filler-Based Photocomposites and Application in 3d Printing. *Macromol. Mater. Eng.* **2021,** 306, 2000720.
27. Xu, Y.; Jambou, C.; Sun, K.; Lalevée, J.; Simon-Masseron, A.; Xiao, P., Effect of Zeolite Fillers on the Photopolymerization Kinetics for Photocomposites and Lithography. *ACS Appl. Polym. Mater.* **2019,** 1, 2854-2861.
28. Li, S.; Zhou, D.; Pei, M.; Zhou, Y.; Xu, W.; Xiao, P., Fast Gelling and Non-Swellable Photopolymerized Poly (Vinyl Alcohol) Hydrogels with High Strength. *Euro. Polym. J.* **2020,** 134, 109854.
29. Zhou, D.; Li, S.; Pei, M.; Yang, H.; Gu, S.; Tao, Y.; Ye, D.; Zhou, Y.; Xu, W.; Xiao, P., Dopamine-Modified Hyaluronic Acid Hydrogel Adhesives with Fast-Forming and High Tissue Adhesion. *ACS Appl. Mater. Interfaces* **2020,** 12, 18225-18234.
30. Zhang, C.; Dong, Q.; Liang, K.; Zhou, D.; Yang, H.; Liu, X.; Xu, W.; Zhou, Y.; Xiao, P., Photopolymerizable Thiol-Acrylate Maleiated Hyaluronic Acid/Thiol-Terminated Poly(Ethylene Glycol) Hydrogels as Potential in-Situ Formable Scaffolds. *Int. J. Biol. Macromol.* **2018,** 119, 270-277.
31. Pirayesh, A.; Salami-Kalajahi, M.; Roghani-Mamaqani, H.; Najafi, F., Polysulfide Polymers: Synthesis, Blending, Nanocomposites, and Applications. *Polymer Reviews* **2019,** 59, 124-148.
32. Zeng, L.; Li, P.; Yao, Y.; Niu, B.; Niu, S.; Xu, B., Recent Progresses of 3d Printing Technologies for Structural Energy Storage Devices. *Materials Today Nano* **2020,** 12, 100094.
33. Bade, S. G. R.; Shan, X.; Hoang, P. T.; Li, J.; Geske, T.; Cai, L.; Pei, Q.; Wang, C.; Yu, Z., Stretchable Light-Emitting Diodes with Organometal-Halide-Perovskite–Polymer Composite Emitters. *Advanced Materials* **2017,** 29, 1607053.
34. Wang, Y.; He, J.; Chen, H.; Chen, J.; Zhu, R.; Ma, P.; Towers, A.; Lin, Y.; Gesquiere, A. J.; Wu, S.-T.; Dong, Y., Ultrastable, Highly Luminescent Organic–Inorganic Perovskite–Polymer Composite Films. *Advanced Materials* **2016,** 28, 10710-10717.
35. Winther-Jensen, B.; Fraser, K.; Ong, C.; Forsyth, M.; MacFarlane, D. R., Conducting Polymer Composite Materials for Hydrogen Generation. *Advanced Materials* **2010,** 22, 1727-1730.
36. Caseri, W., Clay-Containing Polymeric Nanocomposites (2 Volumes). Rapra Technology Limited, Shrewsbury, Uk, 2004. Isbn 1-85957-482-3 (Volume 1). Isbn 1-85957-437-8 (Volume 2). Pp 785 (Both Volumes). *Polymer International* **2005,** 54, 860-860.
37. Rane, A. V.; Kanny, K.; Abitha, V. K.; Thomas, S., Chapter 5 - Methods for Synthesis of Nanoparticles and Fabrication of Nanocomposites. In *Synthesis of Inorganic Nanomaterials*, Mohan Bhagyaraj, S.; Oluwafemi, O. S.; Kalarikkal, N.; Thomas, S., Eds. Woodhead Publishing: 2018; pp 121-139.

38. Alexandre, M.; Dubois, P., Polymer-Layered Silicate Nanocomposites: Preparation, Properties and Uses of a New Class of Materials. *Materials Science and Engineering: R: Reports* **2000,** 28, 1-63.
39. Oksman, K.; Mathew, A. P., Melt Compounding Process of Cellulose Nanocomposites. In *Handbook of Green Materials*, WORLD SCIENTIFIC: 2013; Vol. Volume 5, pp 53-68.
40. Verma, D.; Goh, K. L., Chapter 11 - Functionalized Graphene-Based Nanocomposites for Energy Applications. In *Functionalized Graphene Nanocomposites and Their Derivatives*, Jawaid, M.; Bouhfid, R.; Kacem Qaiss, A. e., Eds. Elsevier: 2019; pp 219-243.
41. Tang, L.-C.; Zhao, L.; Qiang, F.; Wu, Q.; Gong, L.-X.; Peng, J.-P., Chapter Twelve - Mechanical Properties of Rubber Nanocomposites Containing Carbon Nanofillers. In *Carbon-Based Nanofillers and Their Rubber Nanocomposites*, Yaragalla, S.; Mishra, R. K.; Thomas, S.; Kalarikkal, N.; Maria, H. J., Eds. Elsevier: 2019; pp 367-423.
42. Yu, C.; Schimelman, J.; Wang, P.; Miller, K. L.; Ma, X.; You, S.; Guan, J.; Sun, B.; Zhu, W.; Chen, S., Photopolymerizable Biomaterials and Light-Based 3d Printing Strategies for Biomedical Applications. *Chemical reviews* **2020,** 120, 10695-10743.
43. Decker, C., Kinetic Study and New Applications of Uv Radiation Curing. *Macromolecular Rapid Communications* **2002,** 23, 1067-1093.
44. Andrzejewska, E., Photopolymerization Kinetics of Multifunctional Monomers. *Progress in polymer science* **2001,** 26, 605-665.
45. Decker, C., Uv-Curing Chemistry: Past, Present, and Future. *Journal of coatings technology* **1987,** 59, 97-106.
46. Fouassier, J.-P.; Rabek, J. F., *Radiation Curing in Polymer Science and Technology: Fundamentals and Methods*. Springer Science & Business Media: 1993; Vol. 1.
47. Gatechair, L. R.; Wostratzky, D., Photoinitiators: A Review of Mechanisims and Applications. In *Adhesive Chemistry: Developments and Trends*, Lee, L.-H., Ed. Springer US: Boston, MA, 1984; pp 409-438.
48. Zhang, J.; Xiao, P., 3d Printing of Photopolymers. *Polym. Chem.* **2018,** 9, 1530-1540.
49. Borjigin, T.; Schmitt, M.; Giacoletto, N.; Rico, A.; Bidotti, H.; Nechab, M.; Zhang, Y.; Graff, B.; Morlet-Savary, F.; Xiao, P.; Dumur, F.; Lalevée, J., The Blue-Led-Sensitive Naphthoquinone-Imidazolyl Derivatives as Type Ii Photoinitiators of Free Radical Photopolymerization. *Advanced Materials Interfaces* **2023**, 2202352.
50. Chen, H.; Noirbent, G.; Liu, S.; Brunel, D.; Graff, B.; Gigmes, D.; Zhang, Y.; Sun, K.; Morlet-Savary, F.; Xiao, P.; Dumur, F.; Lalevée, J., Bis-Chalcone Derivatives Derived from Natural Products as near-Uv/Visible Light Sensitive Photoinitiators for 3d/4d Printing. *Mater. Chem. Front.* **2021,** 5, 907-916.
51. Chen, H.; Noirbent, G.; Sun, K.; Brunel, D.; Gigmes, D.; Morlet-Savary, F.; Zhang, Y.; Liu, S.; Xiao, P.; Dumur, F.; Lalevée, J., Photoinitiators Derived from Natural Product Scaffolds: Monochalcones in Three-Component Photoinitiating Systems and Their Applications in 3d Printing. *Polym. Chem.* **2020,** 11, 4647-4659.
52. Chen, H.; Noirbent, G.; Zhang, Y.; Brunel, D.; Gigmes, D.; Morlet-Savary, F.; Graff, B.; Xiao, P.; Dumur, F.; Lalevée, J., Novel D–Π-a and a–Π-D–Π-a Three-Component Photoinitiating Systems Based on Carbazole/Triphenylamino Based Chalcones and Application in 3d and 4d Printing. *Polym. Chem.* **2020,** 11, 6512-6528.
53. Chen, H.; Noirbent, G.; Zhang, Y.; Sun, K.; Liu, S.; Brunel, D.; Gigmes, D.; Graff, B.; Morlet-Savary, F.; Xiao, P.; Dumur, F.; Lalevée, J., Photopolymerization and 3d/4d Applications Using Newly Developed Dyes: Search around the Natural Chalcone Scaffold in Photoinitiating Systems. *Dyes and Pigments* **2021,** 188, 109213.
54. Chen, H.; Pieuchot, L.; Xiao, P.; Dumur, F.; Lalevée, J., Water-Soluble/Visible-Light-Sensitive Naphthalimide Derivative-Based Photoinitiating Systems: 3d Printing of Antibacterial Hydrogels. *Polym. Chem.* **2022,** 13, 2918-2932.
55. Chen, H.; Regeard, C.; Salmi, H.; Morlet-Savary, F.; Giacoletto, N.; Nechab, M.; Xiao, P.; Dumur, F.; Lalevée, J., Interpenetrating Polymer Network Hydrogels Using Natural Based Dyes Initiating Systems: Antibacterial Activity and 3d/4d Performance. *Eur. Polym. J.* **2022,** 166, 111042.

56. Chen, H.; Vahdati, M.; Xiao, P.; Dumur, F.; Lalevée, J., Water-Soluble Visible Light Sensitive Photoinitiating System Based on Charge Transfer Complexes for the 3d Printing of Hydrogels. *Polymers* **2021,** 13, 3195.
57. Lai, H.; Zhang, J.; Xing, F.; Xiao, P., Recent Advances in Light-Regulated Non-Radical Polymerisations. *Chem. Soc. Rev.* **2020,** 49, 1867-1886.
58. Lai, H.; Zhu, D.; Peng, X.; Zhang, J.; Lalevée, J.; Xiao, P., N-Aryl Glycines as Versatile Initiators for Various Polymerizations. *Polym. Chem.* **2021,** 12, 1991-2000.
59. Liu, S.; Brunel, D.; Noirbent, G.; Mau, A.; Chen, H.; Morlet-Savary, F.; Graff, B.; Gigmes, D.; Xiao, P.; Dumur, F.; Lalevée, J., New Multifunctional Benzophenone-Based Photoinitiators with High Migration Stability and Their Applications in 3d Printing. *Mater. Chem. Front.* **2021,** 5, 1982-1994.
60. Liu, S.; Brunel, D.; Sun, K.; Xu, Y.; Morlet-Savary, F.; Graff, B.; Xiao, P.; Dumur, F.; Lalevée, J., A Monocomponent Bifunctional Benzophenone–Carbazole Type Ii Photoinitiator for Led Photoinitiating Systems. *Polym. Chem.* **2020,** 11, 3551-3556.
61. Liu, S.; Brunel, D.; Sun, K.; Zhang, Y.; Chen, H.; Xiao, P.; Dumur, F.; Lalevée, J., Novel Photoinitiators Based on Benzophenone-Triphenylamine Hybrid Structure for Led Photopolymerization. *Macromol. Rapid Commun.* **2020,** 41, 2000460.
62. Liu, S.; Giacoletto, N.; Graff, B.; Morlet-Savary, F.; Nechab, M.; Xiao, P.; Dumur, F.; Lalevée, J., N-Naphthalimide Ester Derivatives as Type Ⅰ Photoinitiators for Led Photopolymerization. *Materials Today Chemistry* **2022,** 26, 101137.
63. Liu, S.; Giacoletto, N.; Schmitt, M.; Nechab, M.; Graff, B.; Morlet-Savary, F.; Xiao, P.; Dumur, F.; Lalevée, J., Effect of Decarboxylation on the Photoinitiation Behavior of Nitrocarbazole-Based Oxime Esters. *Macromolecules* **2022,** 55, 2475-2485.
64. Liu, S.; Graff, B.; Xiao, P.; Dumur, F.; Lalevée, J., Nitro-Carbazole Based Oxime Esters as Dual Photo/Thermal Initiators for 3d Printing and Composite Preparation. *Macromol. Rapid Commun.* **2021,** 42, 2100207.
65. Liu, S.; Zhang, Y.; Sun, K.; Graff, B.; Xiao, P.; Dumur, F.; Lalevée, J., Design of Photoinitiating Systems Based on the Chalcone-Anthracene Scaffold for Led Cationic Photopolymerization and Application in 3d Printing. *Euro. Polym. J.* **2021,** 147, 110300.
66. Peng, X.; Zhu, D.; Xiao, P., Naphthoquinone Derivatives: Naturally Derived Molecules as Blue-Light-Sensitive Photoinitiators of Photopolymerization. *Euro. Polym. J.* **2020,** 127, 109569.
67. Sun, K.; Chen, H.; Zhang, Y.; Morlet-Savary, F.; Graff, B.; Xiao, P.; Dumur, F.; Lalevée, J., High-Performance Sunlight Induced Polymerization Using Novel Push-Pull Dyes with High Light Absorption Properties. *Euro. Polym. J.* **2021,** 151, 110410.
68. Sun, K.; Liu, S.; Chen, H.; Morlet-Savary, F.; Graff, B.; Pigot, C.; Nechab, M.; Xiao, P.; Dumur, F.; Lalevée, J., N-Ethyl Carbazole-1-Allylidene-Based Push-Pull Dyes as Efficient Light Harvesting Photoinitiators for Sunlight Induced Polymerization. *Euro. Polym. J.* **2021,** 147, 110331.
69. Sun, K.; Xu, Y.; Dumur, F.; Morlet-Savary, F.; Chen, H.; Dietlin, C.; Graff, B.; Lalevée, J.; Xiao, P., In Silico Rational Design by Molecular Modeling of New Ketones as Photoinitiators in Three-Component Photoinitiating Systems: Application in 3d Printing. *Polym. Chem.* **2020,** 11, 2230-2242.
70. Wang, G.; Hill, N. S.; Zhu, D.; Xiao, P.; Coote, M. L.; Stenzel, M. H., Efficient Photoinitiating System Based on Diaminoanthraquinone for 3d Printing of Polymer/Carbon Nanotube Nanocomposites under Visible Light. *ACS Appl. Polym. Mater.* **2019,** 1, 1129-1135.
71. Xu, Y.; Noirbent, G.; Brunel, D.; Ding, Z.; Gigmes, D.; Graff, B.; Xiao, P.; Dumur, F.; Lalevée, J., Novel Ketone Derivative-Based Photoinitiating Systems for Free Radical Polymerization under Mild Conditions and 3d Printing. *Polym. Chem.* **2020,** 11, 5767-5777.
72. Xu, Y.; Noirbent, G.; Brunel, D.; Ding, Z.; Gigmes, D.; Graff, B.; Xiao, P.; Dumur, F.; Lalevée, J., Allyloxy Ketones as Efficient Photoinitiators with High Migration Stability in Free Radical Polymerization and 3d Printing. *Dyes and Pigments* **2021,** 185, 108900.
73. Li, S.; Pei, M.; Wan, T.; Yang, H.; Gu, S.; Tao, Y.; Liu, X.; Zhou, Y.; Xu, W.; Xiao, P., Self-Healing Hyaluronic Acid Hydrogels Based on Dynamic Schiff Base Linkages as Biomaterials. *Carbohydrate Polymers* **2020,** 250, 116922.
74. Zhang, J.; Lalevée, J.; Hill, N. S.; Kiehl, J.; Zhu, D.; Cox, N.; Langley, J.; Stenzel, M. H.; Coote, M. L.; Xiao, P., Substituent Effects on Photoinitiation Ability of Monoaminoanthraquinone-

Based Photoinitiating Systems for Free Radical Photopolymerization under Leds. *Macromol. Rapid Commun.* **2020,** 41, 2000166.
75. Zhang, J.; Lalevée, J.; Hill, N. S.; Launay, K.; Morlet-Savary, F.; Graff, B.; Stenzel, M. H.; Coote, M. L.; Xiao, P., Disubstituted Aminoanthraquinone-Based Multicolor Photoinitiators: Photoinitiation Mechanism and Ability of Cationic Polymerization under Blue, Green, Yellow, and Red Leds. *Macromolecules* **2018,** 51, 8165-8173.
76. Zhang, J.; Launay, K.; Hill, N. S.; Zhu, D.; Cox, N.; Langley, J.; Lalevée, J.; Stenzel, M. H.; Coote, M. L.; Xiao, P., Disubstituted Aminoanthraquinone-Based Photoinitiators for Free Radical Polymerization and Fast 3d Printing under Visible Light. *Macromolecules* **2018,** 51, 10104-10112.
77. Zhang, J.; Zivic, N.; Dumur, F.; Xiao, P.; Graff, B.; Fouassier, J. P.; Gigmes, D.; Lalevee, J., N-[2-(Dimethylamino)Ethyl]-1,8-Naphthalimide Derivatives as Photoinitiators under Leds. *Polym. Chem.* **2018,** 9, 994-1003.
78. Zhu, D.; Peng, X.; Wagner, P.; Xiao, P., Symmetrically-Substituted Thiazolo[5,4-D]Thiazole Derivatives as Both Photoinitiators and Dyes for 3d Printing under Violet Led. *Dyes and Pigments* **2022,** 206, 110638.
79. Zhu, D.; Peng, X.; Xiao, P., Penta-Hydroxy Flavones-Based Photoinitiating Systems for Free Radical, Cationic, and Thiol-Ene Polymerization Upon Exposure to Mild Blue Leds. *Macromol. Mater. Eng.* **2021,** 306, 2100059.
80. Zhu, D.; Peng, X.; Xiao, P., Indigo Carmine: A Base and Neutral Electrolyte-Mediated Photoinitiator for 3d Printing in High Fidelity. *Additive Manufacturing* **2022,** 59, 103154.
81. Borjigin, T.; Schmitt, M.; Morlet-Savary, F.; Xiao, P.; Lalevée, J., Low-Cost and Recyclable Photocatalysts: Metal Oxide/Polymer Composites Applied in the Catalytic Breakdown of Dyes. *Photochem* **2022,** 2, 733-751.
82. Balcerak, A.; Kabatc, J., Recent Progress in the Development of Highly Active Dyeing Photoinitiators Based on 1,3-Bis(P-Substituted Phenylamino)Squaraines for Radical Polymerization of Acrylates. *Polymer Chemistry* **2022,** 13, 1787-1812.
83. Liu, J.; Gao, Y.; Cao, D.; Zhang, L.; Guo, Z., Nanoparticle Dispersion and Aggregation in Polymer Nanocomposites: Insights from Molecular Dynamics Simulation. *Langmuir* **2011,** 27, 7926-7933.
84. Santagiuliana, G.; Picot, O. T.; Crespo, M.; Porwal, H.; Zhang, H.; Li, Y.; Rubini, L.; Colonna, S.; Fina, A.; Barbieri, E.; Spoelstra, A. B.; Mirabello, G.; Patterson, J. P.; Botto, L.; Pugno, N. M.; Peijs, T.; Bilotti, E., Breaking the Nanoparticle Loading–Dispersion Dichotomy in Polymer Nanocomposites with the Art of Croissant-Making. *ACS Nano* **2018,** 12, 9040-9050.
85. Francis, R.; Joy, N.; Aparna, E. P.; Vijayan, R., Polymer Grafted Inorganic Nanoparticles, Preparation, Properties, and Applications: A Review. *Polymer Reviews* **2014,** 54, 268-347.
86. Li, C.; Shi, G., Functional Gels Based on Chemically Modified Graphenes. *Advanced Materials* **2014,** 26, 3992-4012.
87. Kango, S.; Kalia, S.; Celli, A.; Njuguna, J.; Habibi, Y.; Kumar, R., Surface Modification of Inorganic Nanoparticles for Development of Organic–Inorganic Nanocomposites—a Review. *Progress in Polymer Science* **2013,** 38, 1232-1261.
88. Pakharenko, V.; Pervaiz, M.; Pande, H.; Sain, M.; Sain, M., Chemical and Physical Techniques for Surface Modification of Nanocellulose Reinforcements. In *Interface/Interphase in Polymer Nanocomposites*, 2016; pp 283-310.
89. Fujigaya, T.; Nakashima, N., Fuel Cell Electrocatalyst Using Polybenzimidazole-Modified Carbon Nanotubes as Support Materials. *Advanced Materials* **2013,** 25, 1666-1681.
90. Jung, Y. C.; Shimamoto, D.; Muramatsu, H.; Kim, Y. A.; Hayashi, T.; Terrones, M.; Endo, M., Robust, Conducting, and Transparent Polymer Composites Using Surface-Modified and Individualized Double-Walled Carbon Nanotubes. *Advanced Materials* **2008,** 20, 4509-4512.
91. Chen, J.; Zhao, L.; Zhou, K., Improvement in the Mechanical Performance of Multi Jet Fusion–Printed Aramid Fiber/Polyamide 12 Composites by Fiber Surface Modification. *Additive Manufacturing* **2022,** 51, 102576.
92. Sahin, M.; Krawczyk, K. K.; Roszkowski, P.; Wang, J.; Kaynak, B.; Kern, W.; Schlögl, S.; Grützmacher, H., Photoactive Silica Nanoparticles: Influence of Surface Functionalization on Migration and Kinetics of Radical-Induced Photopolymerization Reactions. *European Polymer Journal* **2018,** 98, 430-438.

93. Van Den Houwe, K.; Van Heyst, A.; Evrard, C.; Van Loco, J.; Bolle, F.; Lynen, F.; Van Hoeck, E., Migration of 17 Photoinitiators from Printing Inks and Cardboard into Packaged Food – Results of a Belgian Market Survey. *Packaging Technology and Science* **2016,** 29, 121-131.
94. Khudyakov, I. V., Fast Photopolymerization of Acrylate Coatings: Achievements and Problems. *Progress in Organic Coatings* **2018,** 121, 151-159.
95. Ligon-Auer, S. C.; Schwentenwein, M.; Gorsche, C.; Stampfl, J.; Liska, R., Toughening of Photo-Curable Polymer Networks: A Review. *Polymer Chemistry* **2016,** 7, 257-286.
96. Bagheri, A.; Jin, J., Photopolymerization in 3d Printing. *ACS Appl. Polym. Mater.* **2019,** 1, 593-611.
97. Sipani, V.; Scranton, A. B., Photopolymerization, Cationic. In *Encyclopedia of Polymer Science and Technology*, 2004.
98. Kowalska, A.; Sokolowski, J.; Bociong, K., The Photoinitiators Used in Resin Based Dental Composite-a Review and Future Perspectives. *Polymers (Basel)* **2021,** 13.
99. Ligon, S. C.; Liska, R.; Stampfl, J.; Gurr, M.; Mülhaupt, R., Polymers for 3d Printing and Customized Additive Manufacturing. *Chemical reviews* **2017,** 117, 10212-10290.
100. Fouassier, J. P.; Allonas, X.; Lalevée, J.; Dietlin, C., Photoinitiators for Free Radical Polymerization Reactions. In *Photochemistry and Photophysics of Polymer Materials*, 2010; pp 351-419.
101. Srivastava, A. K.; Mohan, P., Synthesis, Reactions, and Properties of Modified Epoxy Resins. *Journal of Macromolecular Science, Part C* **1997,** 37, 687-716.
102. Atif, M.; Bongiovanni, R.; Yang, J., Cationically Uv-Cured Epoxy Composites. *Polymer Reviews* **2015,** 55, 90-106.
103. Green, G. E.; Stark, B. P.; Zahir, S. A., Photocross-Linkable Resin Systems. *Journal of Macromolecular Science, Part C* **1981,** 21, 187-273.
104. Tasdelen, M. A.; Lalevée, J.; Yagci, Y., Photoinduced Free Radical Promoted Cationic Polymerization 40 Years after Its Discovery. *Polymer Chemistry* **2020,** 11, 1111-1121.
105. Lai, H.; Peng, X.; Li, L.; Zhu, D.; Xiao, P., Novel Monomers for Photopolymer Networks. *Progress in Polymer Science* **2022,** 128, 101529.
106. Das, S. K.; Chakraborty, S.; Naskar, S.; Rajabalaya, R., 3 - Techniques and Methods Used for the Fabrication of Bionanocomposites. In *Bionanocomposites in Tissue Engineering and Regenerative Medicine*, Ahmed, S.; Annu, Eds. Woodhead Publishing: 2021; pp 17-43.
107. Ahamad Said, M. N.; Hasbullah, N. A.; Rosdi, M. R. H.; Musa, M. S.; Rusli, A.; Ariffin, A.; Shafiq, M. D., Polymerization and Applications of Poly(Methyl Methacrylate)-Graphene Oxide Nanocomposites: A Review. *ACS Omega* **2022,** 7, 47490-47503.
108. dos Santos, M. N.; Opelt, C. V.; Lafratta, F. H.; Lepienski, C. M.; Pezzin, S. H.; Coelho, L. A. F., Thermal and Mechanical Properties of a Nanocomposite of a Photocurable Epoxy-Acrylate Resin and Multiwalled Carbon Nanotubes. *Materials Science and Engineering: A* **2011,** 528, 4318-4324.
109. Wozniak, M.; de Hazan, Y.; Graule, T.; Kata, D., Rheology of Uv Curable Colloidal Silica Dispersions for Rapid Prototyping Applications. *Journal of the European Ceramic Society* **2011,** 31, 2221-2229.
110. Fadel, T. R.; Sharp, F. A.; Vudattu, N.; Ragheb, R.; Garyu, J.; Kim, D.; Hong, E.; Li, N.; Haller, G. L.; Pfefferle, L. D.; Justesen, S.; Herold, K. C.; Fahmy, T. M., A Carbon Nanotube–Polymer Composite for T-Cell Therapy. *Nature Nanotechnology* **2014,** 9, 639-647.
111. Yamada, T.; Hayamizu, Y.; Yamamoto, Y.; Yomogida, Y.; Izadi-Najafabadi, A.; Futaba, D. N.; Hata, K., A Stretchable Carbon Nanotube Strain Sensor for Human-Motion Detection. *Nature Nanotechnology* **2011,** 6, 296-301.
112. Zhang, J.; Xia, Z.; Dai, L., Carbon-Based Electrocatalysts for Advanced Energy Conversion and Storage. *Science Advances* **2015,** 1, e1500564.
113. Dogra, P.; Adolphi, N. L.; Wang, Z.; Lin, Y.-S.; Butler, K. S.; Durfee, P. N.; Croissant, J. G.; Noureddine, A.; Coker, E. N.; Bearer, E. L.; Cristini, V.; Brinker, C. J., Establishing the Effects of Mesoporous Silica Nanoparticle Properties on in Vivo Disposition Using Imaging-Based Pharmacokinetics. *Nature Communications* **2018,** 9, 4551.

114. Kawahara, T.; Takeuchi, Y.; Wei, G.; Shirai, K.; Yamauchi, T.; Tsubokawa, N., Preparation of Antibacterial Polymer-Grafted Silica Nanoparticle and Surface Properties of Composites Filled with the Silica (2). *Polymer Journal* **2009,** 41, 744-751.
115. Zou, H.; Wu, S.; Shen, J., Polymer/Silica Nanocomposites: Preparation, Characterization, Properties, and Applications. *Chemical reviews* **2008,** 108, 3893-3957.
116. Zhang, C.; Liang, K.; Zhou, D.; Yang, H.; Liu, X.; Yin, X.; Xu, W.; Zhou, Y.; Xiao, P., High-Performance Photopolymerized Poly(Vinyl Alcohol)/Silica Nanocomposite Hydrogels with Enhanced Cell Adhesion. *ACS Appl. Mater. Interfaces* **2018,** 10, 27692-27700.
117. Dawson, J. I.; Oreffo, R. O. C., Clay: New Opportunities for Tissue Regeneration and Biomaterial Design. *Advanced Materials* **2013,** 25, 4069-4086.
118. Nicotera, I.; Enotiadis, A.; Angjeli, K.; Coppola, L.; Ranieri, G. A.; Gournis, D., Effective Improvement of Water-Retention in Nanocomposite Membranes Using Novel Organo-Modified Clays as Fillers for High Temperature Pemfcs. *The Journal of Physical Chemistry B* **2011,** 115, 9087-9097.
119. Zhou, D.; Dong, Q.; Liang, K.; Xu, W.; Zhou, Y.; Xiao, P., Photocrosslinked Methacrylated Poly(Vinyl Alcohol)/Hydroxyapatite Nanocomposite Hydrogels with Enhanced Mechanical Strength and Cell Adhesion. *J. Polym. Sci., Part A: Polym. Chem.* **2019,** 57, 1882-1889.
120. Wang, J.; Li, D.; Ye, Y.; Qiu, Y.; Liu, J.; Huang, L.; Liang, B.; Chen, B., A Fluorescent Metal–Organic Framework for Food Real-Time Visual Monitoring. *Advanced Materials* **2021,** 33, 2008020.
121. Lin, J.-B.; Nguyen, T. T. T.; Vaidhyanathan, R.; Burner, J.; Taylor, J. M.; Durekova, H.; Akhtar, F.; Mah, R. K.; Ghaffari-Nik, O.; Marx, S.; Fylstra, N.; Iremonger, S. S.; Dawson, K. W.; Sarkar, P.; Hovington, P.; Rajendran, A.; Woo, T. K.; Shimizu, G. K. H., A Scalable Metal-Organic Framework as a Durable Physisorbent for Carbon Dioxide Capture. *Science* **2021,** 374, 1464-1469.
122. Cheng, X.; Zhang, S.; Liu, H.; Chen, H.; Zhou, J.; Chen, Z.; Zhou, X.; Xie, Z.; Kuang, Q.; Zheng, L., Biomimetic Metal–Organic Framework Composite-Mediated Cascade Catalysis for Synergistic Bacteria Killing. *ACS Applied Materials & Interfaces* **2020,** 12, 36996-37005.
123. Jiang, Z.; Xu, X.; Ma, Y.; Cho, H. S.; Ding, D.; Wang, C.; Wu, J.; Oleynikov, P.; Jia, M.; Cheng, J.; Zhou, Y.; Terasaki, O.; Peng, T.; Zan, L.; Deng, H., Filling Metal–Organic Framework Mesopores with Tio2 for Co2 Photoreduction. *Nature* **2020,** 586, 549-554.
124. Xu, T.; Du, H.; Liu, H.; Liu, W.; Zhang, X.; Si, C.; Liu, P.; Zhang, K., Advanced Nanocellulose-Based Composites for Flexible Functional Energy Storage Devices. *Advanced Materials* **2021,** 33, 2101368.
125. Xi Loh, E. Y.; Fauzi, M. B.; Ng, M. H.; Ng, P. Y.; Ng, S. F.; Ariffin, H.; Mohd Amin, M. C. I., Cellular and Molecular Interaction of Human Dermal Fibroblasts with Bacterial Nanocellulose Composite Hydrogel for Tissue Regeneration. *ACS Applied Materials & Interfaces* **2018,** 10, 39532-39543.
126. Li, T.; Chen, C.; Brozena, A. H.; Zhu, J. Y.; Xu, L.; Driemeier, C.; Dai, J.; Rojas, O. J.; Isogai, A.; Wågberg, L.; Hu, L., Developing Fibrillated Cellulose as a Sustainable Technological Material. *Nature* **2021,** 590, 47-56.
127. Yin, K.; Divakar, P.; Wegst, U. G. K., Plant-Derived Nanocellulose as Structural and Mechanical Reinforcement of Freeze-Cast Chitosan Scaffolds for Biomedical Applications. *Biomacromolecules* **2019,** 20, 3733-3745.
128. Pei, M.; Peng, X.; Wan, T.; Fan, P.; Yang, H.; Liu, X.; Xu, W.; Zhou, Y.; Xiao, P., Double Cross-Linked Poly(Vinyl Alcohol) Microcomposite Hydrogels with High Strength and Cell Compatibility. *Euro. Polym. J.* **2021,** 160, 110786.
129. Pei, M.; Zhu, D.; Yang, J.; Yang, K.; Yang, H.; Gu, S.; Li, W.; Xu, W.; Xiao, P.; Zhou, Y., Multi-Crosslinked Flexible Nanocomposite Hydrogel Fibers with Excellent Strength and Knittability. *Eur. Polym. J.* **2023,** 182, 111737.
130. You, J.; Li, M.; Ding, B.; Wu, X.; Li, C., Crab Chitin-Based 2d Soft Nanomaterials for Fully Biobased Electric Devices. *Advanced Materials* **2017,** 29, 1606895.
131. Li, W.; He, X.; Liu, K.; Wen, W.; Lu, L.; Liu, M.; Zhou, C.; Luo, B., Creating Ultrastrong and Osteogenic Chitin Nanocomposite Hydrogels Via Chitin Whiskers with Different Surface Chemistries. *ACS Sustainable Chemistry & Engineering* **2020,** 8, 17487-17499.

132. Lee, S.; Hao, L. T.; Park, J.; Oh, D. X.; Hwang, D. S., Nanochitin and Nanochitosan: Chitin Nanostructure Engineering with Multiscale Properties for Biomedical and Environmental Applications. *Advanced Materials* **2023,** 35, 2203325.
133. Zhou, Y.; Liang, K.; Zhang, C.; Li, J.; Yang, H.; Liu, X.; Yin, X.; Chen, D.; Xu, W.; Xiao, P., Photocrosslinked Methacrylated Chitosan-Based Nanofibrous Scaffolds as Potential Skin Substitute. *Cellulose* **2017,** 24, 4253-4262.
134. Kim, H.-J.; Oh, H.; Kim, T.; Kim, D.; Park, M., Stretchable Photodetectors Based on Electrospun Polymer/Perovskite Composite Nanofibers. *ACS Applied Nano Materials* **2022,** 5, 1308-1316.
135. Han, T.-H.; Lee, J.-W.; Choi, C.; Tan, S.; Lee, C.; Zhao, Y.; Dai, Z.; De Marco, N.; Lee, S.-J.; Bae, S.-H.; Yuan, Y.; Lee, H. M.; Huang, Y.; Yang, Y., Perovskite-Polymer Composite Cross-Linker Approach for Highly-Stable and Efficient Perovskite Solar Cells. *Nature Communications* **2019,** 10, 520.
136. Li, J.; Bade, S. G. R.; Shan, X.; Yu, Z., Single-Layer Light-Emitting Diodes Using Organometal Halide Perovskite/Poly(Ethylene Oxide) Composite Thin Films. *Advanced Materials* **2015,** 27, 5196-5202.
137. Kachoosangi, R. T.; Musameh, M. M.; Abu-Yousef, I.; Yousef, J. M.; Kanan, S. M.; Xiao, L.; Davies, S. G.; Russell, A.; Compton, R. G., Carbon Nanotube−Ionic Liquid Composite Sensors and Biosensors. *Analytical Chemistry* **2009,** 81, 435-442.
138. Alcantara, M. L.; de Almeida Oliveira, G.; Lião, L. M.; Borges, C. P.; Mattedi, S., Amine/Carboxylic Acid Ionic Liquid Composite Membranes for Co2 Separation. *Industrial & Engineering Chemistry Research* **2021,** 60, 4405-4419.
139. Tee, B. C. K.; Ouyang, J., Soft Electronically Functional Polymeric Composite Materials for a Flexible and Stretchable Digital Future. *Advanced Materials* **2018,** 30, 1802560.
140. Ren, Y.; Guo, J.; Liu, Z.; Sun, Z.; Wu, Y.; Liu, L.; Yan, F., Ionic Liquid–Based Click-Ionogels. *Science Advances* **2019,** 5, eaax0648.
141. Adjemian, K. T.; Dominey, R.; Krishnan, L.; Ota, H.; Majsztrik, P.; Zhang, T.; Mann, J.; Kirby, B.; Gatto, L.; Velo-Simpson, M.; Leahy, J.; Srinivasan, S.; Benziger, J. B.; Bocarsly, A. B., Function and Characterization of Metal Oxide−Nafion Composite Membranes for Elevated-Temperature H2/O2 Pem Fuel Cells. *Chemistry of Materials* **2006,** 18, 2238-2248.
142. Fujiwara, N.; Asaka, K.; Nishimura, Y.; Oguro, K.; Torikai, E., Preparation of Gold−Solid Polymer Electrolyte Composites as Electric Stimuli-Responsive Materials. *Chemistry of Materials* **2000,** 12, 1750-1754.
143. Peng, X.; Zhang, J.; Stachurski, Z. H.; Banaszak Holl, M. M.; Xiao, P., Visible-Light-Sensitive Triazine-Coated Silica Nanoparticles: A Dual Role Approach to Polymer Nanocomposite Materials with Enhanced Properties. *ACS Applied Materials & Interfaces* **2021,** 13, 46033-46042.
144. Roszkowski, P.; Sahin, M.; Ayalur-Karunakaran, S.; Gammer, C.; Schlögl, S.; Kern, W.; Krawczyk, K. K., Synthesis and Evaluation of New Radical Photoinitiators Bearing Trialkoxysilyl Groups for Surface Immobilization. *Polymer* **2017,** 129, 207-220.
145. Li, X.; Liu, Z.; Hong, P.; Chen, L.; Liu, X., Synthesis of Organic and Inorganic Hybrid Nanoparticles as Multifunctional Photoinitiator and Its Application in Uv-Curable Epoxy Acrylate-Based Coating Systems. *Progress in Organic Coatings* **2020,** 141, 105565.
146. Yamaji, K.; Kawasaki, Y.; Yoshitome, K.; Matsunaga, H.; Sendo, T., Quantitation and Human Monocyte Cytotoxicity of the Polymerization Agent 1-Hydroxycyclohexyl Phenyl Ketone (Irgacure 184) from Three Brands of Aqueous Injection Solution. *Biol Pharm Bull* **2012,** 35, 1821-5.
147. Arvanitoyannis, I. S.; Kotsanopoulos, K. V., Migration Phenomenon in Food Packaging. Food–Package Interactions, Mechanisms, Types of Migrants, Testing and Relative Legislation—a Review. *Food and Bioprocess Technology* **2014,** 7, 21-36.
148. El-Abaseri, T. B.; Hansen, L. A., Egfr Activation and Ultraviolet Light-Induced Skin Carcinogenesis. *J Biomed Biotechnol* **2007,** 2007, 97939.
149. Jeong, G.; Park, C. H.; Kim, B.-Y.; Kim, J.; Park, S.-D.; Yang, H.; Lee, W. S., Photocurable Elastomer Composites with Sio2-Mediated Cross-Links for Mechanically Durable 3d Printing Materials. *ACS Applied Polymer Materials* **2020,** 2, 5228-5237.
150. Shah, P. K.; Stansbury, J. W., Photopolymerization Shrinkage-Stress Reduction in Polymer-Based Dental Restoratives by Surface Modification of Fillers. *Dental Materials* **2021,** 37, 578-587.

151. Hocken, A.; Beyer, F. L.; Lee, J. S.; Grim, B. J.; Mithaiwala, H.; Green, M. D., Covalently Integrated Silica Nanoparticles in Poly(Ethylene Glycol)-Based Acrylate Resins: Thermomechanical, Swelling, and Morphological Behavior. *Soft Matter* **2022,** 18, 1019-1033.
152. Zhang, J.; Liu, E.; Hao, S.; Yang, X.; Li, T.; Lou, C.; Run, M.; Song, H., 3d Printable, Ultra-Stretchable, Self-Healable, and Self-Adhesive Dual Cross-Linked Nanocomposite Ionogels as Ultra-Durable Strain Sensors for Motion Detection and Wearable Human-Machine Interface. *Chemical Engineering Journal* **2022,** 431, 133949.
153. Guimarães, L.; Enyashin, A. N.; Seifert, G.; Duarte, H. A., Structural, Electronic, and Mechanical Properties of Single-Walled Halloysite Nanotube Models. *The Journal of Physical Chemistry C* **2010,** 114, 11358-11363.
154. Mohammadi, M.; Khodamorady, M.; Tahmasbi, B.; Bahrami, K.; Ghorbani-Choghamarani, A., Boehmite Nanoparticles as Versatile Support for Organic–Inorganic Hybrid Materials: Synthesis, Functionalization, and Applications in Eco-Friendly Catalysis. *Journal of Industrial and Engineering Chemistry* **2021,** 97, 1-78.
155. Brunton, P. A.; Davies, R. P. W.; Burke, J. L.; Smith, A.; Aggeli, A.; Brookes, S. J.; Kirkham, J., Treatment of Early Caries Lesions Using Biomimetic Self-Assembling Peptides – a Clinical Safety Trial. *British Dental Journal* **2013,** 215, E6-E6.
156. Nieto, S.; Toro, N.; Robles, P.; Gálvez, E.; Gallegos, S.; Jeldres, R. I., Flocculation of Clay-Based Tailings: Differences of Kaolin and Sodium Montmorillonite in Salt Medium. In *Materials*, 2022; Vol. 15.
157. Brown, G., *Crystal Structures of Clay Minerals and Their X-Ray Identification*. The Mineralogical Society of Great Britain and Ireland: 1982; Vol. 5.
158. Turp, O.; Acar, S. B.; Ozdemir, K.; Bouharras, F. E.; Raihane, M.; Tasdelen, M. A., Halloysite Containing Thermoset Nanocomposites Via Free Radical Photocrosslinking Polymerization. *Macromolecular Chemistry and Physics* **2020,** 221, 2000197.
159. Bekin Acar, S.; Ozdemir, K.; Raihane, M.; Lahcini, M.; Tasdelen, M. A., Thermoset Nanocomposites Reinforced by Vinyl-Functionalized Halloysite. *Polymer Composites* **2023,** 44, 148-155.
160. Bekin Acar, S.; Ciftci, M.; Bouharras, F. E.; Raihane, M.; Tasdelen, M. A., In-Situ Preparation of Halloysite Nanotube-Epoxy Thermoset Nanocomposites Via Light-Induced Cationic Polymerization. *European Polymer Journal* **2021,** 158, 110682.
161. Owusu-Adom, K.; Guymon, C. A., Chemical Compatibility and Reaction-Induced Exfoliation in Photopolymerizable Clay Nanocomposites. *Macromolecules* **2009,** 42, 180-187.
162. Han, Y.; Wang, F.; Wang, H.; Jiao, X.; Chen, D., High-Strength Boehmite-Acrylate Composites for 3d Printing: Reinforced Filler-Matrix Interactions. *Composites Science and Technology* **2018,** 154, 104-109.
163. Yoshikawa, H.; Myoui, A., Bone Tissue Engineering with Porous Hydroxyapatite Ceramics. *Journal of Artificial Organs* **2005,** 8, 131-136.
164. Yang, Y.; Zhang, Q.; Xu, T.; Zhang, H.; Zhang, M.; Lu, L.; Hao, Y.; Fuh, J. H.; Zhao, X., Photocrosslinkable Nanocomposite Ink for Printing Strong, Biodegradable and Bioactive Bone Graft. *Biomaterials* **2020,** 263, 120378.
165. Abd-Elsalam, K. A., 1 - Carbon Nanomaterials: 30 Years of Research in Agroecosystems. In *Carbon Nanomaterials for Agri-Food and Environmental Applications*, Abd-Elsalam, K. A., Ed. Elsevier: 2020; pp 1-18.
166. Palaganas, J. O.; Palaganas, N. B.; Ramos, L. J. I.; David, C. P. C., 3d Printing of Covalent Functionalized Graphene Oxide Nanocomposite Via Stereolithography. *ACS Applied Materials & Interfaces* **2019,** 11, 46034-46043.
167. Ramírez-Soria, E.-H.; Bonilla-Cruz, J.; Flores-Amaro, M. G.; García, V. J.; Lara-Ceniceros, T. E.; Longoria-Rodríguez, F. E.; Elizondo, P.; Advincula, R. C., On the Effect of Ultralow Loading of Microwave-Assisted Bifunctionalized Graphene Oxide in Stereolithographic 3d-Printed Nanocomposites. *ACS Applied Materials & Interfaces* **2020,** 12, 49061-49072.
168. Yu, B.; Wang, X.; Xing, W.; Yang, H.; Wang, X.; Song, L.; Hu, Y.; Lo, S., Enhanced Thermal and Mechanical Properties of Functionalized Graphene/Thiol-Ene Systems by Photopolymerization Technology. *Chemical Engineering Journal* **2013,** 228, 318-326.

169. Yuwawech, K.; Wootthikanokkhan, J.; Tanpichai, S., Functionalized Graphene Nanoplatelets as a Barrier Enhancing Filler in Organic Photovoltaic Encapsulant. *Journal of Applied Polymer Science* **2021,** 138, 50351.
170. İlgün, K.; Oktay, B.; Kayaman Apohan, N., Methacrylate Functionalized Mwcnts/Pdms-Polyurethane Methacrylate Uv-Curable Nanocomposites. *Journal of Inorganic and Organometallic Polymers and Materials* **2018,** 28, 1235-1245.
171. Subramanian, A. S.; Hu, X. M., Heterogeneous Photosensitizers: Super-Efficient Dual Functional Polydopamine Nanohybrid for Epoxy Photopolymerization. *Polymer* **2022,** 243, 124558.
172. Wang, J.; Chiappone, A.; Roppolo, I.; Shao, F.; Fantino, E.; Lorusso, M.; Rentsch, D.; Dietliker, K.; Pirri, C. F.; Grützmacher, H., All-in-One Cellulose Nanocrystals for 3d Printing of Nanocomposite Hydrogels. *Angewandte Chemie International Edition* **2018,** 57, 2353-2356.
173. Palaganas, N. B.; Palaganas, J. O.; Doroteo, S. H. Z.; Millare, J. C., Covalently Functionalized Cellulose Nanocrystal-Reinforced Photocurable Thermosetting Elastomer for 3d Printing Application. *Additive Manufacturing* **2023,** 61, 103295.
174. Maturi, M.; Spanu, C.; Fernández-Delgado, N.; Molina, S. I.; Comes Franchini, M.; Locatelli, E.; Sanz de León, A., Fatty Acid – Functionalized Cellulose Nanocomposites for Vat Photopolymerization. *Additive Manufacturing* **2023,** 61, 103342.
175. Feng, X.; Yang, Z.; Chmely, S.; Wang, Q.; Wang, S.; Xie, Y., Lignin-Coated Cellulose Nanocrystal Filled Methacrylate Composites Prepared Via 3d Stereolithography Printing: Mechanical Reinforcement and Thermal Stabilization. *Carbohydrate Polymers* **2017,** 169, 272-281.
176. Maalihan, R. D.; Chen, Q.; Tamura, H.; Sta. Agueda, J. R. H.; Pajarito, B. B.; Caldona, E. B.; Advincula, R. C., Mechanically and Thermally Enhanced 3d-Printed Photocurable Polymer Nanocomposites Containing Functionalized Chitin Nanowhiskers by Stereolithography. *ACS Applied Polymer Materials* **2022,** 4, 2513-2526.
177. D'Acierno, F.; Liu, L.; Nguyen, T. D.; Michal, C. A.; Palma-Dibb, R. G.; Carvalho, R. M.; MacLachlan, M. J., Physical and Mechanical Properties of a Dental Resin Adhesive Containing Hydrophobic Chitin Nanocrystals. *Dent Mater* **2022,** 38, 1855-1865.
178. Abo Elsoud, M. M.; El Kady, E. M., Current Trends in Fungal Biosynthesis of Chitin and Chitosan. *Bulletin of the National Research Centre* **2019,** 43, 59.
179. He, M.; Han, B.; Jiang, Z.; Yang, Y.; Peng, Y.; Liu, W., Synthesis of a Chitosan-Based Photo-Sensitive Hydrogel and Its Biocompatibility and Biodegradability. *Carbohydrate Polymers* **2017,** 166, 228-235.
180. Zhou, Y.; Yang, H.; Liu, X.; Mao, J.; Gu, S.; Xu, W., Potential of Quaternization-Functionalized Chitosan Fiber for Wound Dressing. *International Journal of Biological Macromolecules* **2013,** 52, 327-332.
181. Croisier, F.; Jérôme, C., Chitosan-Based Biomaterials for Tissue Engineering. *European Polymer Journal* **2013,** 49, 780-792.
182. Pei, M.; Mao, J.; Xu, W.; Zhou, Y.; Xiao, P., Photocrosslinkable Chitosan Hydrogels and Their Biomedical Applications. *Journal of Polymer Science Part A: Polymer Chemistry* **2019,** 57, 1862-1871.
183. Matsuda, T.; Magoshi, T., Preparation of Vinylated Polysaccharides and Photofabrication of Tubular Scaffolds as Potential Use in Tissue Engineering. *Biomacromolecules* **2002,** 3, 942-950.
184. Zhou, Y.; Liang, K.; Zhao, S.; Zhang, C.; Li, J.; Yang, H.; Liu, X.; Yin, X.; Chen, D.; Xu, W.; Xiao, P., Photopolymerized Maleilated Chitosan/Methacrylated Silk Fibroin Micro/Nanocomposite Hydrogels as Potential Scaffolds for Cartilage Tissue Engineering. *International Journal of Biological Macromolecules* **2018,** 108, 383-390.
185. Chen, Q.; De Marco, N.; Yang, Y.; Song, T.-B.; Chen, C.-C.; Zhao, H.; Hong, Z.; Zhou, H.; Yang, Y., Under the Spotlight: The Organic–Inorganic Hybrid Halide Perovskite for Optoelectronic Applications. *Nano Today* **2015,** 10, 355-396.
186. Cho, H.; Jeong, S.-H.; Park, M.-H.; Kim, Y.-H.; Wolf, C.; Lee, C.-L.; Heo, J. H.; Sadhanala, A.; Myoung, N.; Yoo, S.; Im, S. H.; Friend, R. H.; Lee, T.-W., Overcoming the Electroluminescence Efficiency Limitations of Perovskite Light-Emitting Diodes. *Science* **2015,** 350, 1222-1225.
187. Choi, J.; Park, S.; Lee, J.; Hong, K.; Kim, D.-H.; Moon, C. W.; Park, G. D.; Suh, J.; Hwang, J.; Kim, S. Y.; Jung, H. S.; Park, N.-G.; Han, S.; Nam, K. T.; Jang, H. W., Organolead Halide

Perovskites for Low Operating Voltage Multilevel Resistive Switching. *Advanced Materials* **2016,** 28, 6562-6567.
188. Yakunin, S.; Sytnyk, M.; Kriegner, D.; Shrestha, S.; Richter, M.; Matt, G. J.; Azimi, H.; Brabec, C. J.; Stangl, J.; Kovalenko, M. V.; Heiss, W., Detection of X-Ray Photons by Solution-Processed Lead Halide Perovskites. *Nature Photonics* **2015,** 9, 444-449.
189. Park, N.-G., Organometal Perovskite Light Absorbers toward a 20% Efficiency Low-Cost Solid-State Mesoscopic Solar Cell. *J. Phys. Chem. Lett.* **2013,** 4, 2423-2429.
190. Gao, P.; Grätzel, M.; Nazeeruddin, M. K., Organohalide Lead Perovskites for Photovoltaic Applications. *Energy & Environmental Science* **2014,** 7, 2448-2463.
191. Wong, Y.-C.; De Andrew Ng, J.; Tan, Z.-K., Perovskite-Initiated Photopolymerization for Singly Dispersed Luminescent Nanocomposites. *Advanced Materials* **2018,** 30, 1800774.
192. Wu, J.; Tong, J.; Gao, Y.; Wang, A.; Zhang, T.; Tan, H.; Nie, S.; Deng, Z., Efficient and Stable Thin-Film Luminescent Solar Concentrators Enabled by near-Infrared Emission Perovskite Nanocrystals. *Angewandte Chemie International Edition* **2020,** 59, 7738-7742.
193. Peng, X.; Hu, L.; Sun, X.; Lu, Y.; Chu, D.; Xiao, P., Fabrication of High-Performance Cspbbr3 Perovskite Quantum Dots/Polymer Composites Via Photopolymerization: Implications for Luminescent Displays and Lighting. *ACS Applied Nano Materials* **2023,** 6, 646-655.
194. Esposito Corcione, C.; Frigione, M.; Maffezzoli, A.; Malucelli, G., Photo – Dsc and Real Time – Ft-Ir Kinetic Study of a Uv Curable Epoxy Resin Containing O-Boehmites. *European Polymer Journal* **2008,** 44, 2010-2023.
195. Melinte, V.; Chibac, A.; Buruiana, T.; Buruiana, E. C., Hybrid Nanocomposites Prepared by in Situ Photopolymerization Using Photoinitiator-Modified Montmorillonite. *Progress in Organic Coatings* **2017,** 104, 125-134.
196. Li, J.-R.; Sculley, J.; Zhou, H.-C., Metal–Organic Frameworks for Separations. *Chemical reviews* **2012,** 112, 869-932.
197. Sumida, K.; Rogow, D. L.; Mason, J. A.; McDonald, T. M.; Bloch, E. D.; Herm, Z. R.; Bae, T.-H.; Long, J. R., Carbon Dioxide Capture in Metal–Organic Frameworks. *Chemical reviews* **2012,** 112, 724-781.
198. Zhang, Y.; Feng, X.; Li, H.; Chen, Y.; Zhao, J.; Wang, S.; Wang, L.; Wang, B., Photoinduced Postsynthetic Polymerization of a Metal–Organic Framework toward a Flexible Stand-Alone Membrane. *Angewandte Chemie International Edition* **2015,** 54, 4259-4263.
199. Satheeshkumar, C.; Yu, H. J.; Park, H.; Kim, M.; Lee, J. S.; Seo, M., Thiol–Ene Photopolymerization of Vinyl-Functionalized Metal–Organic Frameworks Towards Mixed-Matrix Membranes. *Journal of Materials Chemistry A* **2018,** 6, 21961-21968.
200. Lee, J.; Satheeshkumar, C.; Yu, H. J.; Kim, S.; Lee, J. S.; Seo, M.; Kim, M., Pore Engineering of Covalently Connected Metal–Organic Framework Nanoparticle–Mixed-Matrix Membrane Composites for Molecular Separation. *ACS Applied Nano Materials* **2020,** 3, 9356-9362.
201. Kammakakam, I.; Bara, J. E.; Jackson, E. M., Dual Anion–Cation Crosslinked Poly(Ionic Liquid) Composite Membranes for Enhanced Co2 Separation. *ACS Applied Polymer Materials* **2020,** 2, 5067-5076.
202. Liu, J.; Zhu, K.; Jiao, T.; Xing, R.; Hong, W.; Zhang, L.; Zhang, Q.; Peng, Q., Preparation of Graphene Oxide-Polymer Composite Hydrogels Via Thiol-Ene Photopolymerization as Efficient Dye Adsorbents for Wastewater Treatment. *Colloids and Surfaces A: Physicochemical and Engineering Aspects* **2017,** 529, 668-676.
203. Wu, N.; Che, S.; Li, H.-w.; Wang, C.-n.; Tian, X.-j.; Li, Y.-f., A Review of Three-Dimensional Graphene Networks for Use in Thermally Conductive Polymer Composites: Construction and Applications. *New Carbon Materials* **2021,** 36, 911-926.
204. Zhang, L.; Shi, G., Preparation of Highly Conductive Graphene Hydrogels for Fabricating Supercapacitors with High Rate Capability. *The Journal of Physical Chemistry C* **2011,** 115, 17206-17212.
205. Vlassiouk, I.; Polizos, G.; Cooper, R.; Ivanov, I.; Keum, J. K.; Paulauskas, F.; Datskos, P.; Smirnov, S., Strong and Electrically Conductive Graphene-Based Composite Fibers and Laminates. *ACS Applied Materials & Interfaces* **2015,** 7, 10702-10709.

206. Martin-Gallego, M.; Lopez-Manchado, M. A.; Calza, P.; Roppolo, I.; Sangermano, M., Gold-Functionalized Graphene as Conductive Filler in Uv-Curable Epoxy Resin. *Journal of Materials Science* **2015,** 50, 605-610.
207. Roppolo, I.; Chiappone, A.; Bejtka, K.; Celasco, E.; Chiodoni, A.; Giorgis, F.; Sangermano, M.; Porro, S., A Powerful Tool for Graphene Functionalization: Benzophenone Mediated Uv-Grafting. *Carbon* **2014,** 77, 226-235.
208. Liu, Y.; Zeng, Q.; Chen, P.; Li, Z.; Chen, A.; Guan, J.; Wang, A.; Zhang, L., Modified Mof-Based Composite All-Solid-State Polymer Electrolyte with Improved Comprehensive Performance for Dendrite-Free Li-Ion Batteries. *Macromolecular Chemistry and Physics* **2022,** 223, 2100325.
209. Villa, S. M.; Mazzola, V. M.; Santaniello, T.; Locatelli, E.; Maturi, M.; Migliorini, L.; Monaco, I.; Lenardi, C.; Comes Franchini, M.; Milani, P., Soft Piezoionic/Piezoelectric Nanocomposites Based on Ionogel/Batio3 Nanoparticles for Low Frequency and Directional Discriminative Pressure Sensing. *ACS Macro Letters* **2019,** 8, 414-420.

Chapter 2 Visible-Light-Sensitive Triazine-Coated Silica Nanoparticles: A Dual Role Approach to Polymer Nanocomposite Materials with Enhanced Properties

2.1. Preface

The creation of nanocomposite materials has garnered attention due to their enhanced mechanical, optical, and thermal properties, making them suitable for diverse applications such as electronics, medicine, and environmental engineering.[1-5] Traditional synthesis methods often require high temperatures or toxic solvents, posing environmental and health risks. Photopolymerization offers a safer, low-cost, and eco-friendly alternative that provides precise spatial and temporal control over polymerization.[6] Among various types of nanomaterials, silica nanoparticles (Silica NPs) are widely used as fillers due to their functionalizable surfaces, biocompatibility, and structural versatility.[7, 8] However, achieving uniform dispersion is challenging, as nanoparticles naturally tend to aggregate, undermining the material's integrity. Surface modification using photoinitiators helps improve compatibility and dispersion while also minimizing migration, which is essential in applications like food packaging.[9]

This chapter focus on developing triazine-coated silica nanoparticles (Si-triazine NPs) that respond to blue light (LED@410 nm) for safer photopolymerization. The Si-triazine NPs were evaluated for their dual roles: initiating polymerization and reinforcing the matrix. Experimental results, including real-time Fourier-transform infrared spectroscopy (RT-FTIR) and photorheometry, demonstrated their effectiveness in reducing shrinkage, enhancing dispersion, and improving mechanical stability. The study also examines the impact of varying Si-triazine NPs concentrations on photopolymerization kinetics and composite properties.

This chapter advances the field of photopolymerized nanocomposites by presenting an approach that combines safety, functionality, and scalability. By leveraging triazine-coated silica nanoparticles, this work demonstrates a promising pathway for developing durable, low-migration materials for industrial, medical, and environmental applications.

2.2. Statement of contribution

I declare that the research findings presented in this chapter are the original work I conducted as part of my Ph.D. program at the Australian National University. As the primary author, I was responsible for developing the research concept, designing the experiments, analyzing the data, creating the figures, and drafting the initial manuscript, under the guidance of my primary supervisor, Prof. Pu Xiao.

2.3. Publication status

The published manuscript titled “Visible-Light-Sensitive Triazine-Coated Silica Nanoparticles: A Dual Role Approach to Polymer Nanocomposite Materials with Enhanced Properties” and its supporting information are reproduced in this chapter with permission[10] from American Chemical Society, © 2021. This manuscript was published in the journal **ACS Applied Materials & Interfaces** in 2021. The citation for the published work is:

Peng, X.; Zhang, J.; Stachurski, Z. H.; Holl, M. M. B.; Xiao, P. Visible-Light-Sensitive Triazine-Coated Silica Nanoparticles: A Dual Role Approach to Polymer Nanocomposite Materials with Enhanced Properties. ***ACS Applied Materials & Interfaces,*** **2021**, *13* (38), 46033–46042. https://doi.org/10.1021/acsami.1c15420.

2.4. Abstract

Nanocomposite materials are of great interest because of their superior properties. Besides the traditional synthesis methods that require high temperature or toxic solvents, photopolymerization technology provides a simple, low cost, and environmentally friendly route in preparing nanocomposites. In this research, the preparation of blue light-sensitive triazine derivative-coated silica nanoparticles is present. The resulting triazine-coated silica nanoparticles can play a dual role, i.e. acting as both photoinitiators to trigger photopolymerization reactions under the irradiation of LED@410 nm and as fillers to endow

the produced photopolymer nanocomposite materials with enhanced properties. Specifically, the triazine-coated silica nanoparticles can successfully induce free radical polymerization of trimethylolpropane triacrylate efficiently under the irradiation of LED@410 nm and demonstrate comparable photoinitiation ability to the triazine derivative-based photoinitiator. The effects of different loading amounts of triazine-coated silica nanoparticles towards the photopolymerizations kinetics are also evaluated. By coating with the triazine derivative, the nanoparticles show good dispersion in the polymer matrix and significantly reduce the shrinkage of the samples during the photopolymerization. Moreover, the photocured nanocomposites exhibit enhanced migration stability and mechanical properties when an optimal amount of triazine-coated silica nanoparticles are added in the formulation.

2.5. Introduction

Nanocomposites comprise at least two components with a continuous matrix phase and nano-sized non-continuous reinforcement materials.[11, 12] By incorporating different reinforcement materials, the corresponding nanocomposites display enhanced mechanical[1], optical[2], electrical[3], thermal[4], and magnetic[5] properties; thus, nanocomposites have vast applications in several fields such as electronics[13], photocatalysis[14], medicine[15, 16], and drug delivery[17] etc.. Generally, nanocomposites can be fabricated via melt blending[18], solution mixing[19], or in situ polymerization with heat or light[20]. Compared to the preparation approaches with melt bending and solution mixing requiring high temperature or toxic organic solvents, in situ photopolymerizations are more environmentally friendly and energy-efficient and can provide spatial temporal control during the processes.[6] Among different types of nanoparticles (e.g. titanium dioxide[21], aluminium oxide[22], silicon dioxide[23], gold[24], and silver[3] etc.) used as inorganic fillers in nanocomposites, silica nanoparticles (Silica NPs) with easily functionalizable surfaces, good biocompatibility, tunable sizes, and

rich textural properties have been widely used in nanocomposites fabrication[7, 8]. One major concern in synthesizing nanocomposites is the dispersity of inorganic fillers in the matrix since the nanoparticles have a high tendency to agglomerate.[25] The agglomeration usually degrades the properties of the corresponding nanocomposites[26]. To improve dispersion, surface modification of nanoparticles with polymer surfactant or other structures that provide repulsion between nanoparticles is one of the versatile approaches.[9] Photoinitiators become outstanding candidates for coating onto the silica nanoparticles as they can increase dispersity in the organic matrix and exhibit a low migration tendency of photoinitiators after being incorporated into the polymer matrix[27]. In food packaging materials, migration becomes a critical issue as those unreacted photoinitiations can migrate into the food and raise health issues[28-30]. In recent years, researchers have grafted different commercially available photoinitiators onto the surface of Silica NPs to achieve photoactive nanoparticles. For instance, a type II photoinitiator, 2-chlorothioxanthone (CTX), was grafted onto the Silica NPs and photocrosslinked with epoxy acrylate resin (EA) to yield the corresponding composites[31]. The resulting composites showed good dispersity of fillers, low migration and enhanced mechanical properties compared to the polymers prepared with free CTX. In addition, two photoinitiating Silica NPs were synthesized by immobilizing trialkoxysilyl-functionalized bis(acyl)phosphane oxide (TEMSI^2-BAPO) or 1-[4-(2-(3-triethoxysilanylpropylcarbamoyloxy)ethoxy)-phenyl]-2-hydroxy-2-methyl-1-propane-1-one (TESI-IC2959) onto the Silica NPs[27]. The functionalized Silica NPs were then used to induce the thiol-ene polymerization with UV irradiation. Notably, a low migration of residue photoinitiators from the corresponding composites was achieved. Alternatively, ethyl (2,4,6-trimethylbenzoyl) phenylphosphinate (Irgacure TPO-L) bearing trialkoxysilyl units was immobilized onto Silica NPs and UV cross-linked with acrylic monomers to yield the

corresponding composites. Undoubtedly, fillers were well distributed into the polymer matrix and the patterned polymerization with photomask was possible[32].

Although the synthesis of photoinitiating silica nanoparticles achieved great success, the utilization of UV light for polymerization in the above researches is unfavorable as it is harmful to the human body[33]. Thus, it is desirable to design and develop visible light-sensitive photoinitiating Silica NPs with enhanced performance. Blue light-sensitive 2-(4-methoxystyryl)-4,6-bis(trichloromethyl)-1,3,5-triazine (triazine) showed high initiation ability for various photopolymerizations and 3D printing[34-36] which can make it an ideal candidate to be coated onto the surface of Silica NPs to prepare visible light-sensitive photoinitiating Silica NPs for the fabrication of nanocomposites. Besides, the effect of the loading amount of photoinitiaing Silica NPs towards polymerization kinetics and mechanical properties have not been investigated yet.

In the present work, 4-(2-(4,6-bis(trichloromethyl)-1,3,5-triazin-2-yl)vinyl)phenyl (3-(triethoxysilyl)propyl)carbamate (silylated triazine) was synthesized and coated onto the surface of Silica NPs to generate triazine-coated silica nanoparticles (Si-triazine NPs) as shown in Scheme 2.1. The prepared Si-triazine NPs were investigated for their roles as both the photoinitiators to trigger photopolymerization reactions under the irradiation of LED@410 nm and the fillers to endow the produced polymer nanocomposite materials with various properties. Specifically, the photoinitiation abilities of free triazine or the prepared Si-triazine NPs for the photopolymerization of trimethylolpropane triacrylate (TMPTA) were investigated and compared using the real-time Fourier-transform infrared spectroscopy (RT-FTIR). In addition, the percentage shrinkage of the photocured samples was studied using the photorheometer. Finally, the migration stability of the residue photoinitiators from the bulk and mechanical properties of the photocured samples were also evaluated.

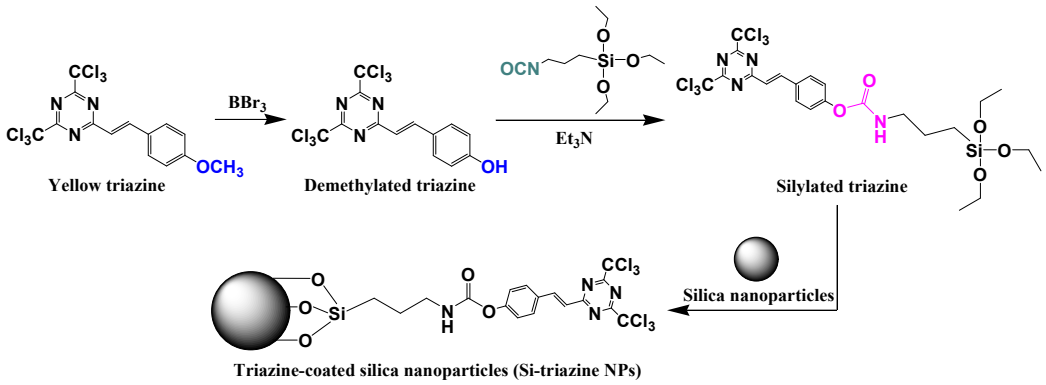

Scheme 2.1. Synthetic procedure to obtain triazine-coated silica nanoparticles (Si-triazine NPs).

2.6. Materials and methods

2.6.1. Materials

Unless specified, all chemicals were used as received. Trimethylolpropane triacrylate (TMPTA), 2-(4-methoxystyryl)-4,6-bis(trichloromethyl)-1,3,5-triazine (triazine), boron tribromide (BBr_3, 1M in heptane), dichloromethane (DCM; Anhydrous), hexane, ethyl acetate (EtOAc), absolute ethanol, ammonium hydroxide (30-33% NH_3 in H_2O), tetraethyl orthosilicate (TEOS), toluene, triethylamine (TEA), 3- (triethoxysilyl)propyl isocyanate, trifluoroacetic acid (TFA), and acetonitrile were all purchased from Sigma-Aldrich. Deuterated NMR solvents (d_6-DMSO) was obtained from Cambridge Isotope Laboratories.

2.6.2. Synthesis

4-(2-(4,6-bis(trichloromethyl)-1,3,5-triazin-2-yl)vinyl)phenol (demethylated triazine). 2-(4-Methoxystyryl)-4,6-bis(trichloromethyl)-1,3,5-triazine (triazine) (0.2 g, 0.45 mmol) was dissolved in 20 mL of anhydrous DCM and stirred at -78°C (immersed in the mixture of dry ice and acetone) with protection by applying a drying tube filled with $CaCl_2$. BBr_3 (6 mL, 6 mmol) was added dropwise into the solution. The mixture was attainted to room temperature overnight and stirred at room temperature for one day. The reaction mixture

was then quenched with ice water (100 mL) and extracted by DCM. The organic layer was dried by anhydrous sodium sulphate and concentrated under vacuum to yield demethylated triazine as a yellow solid (67% yield).

^{1}H NMR (400 MHz, DMSO-d_6) δ 10.37 (s, 1H), 8.36 (d, J = 15.6 Hz, 1H), 7.83 (d, J = 8.3 Hz, 2H), 7.31 (d, J = 15.7 Hz, 1H), 6.88 (d, J = 8.2 Hz, 2H). ^{13}C NMR (101 MHz, DMSO-d_6) δ 175.3, 173.9, 161.7, 147.9, 132.3, 125.7, 120.4, 116.6, 89.8.

4-(2-(4,6-bis(trichloromethyl)-1,3,5-triazin-2-yl)vinyl)phenyl (3-(triethoxysilyl)propyl)carbamate (silylated triazine). Demethylated triazine (0.5 g, 1.15 mmol) was dissolved in toluene (10 mL). TEA (20 uL, 0.14 mmol) and 3-(triethoxysilyl)propyl isocyanate (0.34 mL, 1.38 mmol) were added, the mixture was then stirred at 70°C for two days. The mixture was concentrated in vacuum and purified by silica column chromatography using a mixture of DCM/EtOAc (gradient 0-50% EtOAc). Silylated triazine was obtained as a pale-yellow crystal (64% yield).

^{1}H NMR (400 MHz, DMSO-d_6) δ 8.41 (d, J = 15.8 Hz, 1H), 8.00 (d, J = 8.4 Hz, 2H), 7.52 (d, J = 15.8 Hz, 1H), 7.23 (d, J = 8.3 Hz, 2H), 5.77 (s, 1H), 3.77 (q, J = 7.0 Hz, 6H), 3.07 (q, J = 6.7 Hz, 2H), 1.56 (q, J = 8.0 Hz, 2H), 1.17 (t, J = 7.0 Hz, 9H), 0.64 – 0.58 (m, 2H). ^{13}C NMR (101 MHz, DMSO-d_6) δ 175.1, 174.1, 174.1, 154.2, 146.4, 131.2, 131.2, 131.1, 123.9, 122.7, 95.2, 58.2, 43.7, 23.3, 18.7, 7.6.

Silica nanoparticles (Silica NPs). The silica nanoparticles were prepared following the modified Stöber process reported previously[37]. Specifically, ammonium hydroxide (20 mL) and absolute ethanol (172.5 mL) were stirred at 650 r.p.m under nitrogen for 30 min. TEOS (7.5 mL) was added and the mixture was continued stirring for three days at room temperature. The resulting milky suspension was centrifuged at 3500 r.p.m. for 30 min, then

washed and resuspended in water. The suspension was again centrifuged and washed thrice with absolute ethanol (resuspended and centrifuged for each washing). The Silica NPs was resuspended in ethanol (5 mL) and vacuum dried at 70°C overnight.

Triazine-coated silica nanoparticles (Si-triazine NPs). The coating of triazine on the surface of the prepared silica nanoparticles was achieved following the procedure reported previously[32]. Specifically, silylated triazine (0.25 g) dissolved in toluene (2.5 mL) was added to Silica NPs (1.2 g) dissolved in toluene (27.5mL). The mixture was stirred at room temperature with nitrogen protection for one day. TFA (50 uL) in ethanol (2.5 mL) was added to the mixture and continuously stirred for one day. The mixture was evaporated, and the residue solid was resuspended in ethanol (20 mL) and then TFA (50 uL) was added. The mixture was stirred overnight. The solvent was evaporated and solid was resuspended in ethanol (20 mL). The mixture was centrifuged at 3500 r.p.m for 30 min. After removing of the solvent, toluene (20 mL) was added and the residue solid was resuspended by sonication (10 min). The mixture was again centrifuged at 3500 r.p.m for 30 min. Toluene was removed to yield the pale-yellow triazine-coated silica nanoparticles (Si-triazine NPs).

2.6.3. Photopolymerization experiment

Photopolymerization of TMPTA in the presence of the investigated triazine-coated silica nanoparticles (Si -triazine NPs) upon the exposure to the LED@410 nm (110 mW/cm^2) was investigated using the real-time infrared INVENIO R (RT-FTIR) manufactured by BRUKER. Free radical polymerization of TMPTA was conducted in laminate. Specifically, formulations were added in between two polypropylene films with a thickness of samples approximately 25 µm. The film was then placed on a BaF_2 pellet and placed in the measuring holder. The evolution of the double bond of TMPTA was at the band of 1620 cm^{-1}. Conversions of functional groups of monomers were calculated by the following equation:

$$C = \frac{A_0 - A_t}{A_0} \times 100\%$$

where A_0 the initial peak area before irradiation and A_t the peak area of the functional groups at time t.

2.6.4. Photorheology test

Photorheology characterization was performed using an Anton Paar MCR 702 multidrive rheometer. Tests were conducted at 25°C using a plate geometry (PP25) with a 25 mm diameter. 100 µL of the liquid formula was placed on the holder (glass) with the plate sensor pressing from the top until the gap between the sensor and the bottom holder became 0.2-0.4 mm. Irradiation was located at the bottom of the sample holder and a parallel plate (sensor) was measured from the top of the sample holder. The light passed from the bottom to the top of the samples. Tests were performed at a constant angular frequency of 1 Hz with a shear range of 0.1%. Normal force was set to 0 N for the entire experiment (it means the gap may change during the measurements if the formulation shrinks). Changes in storage/loss modulus of the formulations and gap distance were recorded.

2.6.5. Scanning Electron Microscopy (SEM)

A scanning electron microscope (Zeiss UltraPlus FESEM) was used to reveal the surface morphologies of Silica NPs and Si-triazine NPs, and the internal morphologies of the photocured samples. The Silica NPs and Si-triazine NPs were mounted on the SEM tubs with a conductive adhesive carbon tape; the photocured samples were first sectioned into 1 um thickness slices with a cutter (Lecia EM UC7 Ultramicrotome), the slices were then collected onto the TEM copper grids and mount onto the SEM stubs with conductive

adhesive carbon tape. The SEM images were acquired under vacuum, at 0.7 kV and magnification from 10,000X – 50,000X.

2.6.6. Atomic force microscopy (AFM) and nano-thermal analysis (nanoTA)

The surface of the photocured samples was characterized using AFM and nanoTA which were carried out on a nanoIR3 instrument (Bruker, Santa Barbara, CA, USA) integrated with a nano-thermal analysis module. AFM data were collected in contact mode using nIR2 probes (gold coated silicon cantilever, nominal radius 25 nm, force constant 0.07-0.4 N/m, resonance frequency 13±4 kHz) and the system was purged with dry nitrogen to maintain a constant humidity < 5 %. AFM height images were acquired at a scan rate of 0.5 Hz and a step size of 20 nm. AFM data were processed using Analysis Studio software (Bruker, Santa Barbara, CA, USA) or Gwyddion (version 2.51, http://gwyddion.net). AFM images were plane fitted with 1st fit order. A ThermaLever (AN2-300, Bruker, Santa Barbara, CA, USA) probe was used for nanoTA. After the AFM image was collected, the probe was moved to the point of interest and the temperature of the tip was then ramped linearly with time, while the deflection of the probe was monitored during the thermal ramp.

2.6.7. Other characterizations

2.6.7.1. Fourier-transform infrared spectroscopy (FTIR)

Infrared spectra of demethylated triazine, silylated triazine, 3-(triethoxysilyl)propyl isocyanate, Silica NPs and Si-triazine NPs were acquired using a Spectrum Two Fourier transform infrared (FTIR) spectrometer (Perkin Elmer) fitted with attenuated total reflectance (ATR) accessory Scans with an average over a range of 500 to 4000 cm^{-1} at a resolution of 4 cm^{-1}.

2.6.7.2. Ultraviolet-visible (UV-vis)measurements

Ultraviolet-visible (UV-vis) measurements were conducted on a Varian Cary 50 Bio UV-vis spectrometer from Agilent Technologies.

2.6.7.3. Thermalgravimetric analysis (TGA)

Thermogravimetric analysis was conducted on a thermal analyser TGA Q500 from TA instruments. The samples were heated from room temperature to 900 °C with a heating rate of 4 °C/min under an air atmosphere. The mass loss was used to evaluate the amount of silylated triazine being coated onto the surface of silica nanoparticles.

2.6.7.4. Mechanical test

Mechanical properties (flexural modulus) of the photocured samples were measured by Instron 4505 testing machine. Samples were photopolymerized in a mould with a length between 20 – 22 mm, a width of 5 mm and thickness between 1-2 mm (the instrument can normalize the dimensions). 3 points bending test was performed with a compression rate of 10 mm/min. The load-deflection curves were recorded and the flexural moduli were calculated from the slope of the curves and dimensions of the samples.

2.6.7.5. Dielectric analysis

A dielectric analyzer (DEA 288 Ionic, Netzsch) was used to determine the ion viscosity and temperature change during the photopolymerization processes. All measurements were performed at 215 kHz with interdigitated electrode IDEX sensors (115 um). For each measurement, 100 uL of the sample was evenly distributed onto the sensor and covered with a thin film to avoid the oxygen inhibition for the free radical photopolymerization. The light was irradiated from the top of the sensor and the corresponding information was recorded.

2.6.7.6. Migration test

Photocured samples with a thickness of 0.3 mm were prepared. The comparing samples had equal mass of 0.14 g. The investigated samples were immersed in 5 mL of acetonitrile for 20 h. UV-vis measurements were carried out to determine the migration stability.

2.7. Result and discussion

2.7.1. Synthesis and characterization of silylated triazine

Triazine was first reacted with BBr_3 to form demethylated triazine which has an OH functional group instead. Further reaction of demethylated triazine with 3-(triethoxysilyl)propyl isocyanate was proceeded to obtain silylated triazine. The details on the synthesis of demethylated triazine, silylated triazine and silica nanoparticles were given in the materials and methods section. The success in synthesizing of demethylated triazine and silylated triazine was confirmed by ^{1}H NMR and ^{13}C NMR as shown in Figure S2.1-S2.4. From the FTIR spectra (Figure S2.5), the absence of a characteristic band at 2260 cm^{-1} attributing to the N=C=O stretching[38] and the presence of characteristic bands at 3334 cm^{-1} and 1718 cm^{-1} attributing to the N-H stretching and C=O stretching respectively[38] again confirmed the successful synthesis of silylated triazine from demethylated triazine and 3-(triethoxysilyl)propyl isocyanate. In addition, as presented in Figures S2.6 and S2.7, the prepared silylated triazine showed blue-shifted UV-vis absorption (λ_{max} = 350 nm, $\lambda_{350\ nm}$ = 41000 M^{-1} cm^{-1}) compared to that of 2-(4-methoxystyryl)-4,6-bis(trichloromethyl)-1,3,5-triazine (λ_{max} = 373 nm, $\lambda_{373\ nm}$ = 44000 M^{-1} cm^{-1})[36]. However, it still showed light absorption up to 425 nm, which can overlap with the emission wavelength of the LED@410 nm used in this study.

2.7.2. Preparation of triazine-coated silica nanoparticles

The surface coating of silica nanoparticles with silylated triazine was performed by mixing Silica NPs and silylated triazine in ethanol with a catalytic amount of trifluoroacetic acid at room temperature. Figure 2.1 illustrated the FTIR spectra of Si NPs and Si-triazine NPs. The presence of characteristic bands at 1730 cm^{-1} and 1545 cm^{-1} attributing to the C=O stretching and N-H (secondary amine) bending respectively[38] indicated that silylated triazine has successfully coated onto the surface of Si NPs. To further confirm the different surface morphologies before and after triazine coating, Si NPs and Si-triazine NPs were observed by SEM (Figure 2.2(a) and 2.2(b) respectively). In both samples, the size of nanoparticles was about 400 nm. Si NPs showed smooth sphere surfaces while Si-triazine NPs appeared rougher sphere surfaces[31], which again indicated the success in coating of silylated triazine onto the surfaces of Si NPs.

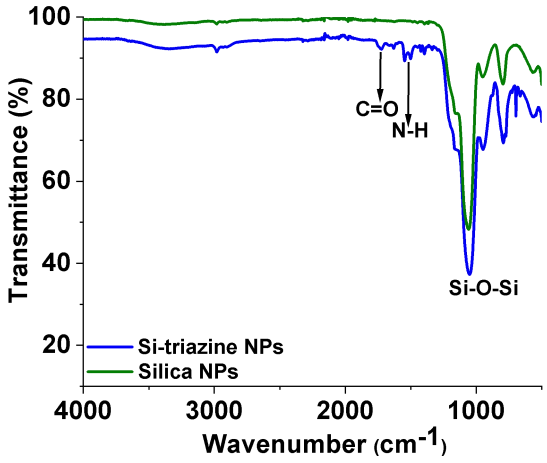

Figure 2. 1.FTIR spectra of Silica NPs and Si-triazine NPs.

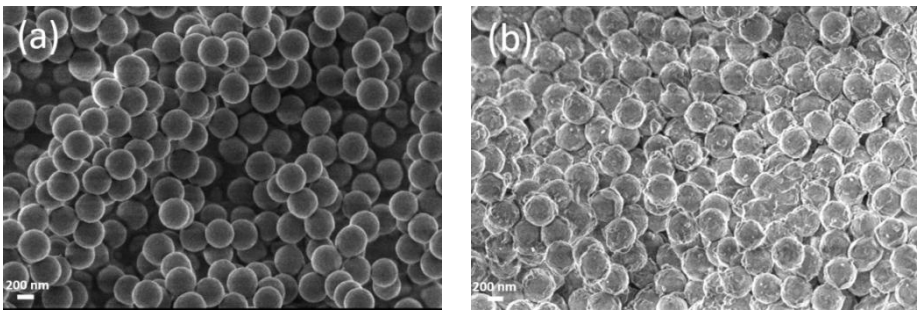

Figure 2. 2. SEM images of (a) Silica NPs and (b) Si-triazine NPs.

Thermogravimetric analysis (TGA) and UV-vis measurements were carried out to determine the amount of the silylated triazine coated onto the surface of Silica NPs. The TGA curve of Si-triazine NPs was compared with that of uncoated Silica NPs in Figure 2.3. In both samples, the weight loss observed below 100°C was attributed to the release of water from silanol groups[39]. The additional weight loss in Si-triazine NPs was attributed to the thermal degradation of silylated triazine. Since the water and silanol content in both samples were similar[39], the coating amount was estimated to be 13 wt%, corresponded to 0.19 mmol of silylated triazine per 1 g of Si-triazine NPs. The coating amount was double confirmed with UV-vis measurements. The UV-vis light absorptions with different known concentrations of silylated triazine or Si-triazine NPs in acetonitrile were plotted (Figure S2.6 and Figure S2.8). As a result, the coating amount of silylated triazine on the surface of Silica NPs was determined to be 13 wt% as detailed in the supporting information (Figure S2.7), which was in agreement with the result obtained from the TGA. Hence the coating amount was calculated as 13 wt% for the following experiments.

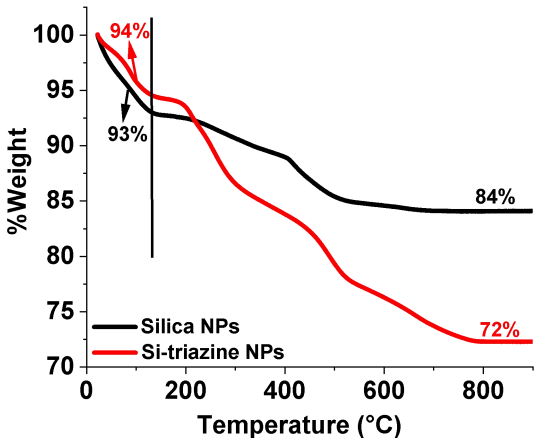

Figure 2. 3. TGA curves of Silica NPs and Si-triazine NPs.

2.7.3. Photoinitiation ability of Si-triazine NPs

The photoinitiation ability of Si-triazine NPs for the photopolymerization of trimethylolpropane triacrylate (TMPTA) in laminate was investigated upon exposure to LED @410 nm. 2-(4-Methoxystyryl)-4,6-bis(trichloromethyl)-1,3,5-triazine (triazine) showed great initiation ability for the free radical photopolymerization[35] and thiol-ene photopolymerization under the irradiation of LED@ 410 nm, 445 nm or 465 nm[34]. The polymerization profiles are given in Figure 2.4, and the double bond conversions of TMPTA after 300 s of photopolymerization and their relevant maximum polymerization rates are summarized in Table 2.1. In Figure 2.4(a), three formulations with the addition of 0.5 wt% triazine, 0.76 wt% silylated triazine and 5.8 wt% Si-triazine NPs were compared. It should be noted that the molar concentration of the triazine moiety (photoinitiator) in all three formulations are equal (i.e. 11.1 umol/g). The double bond conversions were found to be 49%, 51%, and 50% respectively, with negligible differences. And the maximum polymerization rates of the three formulations were found to be 5.5 s^{-1}, 8.7 s^{-1} and 7.3 s^{-1}, respectively. Interestingly, the modified triazines (i.e. silylated triazine and Si-triazine NPs) demonstrated the higher polymerization rate than that of the crude triazine, indicating that the photoinitiation abilities of the triazine-containing compounds were improved with the modification. The slightly decreased polymerization rate of Si-triazine NPs/TMPTA compared to silylated triazine/TMPTA might be due to decreased in mobility of coated triazine moiety in Si-triazine NPs. These results confirmed the effective photoinitiation ability of silylated triazine. More interestingly, the coating of silylated triazine onto the surface of Silica NPs did not significantly affect their photoinitiation abilities. In Figure 2.4(b), the increased amounts of Si-triazine NPs from 10 wt% to 50 wt% resulted in increased of double bond conversions from 55% to 69%. Obviously, the increase of double bond conversions was due to the increased concentrations of triazine moiety in the formulations (i.e. increased from 19.1 to

95.4 umol/g). The maximum polymerization rates had no significant difference when high amount of Si-triazine NPs were added (10 wt%, 20 wt%, and 50 wt%). The difference in the polymerization rates was more pronounced when comparing formulations with low concentration (5.8 wt%, 7.3 s^{-1}) and high amount (50 wt%, 4.0 s^{-1}) of Si-triazine NPs. With fewer Si-triazine NPs added, nanoparticles were further distributed in the formulation and the generated radicals during the light irradiation might be less prone to recombination reaction[27], thus showing greater polymerization rates than the formulation with more Si-triazine NPs added. Formulations with the same concentration of free or coated triazine moiety (19.1 umol/g), i.e. 1.3 wt% silylated triazine + 8.7 wt% Silica NPs/TMPTA vs 10 wt% Si-triazine NPs/TMPTA, were also compared in Figure 2.4(b). No obvious differences were found in double bond conversions of TMPTA, while the slightly decreased in polymerization rate in 10 wt% Si-triazine NPs/TMPTA was again ascribed to the lower mobility of coated photoinitiating triazine moiety.

Alternatively, dielectric analysis (DEA) was performed as a complementary method in evaluating ultra-fast polymerization kinetic. It was claimed that FTIR may lack resolution at the early stage while DEA can provide reliable data instead[40]. DEA (Figure S2.9) was carried out in 0.85 wt% triazine/TMPTA and 10 wt% Si-triazine NPs/TMPTA (the molar concentration of the triazine moiety were equal in both formulations, 19.1 umol/g). When the light was on, the decreased ion viscosity was observed in both samples, which was attributed to the increase of temperature in the system. The increase of temperature led to the increased ion mobility, thus reflected a decrease in ion viscosity[41]. As the polymerization proceeded, liquid samples turned into solid crosslinked state, which dramatically decreased the ion mobility, reflecting an increased in ion viscosity[41] The initial slope of the curves in Figure S2.9 revealed the polymerization rates. It was found that 10 wt% Si-triazine NPs/TMPTA demonstrated a faster polymerization rate than that of 0.85

wt% triazine/TMPTA, which was in agreement with the photopolymerization results obtained using the RT-FTIR as discussed above. In addition, the increased polymerization rate can also be ascribed to the higher temperature (Figure S2.10) resulted during the photopolymerization process in 10 wt% Si-triazine NPs/TMPTA (47.5°C) compared to that in 0.85 wt% triazine/TMPTA (34.5°C).

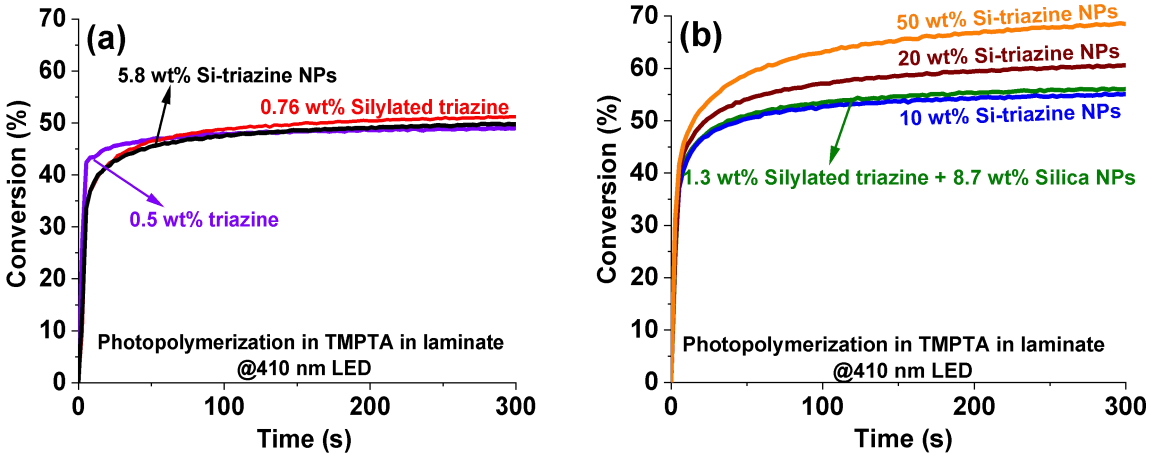

Figure 2. 4.Photopolymerization profiles of TMPTA obtained in laminate upon exposure to LED@410 nm in the presence of (a) 0.5 wt% of triazine, 0.76 wt% of silylated triazine, or 5.8 wt% of Si-triazine NPs (molar concentrations of triazine moieties in formulations are 11.1 umol/g) and (b) different wt% of Si-triazine NPs (molar concentrations of triazine moieties are 19.1, 19.1, 38.2, and 95.4 umol/g for 1.3 wt% Silylated triazien + 8.7 wt% Silica NPs, 10 wt% Si-triazine NPs, 20 wt% Si-triazine NPs, and 50 wt% Si-triazine NPs respectively).

Table 2. 1. Double bond conversions and polymerization rates of TMPTA obtained in laminate upon exposure to LED@410 nm in the presence of triazine, silylated triazine, or different wt% of Si-triazine NPs.

Photopolymerization systems	**LED@410 nm**	
	***C*[a]**	$(\frac{R_p}{[C=C]}) \times 100^b$ **(s^{-1})**
0.5 wt% triazine/TMPTA*	49%	5.5
0.76 wt% silylated triazine/TMPTA*	51%	8.7
5.8 wt% Si-triazine NPs/TMPTA*	50%	7.3
1.3 wt% silylated triazine + 8.7 wt% Silica NPs/TMPTA#	56%	5.7
10 wt% Si-triazine NPs/TMPTA#	55%	4.3
20 wt% Si-triazine NPs/TMPTA	61%	5.4
50 wt% Si-triazine NPs/TMPTA	69%	4.0

[a] double bond conversion of TMPTA after photopolymerization for 300 s;

[b] maximum rates of photopolymerization, calculated from the maximum of the first derivative of the double bond.
[*]Contains equal molar concentration of triazine moiety (11.1 µmol/g)
[#]Contains equal molar concentration of triazine moiety (19.1µmol/g)

2.7.4. Properties of photocured samples

2.7.4.1. Shrinkage of photocured samples

Polymer shrinkage during photopolymerization is always a big issue, especially in dentistry[42]. Generally, inorganic fillers were added to reduce the produced shrinkage stress during photopolymerization[43]. Shrinkage can be evaluated in various techniques, including dilatometry[44], gas pycnometry[45], and linometer[46] etc. Maximum conversion of light-sensitive formulations should be achieved before evaluating the shrinkage[47]. Thus, photorheometer, which can monitor the completion of polymerization and shrinkage simultaneously, becomes the optimal technique to be used here. Photopolymerization of formulations listed in Table 2.1 (except for 0.5 wt% triazine/TMPTA) were evaluated. The changes in storage and loss modulus during the irradiation of LED@410 nm are plotted in Figure S2.11. No significant difference of gel point times (1.8 – 2.5 s) was observed in all samples. However, a longer time was required for samples with higher amount of Si-triazine NPs (20 wt% and 50 wt%, Figure S2.11 (e) and (f) respectively) to reach complete conversion (plateau in curves). The results were correlated with the photopolymerization results obtained using RT-FTIR, where the samples containing higher amounts of Si-triazine NPs showed slower polymerization rates. For shrinkage measurements, the thicknesses of the samples before and after photopolymerization were recorded (reflected as the gap distance between support and the measuring sensor in photorheometer, Figure S2.12). The shrinkage was then calculated as reported previously[47]:

$$\%Shrinkage = \frac{Gap\ distance\ before\ irradiation - gap\ distance\ after\ irradiation}{Gap\ distance\ before\ irradiation}$$

Figure 2.5 illustrates the difference in shrinkage of samples with different concentrations of unmodified triazine or Si-triazine NPs (detailed values are summarized in Table S2.1). Shrinkage occurs as the monomer distances decrease after photopolymerization (change from van der Waals interaction to covalent bonds)[48]. Thus, the increase in shrinkage was expected in samples with increased concentration of either unmodified triazine or Si-triazine NPs as the increased concentration of radicals could be generated and more monomers could participate in the polymerization, resulting in more significant shrinkage. Interestingly, with the same concentration of triazine moiety, samples with Si-triazine NPs showed an apparent decrease of shrinkage (6.0%) compared to that with unmodified triazine (14.6%).

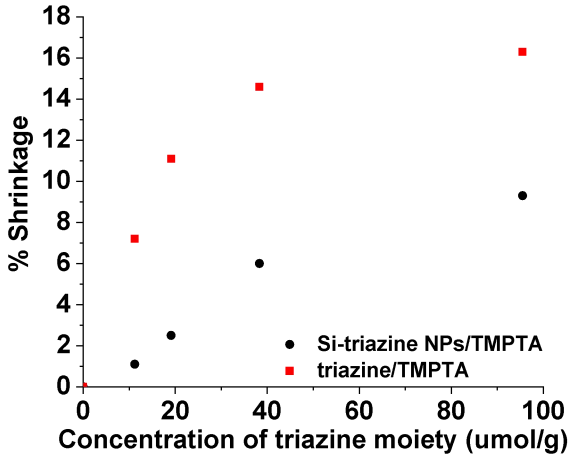

Figure 2. 5. Shrinkage of the photocured samples prepared by the photopolymerization of TMPTA under the irradiation of LED@410 nm in the presence of different molar concentrations of triazine or triazine moiety in Si-triazine NPs. (Corresponded to 5.8 wt%, 10 wt%, 20 wt%, and 50 wt% of Si-triazine NPs respectively)

2.7.4.2. Distribution of nanoparticles in photocured samples

Even though inorganic fillers can reduce shrinkage, agglomeration is always found, as pristine inorganic fillers cannot dissolve in the organic matrix. Composites with a good distribution of inorganic fillers are required to achieve superior properties. Here, the

distribution of nanoparticles in the above-investigated formulations was observed via SEM. It was clearly noticed that in the photocured samples prepared from 1.3 wt% triazine + 8.7 wt% Silica NPs/TMPTA (Figure S2.13 (a)), Silica NPs did not spread evenly in the samples while forming few groups of aggregate. In contrast, in 10 wt% Si-triazine NPs/TMPTA (Figure S2.13 (b)), Si-triazine NPs were well distributed in the sample. With higher loading of Si-triazine NPs (20 wt%, Figure S2.13 (c)), well distribution was observed. However, the further increase loading of Si-triazine NPs to 50 wt% resulted in agglomeration (Figure S2.13 (d)).

The surface morphologies of the photocured samples obtained after the measurements of the photopolymerization kinetics were characterized using AFM. As presented in Figure S2.14 (a), a rough surface was observed in the sample obtained from 10 wt% Si-triazine NPs/TMPTA. The bright spots observed were the silica nanoparticles[49], they were found to uniformly disperse in the whole region of observation. Alternatively, a smoother surface was seen in the sample obtained from 1.3 wt% silylated triazine + 8.7 wt% Silica NPs/TMPTA (Figure S2.14 (c)). With a relatively high loading of silica nanoparticles, one should expect a rough surface which indicated some silica nanoparticles were distributed evenly on the surface. However, the less distribution of silica nanoparticles on the surface reflected an uneven dispersion of Silica NPs in the sample as the Silica NPs might aggregate within the polymer matrix. Besides, more nodules (recognized as highly crosslinked structure) with sizes around 5 nm were observed in the 10 wt% Si-triazine NPs/TMPTA sample (Figure S2.14 (b)) than those in the 1.3 wt% silylated triazine + 8.7 wt% Silica NPs/TMPTA sample (Figure S2.14 (d)). It may be attributed to the fact that for the 10 wt% Si-triazine NPs/TMPTA sample, the polymers formed could easily entangle between the well dispersed nanoparticles, resulted in the formation of more nodules[50]. For the 1.3 wt% silylated triazine + 8.7 wt% Silica NPs/TMPTA sample, since the nanoparticles were more

aggregated, polymers formed were less entangled , thus leading to the formation of less nodulus on the surface.

The local thermal transitions of different regions on the surface of the photocured samples from 10 wt% Si-triazine NPs/TMPTA and 1.3 wt% silylated triazine + 8.7 wt% Silica NPs/TMPTA were investigated using the nano-thermal analysis (Figure 2.6 and Figure S2.15). Specifically, the measured deflections implied the degree of thermal expansion of the materials. The steeper curve referred to a greater thermal expansion of the measured region. In both samples, regions with silica nanoparticles showed decreased thermal expansion compared to the poly(TMPTA) regions. The results were expected as the poly(TMPTA) was restricted by the addition of silica nanoparticles[51]. Interestingly, the difference of deflections between the regions with silica nanoparticles and the poly(TMPTA) regions in the 10 wt% Si-triazine NPs/TMPTA sample were less significant than those in the 1.3 wt% silylated triazine + 8.7 wt% Silica NPs/TMPTA sample, which indicated the better dispersion of silylated triazine-coated silica nanoparticles in the polymer matrix than that of the unmodified Silica NPs. It can be ascribed to the chemical linkage between the silylated triazine-coated silica nanoparticles and the polymer matrix after the photocuring of the 10 wt% Si-triazine NPs/TMPTA sample. Moreover, with the same amount of silica nanoparticles added in the both samples, the 1.3 wt% silylated triazine + 8.7 wt% Silica NPs/TMPTA sample demonstrated smaller thermal expansion than the 10 wt% Si-triazine NPs/TMPTA sample. The significantly reduced thermal expansion reflected the formation of aggregates in the measured region[52]. The thermal analysis results again confirmed the enhanced dispersion of silylated triazine-coated silica nanoparticles in the polymer matrix.

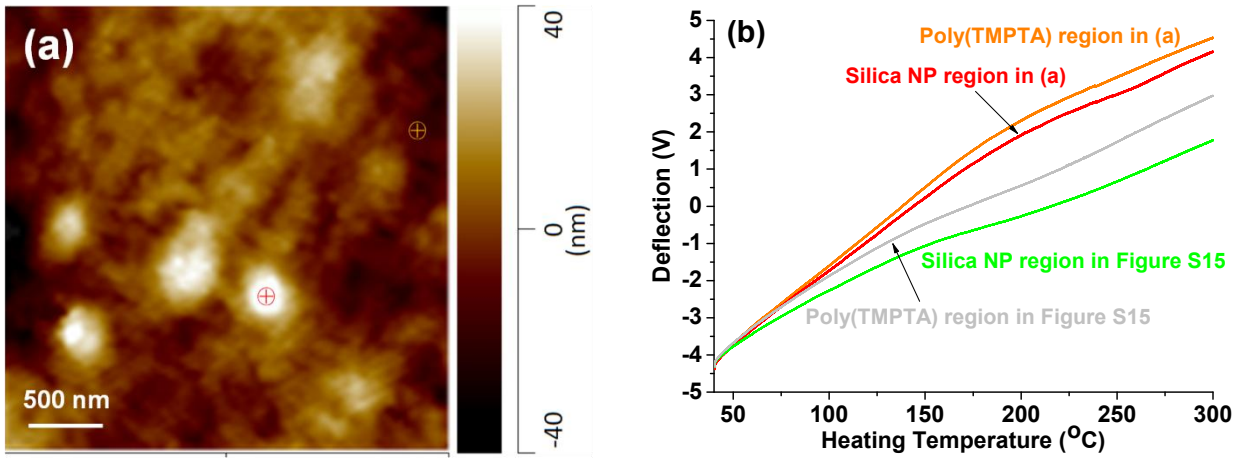

Figure 2. 6. Atomic force micrographs (height image) of the surfaces of photocured samples obtained after the investigation of the photorheology of (a) 10 wt% Si-triazine NPs/TMPTA and (b) nanothermal ramping of poly(TMPTA) or Silica NP regions in the samples of (a) and Figure S2.15.

2.7.4.3. Migration of photoinitiator from the photocured samples

Residue monomers or photoinitiators tend to migrate out from the photocured samples after storage for some time, and this is a major concern, especially in food packaging industries[30]. The coating of photoinitiators onto low-migrating substances is a promising strategy to increase the migration stability[27]. Figure 2.7 illustrates that the sample with free silylated triazine (0.76 wt% silylated triazine/TMPTA) had a greater migration concentration of 1.2 ug/ml than the sample with coated silylated triazine (5.8 wt% Si-triazine NPs/TMPTA, 0.35 ug/ml). It should be noted that the molar concentration of the triazien moiety in both samples are the same (i.e. 11.1 umol/g). By coating photoinitiator onto Silica NPs surface, the migration of the residues from the photocured samples was greatly reduced.

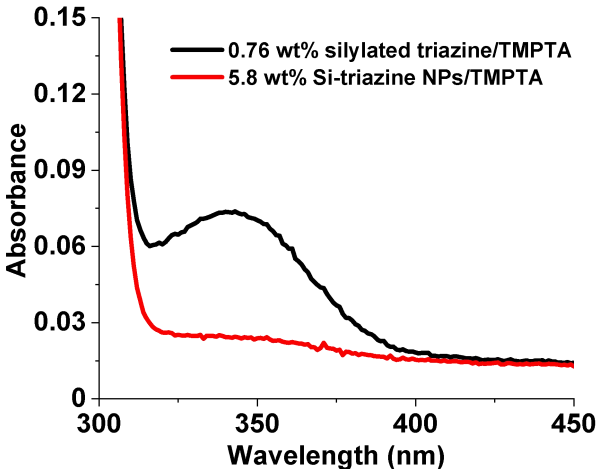

Figure 2. 7. UV-vis absorption spectra of silylated triazine extracted with acetonitrile for 20 h from the polymers prepared by the photopolymerization of TMPTA in the presence of 0.76 wt% silylated triazine and 5.8 wt% Si-triazine NPs (Molar concentrations of triazine moiety are 11.1 umol/g in both samples).

2.7.4.4. Mechanical properties of the photocured samples

The mechanical properties of the photocured samples prepared from the photopolymerization of TMPTA initiated by different triazine-containing photoinitiating systems under the irradiation of LED@410 nm are summarized in Table S2.2, and the representative stress-strain curves, derived from load vs deflection measurements, are shown in Figure 2.8. For all samples, an initial linear region in the stress-strain recording was present, and the flexural modulus, which is a measure of the elastic stiffness (modulus) of the samples, was derived from the gradient of the linear region.[53] After reaching the maximum stress, the sudden drops are referred as the failure of samples. Comparing 0.85 wt% triazine/TMPTA with 10 wt% Si-triazine NPs/TMPTA where the concentrations of triazine moiety are equal (19.1 umol/g), the incorporation of triazine-coated silica nanoparticles into the resin resulted in a significant increase of flexural modulus, i.e. from 43 MPa (triazine/TMPTA) to 286 MPa (Si-triazine NPs/TMPTA). As the nanoparticles were well spread in 10 wt% Si-triazine NPs/TMPTA, the samples showed strong interfacial adhesions between the resin and the surface of the nanoparticles. The adhesion allowed

any built-up stress to transfer from resin to the nanoparticles, lengthening the propagating crack path during fracture[54] and thus resulting in increased flexural strength. Notably, the increase in the composites stiffness, reflected by the increase in the flexural moduli, resulted in a decrease in strain at break[55]. Interestingly, compared to the sample prepared from 10 wt% Si-triazine NPs/TMPTA, 1.3 wt% silylated triazine + 8.7 wt% Silica NPs/TMPTA sample exhibited a reduced flexural modulus (113 MPa) but with a larger flexural strength (75 MPa). The decrease in flexural modulus might be due to the slight agglomeration of silica nanoparticles, as seen in Figure S2.13 (a). And the increase in flexural strength and the strain at break might be attributed to the fact that the different interactions between the fillers and matrix resulted in different failure mechanism. Further increase in the loading of Si-triazine NPs from 10 wt% to 50 wt% resulted in a drastic decrease in flexural modulus from 286 MPa to 27 MPa. The agglomeration found in 50 wt% Si-triazine NPs/TMPTA might initiate cracks easily[54], thereby reducing the overall flexural modulus.

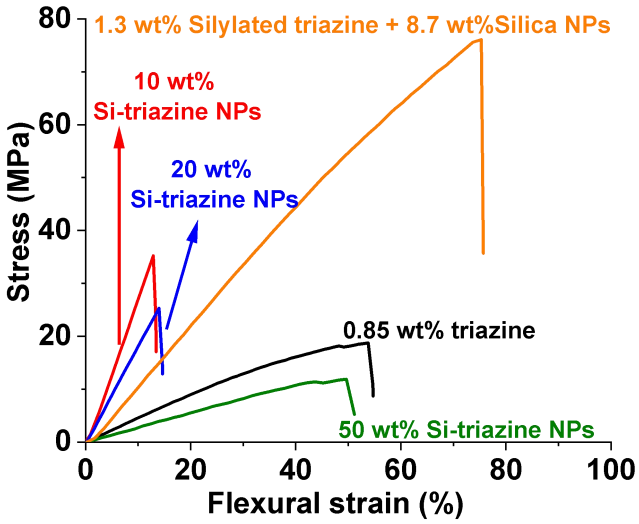

Figure 2. 8. Stress-strain curves in three-point bending test of the photocured samples prepared from the photopolymerization of TMPTA initiated by 0.85 wt% triazine (molar concentration: 19.1 umol/g), 1.3 wt% Silylated triazine + 8.7 wt% Silica NPs (molar concentrations of triazine moieties: 19.1 umol/g), or 10 wt% (molar concentrations of triazine moieties: 19.1 umol/g), 20 wt% (38.2 umol/g), or 50 wt% (95.4 umol/g) Si-triazine NPs.

2.8. Conclusion

In this study, the visible light-sensitive triazine-coated silica nanoparticles (Si-triazine NPs) were prepared by coating 4-(2-(4,6-bis(trichloromethyl)-1,3,5-triazin-2-yl)vinyl)phenyl (3-(triethoxysilyl)propyl)carbamate (silylated triazine) onto the surface of Silica NPs. TGA and UV-vis measurements confirmed that the amount of triazine moiety on Silica NPs was 13 wt%. The Si-triazine NPs were then used to induce free radical photopolymerization of TMPTA under the irradiation of LED@410 nm, and the polymerization kinetics were compared with the system induced by free triazine or silylated triazine. Si-triazine NPs can lead to similar double bond conversions of TMPTA as triazine or silylated triazine when an equal amount of triazine moiety was presence in the formulations. With the increase in the amounts of Si-triaizne NPs, the double bond conversions of TMPTA also increased; however, the change in polymerization rates was negligible. DEA revealed a higher temperature generated in Si-triazine NPs/TMPTA than triazine/TMPTA. The incorporation of nanoparticles into the polymer matrix greatly reduced the shrinkage of the photocured materials. In addition, Si-triazine NPs/TMPTA showed increased migration stability compared to triazine/TMPTA. Finally, the rough surface with even distributed nodules was found in the AFM analysis, which confirmed the improved dispersion of Si triazine NPs in TMPTA compared to the pristine Silica NPs. The good dispersion of Si-triazine NPs in the sample brought to the enhanced mechanical properties compared to those in the presence of free triazine or silylated triazine. It demonstrated that the developed triazine-coated silica nanoparticles can act as both the photoinitiators to trigger photopolymerization reactions under the visible light and as the fillers to endow the produced polymer nanocomposite materials with various enhanced properties.

Looking forward, the unique dual functionality of Si-triazine NPs makes them promising candidates for advanced applications. For instance, they could be employed in visible-light-curable 3D printing resins to minimize shrinkage-induced warping while improving mechanical durability. Their enhanced migration stability and dispersion also position them as ideal fillers for dental composites or biomedical coatings requiring precise spatial control and biocompatibility. Additionally, their energy-efficient curing under mild visible light could benefit sustainable manufacturing processes, such as eco-friendly coatings or adhesives. Further exploration of these nanoparticles in stimuli-responsive materials, optoelectronics, or hybrid nanocomposites for tailored functionalities represents an exciting direction for future research. Our approach paves the way for multifunctional photopolymer nanocomposites that combine efficient visible-light curing with superior material properties, broadening their utility across interdisciplinary fields.

2.9. Reference

1. Wang, Z.; Chen, H.; Wang, Y.; Chen, J.; Arnould, M. A.; Hu, B.; Popovs, I.; Mahurin, S. M.; Dai, S., Polymer-Grafted Porous Silica Nanoparticles with Enhanced Co2 Permeability and Mechanical Performance. *ACS Applied Materials & Interfaces* **2021,** 13, 27411-27418.
2. Chandra, A.; Turng, L.; Gopalan, P.; Rowell, R.; Gong, S. J. C. S.; Technology, Study of Utilizing Thin Polymer Surface Coating on the Nanoparticles for Melt Compounding of Polycarbonate/Alumina Nanocomposites and Their Optical Properties. *Compos. Sci. Technol.* **2008,** 68, 768-776.
3. Jiang, H.; Moon, K.-s.; Li, Y.; Wong, C. P., Surface Functionalized Silver Nanoparticles for Ultrahigh Conductive Polymer Composites. *Chemistry of Materials* **2006,** 18, 2969-2973.
4. Chen, C.-H.; Jian, J.-Y.; Yen, F.-S., Preparation and Characterization of Epoxy/Γ-Aluminum Oxide Nanocomposites. *Composites, Part A* **2009,** 40, 463-468.
5. Ziolo, R. F.; Giannelis, E. P.; Weinstein, B. A.; O'Horo M, P.; Ganguly, B. N.; Mehrotra, V.; Russell, M. W.; Huffman, D. R., Matrix-Mediated Synthesis of Nanocrystalline Ggr-Fe2o3: A New Optically Transparent Magnetic Material. *Science* **1992,** 257, 219-23.
6. Yu, C.; Schimelman, J.; Wang, P.; Miller, K. L.; Ma, X.; You, S.; Guan, J.; Sun, B.; Zhu, W.; Chen, S., Photopolymerizable Biomaterials and Light-Based 3d Printing Strategies for Biomedical Applications. *Chemical reviews* **2020,** 120, 10695-10743.
7. Downing, M. A.; Jain, P. K., Chapter 16 - Mesoporous Silica Nanoparticles: Synthesis, Properties, and Biomedical Applications. In *Nanoparticles for Biomedical Applications*, Chung, E. J.; Leon, L.; Rinaldi, C., Eds. Elsevier: 2020; pp 267-281.
8. Wei, H.; Lv, Y.; Han, L.; Tu, B.; Zhao, D., Facile Synthesis of Transparent Mesostructured Composites and Corresponding Crack-Free Mesoporous Carbon/Silica Monoliths. *Chem. Mater.* **2011,** 23, 2353-2360.

9. Kango, S.; Kalia, S.; Celli, A.; Njuguna, J.; Habibi, Y.; Kumar, R., Surface Modification of Inorganic Nanoparticles for Development of Organic–Inorganic Nanocomposites—a Review. *Progress in Polymer Science* **2013,** 38, 1232-1261.
10. Peng, X.; Zhang, J.; Stachurski, Z. H.; Banaszak Holl, M. M.; Xiao, P., Visible-Light-Sensitive Triazine-Coated Silica Nanoparticles: A Dual Role Approach to Polymer Nanocomposite Materials with Enhanced Properties. *ACS Applied Materials & Interfaces* **2021,** 13, 46033-46042.
11. Ates, B.; Koytepe, S.; Balcioglu, S.; Ulu, A.; Gurses, C., 12 - Biomedical Applications of Hybrid Polymer Composite Materials. In *Hybrid Polymer Composite Materials*, Thakur, V. K.; Thakur, M. K.; Pappu, A., Eds. Woodhead Publishing: 2017; pp 343-408.
12. Ates, B.; Koytepe, S.; Ulu, A.; Gurses, C.; Thakur, V. K., Chemistry, Structures, and Advanced Applications of Nanocomposites from Biorenewable Resources. *Chem. Rev.* **2020,** 120, 9304-9362.
13. Mourdikoudis, S.; Kostopoulou, A.; LaGrow, A. P., Magnetic Nanoparticle Composites: Synergistic Effects and Applications. *Advanced Science* **2021,** 8, 2004951.
14. Jitputti, J.; Rattanavoravipa, T.; Chuangchote, S.; Pavasupree, S.; Suzuki, Y.; Yoshikawa, S., Low Temperature Hydrothermal Synthesis of Monodispersed Flower-Like Titanate Nanosheets. *Catalysis Communications* **2009,** 10, 378-382.
15. Parodi, A.; Evangelopoulos, M.; Arrighetti, N.; Cevenini, A.; Livingston, M.; Khaled, S. Z.; Brown, B. S.; Yazdi, I. K.; Paradiso, F.; Campa-Carranza, J. N.; De Vita, A.; Taraballi, F.; Tasciotti, E., Endosomal Escape of Polymer-Coated Silica Nanoparticles in Endothelial Cells. *Small* **2020,** 16, 1907693.
16. Pina, S.; Oliveira, J. M.; Reis, R. L., Natural-Based Nanocomposites for Bone Tissue Engineering and Regenerative Medicine: A Review. *Adv. Mater.* **2015,** 27, 1143-1169.
17. Nalone, L. A.; Amaral, R. G.; de Lima Oliveira, D. M.; Andrade, L. R.; de Hollanda, L. M.; da Silva, C. F.; Souto, E. B.; Severino, P., 15 - Applications of Nanocomposite Materials in the Delivery of Anticancer Drugs. In *Applications of Nanocomposite Materials in Drug Delivery*, Inamuddin; Asiri, A. M.; Mohammad, A., Eds. Woodhead Publishing: 2018; pp 339-352.
18. Caseri, W., Clay-Containing Polymeric Nanocomposites (2 Volumes). Rapra Technology Limited, Shrewsbury, Uk, 2004. Isbn 1-85957-482-3 (Volume 1). Isbn 1-85957-437-8 (Volume 2). Pp 785 (Both Volumes). *Polymer International* **2005,** 54, 860-860.
19. Rane, A. V.; Kanny, K.; Abitha, V. K.; Thomas, S., Chapter 5 - Methods for Synthesis of Nanoparticles and Fabrication of Nanocomposites. In *Synthesis of Inorganic Nanomaterials*, Mohan Bhagyaraj, S.; Oluwafemi, O. S.; Kalarikkal, N.; Thomas, S., Eds. Woodhead Publishing: 2018; pp 121-139.
20. Alexandre, M.; Dubois, P., Polymer-Layered Silicate Nanocomposites: Preparation, Properties and Uses of a New Class of Materials. *Materials Science and Engineering: R: Reports* **2000,** 28, 1-63.
21. Tchoul, M. N.; Fillery, S. P.; Koerner, H.; Drummy, L. F.; Oyerokun, F. T.; Mirau, P. A.; Durstock, M. F.; Vaia, R. A., Assemblies of Titanium Dioxide-Polystyrene Hybrid Nanoparticles for Dielectric Applications. *Chem. Mater.* **2010,** 22, 1749-1759.
22. Adjemian, K. T.; Dominey, R.; Krishnan, L.; Ota, H.; Majsztrik, P.; Zhang, T.; Mann, J.; Kirby, B.; Gatto, L.; Velo-Simpson, M.; Leahy, J.; Srinivasan, S.; Benziger, J. B.; Bocarsly, A. B., Function and Characterization of Metal Oxide−Nafion Composite Membranes for Elevated-Temperature H2/O2 Pem Fuel Cells. *Chemistry of Materials* **2006,** 18, 2238-2248.
23. Yeo, K. E.; Oh, W.; Jeon, E.; Bae, J.-S.; Nam, J.; Park, J.-W., One-Pot Single-Step Route toward Bicontinuous Nanoporous Membranes of an Organic–Inorganic Core–Shell Network. *Chem. Mater.* **2020,** 32, 8318-8324.
24. Fujiwara, N.; Asaka, K.; Nishimura, Y.; Oguro, K.; Torikai, E., Preparation of Gold−Solid Polymer Electrolyte Composites as Electric Stimuli-Responsive Materials. *Chemistry of Materials* **2000,** 12, 1750-1754.
25. Zare, Y.; Rhee, K. Y.; Hui, D., Influences of Nanoparticles Aggregation/Agglomeration on the Interfacial/Interphase and Tensile Properties of Nanocomposites. *Composites, Part B* **2017,** 122, 41-46.

26. Yang, H.; Li, B.; Wang, K.; Sun, T. e.; Wang, X.; Zhang, Q.; Fu, Q.; Dong, X.; Han, C. C., Rheology and Phase Structure of Pp/Epdm/Sio2 Ternary Composites. *Eur. Polym. J.* **2008,** 44, 113-123.
27. Sahin, M.; Krawczyk, K. K.; Roszkowski, P.; Wang, J.; Kaynak, B.; Kern, W.; Schlögl, S.; Grützmacher, H., Photoactive Silica Nanoparticles: Influence of Surface Functionalization on Migration and Kinetics of Radical-Induced Photopolymerization Reactions. *European Polymer Journal* **2018,** 98, 430-438.
28. Van Den Houwe, K.; Van Heyst, A.; Evrard, C.; Van Loco, J.; Bolle, F.; Lynen, F.; Van Hoeck, E., Migration of 17 Photoinitiators from Printing Inks and Cardboard into Packaged Food – Results of a Belgian Market Survey. *Packaging Technology and Science* **2016,** 29, 121-131.
29. Yamaji, K.; Kawasaki, Y.; Yoshitome, K.; Matsunaga, H.; Sendo, T., Quantitation and Human Monocyte Cytotoxicity of the Polymerization Agent 1-Hydroxycyclohexyl Phenyl Ketone (Irgacure 184) from Three Brands of Aqueous Injection Solution. *Biol. Pharm. Bull.* **2012,** 35, 1821-1825.
30. Arvanitoyannis, I. S.; Kotsanopoulos, K. V., Migration Phenomenon in Food Packaging. Food–Package Interactions, Mechanisms, Types of Migrants, Testing and Relative Legislation—a Review. *Food and Bioprocess Technology* **2014,** 7, 21-36.
31. Li, X.; Liu, Z.; Hong, P.; Chen, L.; Liu, X., Synthesis of Organic and Inorganic Hybrid Nanoparticles as Multifunctional Photoinitiator and Its Application in Uv-Curable Epoxy Acrylate-Based Coating Systems. *Progress in Organic Coatings* **2020,** 141, 105565.
32. Roszkowski, P.; Sahin, M.; Ayalur-Karunakaran, S.; Gammer, C.; Schlögl, S.; Kern, W.; Krawczyk, K. K., Synthesis and Evaluation of New Radical Photoinitiators Bearing Trialkoxysilyl Groups for Surface Immobilization. *Polymer* **2017,** 129, 207-220.
33. El-Abaseri, T. B.; Hansen, L. A., Egfr Activation and Ultraviolet Light-Induced Skin Carcinogenesis. *J. Biomed. Biotechnol.* **2007,** 2007, 097939.
34. Peng, X.; Zhang, J.; Banaszak Holl, M. M.; Xiao, P., Thiol-Ene Photopolymerization under Blue, Green and Red Led Irradiation. *ChemPhotoChem* **2021,** 5, 571-581.
35. Lai, H.; Zhu, D.; Xiao, P., Yellow Triazine as an Efficient Photoinitiator for Polymerization and 3d Printing under Leds. *Macromol. Chem. Phys.* **2019,** 220, 1900315.
36. Zhang, J.; Xiao, P.; Morlet-Savary, F.; Graff, B.; Fouassier, J. P.; Lalevée, J., A Known Photoinitiator for a Novel Technology: 2-(4-Methoxystyryl)-4,6-Bis(Trichloromethyl)-1,3,5-Triazine for near Uv or Visible Led. *Polym. Chem.* **2014,** 5, 6019-6026.
37. Cumbo, A.; Lorber, B.; Corvini, P. F.; Meier, W.; Shahgaldian, P., A Synthetic Nanomaterial for Virus Recognition Produced by Surface Imprinting. *Nature communications* **2013,** 4, 1503.
38. Coates, J., Interpretation of Infrared Spectra, a Practical Approach. In *Encyclopedia of Analytical Chemistry*, 2006.
39. Douaihy, R. Z.; Telegeiev, I.; Nasrallah, H.; Lebedev, O.; Bazin, P.; Vimont, A.; Chailan, J.-F.; Fahs, A.; El-Roz, M., Synthesis of Silica-Polymer Core-Shell Hybrid Materials with Enhanced Mechanical Properties Using a New Bifunctional Silane-Based Photoinitiator as Coupling Agent. *Mater. Today Commun.* **2021,** 27, 102248.
40. Steinhaus, J.; Hausnerova, B.; Haenel, T.; Großgarten, M.; Möginger, B., Curing Kinetics of Visible Light Curing Dental Resin Composites Investigated by Dielectric Analysis (Dea). *Dent. Mater.* **2014,** 30, 372-380.
41. Randolph, L. D.; Steinhaus, J.; Möginger, B.; Gallez, B.; Stansbury, J.; Palin, W. M.; Leloup, G.; Leprince, J. G., Photopolymerization of Highly Filled Dimethacrylate-Based Composites Using Type I or Type Ii Photoinitiators and Varying Co-Monomer Ratios. *Dent. Mater.* **2016,** 32, 136-148.
42. Lu, H.; Stansbury, J. W.; Bowman, C. N., Impact of Curing Protocol on Conversion and Shrinkage Stress. *J. Dent. Res.* **2005,** 84, 822-826.
43. Bociong, K.; Szczesio, A.; Krasowski, M.; Sokolowski, J., The Influence of Filler Amount on Selected Properties of New Experimental Resin Dental Composite. *Open Chem.* **2018,** 16, 905-911.
44. Lai, J. H.; Johnson, A. E., Measuring Polymerization Shrinkage of Photo-Activated Restorative Materials by a Water-Filled Dilatometer. *Dent. Mater.* **1993,** 9, 139-43.
45. Cook, W. D.; Forrest, M.; Goodwin, A. A., A Simple Method for the Measurement of Polymerization Shrinkage in Dental Composites. *Dent. Mater.* **1999,** 15, 447-449.
46. de Gee, A. F.; Feilzer, A. J.; Davidson, C. L., True Linear Polymerization Shrinkage of Unfilled Resins and Composites Determined with a Linometer. *Dent. Mater.* **1993,** 9, 11-4.

47. Schmidt, C.; Scherzer, T., Monitoring of the Shrinkage During the Photopolymerization of Acrylates Using Hyphenated Photorheometry/near-Infrared Spectroscopy. *J. Polym. Sci., Part B: Polym. Phys.* **2015,** 53, 729-739.
48. Kim, R. J.-Y.; Kim, Y.-J.; Choi, N.-S.; Lee, I.-B., Polymerization Shrinkage, Modulus, and Shrinkage Stress Related to Tooth-Restoration Interfacial Debonding in Bulk-Fill Composites. *J. Dent.* **2015,** 43, 430-439.
49. Huang, H.; Dobryden, I.; Thorén, P. A.; Ejenstam, L.; Pan, J.; Fielden, M. L.; Haviland, D. B.; Claesson, P. M., Local Surface Mechanical Properties of Pdms-Silica Nanocomposite Probed with Intermodulation Afm. *Compos. Sci. Technol.* **2017,** 150, 111-119.
50. Matsuura, K. C. K. Y. F., Nodular Structure of Polymers in the Membrane. In *Synthetic Polymeric Membranes: Characterization by Atomic Force Microscopy*, Khulbe, K. C.; Feng, C. Y.; Matsuura, T., Eds. Springer Berlin Heidelberg: Berlin, Heidelberg, 2008; pp 47-100.
51. Suzuki, N.; Kiba, S.; Yamauchi, Y., Bimodal Filler System Consisting of Mesoporous Silica Particles and Silica Nanoparticles toward Efficient Suppression of Thermal Expansion in Silica/Epoxy Composites. *J. Mater. Chem.* **2011,** 21, 14941-14947.
52. Dzenis, Y. A.; Ponomarev, V. M., Thermal Expansion of a Polymer Composite with an Aggregating Disperse Filler. *Mech. Compos. Mater.* **1989,** 25, 61-67.
53. Licari, J. J.; Swanson, D. W., Chapter 7 - Test and Inspection Methods. In *Adhesives Technology for Electronic Applications (Second Edition)*, Licari, J. J.; Swanson, D. W., Eds. William Andrew Publishing: Oxford, 2011; pp 345-377.
54. Azad, E.; Atai, M.; Zandi, M.; Shokrollahi, P.; Solhi, L., Structure–Properties Relationships in Dental Adhesives: Effect of Initiator, Matrix Monomer Structure, and Nano-Filler Incorporation. *Dent. Mater.* **2018,** 34, 1263-1270.
55. Ghafaar, M. A.; Mazen, A. A.; El-Mahallawy, N. A., Behavior of Woven Fabric Reinforced Epoxy Composites under Bending and Compressive Loads. *J. Eng. Sci.* **2006,** 34, 453-469.

2.10. Supporting information

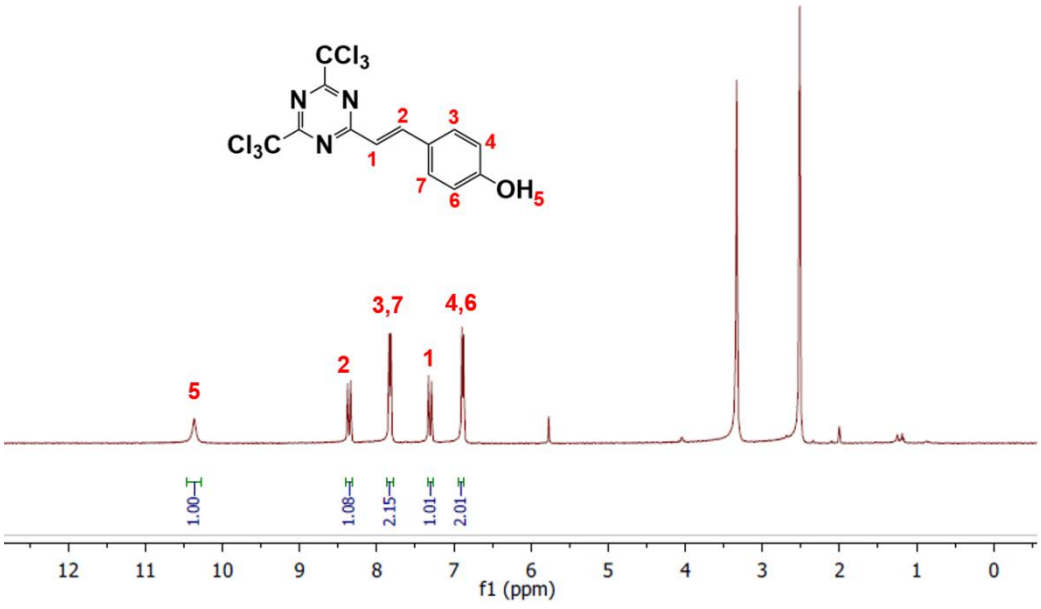

Figure S2. 1. ^{1}H NMR of 4-(2-(4,6-bis(trichloromethyl)-1,3,5-triazin-2-yl)vinyl)phenol (demethylated triazine) in d_6-DMSO (400 MHz).

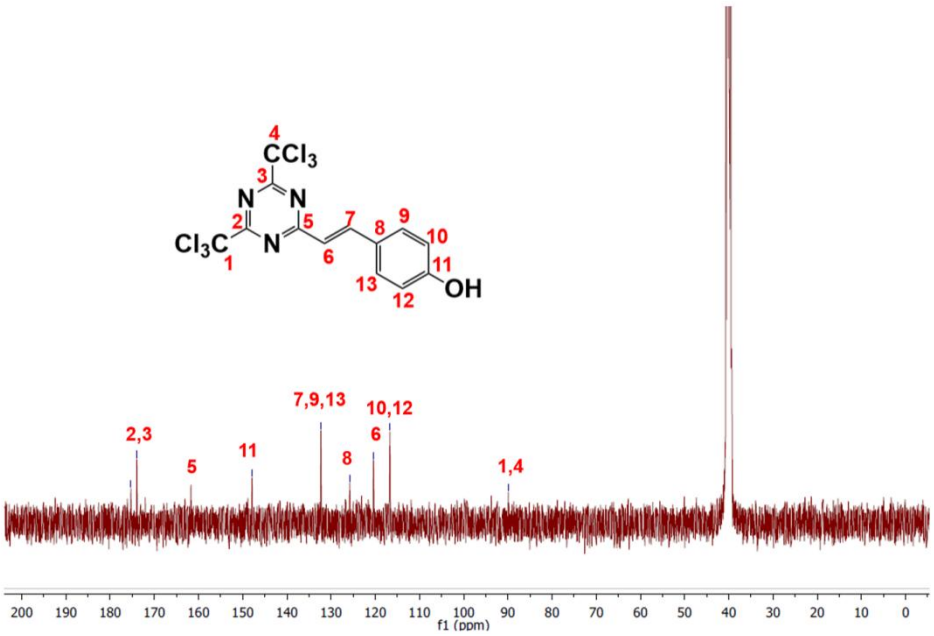

Figure S2. 2. ^{13}C NMR of of 4-(2-(4,6-bis(trichloromethyl)-1,3,5-triazin-2-yl)vinyl)phenol (demethylated triazine) in d_6-DMSO (400 MHz).

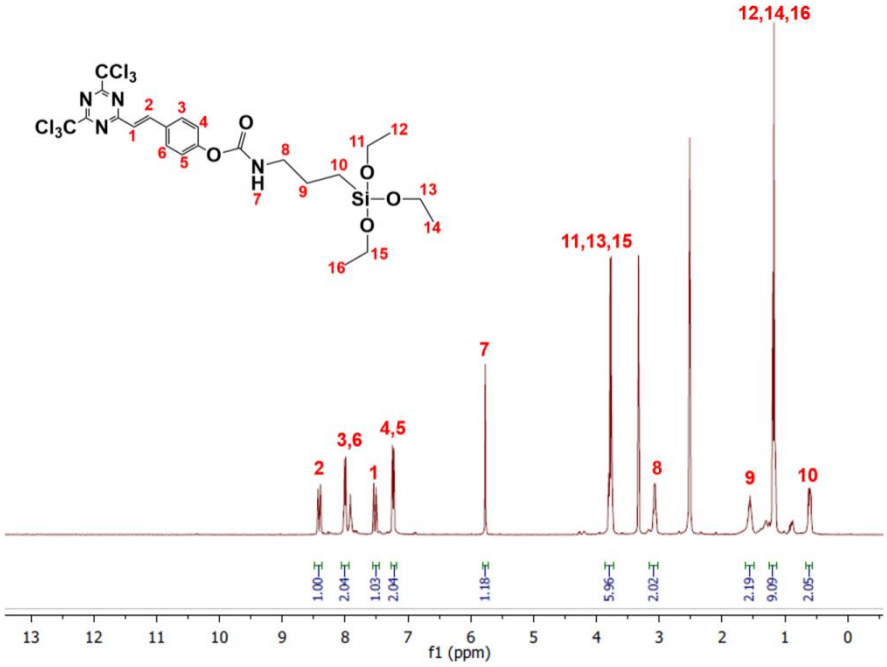

Figure S2. 3. ^{1}H NMR of 4-(2-(4,6-bis(trichloromethyl)-1,3,5-triazin-2-yl)vinyl)phenyl (3-(triethoxysilyl)propyl)carbamate (silylated triazine)in d_6-DMSO (400 MHz).

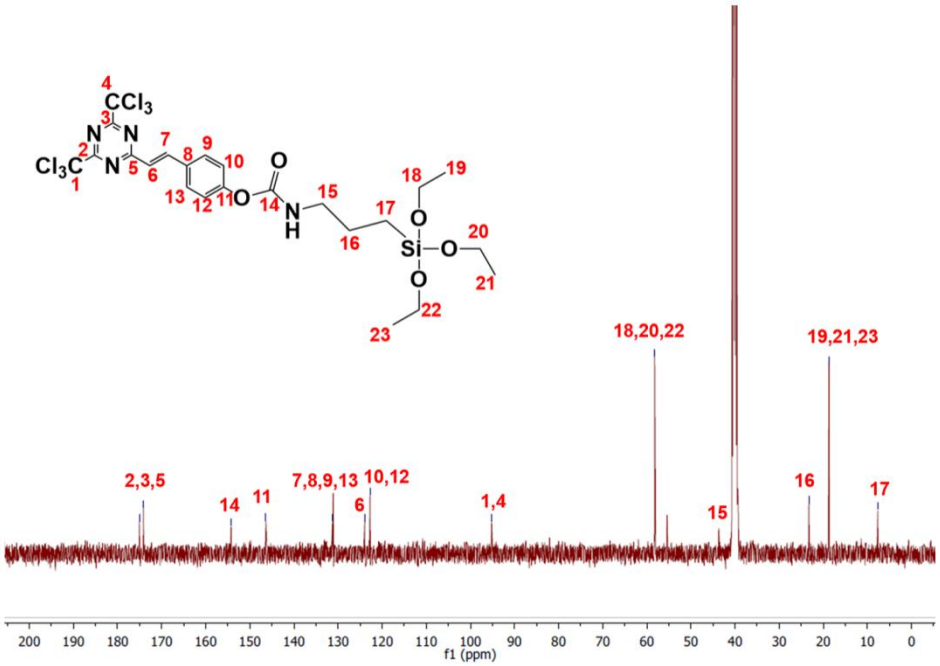

Figure S2. 4. ^{13}C NMR of 4-(2-(4,6-bis(trichloromethyl)-1,3,5-triazin-2-yl)vinyl)phenyl (3-(triethoxysilyl)propyl)carbamate (silylated triazine)in d_6-DMSO (400 MHz).

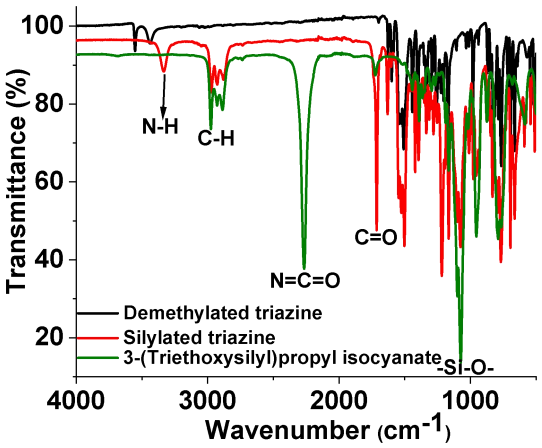

Figure S2. 5. ATR-IR spectra of demethylated triazine, silylated triazine, and 3-(Triethoxysilyl)propyl isocyanate.

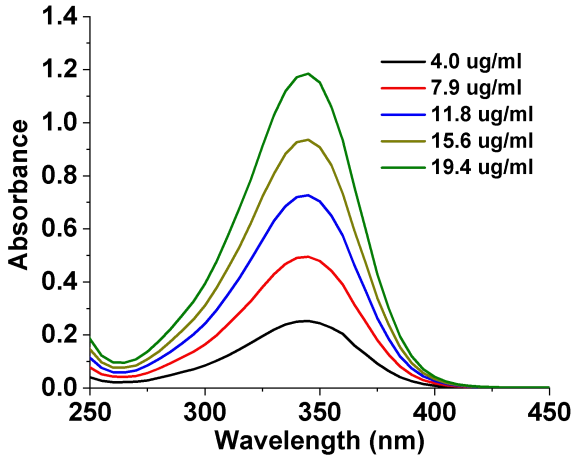

Figure S2. 6. UV-vis spectra of different concentrations of silylated triazine in acetonitrile.

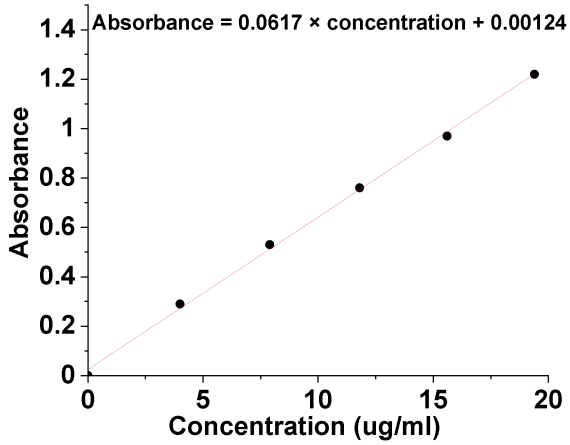

Figure S2. 7. Calibration curve for silylated triazine concentration vs absorbance in acetonitrile.

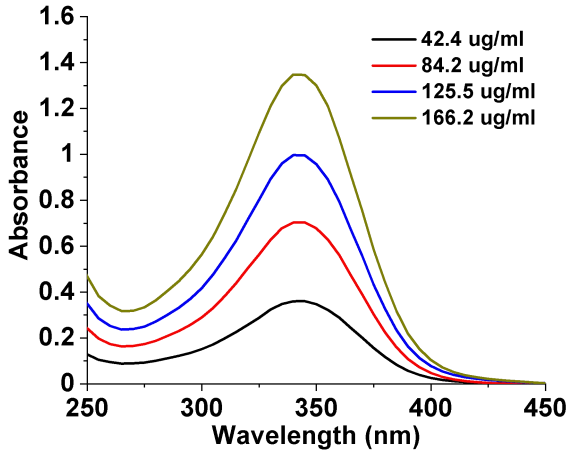

Figure S2. 8. UV-vis spectra of different concentration of Si-triazine NPs in acetonitrile.

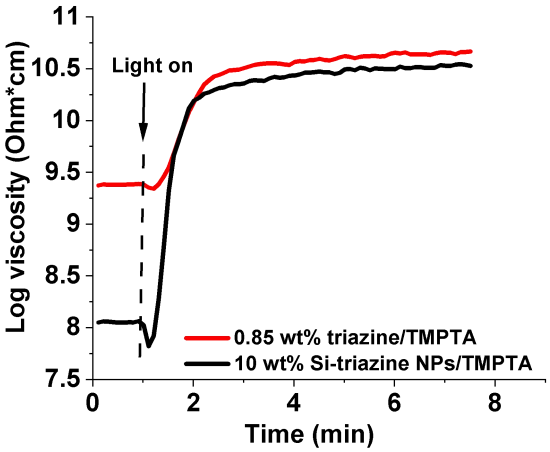

Figure S2. 9. Ion viscosity curves measured at 215 Hz frequency of 0.85 wt% triazine/TPMTA and 10 wt% Si-triazine NPs/TPMTA during the photopolymerization under the irradiation of LED@410 nm. (Molar concentrations of triazine moieties in the formulations are 19.0 umol/g and 19.1 umol/g respectively)

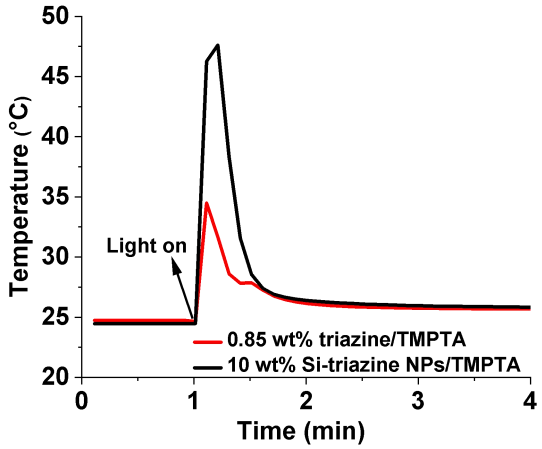

Figure S2. 10. Temperature changes in 0.85 wt% triazine/TPMTA and 10 wt% Si-triazine NPs/TPMTA during the photopolymerization under the irradiation of LED@410 nm. (Molar concentrations of triazine moieties in the formulations are 19.0 umol/g and 19.1 umol/g respectively)

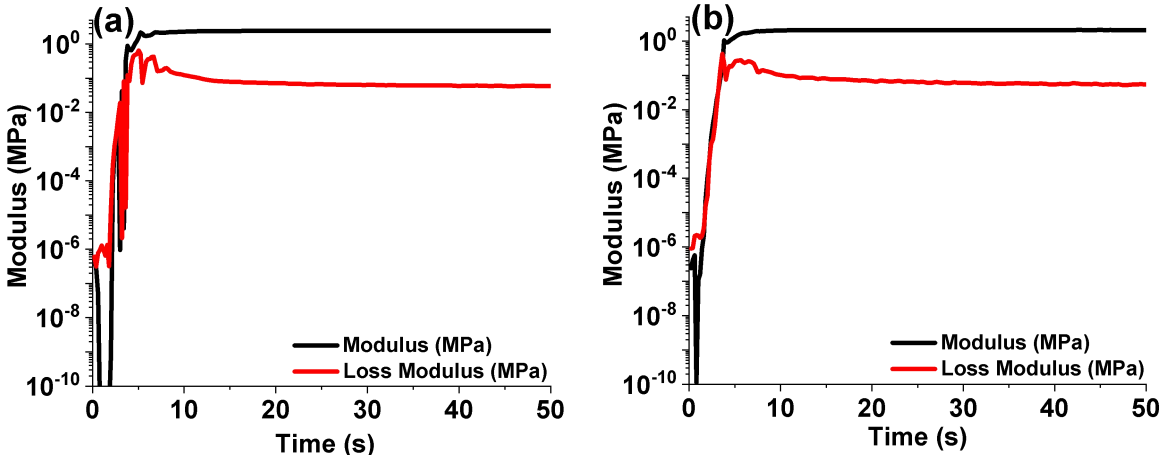

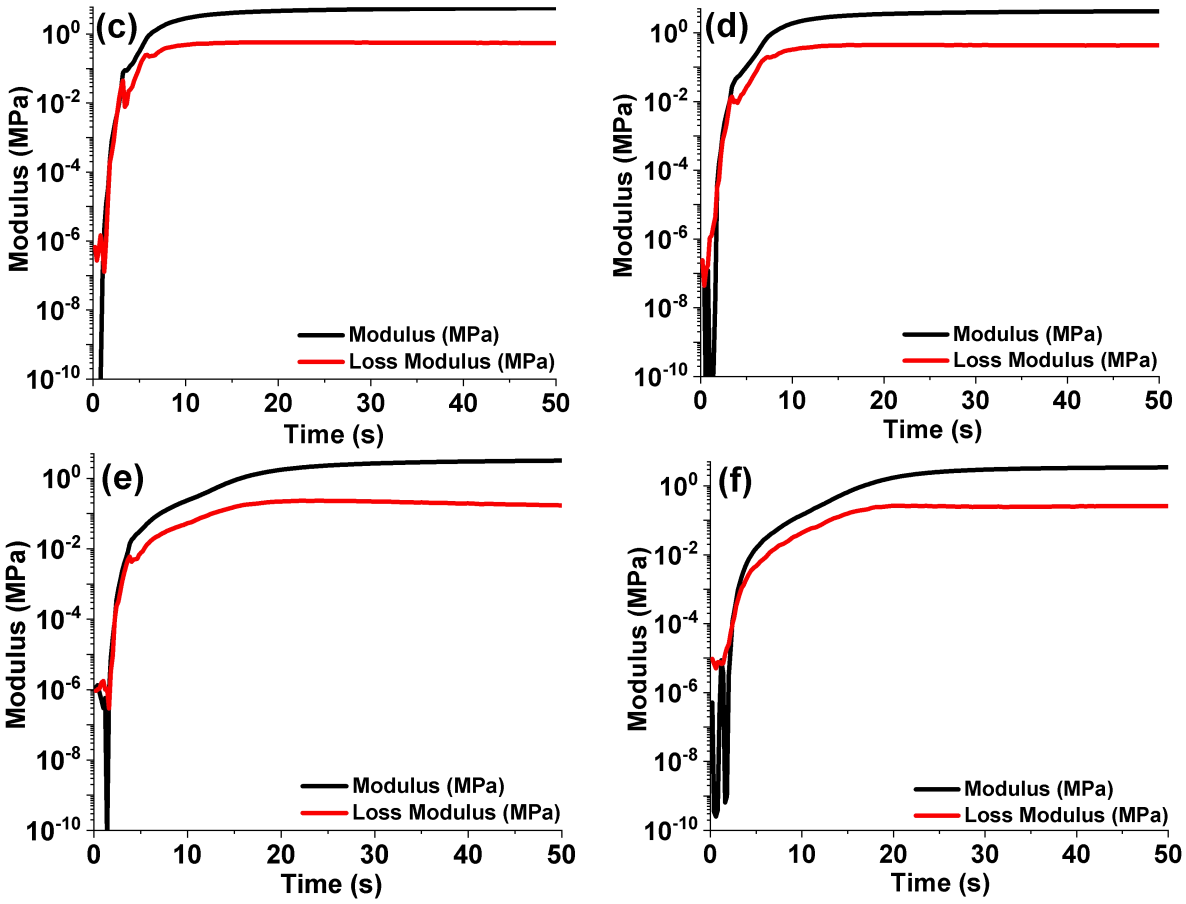

Figure S2. 11. Storage (G') and loss (G'') moduli of the photopolymerization of TMPTA initiated with (a) 0.76 wt% silylated triazine (molar concentration of triazine moiety: 11.1 umol/g), (b) 1.3% silylated triazine + 8.7% Si-NPs (molar concentration of triazine moiety: 19.1 umol/g), or with different concentrations of Si-triazine NPs (c) 5.8 wt% (molar concentration of triazine moiety: 11.1 umol/g), (d) 10 wt% (19.1 umol/g), (e) 20 wt% (38.2 umol/g), and (f) 50 wt% (95.4 umol/g) under the irradiation of LED@410 nm.

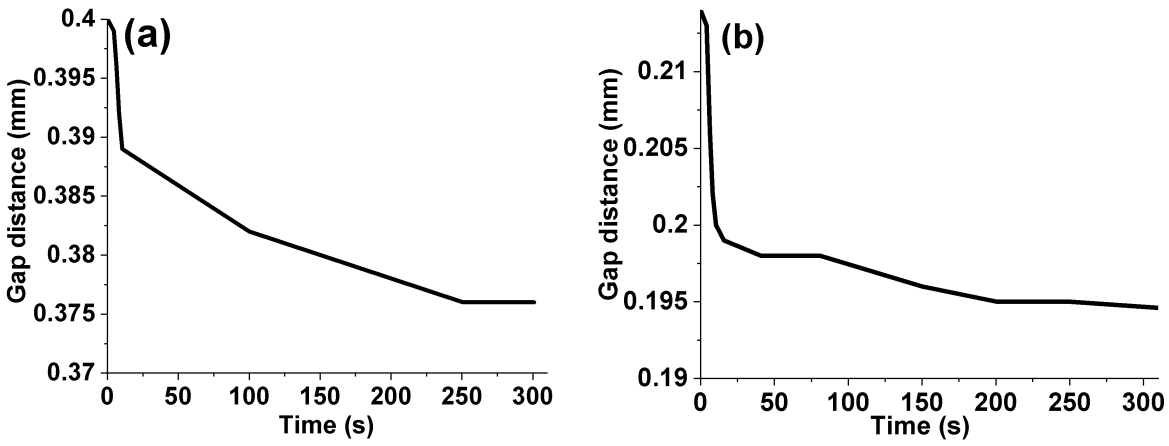

Figure S2. 12. Change of gap distance (reflects the shrinkage of samples during the photopolymerization) measured from photorheometer during the photopolymerization of formulations (a) 20 wt% Si-triazine NPs/TMPTA (Molar concentration of triazine moiety:

38.2 umol/g) and (b) 50 wt% Si-triazine NPs/TMPTA (95.4 umol/g) under the irradiation of LED@410 nm.

Table S2. 1. % Shrinkage of the samples during the photopolymerization of TMPTA under the irradiation of LED@410 nm in the presence of different concentrations of Si-triazine NPs or triazine.

Concentration of photoinitiator (umol/g)	% Shrinkage of Si-triazine NPs/TMPTA	% Shrinkage of triazine/TMPTA
11.1	1.1%	7.2%
19.1	2.5%	11.1%
38.3	6.0%	14.6%
95.5	9.3%	16.3%

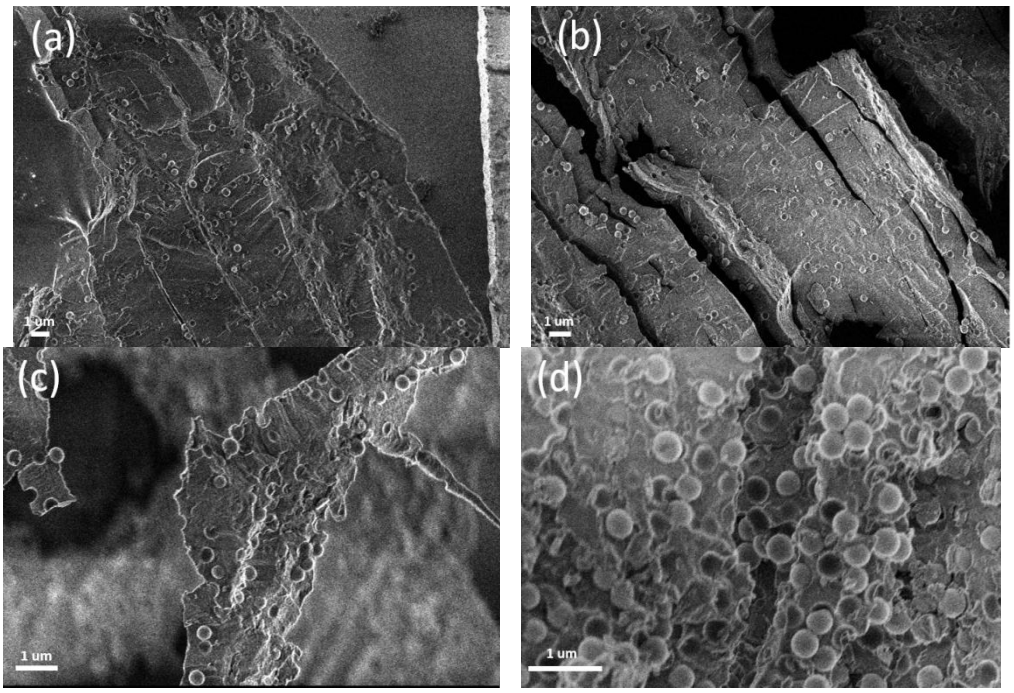

Figure S2. 13. SEM images of photocured samples of the formulations (a) 1.3 wt% silylated triazine + 8.7 wt% Si NPs/TMPTA; (b) 10 wt% Si-triazine NPs/TMPTA; (c) 20 wt% Si-triazine NPs/TMPTA, and (d) 50 wt% Si-triazine NPs/TMPTA under the irradiation of LED@410 nm.

Table S2. 2. Flexural modulus of the photocured samples prepared from the photopolymerization of TMPTA initiated by different triazine-containing photoinitiating systems.

Formulations	Flexural Modulus (MPa)
0.85 wt% triazine/TMPTA	43
1.3 wt% Silylated triazine +8.7 wt% Si NPs/TMPTA	113
10 wt% Si-triazine NPs/TMPTA	286
20 wt% Si-triazine NPs/TMPTA	185
50 wt% Si-triazine NPs/TMPTA	27

Chapter 3 Fabrication of High-performance CsPbBr3 Perovskite Quantum Dot/Polymer Composites via Photopolymerization: Implications for Luminescent Displays and Lighting

3.1. Preface

Beyond silica nanoparticles, halide perovskite quantum dots (QDs), particularly $CsPbBr_3$ QDs, have also attracted considerable interest as functional fillers due to their promising applications in optoelectronics, including light-emitting diodes, photovoltaic cells, and memory devices.[1-6] However, the inherent instability of these QDs, particularly under long-term operational conditions, remains a challenge, often leading to degradation and reduced photoluminescence, thus limiting their broader application.[7, 8]

In this chapter, $CsPbBr_3$ QDs are integrated into a polymer matrix through a photopolymerization process, where they act as photoinitiators under blue LED light (410 nm) to trigger polymerization, while simultaneously enhancing the optical properties of the resulting composites. Through a series of experiments, the chapter examines the photoinitiating efficiency of $CsPbBr_3$ QDs alone and in combination with additives, using real-time Fourier-transform infrared spectroscopy (RT-FTIR) and photochemical analysis via steady-state photolysis and electron paramagnetic resonance spin trapping (EPR-ST) techniques. The findings demonstrate that adding Iod results in superior photoinitiation performance due to efficient electron transfer, reducing the risk of back electron donation, and leading to a more stable polymer network.

Overall, it presents a simple, scalable, and environmentally friendly photopolymerization strategy for producing $CsPbBr_3$ QD-based polymer composites, addressing existing limitations in quantum dot stability. The resulting nanocomposites exhibit enhanced photoluminescence and mechanical stability, showing promise for applications in luminescent displays and lighting devices. This chapter provides a framework for the dual-functional role of halide perovskite QDs, offering a sustainable approach for fabricating advanced optoelectronic composite materials.

3.2. Statement of contribution

I declare that the research findings presented in this chapter are the original work I conducted as part of my Ph.D. program at the Australian National University. As the primary

author, I was responsible for developing the research concept, designing the experiments, analyzing the data, creating the figures, and drafting the initial manuscript, under the guidance of my primary supervisor, Prof. Pu Xiao.

3.3. Publication status

The published manuscript titled “Fabrication of High-Performance CsPbBr3 Perovskite Quantum Dot/Polymer Composites via Photopolymerization: Implications for Luminescent Displays and Lighting” and its supporting information are reproduced in this chapter with permission[9] from American Chemical Society, © 2022. This manuscript was published in the journal **ACS Applied Nano Materials** in 2022. The citation for the published work is:

Peng, X.; Hu, L.; Sun, X.; Lu, Y.; Chu, D.; Xiao, P. Fabrication of High-Performance $CSPbBr_3$ Perovskite Quantum Dots/Polymer Composites via Photopolymerization: Implications for luminescent displays and lighting. ***ACS Applied Nano Materials,*** **2022**, *6* (1), 646–655. https://doi.org/10.1021/acsanm.2c04773.

3.4. Abstract

The all-inorganic perovskites quantum dots (QDs), cesium lead halide QDs ($CsPbBr_3$ QDs) are the topic of interest in the field of optoelectronic devices as they show superior photoluminescence quantum yield and tuneable optical band gaps. However, the long-term stability issue limits their wide applications. In this research, we fabricate $CsPbBr_3$ QDs/polymer composites through photopolymerization strategy, during which $CsPbBr_3$ quantum dots serve as photoinitiators, in combination with the additives (diphenyliodonium hexafluorophosphate (Iod) or ethyl 4-(dimethylamino) benzoate (EDB)), to trigger polymerization processes as well as serve as highly efficient emitters in the resulted composites. More importantly, two types of additives are investigated to optimize the polymerization processes and the final product performance. In addition, steady-state photolysis, fluorescence quenching measurements, and electron spin resonance spin trapping technologies are applied to evaluate the relevant photochemical mechanism, and it demonstrates that their photoinitiation efficiency is greatly enhanced with the addition of the

additives. Specifically, the addition of Iod results in higher photoinitiation ability compared to that of EDB, which can be explained by the absence of back electron donation in $CsPbBr_3$ QDs/Iod combination. Therefore, the strategy provided here is that $CsPbBr_3$ QDs play a dual role in acting as both the efficient photoinitiators and the emitters to yield the desirable composites with superior photoluminescence properties, which are promising to enhance the long-term stability and device performance for the applications of luminescent displays and lighting.

3.5. Introduction

Halide perovskite quantum dots (QDs) have drawn much attention for the applications of photovoltaics, light-emitting diodes, X-ray detectors, and memory devices due to their tunable bandgaps through size dependence or composition control.[1-6] The high absorption and long exciton diffusion length offer them excellent optoelectronic properties, and the simple/accessible synthesis steps make them of interest in industries.[10-12] Among the perovskites QDs family, all-inorganic $CsPbBr_3$ QDs have been widely investigated owing to their excellent thermal stability and photoluminescence quantum yield (PLQY) properties.[13-16] However, they generally suffer from long-term stability issues[7, 8], which significantly limit the potential applications. Therefore it is necessary to come out with feasible approaches to prevent degradations, such as a significant decrease in photoluminescence or structural changes of QDs. [17, 18] Driven by this, polymers have been used to protect the quantum dots through dispersing halide perovskite QDs into polymer solution and spin-coating the solution on substrates. [19-21] Besides, spray-drying, melt encapsulation, and solution electrospinning have been used for the fabrication of halide perovskite QDs/polymer composites. However, these strategies usually lead to a decrease in PLQY and aggregation of QDs.[22-24] The combination of polymers and perovskites can not only improve the stability of the quantum dots but also enhance their processability and rigidity, which endow the corresponding composite materials with vast applications.[25-27] Nevertheless, the major drawbacks are the need for organic solvents and high temperatures during this process.[22, 28, 29]

The outstanding photophysical properties of halide perovskite QDs make them potential candidates as photoinitiators in photopolymerization. However, only a few works have been

done on this approach.[30, 31] Specifically, one has been focused on oxide perovskites ($LaTiO_3$, $LaCrO_3$, $La_{0.6}Sr_{0.4}MnO_3$), where they could initiate free radical polymerization with a combination of co-initiator such as iodonium salt and *N*-vinyl carbazole with irradiation of a Xe–Hg lamp.[31] However, oxide perovskites do not demonstrate similar optoelectronic properties as halide perovskites and are seldom used in the optoelectronic fields. Alternatively, the other has used halide perovskite QDs as photoinitiators and successfully initiated the polymerization of styrene under white light irradiation. The prepared composite delivered QD PLQY of 44% with significantly enhanced stability, demonstrating promising application prospects. However, the polymerization required prolonged irradiation for at least 14 hours, and further purification was required.[30] It should be noted that, instead of a 3D crosslinked network, this approach was achieved via a short polymer chain growing on the surface of the perovskites, which still tended to degrade since they were not fully protected in a dense crosslink network. To improve photopolymerization efficiency, additives are usually added. However, the interaction between QDs and additives might result in a downside effect on their photophysical properties (e.g., a decrease in PLQY).[32] It has been reported that $CsPbI_3$ QDs/PMMA composites were prepared via photopolymerization using different types of commonly used photoinitiators (e.g., TPP, TPO, DMPA, HPK and HMPO).[32] Surprisingly, only the composite with TPP-treated QDs showed approaching 100% PLQY and excellent stability; the rest of the photoinitiators in fact significantly lowered the PLQY of the corresponding composites. Based on the currently reported results[32], additives play an important role in achieving rapid photopolymerization and significantly affect the photophysical properties of the corresponding composite materials. Therefore, it would be interesting to explore the potential of $CsPbBr_3$ QDs as photoinitiators, with interaction with additives, to induce rapid photopolymerization of thiol-ene system. The effects of additives on the final photophysical properties of the resulting composites are also of interest.

So far, the fabrication routes of 3D crosslinked polymer-halide perovskite composites are still limited, and it is desirable to develop a new approach to overcome the current drawback. Jumping out from the majority of the approaches where the perovskites were only used as emitters, we proposed the potential of halide perovskite be used as both photoinitiators and emitters and investigated the effects of the incorporation of additives in the preparation of perovskite-polymer composites. In this case, a simple and environmentally friendly photopolymerization approach can be utilized to achieve a one-pot synthesis of functional composite materials. This new approach is expected to overcome

the current issues and provide a guideline for fabricating new functional composite materials.

In the present work, $CsPbBr_3$ QDs were investigated as both photoinitiators to trigger photopolymerization reactions under the irradiation of LED@410 nm and emitters of final products to endow the produced polymer nanocomposite materials with superior properties such as strong photoluminescence that allows potential application in optical devices (e.g., luminescent displays and lighting). Specifically, the photoinitiation abilities of $CsPbBr_3$ QDs alone or with the addition of additives (Iod or EDB) for the photopolymerization of triethyleneglycol divinyl ether (DVE-3) and pentaerythritol tetrakis(3-mercaptopropionate) (Tetrathiol) (Thiol-ene polymerization) were investigated (Scheme 3.1) and thoroughly compared using real-time Fourier-transform infrared spectroscopy (RT-FTIR). Moreover, photochemistry was studied by steady-state photolysis and electron paramagnetic resonance spin trapping (EPR-ST) techniques. Finally, the composites with high-efficiency CsPbBr3 QD emitters were fabricated and showed superior photoluminescence properties.

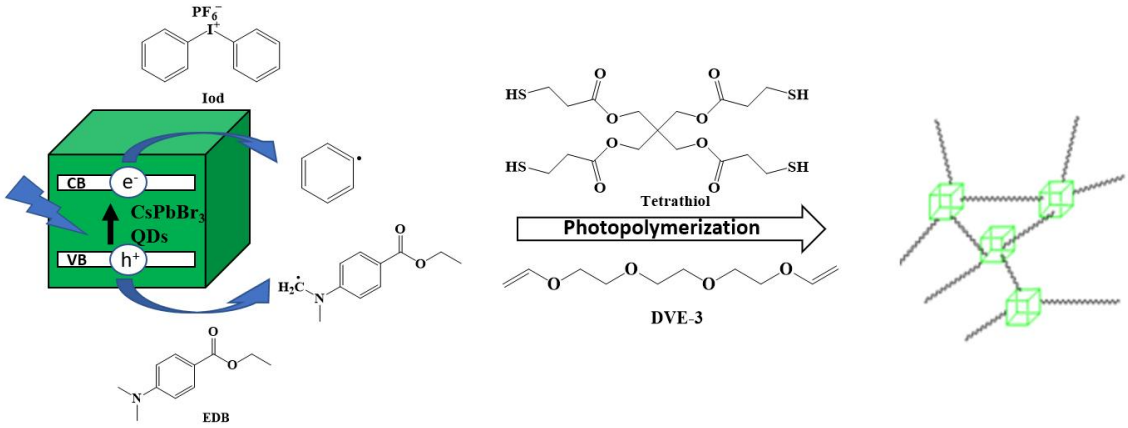

Scheme 3.1. Schematic illustration of possible electron/hole transfer between CsPbBr3 QDs and Iod or EDB under light irradiation.

3.5. Materials and methods

3.5.1. Materials

Diphenyliodonium hexafluorophosphate (Iod), ethyl 4-(dimethylamino) benzoate (EDB), dichloromethane (DCM; Anhydrous), triethyleneglycol divinyl ether (DVE-3), and pentaerythritol tetrakis(3- mercaptopropionate) (Tetrathiol) were all purchased from Sigma-Aldrich and used as received without further purification. The chemical structures of

mentioned compounds are summarized in Scheme 3.2. CsPbBr3 QDs were prepared following the procedure reported previously.[33]

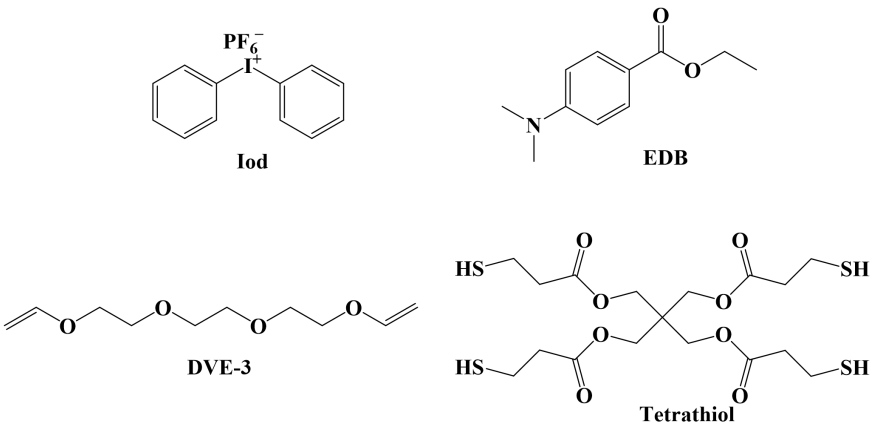

Scheme 3.2. Chemical structures of investigated additives and monomers

3.5.2. Irradiation sources

Three LED irradiation sources from Thorlabs were used for the photopolymerization experiments: 410 nm (110 mW cm^{-2}), 530 nm (30 mW cm^{-2}) and 640 nm (40 mW cm^{-2}).

3.5.3. Photopolymerization reaction

The photopolymerizations were investigated using real-time Fourier Transform Infrared Spectroscopy (RT-FTIR) (Bruker). All the photopolymerization reactions were conducted in laminate (a drop of the formulation was cast between two layers of polyethylene membranes, which were sandwiched between two pieces of BaF_2 salt plates). The thickness of the samples is approximately 25 µm. The evolution of the thiol conversion of Tetrathiol and the double bond conversion of DVE-3 was monitored at 2595–2535 cm^{-1}) and 1660–1570 cm^{-1}, respectively. Conversions of thiols or enes were calculated by the following equation:

$$\mathrm{C} = \frac{A_0 - A_t}{A_0} \times 100\%$$

where A_0 the initial peak area before irradiation and A_t the peak area of the functional groups at time t.

3.5.4. Ultraviolet-visible (UV-vis) measurements

Ultraviolet-visible (UV–vis) measurements were conducted on a Varian Cary 50 Bio UV–vis spectrometer from Agilent Technologies.

3.5.5. Transmission electron microscopy (TEM)

TEM measurement was performed by a JEOL JEM-2010 and JEOL JEM-F200 operated at 200 kV.

3.5.6. Steady-state photolysis

Varian Cary 50 Bio UV-visible (UV-vis) spectrophotometer from Agilent Technologies was utilized in steady-state photolysis investigation. The studied $CsPbBr_3$ QDs in dichloromethane were irradiated under LED@410 nm either alone or in the presence of additives (Iod or EDB) or monomers (DVE-3 or tetrathiol), being recorded by UV-vis at different irradiation time.

3.5.7. Fluorescence quenching experiments

A Varian Cary Eclipse Fluorescence Spectrophotometer from Agilent Technologies and QuantaMaster 500 from Horiba were used in the investigation of fluorescence quenching and photoluminescence quantum yield (PLQY). The investigated $CsPbBr_3$ QDs were dispersed in dichloromethane. After the addition of additives (Iod or EDB) or monomers (DVE-3 or tetrathiol), the fluorescence or photoluminescence (PL) spectra were recorded.

3.5.8. Electron Paramagnetic Resonance Spin Trapping (EPR-ST) Experiments

EPR-ST experiments were conducted via a Bruker E500 spectrometer equipped with a Bruker ER4103TM resonator. Samples were loaded into standard X-band EPR tubes of 2.8 mm i.d. Radicals were generated at room temperature by irradiating with LED@530 nm and trapped by phenyl-N-tert-butylnitrone (PBN) or 5,5-Dimethyl-1-pyrroline N-oxide (DMPO)

according to the previous procedure.[34] Simulation was processed via the WINSIM application.

3.5.9. Fabrication of $CsPbBr_3$ QDs/polymer composites

The investigated formulations, $CsPbBr_3$ QDs/Iod/DVE-3/tetrathiol and $CsPbBr_3$ QDs/EDB/DVE-3/tetrathiol were added into a Teflon mold with a dimension of 40 mm x 10 mm x 2 mm. the mold was then covered with a transparent polyethylene film to avoid the potential oxygen inhibition effect for the free radical photopolymerization. The formulations were then exposed to LED@410 nm for 10 min to allow complete photopolymerization.

3.6. Results and discussion

3.6.1. Light absorption properties of $CsPbBr_3$ QDs

The light absorption of $CsPbBr_3$ QDs was first measured with a UV-vis absorption spectrometer to confirm the suitable wavelength of irradiation to be used in the following experiment. As illustrated in Figure 3.1 (a), the absorption tail of the $CsPbBr_3$ QDs could reach up to 700 nm. This implied that a wide range of irradiations could be involved in the initiation process. Based on the UV-vis spectrum, we therefore selected three light sources, LED @ 410 nm, 530 nm and 640 nm, for the rest of the investigations. Besides, a PL spectrum (Figure S3.1) with a maximum emission of 497 nm has a full width at half maximum (FWHM) of 41.11 nm, which indicated the good monodispersity of the $CsPbBr_3$ QDs. The photoluminescence quantum yield (PLQY) was measured to be 70% in solution. In addition, transmission electron microscopy (TEM) was used to study the structural and morphological properties of the $CsPbBr_3$ QDs. Figure 3.1b shows the as-synthesized $CsPbBr_3$ QDs with a scale bar of 100 nm, which confirmed the highly uniform size (8.7 nm) and cubic morphology of the $CsPbBr_3$ QDs.

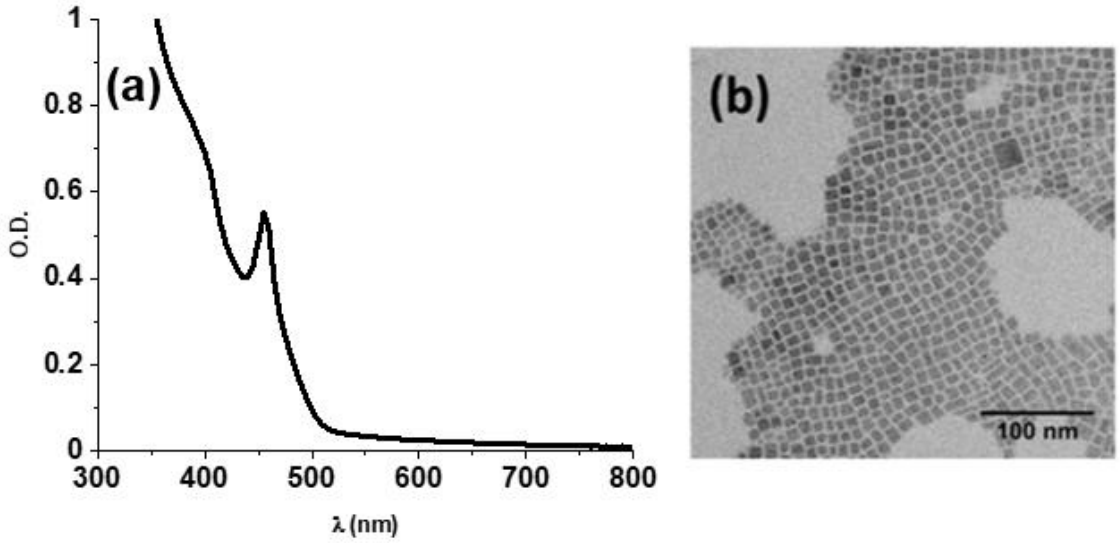

Figure 3. 1. (a) UV-vis absorption and $CsPbBr_3$ QDs dispersed in dichloromethane ([$CsPbBr_3$ QDs]: 0.2 mg/mL), (b) TEM image of $CsPbBr_3$ QDs.

3.6.2. Photoinitiation ability of $CsPbBr_3$ QDs-based photoinitiating system

The photoinitiation ability of $CsPbBr_3$ QDs alone towards 3D crosslinking reactive thiol-ene systems was first accessed. The polymerization profiles are given in Figure 3.2, and the double bond conversions of DVE-3 and the thiol conversions of tetrathiol after 300 s of photopolymerization and their relevant maximum polymerization rates are summarized in Table 3.1. As shown in Figure 3.2 and Figure S3.2, it is intriguing to observe that with 2 wt% of $CsPbBr_3$ QDs alone, the double bond conversion of DVE-3 and the thiol conversion of tetrathiol can reach 52% and 88% when LED@410 nm was used and 47% and 62% when LED@530 nm was used. Specifically, the polymerization rate was significantly higher when the reaction proceeded under LED@410 nm compared to LED@530 nm (0.9 s^{-1}/3.6 s^{-1} and 0.5 s^{-1}/1.5 s^{-1}, respectively). This was expected since $CsPbBr_3$ QDs have greater absorption under 410 nm than 530 nm (Figure 3.1) and the light intensity of LED@410 nm was about three times higher than the LED@530 nm (110 mW cm^{-2} and 30 mW $cm^{-2,}$ respectively). Alternatively, even though the absorption tail of $CsPbBr_3$ QDs can reach up to 700 nm, LED@640 nm was unable to initiate the polymerization of $CsPbBr_3$ QDs/DVE-3/tetrathiol formula. This might be due to the extremely low absorption of $CsPbBr_3$ QDs at 640 nm and the low intensity of the 640 nm LED used (40 mW cm^{-2}). Since a high concentration of $CsPbBr_3$ QDs may lead to potential aggregation, the photoinitiation ability of a lower concentration of $CsPbBr_3$ QDs has also been accessed (Figure S3.3). As

expected, the overall conversion and polymerization rate has decreased to 23%/56% and 0.4 s^{-1}/2.4 s^{-1} due to the decreased concentration of the photoinitiator. Nevertheless, even when the concentration of $CsPbBr_3$ QDs has reduced to 25% of the original, the decrease of photoinitiation ability was less than 50% of the original. Therefore, 0.5 wt% of $CsPbBr_3$ QDs was used in the following research.

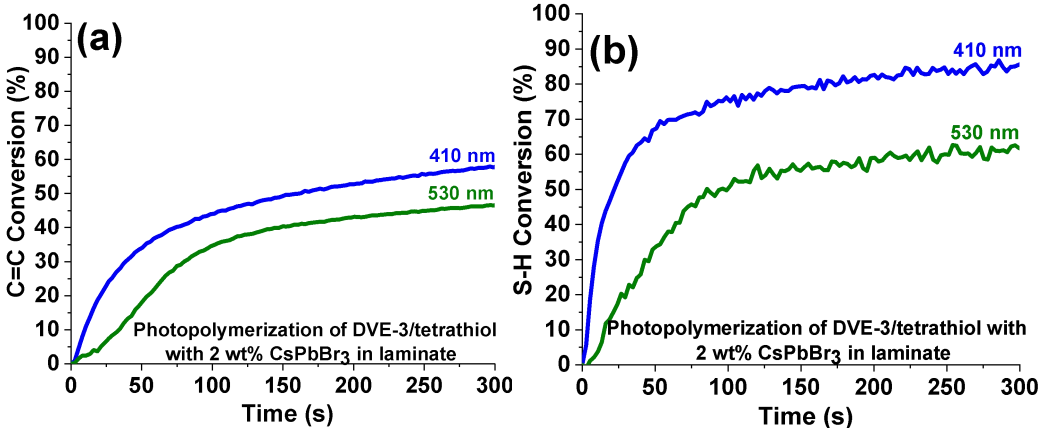

Figure 3. 2. Photopolymerization profiles of DVE-3/tetrathiol obtained in laminate upon exposure to LED@410 nm and 530 nm in the presence of $CsPbBr_3$ [$CsPbBr_3$ QDs: 2 wt%; ene : thiol = 1 : 1 in functionality]. Diagram labelled (a) represents double bond conversions vs. time; diagram labelled (b) represents thiol bond conversions vs. time.

Table 3. 1. Conversions of functional groups and polymerization rates for the photopolymerization of DVE-3/tetrathiol in laminate upon exposure to LED@410 nm, 530 nm, and 640 nm in the presence of Iod or $CsPbBr_3$-based photoinitiating systems ($CsPbBr_3$: 0.5 wt%; Iod or EDB: 0.5 wt%; ene : thiol = 1 : 1 in functionality)

	LED@410 nm		**LED@530 nm**		**LED@640 nm**	
PISs	C^a/C^b	$(\frac{R_p}{[C=C]}) \times 100^c / (\frac{R_p}{[S-H]}) \times 100^c$ (s^{-1})	C^a/C^b	$(\frac{R_p}{[C=C]}) \times 100^c / (\frac{R_p}{[S-H]}) \times 100^c$ (s^{-1})	C^a/C^b	$(\frac{R_p}{[C=C]}) \times 100^c / (\frac{R_p}{[S-H]}) \times 100^c$ (s^{-1})
Iod	51%/73%	0.3/2.2	np[d]	np[d]	np[d]	np[d]
$CsPbBr_3$	23%/56%[e] 52%/88%[f]	0.4/2.4[e] 0.9/3.6[f]	47%/62%[f]	0.5/1.5[f]	np[d]	np[d]

$CsPbBr_3$/Iod[e]	87%/98%	4.2/6.0	58%/68%	3.1/2.5	28%/44%	1.2/1.1
$CsPbBr_3$/EDB[e]	52%/87%	1.0/3.6	18%/22%	0.4/1.2	np[d]	np[d]

[a] double bond conversions of DVE-3 after thiol-ene photopolymerization for 300 s
[b] S-H bond conversions of tetrathiol after thiol-ene photopolymerization for 300 s
[c] maximum rates of photopolymerization, calculated from the maximum of the first derivative of the double bond conversions versus time curves during photopolymerization.
[d] no photopolymerization
[e] The concentration of $CsPbBr_3$ QDs is 0.5 wt%
[f] The concentration of $CsPbBr_3$ QDs is 2 wt%

To improve the photoinitiation ability of $CsPbBr_3$ QDs, two commonly used additives, Iod and EDB were added separately to the photoinitiating systems. It should be noted that the concentration of $CsPbBr_3$ QDs has decreased to 0.5 wt% in the system to allow well dispersion and avoid potential aggregation of $CsPbBr_3$ QDs. The polymerization profiles are given in Figure 3.3, and the double bond conversions and the thiol bond conversions of DVE-3 and tetrathiol, respectively after 300 s of photopolymerization and their relevant maximum polymerization rates are summarized in Table 3.1. Interestingly, the addition of Iod or EDB significantly enhanced the conversions of DVE-3/tetrathiol from 23%/56% to 87%/98% and 52%/87%, respectively. Specifically, the addition of Iod drastically increased the polymerization rate from 0.4/2.4 s^{-1} to 4.2/6.0 s^{-1} for DVE-3 and tetrathiol. On the other hand, the addition of EDB showed less photoinitiation efficiency than Iod where the polymerization rate only increased to 1.0/3.6 s^{-1} for DVE-3 and tetrathiol. Nevertheless, it still appeared to be more efficient than the system with Iod or $CsPbBr_3$ QDs alone added. The outstanding enhancement of the photoinitiation ability by adding Iod can be explained by the less back electron transfer[35] in $CsPbBr_3$ QDs/Iod complex. Upon irradiation, an excited state complex was formed between Iod and the excited $CsPbBr_3$ QDs, followed by the reduction of Iod by electron transfer. The resulting unstable diaryliodine radical is readily decomposed and prevents back electron transfer. [35, 36] Alternatively, EDB being an electron donor, could also perform electron transfer with holes in $CsPbBr_3$ QDs during irradiation,[37] however, the unavoidable charge recombination could significantly lower the quantum yield of radicals generated, resulting in lower conversion and polymerization rate of EDB containing formula compared to the Iod containing one.[38] Besides irradiating under

LED@410 nm, two formulas were polymerized under LED@530 nm and LED@640 nm. Interestingly, with the addition of Iod, the formula was successfully polymerized under both LED@530 nm and LED@640 nm (Figure S3.4), while the formula with EDB could only be polymerized under LED@530 nm (Figure S3.5). It can be again ascribed to the higher quantum yield of radicals generated in $CsPbBr_3$ QDs/Iod-based system than the $CsPbBr_3$ QDs/EDB.

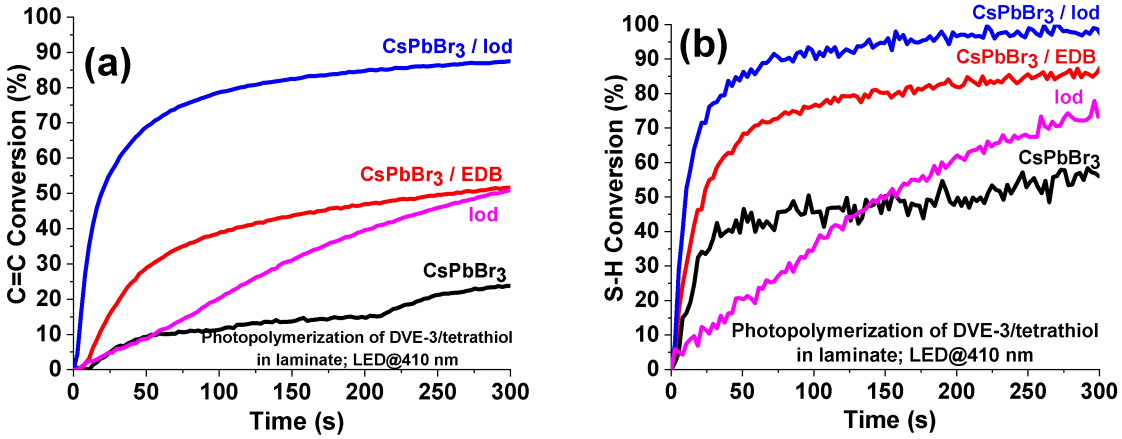

Figure 3. 3. Photopolymerization profiles of DVE-3/tetrathiol obtained in laminate upon exposure to LED@410 nm in the presence of Iod or $CsPbBr_3$-based photoinitiating systems [$CsPbBr_3$: 0.5 wt%, Iod: 0.5 wt%, EDB: 0.5 wt %; ene : thiol =1 : 1 in functionality]. Diagram labelled (a) represents double bond conversions vs. time; diagram labelled (b) represents thiol bond conversions vs. time.

Generally, a higher concentration of $CsPbBr_3$ QDs reflected enhanced photovoltaic properties beneficial from a larger light harvesting. However, once exceeding the optimal amount, the properties are greatly deteriorated by agglomeration.[39] Here, the photoinitiating systems containing different concentrations of $CsPbBr_3$ QDs and 0.5 wt% EDB were prepared in DVE-3/tetrathiol and the corresponding conversions and rate of polymerization were investigated and summarized in Figure 3.4. It is obvious that 0.2 wt% QDs was inefficient in initiating the polymerization of DVE-3/tetrathiol. When the concentration of $CsPbBr_3$ QDs increased to 0.5 wt%, the conversions and rate of polymerization drastically increased to 59%/92% and 0.98/3.62 $s^{-1,}$ respectively. Further increased to 2 wt% did not show significant improvement. Since a high concentration of $CsPbBr_3$ QDs might result in agglomeration, 0.5 wt% $CsPbBr_3$ QDs was used as the optimal amount for the rest of the experiment.

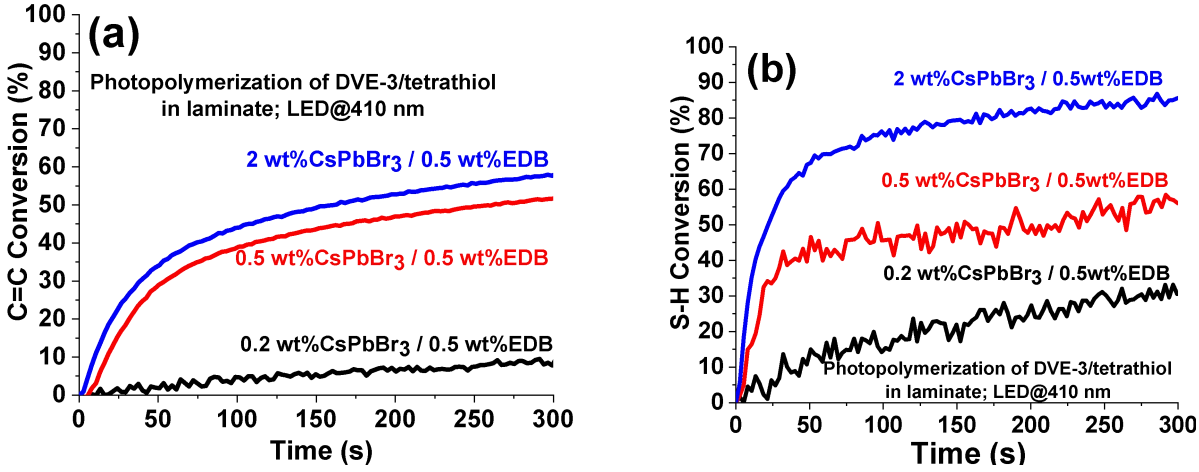

Figure 3. 4. Photopolymerization profiles of DVE-3/tetrathiol obtained in laminate upon exposure to LED@410 nm in the presence of $CsPbBr_3$-based photoinitiating systems [$CsPbBr_3$: 0.2 wt%, 0.5 wt%, or 2 wt%; EDB: 0.5 wt %; ene : thiol =1 : 1 in functionality]. Diagram labelled (a) represents double bond conversions vs. time; diagram labelled (b) represent thiol bond conversions vs. time.

3.6.3. Photochemistry of $CsPbBr_3$ QDs

3.6.3.1. Steady-state photolysis

The photostability of $CsPbBr_3$ QDs with additives or monomers in dichloromethane upon exposure to LED@410 nm was investigated. As shown in Figure 3.5a, a significant blueshift occurred after irradiating the $CsPbBr_3$ QDs /DCM solution using LED@410 nm for 5 min. This is due to the photoinduced anion exchange between the bromide anions in $CsPbBr_3$ QDs and chloride anions in DCM.[40] Same trends were found with the addition of EDB or tetrathiol as shown in Figure 3.5c and 5e. However, a different phenomenon was observed when combined with Iod and DVE-3. The clear, bright green solution quickly turned into a slightly opaque suspension when Iod was added. This was also reflected in the UV-vis spectrum (Figure 3.5b), where a significant increase of absorption offset was due to the light scattering of the suspension formed. Alternatively, a decrease of a peak at ~450 nm and an increase of a peak at ~500 nm was observed for the first 5 min of irradiation rather than blueshift with the addition of DVE-3. (Figure 3.5d) This is referred to as a weakening of quantum confinement, where the sizes of the $CsPbBr_3$ QDs have increased. [41-43] When the solution was further irradiated, a blueshift was observed, again referring to the photoinduced anion exchange between $CsPbBr_3$ QDs and DCM.

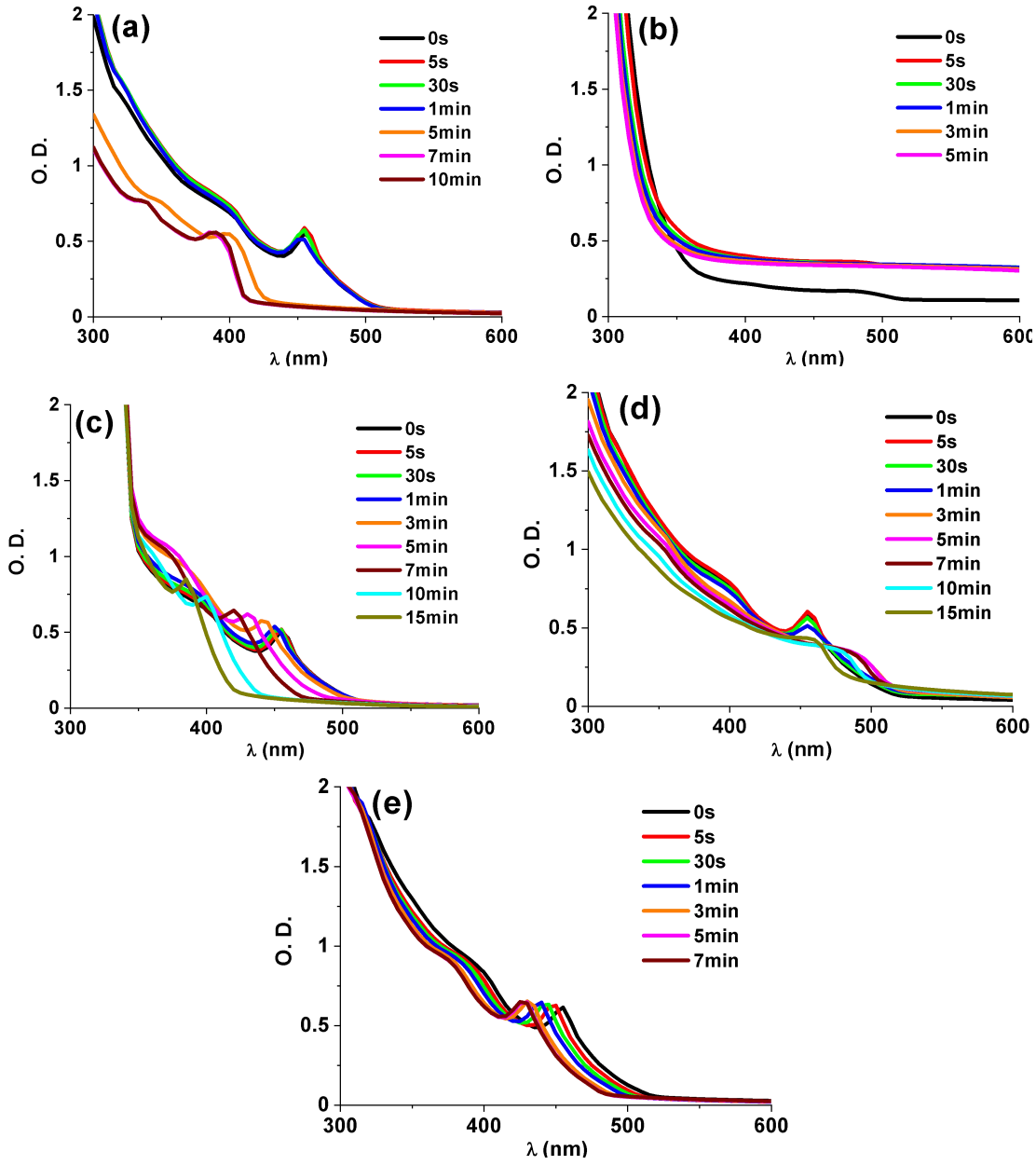

Figure 3. 5. Steady-state photolysis of (a) $CsPbBr_3$, (b) $CsPbBr_3$/Iod, (c) $CsPbBr_3$/EDB, (d) $CsPbBr_3$/DVE-3, and (e) $CsPbBr_3$/tetrathiol in dichloromethane ([Iod] = 3.4 mM; [EDB] = 7.4 mM; [DVE-3] = 23.6 mM; [tetrathiol] = 12.76 mM); UV-vis spectra recorded at different irradiation time; LED@410 nm irradiation (110 mW cm^{-2}).

3.6.3.2. Fluorescence quenching

The interactions between $CsPbBr_3$ QDs and additives or monomers were also investigated using the fluorescence quenching approach. The maximum fluorescence emission of $CsPbBr_3$ QDs was centered at 494 nm. Interestingly, the fluorescence was quickly quenched when a tiny amount of Iod or tetrathiol was added (Figure 3.6a, d), while the fluorescence was slowly quenched when EDB or DVE-3 was added (figure 3.6b, c).

Specifically, the fluorescence was first decreased when DVE-3 was added, then remained constant for further excess addition of DVE-3. It is possibly suggested that the interaction between DVE-3 and $CsPbBr_3$ QDs has passivated the surface defects of $CsPbBr_3$ QDs, thereby stabilizing the $CsPbBr_3$ QDs and resulting in the retention of fluorescence.[44] The quick quenching of $CsPbBr_3$ QDs/Iod combination compared to $CsPbBr_3$ QDs/EDB combination was correlated with the FTIR results that $CsPbBr_3$ QDs/Iod proceeded with higher photoinitiation ability than $CsPbBr_3$ QDs/EDB. Besides the observation of quenching, another interesting phenomenon happened in the investigated solutions with the addition of EDB (Figure 3.6b) or DVE-3 (Figure 3.6c), that is, showing a redshift in maximum fluorescence emission. This was possibly due to the formation of the superlattice.[45] The observation was correlated with the UV-vis results, where the $CsPbBr_3$ QDs/DVE-3 solution showed a redshift in absorption (referred to increase of size) upon irradiation before the anion exchange with DCM.

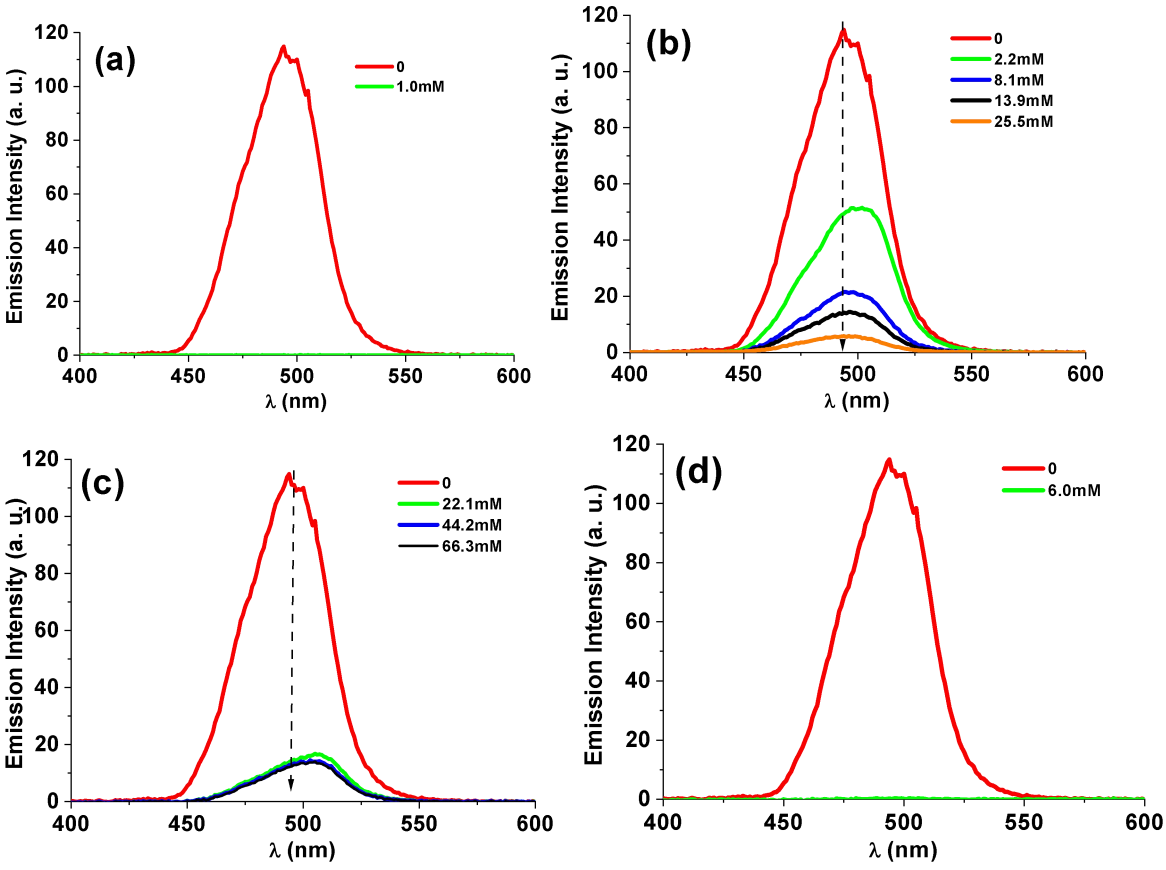

Figure 3. 6. Fluorescence spectra of $CsPbBr_3$ as the function of (a) [Iod], (b) [EDB], (c) [DVE-3], and (d) [tetrathiol] in dichloromethane.

3.6.4. EPR-ST experiment and proposed chemical mechanism

Upon irradiation, the CsPbBr3 QDs were excited from the ground state to an excited state (r1). Electron transfer due to the oxidation process between CsPbBr3 QDs and Iod occurred subsequently, resulting in the formation of CsPbBr3 QDs$^{\cdot+}$ and $Ph_2I^{\cdot}$ (r2). Phenyl radicals (Ph·) were then formed by the rapid cleavage of weak C-I bonds (r3).[31] Alternatively, the combination of CsPbBr3 QDs and EDB or CsPbBr3 QDs and tetrathiol followed the photo-reduction mechanism, where a hole transfer followed by an H-abstraction occurred. [46-48] The formation of $EDB_{(-H)}^{\cdot}$ (r4) and thiyl radical (r5) was responsible for the initiation of the polymerization. (Scheme 3.3)

$$\text{CsPbBr3 QDs} \xrightarrow{h\nu} \text{CsPbBr3 QDs}^{*} \quad \text{(r1)}$$

$$\text{CsPbBr3 QDs}^{*} + Ph_2I_{+} \rightarrow \text{CsPbBr3 QDs}^{\cdot+} + Ph_2I^{\cdot} \quad \text{(r2)}$$

$$Ph_2I^{\cdot} \rightarrow \text{Ph-I} + Ph^{\cdot} \quad \text{(r3)}$$

$$\text{CsPbBr3 QDs}^{*} + \text{EDB} \rightarrow \text{CsPbBr3 QDs - H}^{\cdot} + EDB_{(-H)}^{\cdot} \quad \text{(r4)}$$

$$\text{CsPbBr3 QDs}^{*} + 4\text{SH} \rightarrow \text{CsPbBr3 QDs - H}^{\cdot} + 4\text{S}^{\cdot} \quad \text{(r5)}$$

Scheme 3.3. Proposed chemical mechanisms for CsPbBr3 QDs-based photoinitiating systems.

The generation of radicals upon the light exposure of $CsPbBr_3$ QDs/Iod, $CsPbBr_3$ QDs/EDB and $CsPbBr_3$ QDs/tetrahtiol to LED@530 nm was further confirmed by the EPR-ST approach. The radicals generated were trapped by phenyl-N-tert-butylnitrone (PBN) or 5,5-Dimethyl-1-pyrroline N-oxide (DMPO) and characterized. For $CsPbBr_3$ QDs/Iod combination, the hyperfine splitting (HFS) constants were found to be a_N = 14.3 G, a_H = 2.2 G (Figure 3.7A), which was consistent with the simulated spectrum of PBN/phenyl radical adducts as previously reported.[49-51] For $CsPbBr_3$ QDs/EDB combination, the HFS constants were obtained as a_N = 14.3 G, a_H = 2.3 G (Figure 3.7B), which could be assigned to the PBN/aminoalkyl radical adducts.[52] For $CsPbBr_3$ QDs/tetrathiol combination, DMPO was used as a spin trap reagent instead of PBN since DMPO showed a greater reaction rate with thiyl radical and generally gave a more intense signal compared to PBN.[53, 54] The HFS of a_N = 13.5 G, a_H = 11.8 G was shown in Figure 3.7C, reflected the formation of DMPO/thiyl radical adducts and this was consistent with the previously published report. [55]

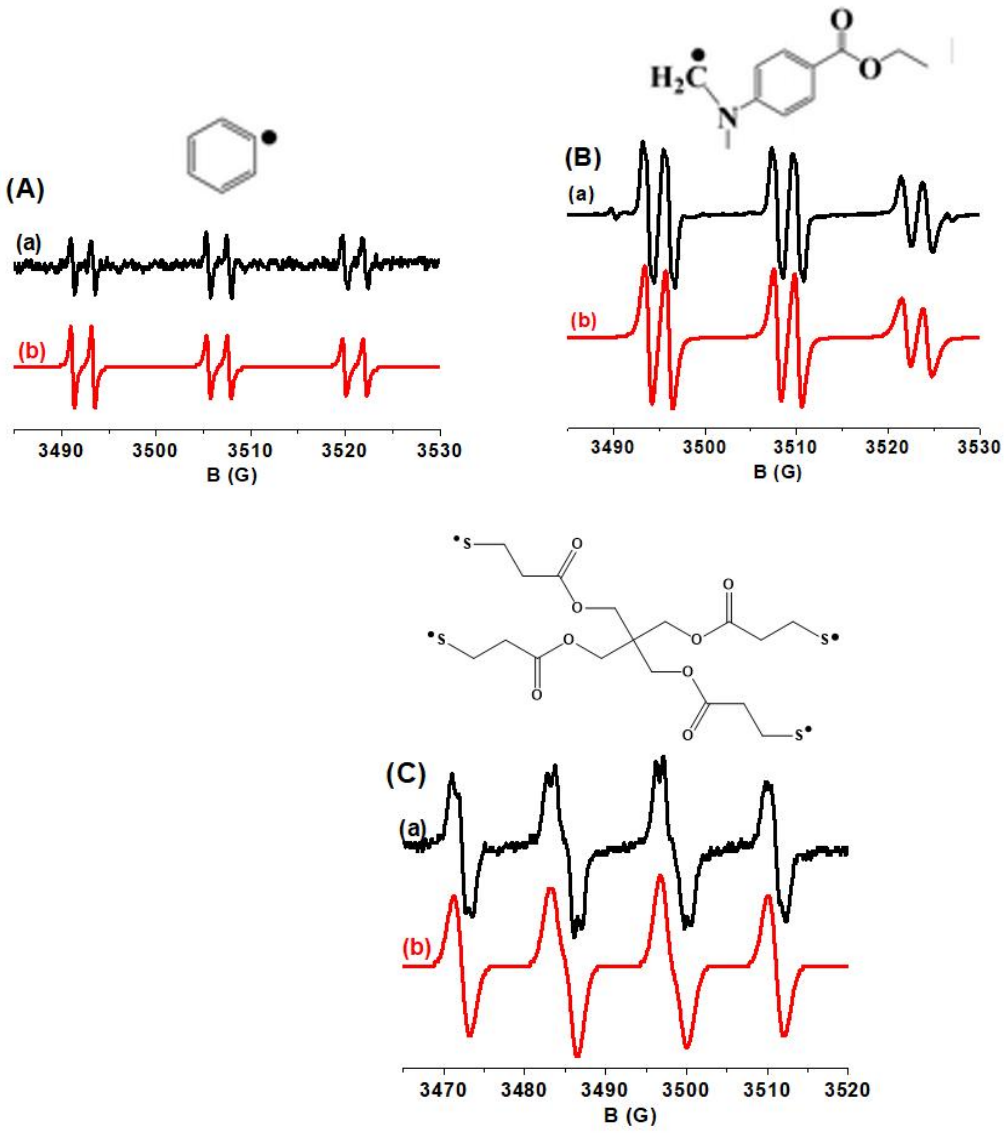

Figure 3. 7. EPR-SP spectra of the radicals generated in (A) $CsPbBr_3$ QDs /Iod and (B) $CsPbBr_3$ QDs/EDB combination upon exposure to UV LED@530 nm and trapped by PBN in *tert*-butylbenzene; (C) $CsPbBr_3$ QDs/tetrahtiol combination upon exposure to UV LED@530 nm and trapped by DMPO in *tert*-butylbenzene: (a) experimental and (b) simulated spectra.

3.6.5. Fabrication of functional composites in mold

In order to proceed with further material characterizations, the investigated formulas were photocured in Teflon mold. As shown in Figure 3.8, $CsPbBr_3$ QDs/Iod/DVE-3/tetrathiol (left corner) and $CsPbBr_3$ QDs/EDB/DVE-3/tetrathiol (right corner) were polymerized under the irradiation of LED@410 nm. It was clearly noticed that the photocured sample with the addition of EDB gave much brighter fluorescence than the one with the addition of Iod

under the LED@410 nm irradiation. This was consistent with the fluorescence measurements where Iod nearly fully quenched the $CsPbBr_3$ QDs. One should be doubted that some fluorescence was still found in $CsPbBr_3$ QDs/Iod/DVE-3/tetrathiol chips, but the fluorescence quenching measurements showed a fully quenched fluorescence by adding Iod or tetrathiol (Figure 3.6). When the $CsPbBr_3$ QDs were dispersed in solution, the oleic acid used to stabilize the $CsPbBr_3$ QDs was desorbed from the surface of the $CsPbBr_3$ QDs and allowed fast electron transfer with additives or monomers. Alternatively, when preparing the investigated formulas, the $CsPbBr_3$ QDs solution was first evaporated with a rotary evaporator and then re-dissolved in the viscous monomers (instead of the solvent used for dispersion). In this case, the oleic acid is less likely to be desorbed from the surface, remaining stabilizing the $CsPbBr_3$ QDs. It should be noted that electron transfer with additives or monomers still proceeded, leaving the sample with minor fluorescence after polymerization (with the addition of Iod, Figure 3.8 left). As EDB performed less quenching ability than Iod and possibly promoted the formation of a superlattice of $CsPbBr_3$ QDs, the sample containing EDB showed much greater fluorescence after polymerization (Figure 3.8, right). The PL stabilities of the photopolymerized samples under heat and oxygen plasma were finally evaluated. For the pristine photopolymerized $CsPbBr_3$ QDs/EDB/DVE-3/tetrathiol composite, the PLQY was determined as 34%. Compared to a PLQY of 70% of the $CsPbBr_3$ QDs solution, the dropped after photopolymerization was expected since the addition of EDB slightly quenched the $CsPbBr_3$ QDs. However, the photopolymerized composite showed a negligible change of PL under heating or oxygen plasma (PLQY were measured as 24% and 26%, respectively.) conditions (Figure S3.6). It confirmed the excellent protection of $CsPbBr_3$ QDs in polymer and revealed the potential of using a simple photopolymerization approach in preparing highly efficient composite materials.

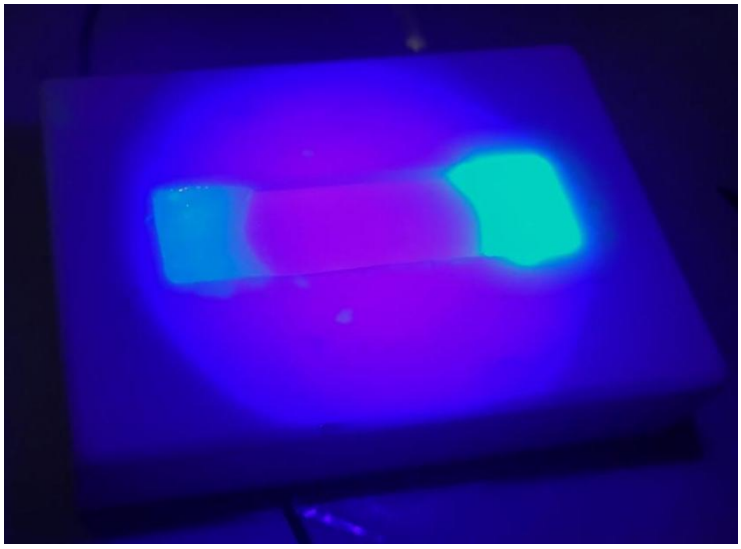

Figure 3. 8. Photocured DVE-3/tetrathiol samples (1:1 ene: thiol in functionality) in the presence of $CsPbBr_3$ QDs/Iod (left) and $CsPbBr_3$ QDs/EDB (right) ($CsPbBr_3$: 0.5 wt%; Iod: 0.5 wt%; EDB: 0.5 wt%) upon exposure to LED@410 nm (110 mW cm^{-2}).

3.7. Conclusion

In this study, all-inorganic perovskite quantum dots, $CsPbBr_3$ QDs were investigated to work as both the photoinitiator and the filler in preparing functional composite materials. They have successfully initiated thiol-ene polymerization (DVE-3/tetrahthiol) under irradiation of LED@410 nm and 530 nm. Specifically, the photoinitiation ability of $CsPbBr_3$ QDs could be further enhanced with the addition of additives, Iod or EDB, where the combination with Iod could render the thiol-ene polymerization to nearly complete conversions. Steady-state photolysis revealed the photoinduced anion exchange between CsPbBr3 QDs and DCM with a blue shift in absorption. In addition, fluorescence quenching measurements showed a quick quenching of $CsPbBr_3$ QDs with the addition of Iod or thiol, but much slower quenching with the addition of EDB or DVE-3. Specifically, the red shift of fluorescence emission peak with the addition of DVE-3 or EDB reflected the possible formation of the superlattice. Alternatively, the EPR experiment revealed the formation of phenyl radicals, aminoalkyl radicals, or thiyl radicals generated from Iod, EDB, or tetrathiol by interacting with $CsPbBr_3$ QDs under light irradiation. Finally, $CsPbBr_3$ QDs polymer composites with strong photoluminescence were prepared by simply polymerizing the investigated formulas in Teflon mold under ambient conditions. The photopolymer showed excellent PL stability under heating or oxygen plasma. With their high-performance properties, they are highly applicable in making luminescent displays and lighting. Overall,

this research provides a versatile approach for fabricating new functional composite materials.

3.8. Reference

1. Chen, Q.; De Marco, N.; Yang, Y.; Song, T.-B.; Chen, C.-C.; Zhao, H.; Hong, Z.; Zhou, H.; Yang, Y., Under the Spotlight: The Organic–Inorganic Hybrid Halide Perovskite for Optoelectronic Applications. *Nano Today* **2015,** 10, 355-396.
2. Cho, H.; Jeong, S.-H.; Park, M.-H.; Kim, Y.-H.; Wolf, C.; Lee, C.-L.; Heo Jin, H.; Sadhanala, A.; Myoung, N.; Yoo, S.; Im Sang, H.; Friend Richard, H.; Lee, T.-W., Overcoming the Electroluminescence Efficiency Limitations of Perovskite Light-Emitting Diodes. *Science* **2015,** 350, 1222-1225.
3. Choi, J.; Park, S.; Lee, J.; Hong, K.; Kim, D.-H.; Moon, C. W.; Park, G. D.; Suh, J.; Hwang, J.; Kim, S. Y.; Jung, H. S.; Park, N.-G.; Han, S.; Nam, K. T.; Jang, H. W., Organolead Halide Perovskites for Low Operating Voltage Multilevel Resistive Switching. *Advanced Materials* **2016,** 28, 6562-6567.
4. Yakunin, S.; Sytnyk, M.; Kriegner, D.; Shrestha, S.; Richter, M.; Matt, G. J.; Azimi, H.; Brabec, C. J.; Stangl, J.; Kovalenko, M. V.; Heiss, W., Detection of X-Ray Photons by Solution-Processed Lead Halide Perovskites. *Nature Photonics* **2015,** 9, 444-449.
5. Kim, Y.-H.; Wolf, C.; Kim, Y.-T.; Cho, H.; Kwon, W.; Do, S.; Sadhanala, A.; Park, C. G.; Rhee, S.-W.; Im, S. H.; Friend, R. H.; Lee, T.-W., Highly Efficient Light-Emitting Diodes of Colloidal Metal–Halide Perovskite Nanocrystals Beyond Quantum Size. *ACS Nano* **2017,** 11, 6586-6593.
6. Lee, T.; Im, S.; Kim, Y.; Cho, H. Perovskite Nanocrystalline Particles and Optoelectronic Device Using Same. U.S. Patent 010193088B2 Jan.29,2019.
7. Frost, J. M.; Butler, K. T.; Brivio, F.; Hendon, C. H.; van Schilfgaarde, M.; Walsh, A., Atomistic Origins of High-Performance in Hybrid Halide Perovskite Solar Cells. *Nano Letters* **2014,** 14, 2584-2590.
8. Li, F.; Liu, Y.; Wang, H.; Zhan, Q.; Liu, Q.; Xia, Z., Postsynthetic Surface Trap Removal of Cspbx3 (X = Cl, Br, or I) Quantum Dots Via a Znx2/Hexane Solution toward an Enhanced Luminescence Quantum Yield. *Chemistry of Materials* **2018,** 30, 8546-8554.
9. Peng, X.; Hu, L.; Sun, X.; Lu, Y.; Chu, D.; Xiao, P., Fabrication of High-Performance Cspbbr3 Perovskite Quantum Dots/Polymer Composites Via Photopolymerization: Implications for Luminescent Displays and Lighting. *ACS Applied Nano Materials* **2023,** 6, 646-655.
10. Park, N.-G., Organometal Perovskite Light Absorbers toward a 20% Efficiency Low-Cost Solid-State Mesoscopic Solar Cell. *The Journal of Physical Chemistry Letters* **2013,** 4, 2423-2429.
11. Xing, G.; Mathews, N.; Sun, S.; Lim Swee, S.; Lam Yeng, M.; Grätzel, M.; Mhaisalkar, S.; Sum Tze, C., Long-Range Balanced Electron- and Hole-Transport Lengths in Organic-Inorganic Ch3nh3pbi3. *Science* **2013,** 342, 344-347.
12. Gao, P.; Grätzel, M.; Nazeeruddin, M. K., Organohalide Lead Perovskites for Photovoltaic Applications. *Energy & Environmental Science* **2014,** 7, 2448-2463.
13. Li, X.; Wu, Y.; Zhang, S.; Cai, B.; Gu, Y.; Song, J.; Zeng, H., Cspbx3 Quantum Dots for Lighting and Displays: Room-Temperature Synthesis, Photoluminescence Superiorities, Underlying Origins and White Light-Emitting Diodes. *Advanced Functional Materials* **2016,** 26, 2435-2445.
14. Koscher, B. A.; Swabeck, J. K.; Bronstein, N. D.; Alivisatos, A. P., Essentially Trap-Free Cspbbr3 Colloidal Nanocrystals by Postsynthetic Thiocyanate Surface Treatment. *Journal of the American Chemical Society* **2017,** 139, 6566-6569.
15. Liu, F.; Zhang, Y.; Ding, C.; Kobayashi, S.; Izuishi, T.; Nakazawa, N.; Toyoda, T.; Ohta, T.; Hayase, S.; Minemoto, T.; Yoshino, K.; Dai, S.; Shen, Q., Highly Luminescent Phase-Stable Cspbi3 Perovskite Quantum Dots Achieving near 100% Absolute Photoluminescence Quantum Yield. *ACS Nano* **2017,** 11, 10373-10383.

16. Song, J.; Li, J.; Li, X.; Xu, L.; Dong, Y.; Zeng, H., Quantum Dot Light-Emitting Diodes Based on Inorganic Perovskite Cesium Lead Halides (Cspbx3). *Advanced Materials* **2015,** 27, 7162-7167.
17. Li, J.; Wang, L.; Yuan, X.; Bo, B.; Li, H.; Zhao, J.; Gao, X., Ultraviolet Light Induced Degradation of Luminescence in Cspbbr3 Perovskite Nanocrystals. *Materials Research Bulletin* **2018,** 102, 86-91.
18. Huang, S.; Li, Z.; Wang, B.; Zhu, N.; Zhang, C.; Kong, L.; Zhang, Q.; Shan, A.; Li, L., Morphology Evolution and Degradation of Cspbbr3 Nanocrystals under Blue Light-Emitting Diode Illumination. *ACS Applied Materials & Interfaces* **2017,** 9, 7249-7258.
19. Khan, A. A.; Rana, M. M.; Huang, G.; Mei, N.; Saritas, R.; Wen, B.; Zhang, S.; Voss, P.; Rahman, E.-A.; Leonenko, Z.; Islam, S.; Ban, D., Maximizing Piezoelectricity by Self-Assembled Highly Porous Perovskite–Polymer Composite Films to Enable the Internet of Things. *Journal of Materials Chemistry A* **2020,** 8, 13619-13629.
20. Qaid, S. M. H.; Ghaithan, H. M.; Al-Asbahi, B. A.; Aldwayyan, A. S., Ultra-Stable Polycrystalline Cspbbr(3) Perovskite-Polymer Composite Thin Disk for Light-Emitting Applications. *Nanomaterials (Basel)* **2020,** 10, 2382.
21. Hu, Q.; Guo, J.; Lu, M.; Lu, P.; Zhang, Y.; Yu, W. W.; Bai, X., Efficient and Stable Mg2+-Doped Cspbcl3 Nanocrystals for Violet Leds. *The Journal of Physical Chemistry Letters* **2021,** 12, 8203-8211.
22. Boussoufi, F.; Pousthomis, M.; Kuntzmann, A.; D'Amico, M.; Patriarche, G.; Dubertret, B., Spray-Drying Polymer Encapsulation of Cspbbr3 Perovskite Nanocrystals with Enhanced Photostability for Led Downconverters. *ACS Applied Nano Materials* **2021,** 4, 7502-7512.
23. Wang, Z.; Fu, R.; Li, F.; Xie, H.; He, P.; Sha, Q.; Tang, Z.; Wang, N.; Zhong, H., One-Step Polymeric Melt Encapsulation Method to Prepare Cspbbr3 Perovskite Quantum Dots/Polymethyl Methacrylate Composite with High Performance. *Advanced Functional Materials* **2021,** 31, 2010009.
24. Güner, T.; Topçu, G.; Savacı, U.; Genç, A.; Turan, S.; Sari, E.; Demir, M. M., Polarized Emission from Cspbbr₃ Nanowire Embedded-Electrospun Pu Fibers. *Nanotechnology* **2018,** 29, 135202.
25. Xin, Y.; Zhao, H.; Zhang, J., Highly Stable and Luminescent Perovskite–Polymer Composites from a Convenient and Universal Strategy. *ACS Applied Materials & Interfaces* **2018,** 10, 4971-4980.
26. Brahmi, C.; Benltifa, M.; Vaulot, C.; Michelin, L.; Dumur, F.; Airoudj, A.; Morlet-Savary, F.; Raveau, B.; Bousselmi, L.; Lalevée, J., New Hybrid Perovskites/Polymer Composites for the Photodegradation of Organic Dyes. *European Polymer Journal* **2021,** 157, 110641.
27. Carrillo-Carrión, C.; del Pino, P.; Pelaz, B., Aqueous Stable Luminescent Perovskite-Polymer Composites. *Applied Materials Today* **2019,** 15, 562-569.
28. Yang, W.; Fei, L.; Gao, F.; Liu, W.; Xu, H.; Yang, L.; Liu, Y., Thermal Polymerization Synthesis of Cspbbr3 Perovskite-Quantum-Dots@Copolymer Composite: Towards Long-Term Stability and Optical Phosphor Application. *Chemical Engineering Journal* **2020,** 387, 124180.
29. Cai, Y.; Li, Y.; Wang, L.; Xie, R.-J., A Facile Synthesis of Water-Resistant Cspbbr3 Perovskite Quantum Dots Loaded Poly(Methyl Methacrylate) Composite Microspheres Based on in Situ Polymerization. *Advanced Optical Materials* **2019,** 7, 1901075.
30. Wong, Y.-C.; De Andrew Ng, J.; Tan, Z.-K., Perovskite-Initiated Photopolymerization for Singly Dispersed Luminescent Nanocomposites. *Advanced Materials* **2018,** 30, 1800774.
31. Mokbel, H.; Dumur, F.; Raveau, B.; Morlet-Savary, F.; Simonnet-Jégat, C.; Gigmes, D.; Toufaily, J.; Hamieh, T.; Fouassier, J. P.; Lalevée, J., Perovskites as New Radical Photoinitiators for Radical and Cationic Polymerizations. *Tetrahedron* **2016,** 72, 7686-7690.
32. Wu, J.; Tong, J.; Gao, Y.; Wang, A.; Zhang, T.; Tan, H.; Nie, S.; Deng, Z., Efficient and Stable Thin-Film Luminescent Solar Concentrators Enabled by near-Infrared Emission Perovskite Nanocrystals. *Angewandte Chemie International Edition* **2020,** 59, 7738-7742.
33. Yen, M.-C.; Lee, C.-J.; Liu, K.-H.; Peng, Y.; Leng, J.; Chang, T.-H.; Chang, C.-C.; Tamada, K.; Lee, Y.-J., All-Inorganic Perovskite Quantum Dot Light-Emitting Memories. *Nature Communications* **2021,** 12, 4460.
34. Zhang, J.; Frigoli, M.; Dumur, F.; Xiao, P.; Ronchi, L.; Graff, B.; Morlet-Savary, F.; Fouassier, J. P.; Gigmes, D.; Lalevée, J., Design of Novel Photoinitiators for Radical and Cationic

Photopolymerizations under near Uv and Visible Leds (385, 395, and 405 Nm). *Macromolecules* **2014,** 47, 2811-2819.
35. Hua, Y.; Crivello, J. V., Development of Polymeric Photosensitizers for Photoinitiated Cationic Polymerization. *Macromolecules* **2001,** 34, 2488-2494.
36. Kabatc, J.; Ortyl, J.; Kostrzewska, K., New Kinetic and Mechanistic Aspects of Photosensitization of Iodonium Salts in Photopolymerization of Acrylates. *RSC Advances* **2017,** 7, 41619-41629.
37. Wu, K.; Liang, G.; Shang, Q.; Ren, Y.; Kong, D.; Lian, T., Ultrafast Interfacial Electron and Hole Transfer from Cspbbr3 Perovskite Quantum Dots. *Journal of the American Chemical Society* **2015,** 137, 12792-12795.
38. Ley, C.; Christmann, J.; Ibrahim, A.; Stefano, L. H. D.; Allonas, X., Tailoring of Organic Dyes with Oxidoreductive Compounds to Obtain Photocyclic Radical Generator Systems Exhibiting Photocatalytic Behavior. *Beilstein Journal of Organic Chemistry* **2014,** 10, 936-947.
39. Soltani, R.; Katbab, A. A.; Schaumberger, K.; Gasparini, N.; Brabec, C. J.; Rechberger, S.; Spiecker, E.; Alabau, A. G.; Ruland, A.; Saha, A.; Guldi, D. M.; Sgobba, V.; Ameri, T., Light Harvesting Enhancement Upon Incorporating Alloy Structured Cdsexte1−X Quantum Dots in Dpp:Pc61bm Bulk Heterojunction Solar Cells. *Journal of Materials Chemistry C* **2017,** 5, 654-662.
40. Parobek, D.; Dong, Y.; Qiao, T.; Rossi, D.; Son, D. H., Photoinduced Anion Exchange in Cesium Lead Halide Perovskite Nanocrystals. *Journal of the American Chemical Society* **2017,** 139, 4358-4361.
41. Koolyk, M.; Amgar, D.; Aharon, S.; Etgar, L., Kinetics of Cesium Lead Halide Perovskite Nanoparticle Growth; Focusing and De-Focusing of Size Distribution. *Nanoscale* **2016,** 8, 6403-6409.
42. Cottingham, P.; Brutchey, R. L., On the Crystal Structure of Colloidally Prepared Cspbbr3 Quantum Dots. *Chemical Communications* **2016,** 52, 5246-5249.
43. Chen, J.; Liu, D.; Al-Marri, M. J.; Nuuttila, L.; Lehtivuori, H.; Zheng, K., Photo-Stability of Cspbbr3 Perovskite Quantum Dots for Optoelectronic Application. *Science China Materials* **2016,** 59, 719-727.
44. Luo, B.; Naghadeh, S. B.; Zhang, J. Z., Lead Halide Perovskite Nanocrystals: Stability, Surface Passivation, and Structural Control. *ChemNanoMat* **2017,** 3, 456-465.
45. Baranov, D.; Toso, S.; Imran, M.; Manna, L., Investigation into the Photoluminescence Red Shift in Cesium Lead Bromide Nanocrystal Superlattices. *The Journal of Physical Chemistry Letters* **2019,** 10, 655-660.
46. Liu, S.; Brunel, D.; Noirbent, G.; Mau, A.; Chen, H.; Morlet-Savary, F.; Graff, B.; Gigmes, D.; Xiao, P.; Dumur, F.; Lalevée, J., New Multifunctional Benzophenone-Based Photoinitiators with High Migration Stability and Their Applications in 3d Printing. *Materials Chemistry Frontiers* **2021,** 5, 1982-1994.
47. Lowe, A. B., Thiol-Ene “Click” Reactions and Recent Applications in Polymer and Materials Synthesis. *Polymer Chemistry* **2010,** 1, 17-36.
48. Luo, X.; Liang, G.; Han, Y.; Li, Y.; Ding, T.; He, S.; Liu, X.; Wu, K., Triplet Energy Transfer from Perovskite Nanocrystals Mediated by Electron Transfer. *Journal of the American Chemical Society* **2020,** 142, 11270-11278.
49. Tehfe, M.-A.; Lalevée, J.; Telitel, S.; Contal, E.; Dumur, F.; Gigmes, D.; Bertin, D.; Nechab, M.; Graff, B.; Morlet-Savary, F.; Fouassier, J.-P., Polyaromatic Structures as Organo-Photoinitiator Catalysts for Efficient Visible Light Induced Dual Radical/Cationic Photopolymerization and Interpenetrated Polymer Networks Synthesis. *Macromolecules* **2012,** 45, 4454-4460.
50. Lalevée, J.; Blanchard, N.; Tehfe, M.-A.; Morlet-Savary, F.; Fouassier, J. P., Green Bulb Light Source Induced Epoxy Cationic Polymerization under Air Using Tris(2,2′-Bipyridine)Ruthenium(Ii) and Silyl Radicals. *Macromolecules* **2010,** 43, 10191-10195.
51. Zhao, J.; Lalevée, J.; Lu, H.; MacQueen, R.; Kable, S. H.; Schmidt, T. W.; Stenzel, M. H.; Xiao, P., A New Role of Curcumin: As a Multicolor Photoinitiator for Polymer Fabrication under Household Uv to Red Led Bulbs. *Polymer Chemistry* **2015,** 6, 5053-5061.
52. Lalevée, J.; Gigmes, D.; Bertin, D.; Graff, B.; Allonas, X.; Fouassier, J. P., Comparative Reactivity of Aminyl and Aminoalkyl Radicals. *Chemical Physics Letters* **2007,** 438, 346-350.

53. Josephy, P. D.; Rehorek, D.; Janzen, E. G., Electron Spin Resonance Spin Trapping of Thiyl, Radicals from the Decomposition of Thionitrites. *Tetrahedron Letters* **1984,** 25, 1685-1688.
54. Ito, O.; Matsuda, M., Flash Photolysis Study for Substituent and Solvent Effects on Spin-Trapping Rates of Phenylthiyl Radicals with Nitrones. *Bulletin of the Chemical Society of Japan* **1984,** 57, 1745-1749.
55. Buettner, G. R., Spin Trapping: Esr Parameters of Spin Adducts 1474 1528v. *Free Radical Biology and Medicine* **1987,** 3, 259-303.

3.9. Supporting information

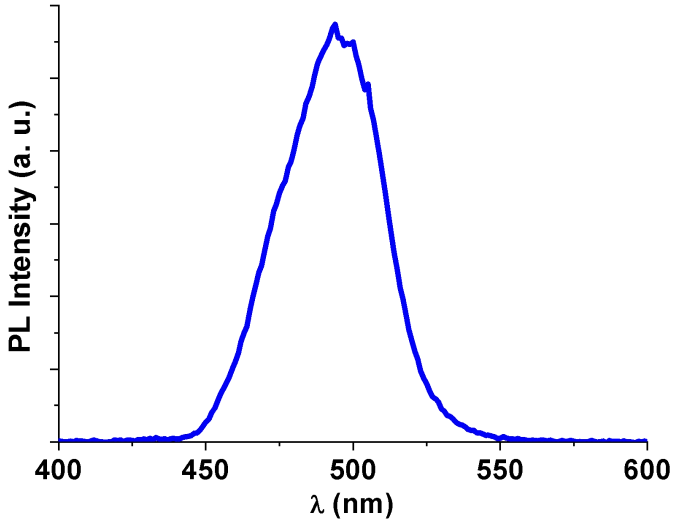

Figure S3. 1. PL spectra of $CsPbBr_3$ QDs dispersed in dichloromethane.

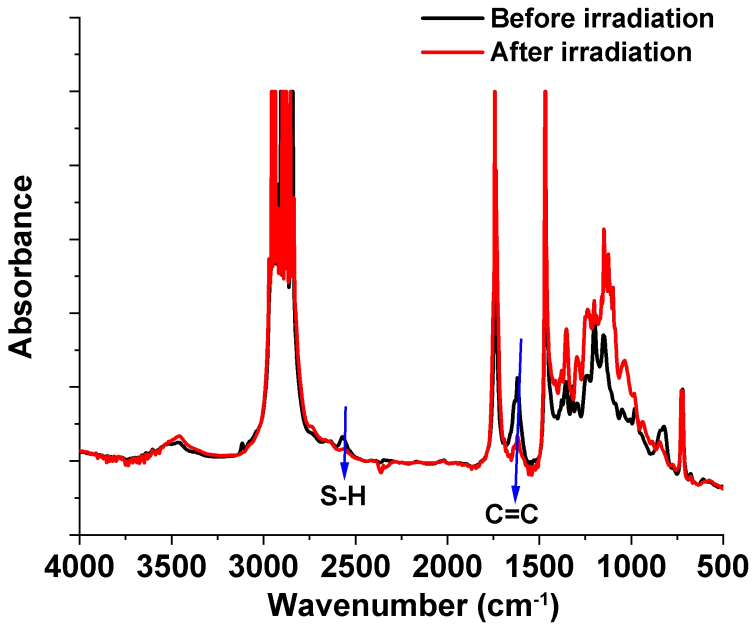

Figure S3. 2. FTIR spectra of $CsPbBr_3$ QDs/DVE-3/tetrathiol before and after photopolymerization.

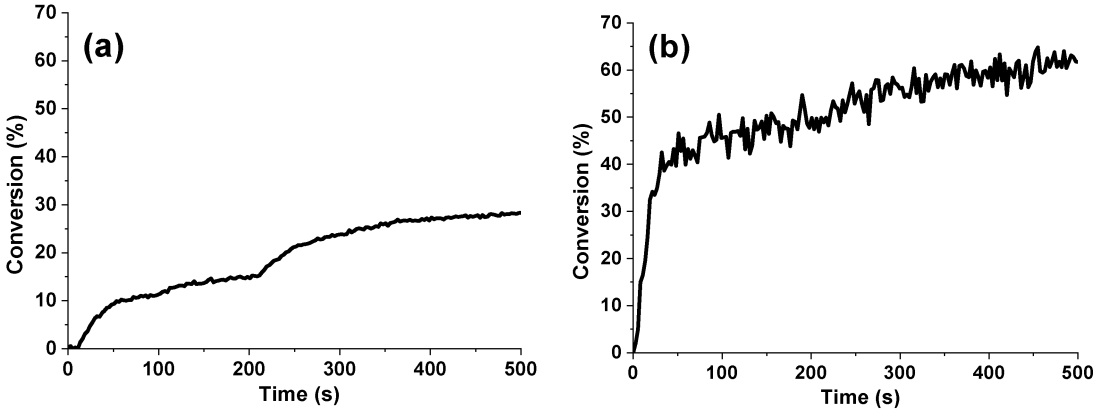

Figure S3. 3. Photopolymerization profiles of DVE-3/tetrathiol obtained in laminate upon exposure to LED@410 nm in the presence of $CsPbBr_3$ QDs [$CsPbBr_3$ QDs: 0.5 wt**%,** ene : thiol =1 : 1 in functionality]. Diagram labelled (a) represent double bond conversions vs. time; diagram labelled (b) represent thiol bond conversions vs. time.

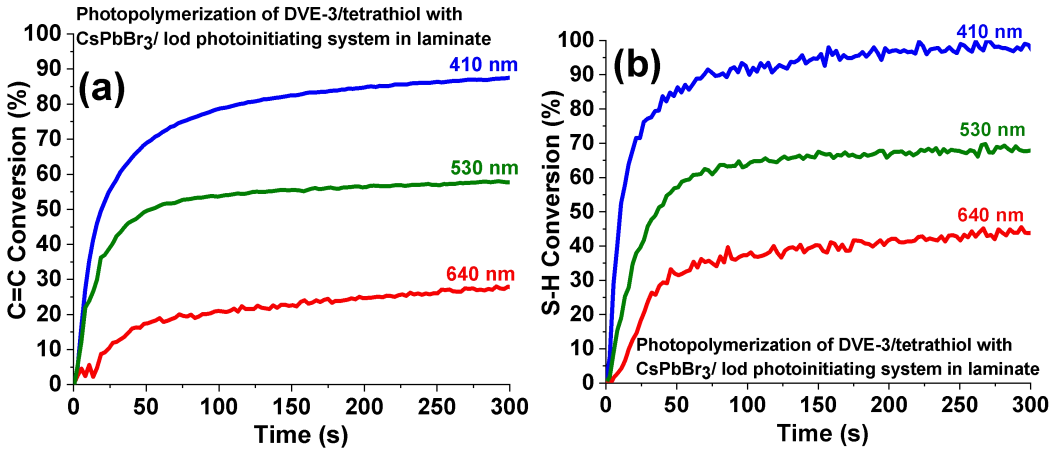

Figure S3. 4. Photopolymerization profiles of DVE-3/tetrathiol obtained in laminate upon exposure to LED@410 nm, 530 nm, and 640 nm in the presence of $CsPbBr_3$ QDs-based photoinitiating systems [$CsPbBr_3$ QDs: 0.5 wt%, Iod: 0.5 wt%; ene : thiol =1 : 1 in functionality]. Diagram labelled (a) represent double bond conversions vs. time; diagram labelled (b) represent thiol bond conversions vs. time.

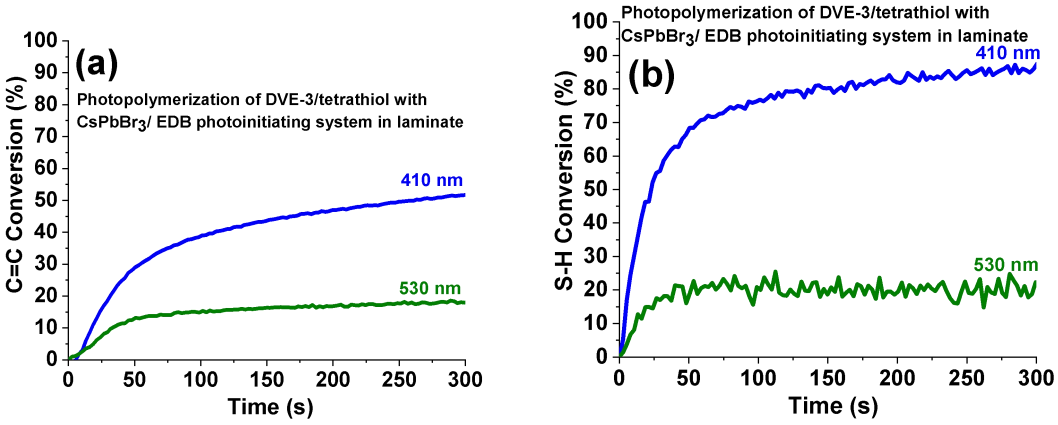

Figure S3. 5. Photopolymerization profiles of DVE-3/tetrathiol obtained in laminate upon exposure to LED@410 nm or 530 nm in the presence of $CsPbBr_3$ QDs-based photoinitiating systems [$CsPbBr_3$ QDs: 0.5 wt%, EDB: 0.5 wt%; ene : thiol =1 : 1 in functionality]. Diagram labelled (a) represent double bond conversions vs. time; diagram labelled (b) represent thiol bond conversions vs. time.

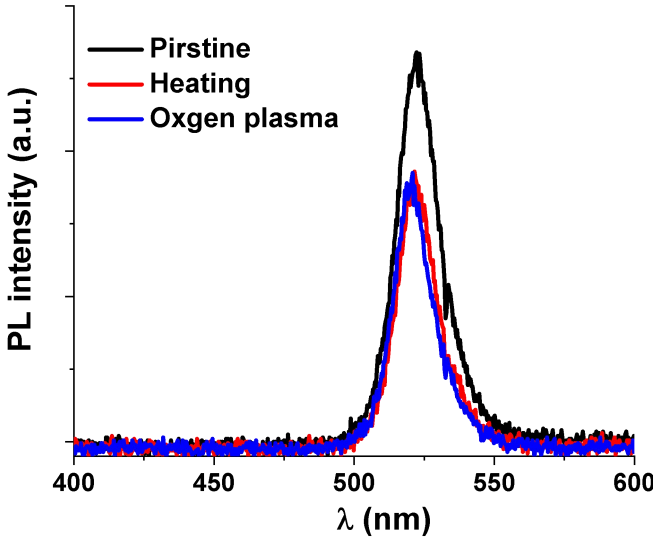

Figure S3. 6. PL spectra of photopolymerized $CsPbBr_3$ QDs/EDB/DVE-3/tetrathiol composite material under heating or oxygen plasma.

Chapter 4 Rapid Fabrication and High-Resolution 3D printing of Photopolymer/MOFs composites with Superior Selective Absorption

4.1. Preface

Beyond enhancing mechanical and optical properties, we are also interested in developing polymer nanocomposites with selective absorption capabilities. Metal-organic frameworks (MOFs) are renowned for their high surface area, tunable pore structure, and versatility, making them useful in a range of applications from catalysis to gas storage.[1-9] However, the practical use of MOFs is often limited due to their inherent fragility, susceptibility to moisture, and difficulty in processing. Integrating MOFs into polymer matrices helps to enhance their stability and mechanical properties, yet achieving effective dispersion and compatibility remains challenging.[10-12]

In this chapter, we address these challenges by functionalizing zirconium-based UiO-66 MOFs with two visible-light-sensitive photoinitiators, *N*-(1-pyrenyl)glycine (NPYG) and 2-(4-methoxystyryl)-4,6-bis(trichloromethyl)-1,3,5-triazine (triazine), creating UiO-66-NPYG and UiO-66-Tz. These modified MOFs serve a dual purpose in the thiol-ene photopolymerization process: as photoinitiators under blue LED light (410 nm) and as reinforcing fillers, which enhance the structural integrity and functionality of the resulting composites. Through experiments using real-time Fourier-transform infrared spectroscopy (RT-FTIR), the study demonstrates the photoinitiation capabilities and thick-curing potential of the UiO-66-based composites. UiO-66-NPYG enabled stable thiol-ene systems for high-resolution 3D printing, showing applications in direct laser writing. UiO-66-Tz-based composites exhibited unique selectivity for absorbing cationic dyes, indicating their potential for water treatment applications. This chapter highlights the versatility of photopolymer/MOF composites, providing a foundation for future industrial, environmental, and advanced manufacturing applications.

4.2. Statement of contribution

I declare that the research findings presented in this chapter are the original work I conducted as part of my Ph.D. program at the Australian National University. As the primary

author, I was responsible for developing the research concept, designing the experiments, analyzing the data, creating the figures, and drafting the initial manuscript, under the guidance of my primary supervisor, Prof. Pu Xiao.

4.3. Abstract

The fabrication of polymer/metal-organic framework (MOF) composites presents an innovative approach to optimizing space utilization and harnessing material properties, thereby opening up new avenues in the design and manufacturing of lightweight yet robust materials. Nevertheless, persistent hurdles exist in ensuring compatibility, stability, scalability, and in devising efficacious fabrication methodologies for tangible applications. In this research, we introduce a novel strategy for the rapid assembly of photopolymer/MOF composites utilizing visible-light-triggered photopolymerization. Specifically, two visible-light-sensitive photoinitiators, *N*-(1-pyrenyl)glycine (NPYG) and 2-(4-methoxystyryl)-4,6-bis(trichloromethyl)-1,3,5-triazine (triazine), are functionalized onto the UiO-66 MOFs, yielding UiO-66-NPYG and UiO-66-Tz. These compounds serve a dual role as both photoinitiators and fillers in the thiol-ene photopolymerization process, facilitating the creation of polymer nanocomposite materials under the irradiation of LED at 410 nm. Both UiO-66-NPYG and UiO-66-Tz exhibit remarkable photoinitiation abilities and significant potential for thick curing, thereby accelerate the production of corresponding composite materials. Furthermore, UiO-66-NPYG stabilizes the reactive thiol-ene system, enabling its application in direct laser writing, leading to high-resolution 3D printing. On the other hand, the UiO-66-Tz based polymer composite reveals exceptional selective absorption of cationic dyes over anionic dyes. This study pioneers a promising avenue for the development of photopolymer/MOF composites, showcasing their versatility and potential utility across a wide range of industrial and environmental applications.

4.4. Introduction

Metal-organic frameworks (MOFs) represent a class of highly versatile and customizable materials known for their exceptional properties and wide-ranging applications.[13-19] These materials are conceived through the orchestrated assembly of metal nodes and organic linkers, facilitating the construction of porous architectures with precise geometries. This unique structural characteristic results in a substantial surface area, greatly enhancing adsorption capacities. Additionally, the facile tunability of MOF structures makes them adaptable to diverse applications, including gas storage, separation processes, catalytic conversions, and drug delivery systems.[1-9] Typically, MOFs are synthesized by simple solvothermal or hydrothermal conditions and yield either large crystals or micro-crystalline powders.[20, 21] Despite their superior properties, MOFs come with inherent challenges, primarily owing to their powder-like nature. Their susceptibility to moisture absorption, coupled with a lack of malleability and poor processability, compromises their stability when exposed to aggressive chemicals.[10-12] Consequently, their industrial potential remains limited.

To address these limitations, MOFs are frequently integrated with polymer matrices to develop composite materials that harness the advantages of both constituents. These MOF-polymer composites, offer amplified surface areas, enhanced mechanical properties and improved processability. [22-25] Nevertheless, challenges persist, such as the compatibility between polymers and MOFs, and the dispersion of MOFs in polymer matrices. [26, 27] To enhance the interfacial interaction between MOFs and polymer matrix, previous approaches often involved complex chemical modification of MOFs, including grafting organic molecules onto MOFs [28-31] or introducing polymerizable groups into MOFs [11, 32, 33]. Nevertheless, the majority of them required tedious reaction routes and harsh

reaction conditions such as high temperatures. An alternative and more environmentally friendly approach is photopolymerization technology, offering precise spatial and temporal control. [34] For instance, zirconium-based UiO-66 MOF was modified with vinyl functional groups and was subsequently photopolymerized with thiols using 2,2-dimethoxy-2-phenylacetophenone (DMPA) as a photoinitiator under the irradiation of 365 nm UV light.[11] This process produced a mixed matrix membrane with improved mechanical properties and gas permeability. Similarly, UiO-66 with methacrylate groups was synthesized and photopolymerized with butyl methacrylate under UV irradiation. This polymerized composite membrane demonstrated an outstanding ability to separate Cr(VI) ions from water.[35] Nevertheless, these approaches involve UV irradiation, and there was a high tendency for the photoinitiators to be released as they were not immobilized on the fillers, which raised health and environmental concerns.[36, 37] Apart from cross-linkable MOFs, chromophores was utilized as the organic linkers to produce MOFs, which can successfully achieve controlled/living radical polymerization under the 520 nm irradiation.[38] Despite this, the low polymerization conversions under prolonged irradiation limited its potential industrial applications.

To address the relevant issues, the present study focused on the fabrication of two types of visible-light-sensitive photoinitiator functionalized UiO-66 MOFs as shown in Scheme 4.1 and subsequently using thiol-ene photopolymerization to yield the corresponding functional phtopolymer/MOF composites. Specifically, two blue light-sensitive photoinitiators we have studied previously, i.e., *N*-(1-pyrenyl)glycine (NPYG) and 2-(4-methoxystyryl)-4,6-bis(trichloromethyl)-1,3,5-triazine (triazine), were chosen as promising candidates for MOF modification as they exhibited excellent photoinitiation abilities for various photopolymerizations.[39, 40] Subsequently, the roles of the two modified UiO-66 MOFs were explored as photoinitiators to initiate photopolymerization reactions under LED irradiation at

410 nm, while also serving as fillers to impart diverse properties to the resulting photopolymer nanocomposite materials. Particularly, the photoinitiation abilities of UiO-66, UiO-66-NH_2, and the two modified UiO-66 for the thiol-ene photopolymerization of pentaerythritol tetrakis(3-mercaptopropionate) (tetrathiol) and Triethylenglycoldivinyl ether (DVE-3) were investigated and compared using real-time Fourier-transform infrared spectroscopy (RT-FTIR). Both UiO-66-NPYG and UiO-66-Tz demonstrated superior photoinitiation capabilities and a robust potential for thick curing, accelerating the synthesis of the respective composite materials. Additionally, UiO-66-NPYG managed to stabilize the reactive thiol-ene system, paving the way for applications in direct laser writing where high-resolution 3D printing was realized. Conversely, the polymer composite based on UiO-66-Tz showcased a remarkable selectivity in absorbing cationic dyes over anionic ones, shedding light on the potential application of the investigated modified MOFs in water treatment processes.

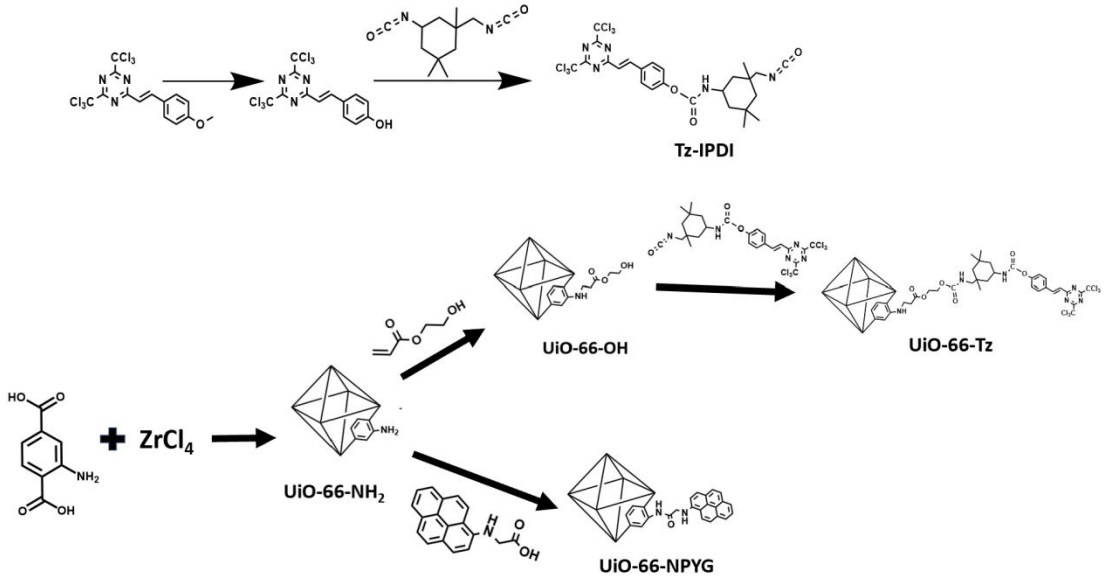

Scheme 4.1. Synthetic procedure to obtain photoinitiator-modified MOFs (UiO-66-Tz and UiO-66-NPYG).

4.5. Experimental

4.5.1. Materials

Unless specified, all chemicals were used as received. Zirconium tetrachloride, terephthalic acid (TA), 2-aminoterephthalic acid (ATA), acetic acid, 2-(4-methoxystyryl)-4,6-bis(trichloromethyl)-1,3,5-triazine (triazine), boron tribromide (BBr_3, 1 M in heptane), dichloromethane (DCM; Anhydrous), triethylamine (TEA), isophorone diisocyanate, dibutyltindilaurate (DBTL), diazabicyclo[2.2.2]octane (DABCO), 1-ethyl-3-(3-dimethylaminopropyl)carbodiimide (EDC), N-hydroxysuccinimide (NHS), diphenyliodonium hexafluorophosphate (Iod), tri(ethylene glycol) divinyl ether (DVE-3), pentaerythritol tetrakis(3-mercaptopropionate) (tetrathiol), poly(ethylene glycol) diacrylate (PEGDA, Mn = 700), 3,4-epoxycyclohexylmethyl-3',4'-epoxycyclohexane carboxylate (EPOX), methyl orange, methylene blue, and 2-hydroxyethyl acrylate were all purchased from Sigma-Aldrich. Deuterated NMR solvents (d_6-DMSO) were obtained from Cambridge Isotope Laboratories.

4.5.2. Synthesis and methods

***N*-(1-pyrenyl)glycine (NPYG).** The synthesis of NPYG was reported in our previous publication.[39] To summarize, pyrene-1-amine (0.90 g, 4.15 mmol) was dissolved in 20 mL of ethanol, concurrently bromoacetic acid (0.86 g, 6.19 mmol) was dissolved in a separate 5 mL ethanol solution. Following this, an aqueous solution of NaOH (0.25 g dissolved in 1 mL of water) was incrementally added to the bromoacetic acid solution. Subsequently, these solutions were combined and subjected to a 24-hour reflux process. After this period, the solvent was evaporated, leaving behind a residue. This residue was then purified through column chromatography, utilizing a DCM/methanol mixture (10/1, v/v) as the eluent, which resulted in a brown powder. (330 mg, 29% yield). ^{1}H NMR (300 MHz, d_6-DMSO): δ = 8.33

(d, 1H), 8.06 (m, 4H), 7.83 (m, 2H), 7.75 (d, 1H), 7.16 (d, 1H), 4.16 (s, 2H). ^{1}H NMR can be found in Figure S4.1.

4-(2-(4,6-Bis(trichloromethyl)-1,3,5-triazin-2-yl)vinyl)phenol (Demethylated Triazine). The preparation of demethylated triazine was reported in our previous publication.[40] Briefly, 2-(4-methoxystyryl)-4,6-bis(trichloromethyl)-1,3,5-triazine (triazine, 0.2 g, 0.45 mmol) dissolved in DCM (20 mL) was stirred at -78°C (immersed in dry ice and acetone mixture) with the protection of a $CaCl_2$-filled drying tube. After dropwise addition of BBr_3 (6 mL, 6 mmol) into the solution, the mixture was slowly warmed up to room temperature and stirred overnight. The solution was stirred under room temperature for another 24 h. Finally, the mixture was quenched with ice water (100 mL), extracted with DCM and subsequently dried with anhydrous sodium sulfate. Demethylated triazine was collected as yellow solid in a yield of 67%. ^{1}H NMR (400 MHz, DMSO-d_6): δ 10.37 (s, 1H), 8.36 (d, J = 15.6 Hz, 1H), 7.83 (d, J = 8.3 Hz, 2H), 7.31 (d, J = 15.7 Hz, 1H), 6.88 (d, J = 8.2 Hz, 2H). ^{1}H NMR can be found in Figure S4.2.

4-(2-(4,6-Bis(trichloromethyl)-1,3,5-triazin-2-yl)vinyl)phenyl (3-(isocyanatomethyl)-3,5,5-trimethylcyclohexyl)carbamate (Tz-IPDI). Demethylated triazine (1 g, 2.3 mmol) dissolved in toluene (30 mL) was added with IPDI (0.51 g, 2.3 mmol) and DBTL (10 uL). The mixture was heated at 60°C for 5h. The solvent was evaporated and yielded the Tz-IPDI as a yellowish paste. ^{1}H NMR (400 MHz, DMSO) δ 7.38 – 7.10 (m, 6H), 1.89 (d, J = 11.6 Hz, 2H), 1.71 – 0.60 (m, 18H). ^{1}H NMR can be found in Figure S4.3.

UiO-66. UiO-66 was prepared according to the previously reported procedure with minor modification.[41] In brief, $ZrCl_4$ (0.106 g, 0.454 mmol) and terephthalic acid (0.068 g, 0.454 mmol) were dissolved in 50 mL of DMF. Subsequently, acetic acid (0.8 g) and water (33 uL) were added to the mixture. The reaction mixture was then heated at 120°C for 21 h. The obtained white precipitate was centrifuged at 4000 r.p.m. for 30 min and washed three

times with DMF and then one time with DCM. UiO-66 was then dried in a vacuum oven at 140°C overnight.

UiO-66-NH_2. UiO-66-NH_2 was prepared according to the previously reported procedure with some modifications.[42] In brief, $ZrCl_4$ (1 g, 5.5 mmol) and 2-aminoterephthalic acid (1.29 g, 5.5 mmol) were dissolved in 100 mL of DMF with the addition of 10 g of acetic acid and 0.4 mL of water. The reaction mixture was then heated at 120°C for 21 h. The obtained pale-yellow precipitate was centrifuged at 4000 r.p.m. for 30 min and washed three times with ethanol. UiO-66-NH_2 was then dried in a vacuum oven at 140°C overnight.

UiO-66-OH. UiO-66-OH was prepared according to the previously reported procedure with some modifications.[43] In brief, UiO-66-NH_2 (1.5 g, ~5.2 mmol NH_2) and 2-hydroxyethyl acrylate (2.4 g, 0.021 mol) were dissolved in 30 mL of water. The mixture was refluxed for 20 h. The white precipitate was centrifuged at 4000 r.p.m. for 30 min and washed three times with ethanol. UiO-66-OH was then dried in a vacuum oven at 140°C overnight.

UiO-66-NPYG. UiO-66-NH_2 (270 mg, ~0.092 mmol NH_2) and NPYG (100 mg, 0.37 mmol) were dissolve in 5 mL of DMF. EDC (50 mg), NHS (40 mg) and TEA (150 uL) were added to the mixture and stirred at room temperature overnight. The yellow precipitate was centrifuged at 4000 r.p.m. for 30 min and washed three times with ethanol. UiO-66-NPYG was then dried in a vacuum oven at 100°C overnight.

UiO-66-Tz. UiO-66-OH (1 g, ~3.4 mmol OH) and Tz-IPDI (2.24 g, 3.4 mmol) were dissolved in 50 mL of toluene. A catalytic amount (10 mg) of DABCO was added to the mixture. It was heated at 60°C for 10h. The yellow precipitate was centrifuged at 4000 r.p.m. for 30 min and washed three times with DMF. UiO-66-Tz was then dried in a vacuum oven at 100°C overnight.

4.5.3. Photopolymerization Experiments.

Photopolymerization processes were analyzed using real-time Fourier transform infrared spectroscopy (RT-FTIR) with a Bruker instrument. Each photopolymerization reaction was set up in a laminate configuration, wherein a droplet of the specific formulation was positioned between two sheets of polyethylene membranes. These membranes were then compressed between two slabs of BaF_2 salt plates. The subsequent reactions were facilitated under the irradiation of a 410 nm LED light source, emitting at a light intensity of 110 mW cm^{-2}, obtained from Thorlabs. The laminates harbored samples with an estimated thickness of 25 μm. Throughout the process, the variations in bond conversions were tracked. Specifically, the thiol bond transformation within tetrathiol and the alteration in the double bond of DVE-3 were monitored within the wavenumber ranges of 2595–2535 cm^{-1} and 1660–1570 cm^{-1}, respectively. Similarly, the changes in the epoxy bond within EPOX were monitored at a wavenumber of 790 cm^{-1}. Furthermore, the double bond changes in PEGDA were observed at a distinct wavenumber of 1630 cm^{-1}. The conversions of thiol, ene, or epoxy were calculating with the following equation (1):

$$C = \frac{A_0 - A_t}{A_0} \times 100\% \qquad (1)$$

where A_0 is the initial peak area before irradiation and A_t is the peak area of the functional groups at time t.

4.5.4. Fourier-Transform Infrared Spectroscopy (FTIR)

Infrared spectra of UiO-66, UiO-66-NH_2, UiO-66-OH, UiO-66-NPYG, UiO-66-Tz, and Tz-IPDI were acquired using a Spectrum Two Fourier transform infrared (FTIR) spectrometer (Perkin Elmer) fitted with an attenuated total reflectance (ATR) accessory, which scanned with an average over a range of 500–4000 cm^{-1} at a resolution of 4 cm^{-1}.

4.5.5. Powder X-ray diffraction Analysis (PXRD)

The X-ray diffraction (XRD) patterns of all the synthesized Metal-Organic Frameworks (MOFs) were documented using an Empyrean diffractometer. This equipment was operated with CuKα radiation (λ = 1.5406 Å), employing a voltage parameter of 40 kV, coupled with a current setting of 30 mA.

4.5.6. Thermogravimetric Analysis (TGA)

Thermal analyzer TGA Q500 from TA Instruments was utilized to perform thermogravimetric analysis on the samples. Starting at room temperature, the samples were gradually heated up to 900 °C at a consistent rate of 4 °C/min, all within an air atmosphere. The measurement of mass loss during this process was used to assess the quantity of NPYG or Tz that had adhered to the surface of the UiO-66-NH_2.

4.5.7. Photorheology Test

The process of photorheology characterization was facilitated using an Anton Paar MCR 702 multidrive rheometer. These experiments were performed at a temperature of 25 °C, utilizing a plate geometry characterized as PP25 and having a diameter of 25 mm. In a precise manner, a volume of 100 µL of the liquid formulation was dispensed onto a glass plate. A plate sensor was then applied from above, pressing down until the separation between the sensor and the glass plate narrowed to a range of 0.2 to 0.4 mm. The irradiation source was positioned at the lower section of the sample holder, illuminating from the bottom upwards, passing through the sample. Concurrently, measurements were taken at the top section of the sample. This experimental setup operated at a fixed angular frequency of 1 Hz, within a shear spectrum of 0.1%. Notably, the normal force parameter was maintained at a null value (0 N) throughout the experiment, implying a potential alteration in the gap during the course of measurements due to potential shrinking of the

formulation. Throughout this procedure, changes in both the storage and loss modulus of the formulations were carefully documented, along with any variations in the gap distance between the sensor and the glass plate.

4.5.8. Direct Laser Writing

UiO-66-NH_2/PEGDA/tetrathiol and UiO-66-NPYG/PEGDA/tetrathiol were used as resins for direct laser writing using a high-resolution direct laser lithography system Dilase 650. UiO-66-NH_2/PEGDA/tetrathiol (ene: thiol = 1:1 in functionality) or UiO-66-NPYG/PEGDA/tetrathiol formulation were well mixed and a thin layer was spread on a glass slide. A laser (spot size: 10 μm) at 375 nm was used to irradiate the resins under air at a speed of 10 mm/s to allow photocuring. The detailed morphology was observed using the VEECO WYKO NT9100 optical profilometer

4.5.9. Absorption measurements

The absorption capacities of the MOFs/polymer composites produced from the photocuring of UiO-66/PEGDA/tetrathiol, UiO-66-NH_2/PEGDA/tetrathiol, and UiO-66-NPYG/PEGDA/tetrathiol for methyl orange (MO) or methylene blue (MB) under different time and initial concentrations were evaluated. Three MOFs/polymer composites prepared by photopolymerization under the irradiation of LED@410 nm were cut into small pieces with the same mass of 0.02 g. They were then added to MO or MB and remained stirring. To investigate the effect of absorption time, the MO or MB solution was measured with a UV-Vis spectrophotometer (Varian Cary 50 Bio UV–vis spectrometer from Agilent Technologies) to determine the remaining concentrations after treatment. Specifically, the UV–vis light absorptions with different known concentrations of MO or MB in water and the corresponding calibration curves were plotted in Figure S4.4-S4.6 to determine the remaining dye concentrations after absorption. In this study, the remaining concentrations

of MO or MB were determined after absorption of 30, 60, 120, 180, 1200, and 1500 min. To investigate the effect of initial concentrations, three MOFs/polymer composites with 0.02 g were added into MO or MB solution with initial concentrations of 4, 8, 50, and 120 mg/L, respectively, and remained stirring. The remaining concentrations of MO or MB were determined after 24 h of absorption. The absorption capacity was calculated with the following equation (2) [44]:

$$Absorption\ capacity = \frac{(C_0 - C_t) \times V}{W} \qquad (2)$$

where C_o and C_t (mg/L) are the initial and final concentrations of the adsorbate at equilibrium, respectively; V (L) is the volume of the adsorbate (MO or MB solution); and W (g) is the amount of adsorbent used (investigated photopolymer/MOFs composites). Moreover, the absorption isotherms were fitted and analyzed with Langmuir and Freundlich models with the following equations (3)[45] and (4)[46], respectively:

$$Absorption\ capacity = \frac{Q_m K_L C_e}{1 + K_L C_e} \qquad (3)$$

$$Absorption\ capacity = K_F C_e^{\frac{1}{n}} \qquad (4)$$

where Q_m (mg/L) was the largest monolayer adsorption capacity; C_e (mg/ L) was the equilibrium concentration of MB; K_L (L/mg) and K_F ((mg/g)/(mg)$^{1/n}$) were the constants from the adsorption isotherm model, respectively.

4.5.10. Selective absorption measurements

To evaluate the degree of selectivity, 0.02 g of MOFs/polymer composites produced from UiO-66/PEGDA/tetrathiol, UiO-66-NH_2/PEGDA/tetrathiol, or UiO-66-NPYG/PEGDA/tetrathiol were added into a 3 mL MO/MB mixed solution with a concentration of 4 mg/L for each dye. The mixture was stirred, and the remaining concentrations were determined. The competitive adsorption of anionic and cationic dyes

was discernible through the selectivity values derived from individual adsorption isotherms. The selectivity is calculated with the following equation (3) [47, 48]:

$$Selectivity_{cationic/anionic} = \frac{(Q_{cationic})}{(Q_{anionic})} \times \frac{(C_{anionic})}{(C_{cationic})} \qquad (3)$$

where Q_i and C_i (i: MO or MB) represent the adsorption capacity at equilibrium and the concentrations at equilibrium in the supernatant, respectively.

4.6. Results and discussion

4.6.1. Synthesis and characterization of modified UiO-66 MOFs

Four zirconium-based MOFs (UiO-66) were synthesized in this work. The two unmodified MOFs (UiO-66 and UiO-66-NH_2) were synthesized according to the previously reported studies, and then UiO-66-NH_2 was further modified to synthesize UiO-66-Tz and UiO-66-NPYG. [41-43, 49, 50] Specifically, UiO-66-NPYG was simply achieved by one one-step amidation reaction between UiO-66-NH_2 and NPYG, while the synthesis of UiO-66-Tz was more complicated. In detail, the UiO-66-NH_2 was first reacted with 2-hydroxyethyl acrylate via an aza-Michael addition to yield UiO-66-OH that contains a flexible OH group on the MOFs. Simultaneously, 2-(4-methoxystyryl)-4,6-bis(trichloromethyl)-1,3,5-triazine was demethylated first to reveal its OH reactive site, followed by a reaction with isophorone diisocyanate (IPDI) in the presence of a catalyst, dibutyltin dilaurate (DBTL). This specific catalyst ensures the selective reaction between -OH groups in Tz and secondary cycloaliphatic isocyanate group in IPDI [51], thereby yielding 4-(2-(4,6-bis(trichloromethyl)-1,3,5-triazin-2-yl)vinyl)phenyl (3-(isocyanatomethyl)-3,5,5-trimethylcyclohexyl)carbamate (Tz-IPDI). In the final stage, UiO-66-OH reacted with Tz-IPDI in the presence of diazabicyclo[2.2.2]octane (DABCO) to yield UiO-66-Tz. Again, this catalyst ensures the selective reaction between UiO-66-OH and the primary isocyanate groups in Tz-IPDI. [51]

The successful synthesis of various UiO-66-based MOFs was evidenced by ATR-IR spectroscopy. (Figure 4.1 and Figure S4.7). For instance, the presence of double peaks at 3473 cm^{-1} and 3359 cm^{-1} in Figure 4.1a corresponded to symmetric and asymmetric N-H stretching [52] confirming the formation of UiO-66-NH_2. The transition from double peaks (NH_2) to a single peak at ~3200-3500 cm^{-1} (corresponded to secondary amide) and transformation of C=O in NPYG (carboxylic group,1720 cm^{-1}) to C=O and C-N in UiO-66-NPYG (amide group, 1655 cm^{-1} and 1516 cm^{-1} respectively)[53] signified the formation of UiO-66-NPYG. As for Tz-IPDI, the appearance of peaks at 2258 cm^{-1} and 1724 cm^{-1} in Figure S4.7a, corresponding to N=C=O stretching and C=O stretching, confirmed the successful formation of the compound. [52] In Figure S4.7b, the vanishing of the peak at 1626 cm^{-1} (C=C stretching) and the emergence of a broad peak at 3300 cm^{-1} (OH group) provided the clear evidence of the formation of UiO-66-OH. Finally, the complete disappearance of N=C=O peak (~1720 cm^{-1}) in Figure 4.1b confirmed the formation of UiO-66-Tz.[52]

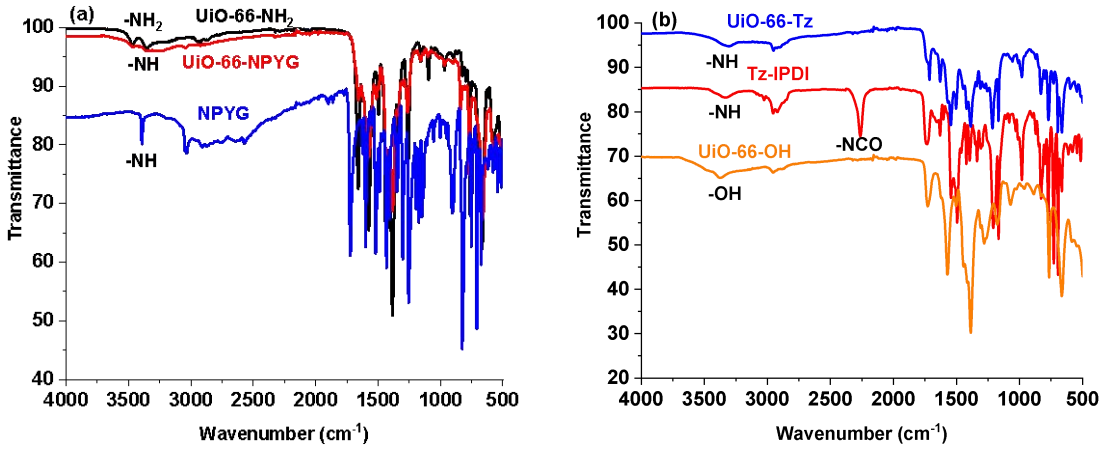

Figure 4. 1. FTIR spectra of (a) UiO-66-NH_2, NPYG, and UiO-66-NPYG and (b) UiO-66-Tz, Tz-IPDI, and UiO-66-OH.

In addition to FTIR spectroscopy analysis, the crystallographic structures of the as-synthesized MOFs were assessed using the powder X-ray diffraction (PXRD) pattern.

Interestingly, the PXRD patterns (Figure 4.2) for all the synthesized MOFs exhibited a strong correlation with the UiO-66, as evidenced by the characteristic peaks appearing at 7.4°, 8.6°, and 25.9°. These peaks indicated that they were isostructural to UiO-66 and underwent no alterations in their crystal structures.[54] This not only confirmed the porous structures of all the synthesized MOFs,[55] but also proved the high stability of these UiO-66 MOFs. This stability is particularly noteworthy, as certain MOFs may undergo decomposition under complex reaction conditions, limiting their potential applications.[56]

Thermogravimetric analysis (TGA) was then carried out to determine the amount of the photoinitiators (NPYG or Tz) that were functionalized onto the corresponding MOFs. In both of the cases (UiO-66-NPYG and UiO-66-Tz in Figure S4.8a and Figure S4.8b respectively), the weight loss below 200°C was due to the solvent vaporization while the drastic weight loss above 300°C was attributed to the decomposition of organic moieties. [57] By simply comparing the weight loss between UiO-66-NH_2 and UiO-66-NPYG or UiO-66-OH and UiO-66-Tz, the amount of NPYG or Tz grafted was calculated as 4 wt% and 3 wt% respectively.

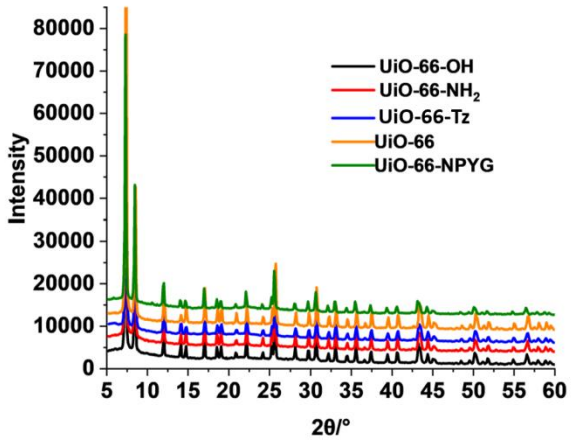

Figure 4. 2. PXRD spectra of the as-synthesized MOFs.

4.6.2. Photoinitiation ability of modified UiO-66 MOFs

To establish a control, the photoinitiation abilities of UiO-66 and UiO-66-NH_2 for the thiol-ene photopolymerization were first assessed, as illustrated in Figure 4.3. Thiol-ene photopolymerization was chosen for its superior efficiency and precision compared to other polymerization techniques. This system provides rapid polymerization under mild conditions, with excellent control over the material properties and minimal side reactions. Additionally, thiol-ene polymerization is highly tolerant to oxygen inhibition, which is often a limiting factor in other photopolymerization systems. As expected, UiO-66 was unable to initiate thiol-ene photopolymerization. Conversely, UiO-66-NH_2 effectively initiated thiol-ene photopolymerization, achieving a commendable final double conversion and thiol bond conversion of 68% and 74% respectively in laminate. This successful initiation can be attributed to the presence of amine groups in UiO-66-NH_2 compared to UiO-66, facilitating a base-catalyzed thiol-ene polymerization process.[58] To further confirm the pivotal role of the organic linker in photopolymerization, the photoinitiation abilities of the organic linker itself were also evaluated. Not surprisingly, terephthalic acid (TA, organic linker for UiO-66) was unable to initiate thiol-ene photopolymerization. Conversely, when employing 2-aminoterephthalic acid (ATA) at 0.6 wt%, equivalent to the molar amount of linker as in 1 wt% UiO-66-NH_2, we achieved double conversion and thiol bond conversions of 89% and 100% respectively in laminate. Interestingly, the utilization of ATA led to a greater photopolymerization rate compared to UiO-66-NH_2 (8.8 s^{-1} /10.2 s^{-1} and 2.7 s^{-1} /3 s^{-1} for ATA and UiO-66-NH_2, respectively; in terms of ene/thiol polymerization rate). However, it suffered from more severe oxygen inhibition. The systems initiated by ATA showed a substantial decrease in ene/thiol conversions, dropping from 89%/100% to 19%/31% when photopolymerized under air. In contrast, the systems initiated by UiO-66-NH_2 exhibited a lesser impact under similar conditions.

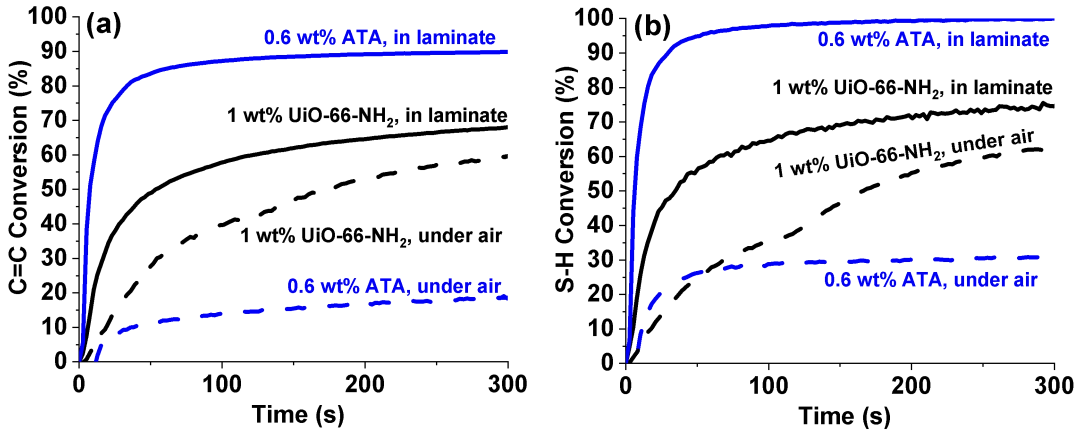

Figure 4. 3. Photopolymerization profiles of DVE-3/tetrathiol obtained in laminate/under air upon exposure to LED@410 in the presence of UiO-66-NH_2 or ATA [UiO-66-NH_2: 1 wt %; ATA: 0.6 wt %; ene/thiol = 1:1 in functionality]. The diagram labelled (a) represents double bond conversions vs. time and the diagram labelled (b) represents thiol bond conversions vs. time.

Furthermore, the photoinitiation abilities of UiO-66-NPYG and UiO-66-Tz for thiol-ene photopolymerization were then investigated, as detailed in Figure 4.4 and 4.5. As previously mentioned, the photoinitiator grafting amounts onto the MOFs are 4 wt% and 3 wt% for UiO-66-NPYG and UiO-66-Tz respectively. As shown in Figure 4.4 and Figure S4.9, with the same wt% of NPYG (0.04 wt%), UiO-66-NPYG/DVE-3/tetrathiol showed similar final conversions (90%/100% in laminate and 72%/97% under air, for ene and thiol bond conversions respectively) as the pristine NPYG/DVE-3/tetrathiol system (92%/100% in laminate and 77%/95% under air, for ene and thiol bond conversions respectively). It indicated the photoinitiation abilities of NPYG remained intact even after being grafted onto the MOFs. Notably, elevating the concentration of UiO-66-NPYG (from 1 wt% to 5 wt%) further increased the double bond conversion to 100%. This is promising, as the high filler loading typically hinders the photopolymerization process due to poor light penetration. On the other hand, in Figure 4.5, with the same wt% of Tz (0.15 wt%), UiO-66-Tz/DVE-3/tetrathiol showed a higher final conversion (98%/99% compared to 89%/94%) but slower

photopolymerization rate (5.9 s^{-1} /4.3 s^{-1} compared to 26 s^{-1} /33 s^{-1}) as compared to the pristine Tz/DVE-3/tetrathiol system. The slower photopolymerization rate may be attributed to the decreased mobility of Tz moiety in UiO-66-Tz. Nevertheless, this allowed better diffusion of UiO-66-Tz throughout the monomer system instead of being trapped in a rapidly polymerized system (the pristine Tz/DVE-3/tetrathiol system), therefore contributing to a greater final conversion. To expand the application scope of modified UiO-66 MOFs in photopolymerization, the photopolymerization abilities of UiO-66-NPYG and UiO-66-Tz were also evaluated in PEGDA (free radical photopolymerization, FRP) and EPOX systems (cationic photopolymerization, CP). As shown in Figure S4.10, both UiO-66-NPYG and UiO-66-Tz were capable of initiating FRP of PEGDA in laminate. However, the final conversions remained relatively low (< 25%). Alternatively, UiO-66-NPYG, when combined with an additive (Iod), exhibited the ability to initiate cationic photopolymerization of EPOX. These results collectively confirmed the versatility of UiO-66-NPYG and UiO-66-Tz across various types of photopolymerization reactions.

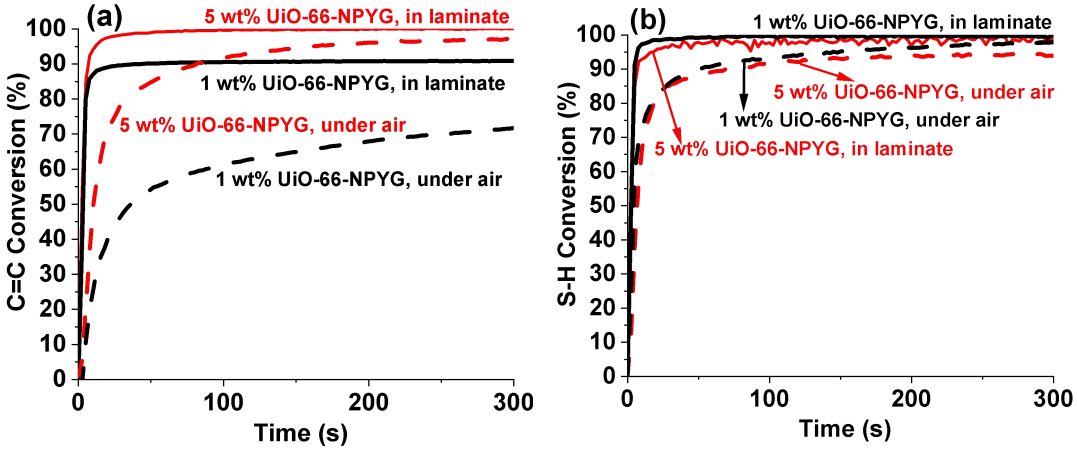

Figure 4. 4. Photopolymerization profiles of DVE-3/tetrathiol obtained in laminate/under air upon exposure to LED@410 in the presence of UiO-66-NPYG [UiO-66-NPYG: 1 wt % or 5 wt%; ene/thiol = 1:1 in functionality]. The diagram labelled (a) represents double bond conversions vs. time and the diagram labelled (b) represents thiol bond conversions vs. time.

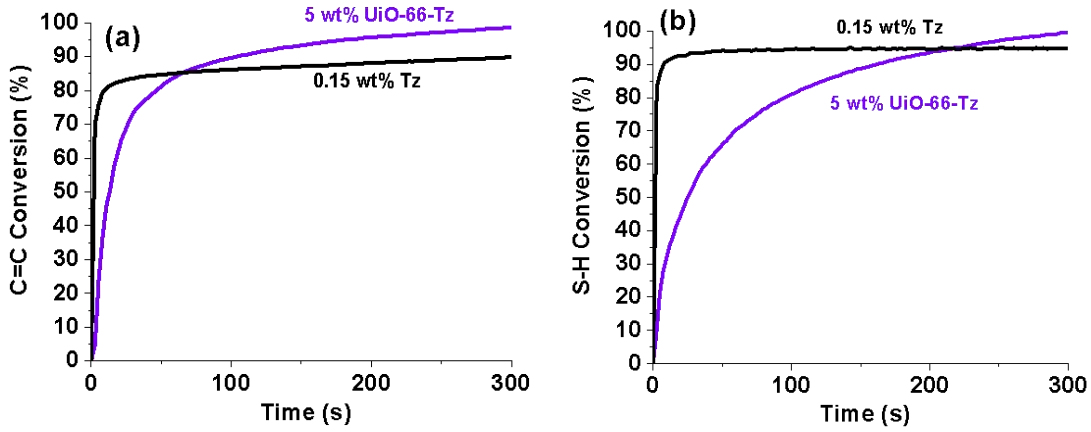

Figure 4. 5. Photopolymerization profiles of DVE-3/tetrathiol obtained in laminate upon exposure to LED@410 in the presence of UiO-66-Tz or pristine Tz [UiO-66-Tz: 5 wt%; pristine Tz: 0.15 wt%, ene/thiol = 1:1 in functionality]. The diagram labelled (a) represents double bond conversions vs. time and the diagram labelled (b) represents thiol bond conversions vs. time.

4.6.3. The potential of thick curing of modified UiO-66 MOFs

While photopolymerization offers advantages such as rapid curing and precise control, it encounters limitations when applied to thick composite structures.[59, 60] The primary impediment lies in the attenuation of light as it penetrates deeper into materials. The issue becomes even more pronounced when fillers are added, as they can reflect light, further impeding the light penetration. In the current research, the possibility of thick curing with the use of UiO-66-NPYG and UiO-66-Tz was evaluated with a photorheometer. The photorheometer setup is shown in Figure S4.11. The sensor can record the change of modulus of the pre-polymer during light irradiation. As the sensor was positioned above the sample, with irradiation emanating from the bottom, a delay of change of modulus would typically be expected when a greater gap distance (indicating a greater sample thickness) was applied. This delay occurs because the light penetration was affected and the pre-polymer that was close to the sensor was more likely to remain in liquid state instead of solid state (indicated by an increase in modulus). However, this phenomenon was not observed during the irradiation of UiO-66-NPYG/DVE-3/tetrathiol or UiO-66-Tz/DVE-3/tetrathiol. As demonstrated in Figure 4.6, even though the sample thickness increased by

a factor of 10 (UiO-66-NPYG/DVE-3/tetrathiol) or 5 (UiO-66-Tz/DVE-3/tetrathiol), the delay period remained (5-10 s) nearly constant. The only difference was the photopolymerization rate which was referred to the slope of the resultant curve. Note that the increased initial modulus in thinner samples arises from the greater confinement of the sample between the sensor and glass plate. This finding underscored the significant potential for achieving thick curing when using UiO-66-NPYG and UiO-66-Tz in photopolymerization.

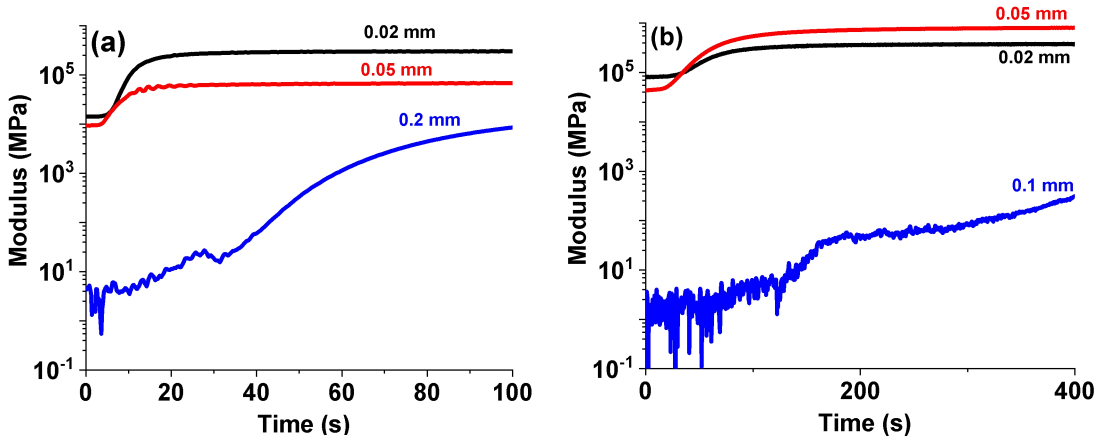

Figure 4. 6. Modulus change of (a) UiO-66-NPYG/DVE-3/tetrathiol and (b) UiO-66-Tz/DVE-3/tetrathiol during light irradiation with LED@410 nm with different gap distances (indicated to the thickness of samples).

4.6.4. Storage stability of UiO-66-NPYG/DVE-3/tetrathiol pre-polymer system and application in 3D LASER writing

Despite demonstrating favourable kinetic characteristics, thiol-ene systems often suffer from insufficient storage stability. Depending on the reactivity profiles of the utilized ene monomers and thiols, these systems may undergo gelation rapidly, sometimes within as little as 2 days or even as quickly as 12 hours. This phenomenon was observed in the case of DVE-3/tetrathiol in the presence of 1 wt% concentration of 2,2-dimethoxy-2-phenylacetophenone (DMPA), even in the absence of light irradiation.[58] A similar behavior was observed for the 0.04 wt% NPYG/DVE-3/tetrathiol system, which underwent self-polymerization within three days without any irradiation. The poor storage stability of the

thiol-ene system significantly limits their potential applications. However, the introduction of UiO-66-NPYG was found to extend the storage life of the thiol-ene system. As depicted in Figure 4.7, the photopolymerization profile of UiO-66-NPYG/DVE-3/tetrathiol following a one week of storage (black curves) closely resembled that of the freshly prepared one. Therefore, the incorporation of UiO-66-NPYG not only stabilized the otherwise unstable thiol-ene system but also maintained the excellent photoinitiation capabilities throughout the photopolymerization process.

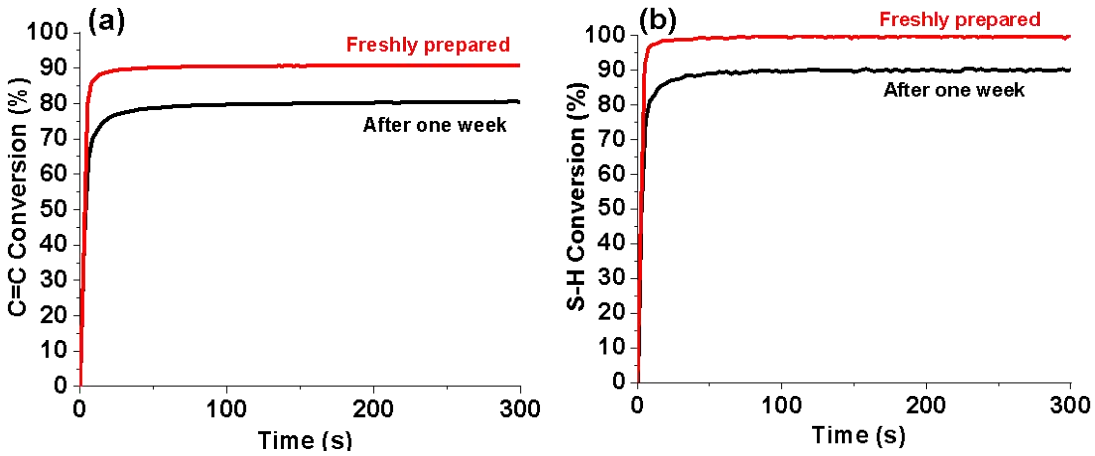

Figure 4. 7. Photopolymerization profiles of DVE-3/tetrathiol obtained in laminate upon exposure to LED@410 nm in the presence of UiO-66-NPYG [UiO-66-NPYG: 1 wt%; ene/thiol = 1:1 in functionality]. Specifically, red curves refer to samples measured as prepared, and black curves refer to samples measured after one week of storage. The diagram labelled (a) represents double bond conversions vs. time and the diagram labelled (b) represents thiol bond conversions vs. time.

The unique properties of UiO-66-NPYG therefore prompted us to explore its application in direct laser writing (DLW) application. For comparison, both UiO-66-NH_2 and UiO-66-NPYG were investigated in DLW for the photopolymerization of DVE-3/tetrathiol using a laser diode at 375 nm (spot size: 10 μm). Specifically, a repeated square block pattern was chosen as the printed model. Given the excellent photoinitiation ability and stability of UiO-66-NPYG, the corresponding 3D patterns were achieved with high spatial resolution as anticipated. Notably, the curing thickness of the printed blocks reached up to 74 μm (Figure

4.8a) and the edge of each square block were distinct and well-defined (Figure 4.8b). On the contrary, the 3D patterns of the UiO-66-NH_2/DVE-3/tetrathiol system generated by DLW exhibited poor resolution (Figure 4.8c). Specifically, it was challenging to print a block with a square shape of a certain thickness and the edge of the printed part appeared blunt (Figure 4.8d). This is due to the slow photopolymerization rate of the pre-polymer system, where the irradiated region cannot fully polymerize within a very short irradiation time. Based on these findings, UiO-66-NPYG emerges as a promising candidate for 3D printing applications, especially when dealing with unstable pre-polymer systems.

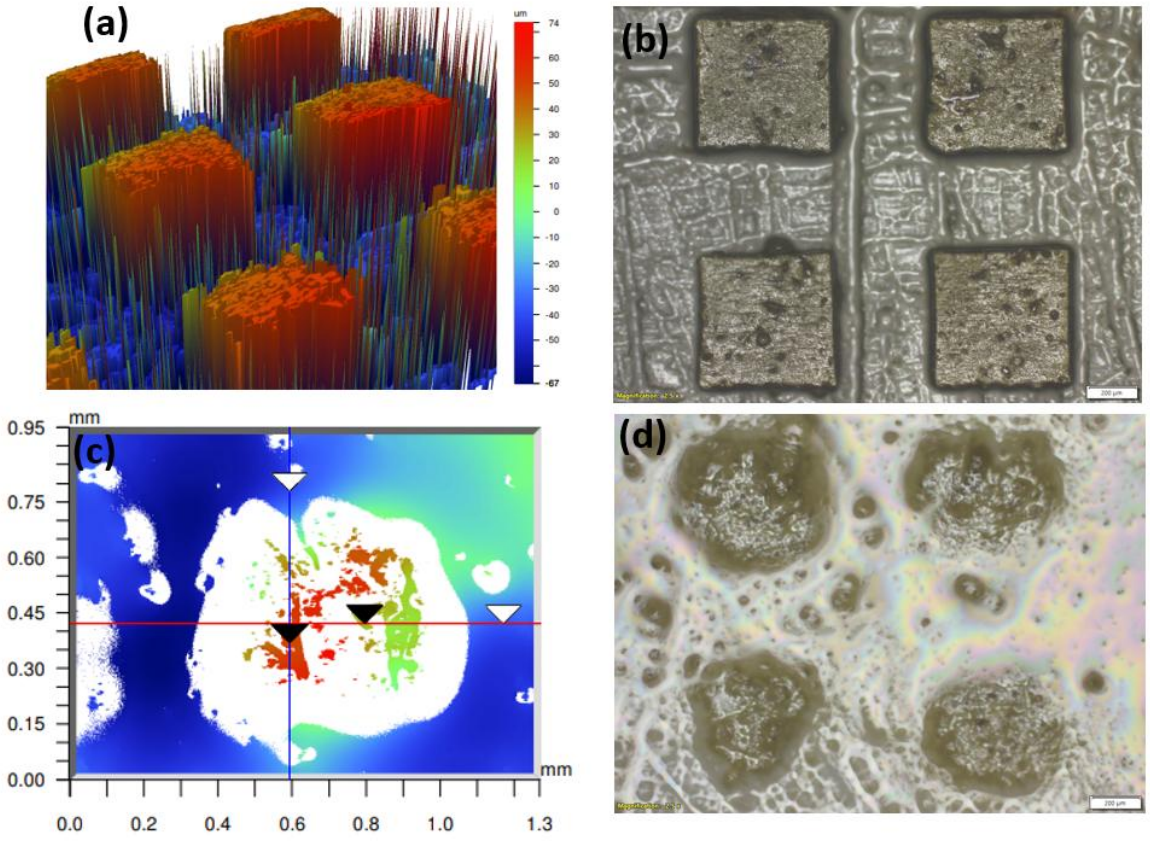

Figure 4. 8. (a) 3D surface topography of UiO-66-NPYG/DVE-3/tetrathiol based polymer composite fabricated using direct laser writing; (b) Optical microscopy image of UiO-66-NPYG/DVE-3/tetrathiol based polymer composite; (c) Surface topography of UiO-66-NH_2/DVE-3/tetrathiol based polymer composite fabricated by direct laser writing; (d) Optical microscopy image of UiO-66-NH_2/DVE-3/tetrathiol based polymer composite.

4.6.5. Absorption performance of modified UiO-66/PEGDA/tetrathiol based polymer composites

MOF polymer composites are highly valued in dye absorption applications due to their extensive surface area and adaptable adsorption properties.[61-64] By customizing the composition and structure of the composites, they can efficiently eliminate organic dyes from wastewater, presenting an eco-friendly and effective solution for water purification and environmental remediation. Here, the absorption properties of three MOF/polymer composites, i.e., UiO-66/Tz/PEGDA/tetrathiol (UiO-66: 4.85 wt%, Tz: 0.15 wt%). Pristine Tz was used since UiO-66 cannot initiate thiol-ene photopolymerization, specifically, the wt% of Tz used is the same as UiO-66-Tz/PEGDA/tetrathiol system), UiO-66-NH_2/PEGDA/tetrathiol (UiO-66-NH_2: 5 wt%), and UiO-66-Tz/PEGDA/tetrathiol (UiO-66-Tz: 5 wt%) were evaluated and compared for their abilities to absorb a cationic dye, methylene blue (MB), and an anionic dye, methyl orange (MO) in water. Specifically, three investigated MOF/polymer composites were first photopolymerized in a rectangular Teflon mold (40 x 10 x 2 mm) under irradiation of LED@410 nm for 15 min followed by cutting into a small piece with the same mass of 0.02 g for the subsequent absorption measurements. In practical adsorption applications, the contact time between adsorbents and adsorbates plays a pivotal role. Thus, the effect of contact time on dye absorption was first examined. In brief, 0.02 g of the three investigated MOF/polymer composites were immersed in 3 mL of MO (4 mg/L) or MB (4 mg/L) dye solutions (in water) and the change of absorption peaks (MO: λ_{max} = 464 nm; MB: λ_{max} = 664 nm) were monitored over varying time intervals. For the absorption capacities in MO solution as shown in Figure S4.12a, three MOFs/polymer composites showed improved absorption capacities for the first 200 min. This can be attributed to the abundance of available absorption sites initially, leading to an accelerated absorption rate and enhanced absorption capacities. However, the absorption capacities of UiO-66/Tz/PEGDA/tetrathiol and UiO-66-NH_2/PEGDA/tetrathiol exhibited a slower rate of

increase from 300 min to 1200 min compared to the first 200 min, while the absorption capacity of UiO-66-Tz/PEGDA/tetrathiol barely increased. The slowdown was due to the decrease in absorption sites and, therefore a decrease in absorption rate and capacity. The barely increased absorption capacity indicated an equilibrium or saturation condition. At 1600 min, all three MOFs/polymer composites reached the equilibrium conditions, and the absorption capacities were 0.4 mg/g, 0.25 mg/g, and 0.1 mg/g for UiO-66/Tz/PEGDA/tetrathiol, UiO-66-NH_2/PEGDA/tetrathiol, and UiO-66-Tz/PEGDA/tetrathiol, respectively. Figure S4.12b shows the absorption capacities in the MB solution. In this scenario, UiO-66/Tz/PEGDA/tetrathiol exhibited a similar absorption capacity (0.5 mg/g) on MB, while UiO-66-NH_2/PEGDA/tetrathiol and UiO-66-Tz/PEGDA/tetrathiol demonstrated greater absorption capacities on MB (0.55 mg/g and 0.55 mg/g respectively). Interestingly, the absorption capacities for MB quickly reached equilibrium/saturation for all three MOFs/polymer composites (within 200 min). This was likely due to the larger size and molecular weight of MB compared to MO, which slowed down the diffusion from the saturated exterior absorption site to the interior absorption sites.[65]

In addition to examining various contact times, capacity measurements were also performed with different initial dye concentrations under equilibrium conditions. Specifically, the impact of varying initial concentrations of MO and MB, ranging from 4 mg/L to 120 mg/L, on the absorption abilities of the MOFs/polymer composites (Figure S4.13). For all three MOFs/polymer composites, the absorption capacities for both MO and MB increased as the initial concentrations became higher. This was ascribed to the larger concentration difference between the exterior environment and interior environment, serving as a driving force that enabled greater absorption.[48, 66] Once again, the absorption capacities eventually reached saturation even with a further increase in the concentration of MB solution. To evaluate the interaction between MB and three MOFs/polymer composites, two isotherm

models were selected to fit the absorption data as shown in Figure S4.14 and Table S4.1. All three samples exhibited a closer fit with the Langmuir model, indicated by a higher R^2 values (0.99 for all three samples) compared to those of the Freundlich model (0.91 for UiO-66/Tz/PEGDA/tetrathiol and UiO-66-Tz/PEGDA/tetrathiol while 0.78 for UiO-66-NH_2/PEGDA/tetrathiol).[67] The strong fit with Langmuir models suggested that all three MOFs/polymer composites followed a monolayer absorption mechanism, where only one dye molecule can be absorbed at a single site, and no further absorption occurred once the absorption site was occupied.[68-70]

Finally, the selective absorption of three MOFs/polymer composites was evaluated using a mixture of MO and MB solution. As shown in Figure 4.9, the selectivity of MB over MO was 5, 5, and 18 for UiO-66/Tz/PEGDA/tetrathiol, UiO-66-NH_2/PEGDA/tetrathiol, and UiO-66-Tz/PEGDA/tetrathiol-based MOFs/polymer composites, respectively. The exceptional selectivity of MB over MO for UiO-66-Tz/PEGDA/tetrathiol-based MOFs/polymer composite was likely due to the presence of a larger amount of N-donor sites (triazine moiety), which enhanced the interaction with cationic dye (MB).[71]

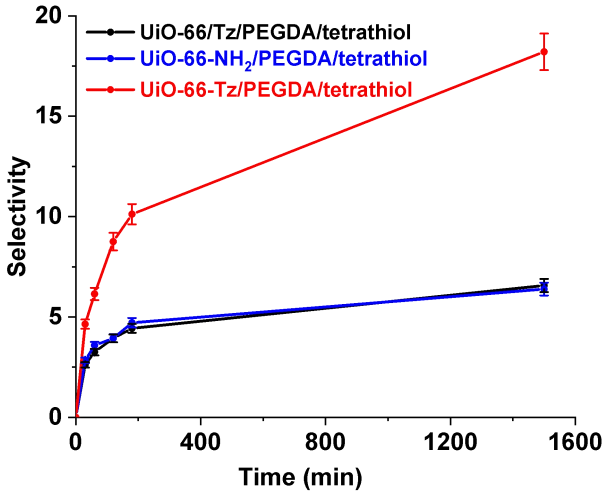

Figure 4. 9. The adsorption selectivity of MB over MO by UiO-66/Tz/PEGDA/tetrathiol, UiO-66-NH_2/PEGDA/tetrathiol, and UiO-66-Tz/PEGDA/tetrathiol based MOFs/polymer composites in a mixed MB/MO solution.

4.6.6. Recyclability of modified UiO-66/PEGDA/tetrathiol based polymer composites

In general, the regeneration and reuse of adsorbents are crucial for industrial applications. To assess the potential for reuse of UiO-66/Tz/PEGDA/tetrathiol, UiO-66-NH_2/PEGDA/tetrathiol, and UiO-66-Tz/PEGDA/tetrathiol for the MO dye over multiple cycles, the adsorbate desorption process using a 0.01 M HCl solution as eluent was examined. In brief, the dye-absorbed samples were soaked in HCl solution for 90 min, washed a few times with ethanol, and dried at 60°C for 24h then reused for the next absorption measurement.[72, 73] Generally, the absorption capacities of MOFs may slightly decrease after regeneration since there could be some trapped dyes that are not fully washed out, potentially blocking the absorption sites.[74, 75] However, when the UiO-66, UiO-66-NH_2, or UiO-66-Tz were embedded in the PEGDA/tetrathiol matrix, the resulting MOFs/polymer composites demonstrated even greater absorption capacities after three cycles (Figure 4.10). This could be attributed to the inevitable degradation of PEGDA after each round of washing, as the samples need to be washed under acidic solution with a long immersion time.[76] The degradation of polymer matrix unveiled more absorption sites and thereby resulted in the increased dye absorption capacities.

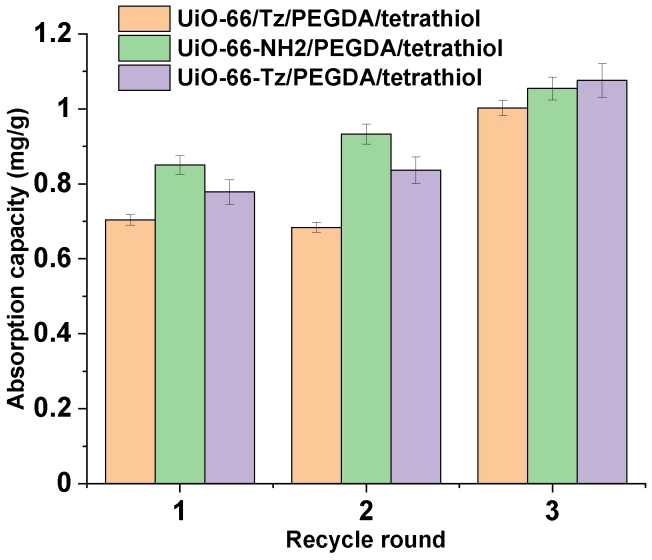

Figure 4. 10. Effect of recycle times on the adsorption capacities of MO on UiO-66/Tz/PEGDA/tetrathiol, UiO-66-NH_2/PEGDA/tetrathiol, and UiO-66-Tz/PEGDA/tetrathiol based MOFs/polymer composites.

4.7. Conclusion

In this study, two blue-light-sensitive photoinitiator-modified zirconium-based metal-organic frameworks (UiO-66 MOFs), namely UiO-66-NPYG and UiO-66-Tz, were synthesized by functionalizing *N*-(1-pyrenyl)glycine (NPYG) or 4-(2-(4,6-bis(trichloromethyl)-1,3,5-triazin-2-yl)vinyl)phenyl (3-(isocyanatomethyl)-3,5,5-trimethylcyclohexyl)carbamate (Tz-IPDI) onto UiO-66 MOFs. PXRD analysis confirmed the consistent crystalline structures of both UiO-66-NPYG and UiO-66-Tz, while TGA measurements revealed that the amounts of NPYG or Tz functionalized were 4 wt% and 3 wt%, respectively. These frameworks were then utilized to induce thiol-ene photopolymerization of DVE-3/tetrathiol under irradiation of LED@410 nm, and the polymerization kinetics were compared to those induced by free triazine or NPYG. Specifically, UiO-66-NPYG exhibited similar final conversions and photopolymerization rates compared to pristine NPYG, while UiO-66-Tz showed increased final conversions but a slower photopolymerization rate than pristine Tz when equal amounts of photoinitiator moieties were present in the formulations. More interestingly, photorheometer measurements highlighted the high potential of both UiO-66-NPYG and UiO-66-Tz for thick-curing. Notably, UiO-66-NPYG demonstrated its ability to stabilize the reactive thiol-ene system, with the pre-polymer system containing UiO-66-NPYG exhibiting similar photopolymerization kinetics (final conversions and photopolymerization rates) as the freshly prepared pre-polymer, even after a week of storage. Taking advantage of its promising photoinitiation ability and stabilization properties in the reactive thiol-ene system, UiO-66-NPYG was subsequently employed in direct laser writing applications, resulting in a 3D printed UiO-66-NPYG/DVE-3/tetrathiol polymer composite with high spatial resolution. Furthermore, the photopolymerized UiO-66-Tz/PEGDA/tetrathiol polymer composite

demonstrated the ability to absorb both anionic (methyl orange) and cationic (methylene blue) dyes, exhibiting approximately 3 times greater selectivity for the cationic dye compared to other MOF/polymer composites like UiO-66/Tz/PEGDA/tetrathiol and UiO-66-NH_2/DVE-3/tetrathiol-based ones. Overall, the developed UiO-66-NPYG and UiO-66-Tz can serve a dual purpose: as photoinitiators that trigger photopolymerization reactions under visible light and as fillers that enhance the various properties of the resulting polymer composite materials. This study paves the way for the further advancement of MOF-based photoinitiators and their integration into photopolymerization methodologies, showcasing their potential utility across a spectrum of industrial and environmental contexts.

4.8. Reference

1. Kitagawa, S.; Kitaura, R.; Noro, S.-i., Functional Porous Coordination Polymers. *Angewandte Chemie International Edition* **2004,** 43, 2334-2375.
2. Kim, C. R.; Uemura, T.; Kitagawa, S., Inorganic Nanoparticles in Porous Coordination Polymers. *Chemical Society Reviews* **2016,** 45, 3828-3845.
3. Dang, S.; Zhu, Q.-L.; Xu, Q., Nanomaterials Derived from Metal–Organic Frameworks. *Nature Reviews Materials* **2017,** 3, 17075.
4. Bindra, A. K.; Wang, D.; Zhao, Y., Metal–Organic Frameworks Meet Polymers: From Synthesis Strategies to Healthcare Applications. *Advanced Materials* **2023,** n/a, 2300700.
5. Kalaj, M.; Bentz, K. C.; Ayala, S., Jr.; Palomba, J. M.; Barcus, K. S.; Katayama, Y.; Cohen, S. M., Mof-Polymer Hybrid Materials: From Simple Composites to Tailored Architectures. *Chemical Reviews* **2020,** 120, 8267-8302.
6. Lim, J. Y. C.; Goh, L.; Otake, K.-i.; Goh, S. S.; Loh, X. J.; Kitagawa, S., Biomedically-Relevant Metal Organic Framework-Hydrogel Composites. *Biomaterials Science* **2023,** 11, 2661-2677.
7. Kalaj, M.; Denny Jr, M. S.; Bentz, K. C.; Palomba, J. M.; Cohen, S. M., Nylon–Mof Composites through Postsynthetic Polymerization. *Angewandte Chemie International Edition* **2019,** 58, 2336-2340.
8. Wang, S.; Ai, Z.; Niu, X.; Yang, W.; Kang, R.; Lin, Z.; Waseem, A.; Jiao, L.; Jiang, H.-L., Linker Engineering of Sandwich-Structured Metal–Organic Framework Composites for Optimized Photocatalytic H2 Production. *Advanced Materials* **2023,** n/a, 2302512.
9. Xu, T.; Zhang, P.; Cui, F.; Li, J.; Kan, L.; Tang, B.; Zou, X.; Liu, Y.; Zhu, G., Fine-Tuned Ultra-Microporous Metal–Organic Framework in Mixed-Matrix Membrane: Pore-Tailoring Optimization for C2h2/C2h4 Separation. *Advanced Materials* **2023,** 35, 2204553.
10. Guo, P.; Dutta, D.; Wong-Foy, A. G.; Gidley, D. W.; Matzger, A. J., Water Sensitivity in Zn4o-Based Mofs Is Structure and History Dependent. *Journal of the American Chemical Society* **2015,** 137, 2651-2657.
11. Satheeshkumar, C.; Yu, H. J.; Park, H.; Kim, M.; Lee, J. S.; Seo, M., Thiol–Ene Photopolymerization of Vinyl-Functionalized Metal–Organic Frameworks Towards Mixed-Matrix Membranes. *Journal of Materials Chemistry A* **2018,** 6, 21961-21968.
12. Ban, Y.; Cao, N.; Yang, W., Metal-Organic Framework Membranes and Membrane Reactors: Versatile Separations and Intensified Processes. *Research (Washington, D.C.)* **2020,** 2020, 1583451.
13. Furukawa, H.; Cordova, K. E.; O'Keeffe, M.; Yaghi, O. M., The Chemistry and Applications of Metal-Organic Frameworks. *Science* **2013,** 341, 1230444.
14. Yaghi, O. M.; O'Keeffe, M.; Ockwig, N. W.; Chae, H. K.; Eddaoudi, M.; Kim, J., Reticular Synthesis and the Design of New Materials. *Nature* **2003,** 423, 705-714.
15. Wang, Q.; Astruc, D., State of the Art and Prospects in Metal–Organic Framework (Mof)-Based and Mof-Derived Nanocatalysis. *Chemical Reviews* **2020,** 120, 1438-1511.
16. Introduction to Metal–Organic Frameworks. *Chemical Reviews* **2012,** 112, 673-674.
17. Qian, Y.; Zhang, F.; Kang, D. J.; Pang, H., A Review of Metal–Organic Framework-Based Compounds for Environmental Applications. *ENERGY & ENVIRONMENTAL MATERIALS* **2023,** 6, e12414.
18. Dong, P.; Zhang, X.; Hiscox, W.; Liu, J.; Zamora, J.; Li, X.; Su, M.; Zhang, Q.; Guo, X.; McCloy, J.; Song, M.-K., Toward High-Performance Metal–Organic-Framework-Based Quasi-Solid-State Electrolytes: Tunable Structures and Electrochemical Properties. *Advanced Materials* **2023,** 35, 2211841.
19. Indra, A.; Song, T.; Paik, U., Metal Organic Framework Derived Materials: Progress and Prospects for the Energy Conversion and Storage. *Advanced Materials* **2018,** 30, 1705146.
20. Zhang, W.; Bojdys, M. J.; Pinna, N., A Universal Synthesis Strategy for Tunable Metal-Organic Framework Nanohybrids**. *Angewandte Chemie International Edition* **2023,** 62, e202301021.

21. Farha, O. K.; Özgür Yazaydın, A.; Eryazici, I.; Malliakas, C. D.; Hauser, B. G.; Kanatzidis, M. G.; Nguyen, S. T.; Snurr, R. Q.; Hupp, J. T., De Novo Synthesis of a Metal–Organic Framework Material Featuring Ultrahigh Surface Area and Gas Storage Capacities. *Nature Chemistry* **2010,** 2, 944-948.
22. Denny Jr, M. S.; Cohen, S. M., In Situ Modification of Metal–Organic Frameworks in Mixed-Matrix Membranes. *Angewandte Chemie International Edition* **2015,** 54, 9029-9032.
23. Peterson, G. W.; Lu, A. X.; Hall, M. G.; Browe, M. A.; Tovar, T.; Epps, T. H., III, Mofwich: Sandwiched Metal–Organic Framework-Containing Mixed Matrix Composites for Chemical Warfare Agent Removal. *ACS Applied Materials & Interfaces* **2018,** 10, 6820-6824.
24. Gong, H.; Nguyen, T. H.; Wang, R.; Bae, T.-H., Separations of Binary Mixtures of Co2/Ch4 and Co2/N2 with Mixed-Matrix Membranes Containing Zn(Pyrz)2(Sif6) Metal-Organic Framework. *Journal of Membrane Science* **2015,** 495, 169-175.
25. Zornoza, B.; Martinez-Joaristi, A.; Serra-Crespo, P.; Tellez, C.; Coronas, J.; Gascon, J.; Kapteijn, F., Functionalized Flexible Mofs as Fillers in Mixed Matrix Membranes for Highly Selective Separation of Co2 from Ch4 at Elevated Pressures. *Chemical Communications* **2011,** 47, 9522-9524.
26. Shahid, S.; Nijmeijer, K.; Nehache, S.; Vankelecom, I.; Deratani, A.; Quemener, D., Mof-Mixed Matrix Membranes: Precise Dispersion of Mof Particles with Better Compatibility Via a Particle Fusion Approach for Enhanced Gas Separation Properties. *Journal of Membrane Science* **2015,** 492, 21-31.
27. Shen, J.; Liu, G.; Huang, K.; Li, Q.; Guan, K.; Li, Y.; Jin, W., Uio-66-Polyether Block Amide Mixed Matrix Membranes for Co2 Separation. *Journal of Membrane Science* **2016,** 513, 155-165.
28. Tien-Binh, N.; Vinh-Thang, H.; Chen, X. Y.; Rodrigue, D.; Kaliaguine, S., Polymer Functionalization to Enhance Interface Quality of Mixed Matrix Membranes for High Co2/Ch4 Gas Separation. *Journal of Materials Chemistry A* **2015,** 3, 15202-15213.
29. Wang, H.; He, S.; Qin, X.; Li, C.; Li, T., Interfacial Engineering in Metal–Organic Framework-Based Mixed Matrix Membranes Using Covalently Grafted Polyimide Brushes. *Journal of the American Chemical Society* **2018,** 140, 17203-17210.
30. Venna, S. R.; Lartey, M.; Li, T.; Spore, A.; Kumar, S.; Nulwala, H. B.; Luebke, D. R.; Rosi, N. L.; Albenze, E., Fabrication of Mmms with Improved Gas Separation Properties Using Externally-Functionalized Mof Particles. *Journal of Materials Chemistry A* **2015,** 3, 5014-5022.
31. Chang, Y.; Huang, H.; Wang, L.; Li, Y.; Zhong, C., Synergistic Dual-Li+ Sites for Co2 Separation in Metal-Organic Framework Composites. *Chemical Engineering Journal* **2020,** 402, 126201.
32. Hou, L.; Wang, L.; Zhang, N.; Xie, Z.; Dong, D., Polymer Brushes on Metal–Organic Frameworks by Uv-Induced Photopolymerization. *Polymer Chemistry* **2016,** 7, 5828-5834.
33. Chen, Z.; Yan, D.; Ma, L.; Zhang, Y.; Zhang, J.; Li, H.; Khoo, R.; Zhang, J.; Svec, F.; Lv, Y.; Tan, T., Polymerizable Metal-Organic Frameworks for the Preparation of Mixed Matrix Membranes with Enhanced Interfacial Compatibility. *iScience* **2021,** 24, 102560.
34. Yu, C.; Schimelman, J.; Wang, P.; Miller, K. L.; Ma, X.; You, S.; Guan, J.; Sun, B.; Zhu, W.; Chen, S., Photopolymerizable Biomaterials and Light-Based 3d Printing Strategies for Biomedical Applications. *Chemical reviews* **2020,** 120, 10695-10743.
35. Zhang, Y.; Feng, X.; Li, H.; Chen, Y.; Zhao, J.; Wang, S.; Wang, L.; Wang, B., Photoinduced Postsynthetic Polymerization of a Metal–Organic Framework toward a Flexible Stand-Alone Membrane. *Angewandte Chemie International Edition* **2015,** 54, 4259-4263.
36. Van Den Houwe, K.; Van Heyst, A.; Evrard, C.; Van Loco, J.; Bolle, F.; Lynen, F.; Van Hoeck, E., Migration of 17 Photoinitiators from Printing Inks and Cardboard into Packaged Food – Results of a Belgian Market Survey. *Packaging Technology and Science* **2016,** 29, 121-131.
37. Arvanitoyannis, I. S.; Kotsanopoulos, K. V., Migration Phenomenon in Food Packaging. Food–Package Interactions, Mechanisms, Types of Migrants, Testing and Relative Legislation—a Review. *Food and Bioprocess Technology* **2014,** 7, 21-36.
38. Xing, H.; Chen, D.; Li, X.; Liu, Y.; Wang, C.; Su, Z., A Visible-Light Responsive Zirconium Metal–Organic Framework for Living Photopolymerization of Methacrylates. *RSC Advances* **2016,** 6, 66444-66450.

39. Lai, H.; Zhu, D.; Peng, X.; Zhang, J.; Lalevée, J.; Xiao, P., N-Aryl Glycines as Versatile Initiators for Various Polymerizations. *Polymer Chemistry* **2021,** 12, 1991-2000.
40. Peng, X.; Zhang, J.; Stachurski, Z. H.; Banaszak Holl, M. M.; Xiao, P., Visible-Light-Sensitive Triazine-Coated Silica Nanoparticles: A Dual Role Approach to Polymer Nanocomposite Materials with Enhanced Properties. *ACS Applied Materials & Interfaces* **2021,** 13, 46033-46042.
41. Winarta, J.; Shan, B.; McIntyre, S. M.; Ye, L.; Wang, C.; Liu, J.; Mu, B., A Decade of Uio-66 Research: A Historic Review of Dynamic Structure, Synthesis Mechanisms, and Characterization Techniques of an Archetypal Metal–Organic Framework. *Crystal Growth & Design* **2020,** 20, 1347-1362.
42. Luan, Y.; Qi, Y.; Gao, H.; Andriamitantsoa, R. S.; Zheng, N.; Wang, G., A General Post-Synthetic Modification Approach of Amino-Tagged Metal–Organic Frameworks to Access Efficient Catalysts for the Knoevenagel Condensation Reaction. *Journal of Materials Chemistry A* **2015,** 3, 17320-17331.
43. Amer Hamzah, H.; Crickmore, T. S.; Rixson, D.; Burrows, A. D., Post-Synthetic Modification of Zirconium Metal–Organic Frameworks by Catalyst-Free Aza-Michael Additions. *Dalton Transactions* **2018,** 47, 14491-14496.
44. Torad, N. L.; Salunkhe, R. R.; Li, Y.; Hamoudi, H.; Imura, M.; Sakka, Y.; Hu, C.-C.; Yamauchi, Y., Electric Double-Layer Capacitors Based on Highly Graphitized Nanoporous Carbons Derived from Zif-67. *Chemistry – A European Journal* **2014,** 20, 7895-7900.
45. Langmuir, I., The Constitution and Fundamental Properties of Solids and Liquids. Part I. Solids. *Journal of the American Chemical Society* **1916,** 38, 2221-2295.
46. Freundlich, H. J. J. P. c., Over the Adsorption in Solution. **1906,** 57, 1100-1107.
47. Usman, M. A.; Khan, A. Y., Selective Adsorption of Anionic Dye from Wastewater Using Polyethyleneimine Based Macroporous Sponge: Batch and Continuous Studies. *Journal of Hazardous Materials* **2022,** 428, 128238.
48. Hu, P.; Zhao, Z.; Sun, X.; Muhammad, Y.; Li, J.; Chen, S.; Pang, C.; Liao, T.; Zhao, Z., Construction of Crystal Defect Sites in N-Coordinated Uio-66 Via Mechanochemical in-Situ N-Doping Strategy for Highly Selective Adsorption of Cationic Dyes. *Chemical Engineering Journal* **2019,** 356, 329-340.
49. Kandiah, M.; Nilsen, M. H.; Usseglio, S.; Jakobsen, S.; Olsbye, U.; Tilset, M.; Larabi, C.; Quadrelli, E. A.; Bonino, F.; Lillerud, K. P., Synthesis and Stability of Tagged Uio-66 Zr-Mofs. *Chemistry of Materials* **2010,** 22, 6632-6640.
50. Jrad, A.; Abu Tarboush, B. J.; Hmadeh, M.; Ahmad, M., Tuning Acidity in Zirconium-Based Metal Organic Frameworks Catalysts for Enhanced Production of Butyl Butyrate. *Applied Catalysis A: General* **2019,** 570, 31-41.
51. Lomölder, R.; Plogmann, F.; Speier, P., Selectivity of Isophorone Diisocyanate in the Urethane Reaction Influence of Temperature, Catalysis, and Reaction Partners. *Journal of Coatings Technology* **1997,** 69, 51-57.
52. Coates, J., Interpretation of Infrared Spectra, a Practical Approach. In *Encyclopedia of Analytical Chemistry*, 2006.
53. Singh, B. R., Basic Aspects of the Technique and Applications of Infrared Spectroscopy of Peptides and Proteins. In *Infrared Analysis of Peptides and Proteins*, American Chemical Society: 1999; Vol. 750, pp 2-37.
54. Shi, J.; Chen, F.; Hou, L.; Li, G.; Li, Y.; Guan, X.; Liu, H.; Guo, L., Eosin Y Bidentately Bridged on Uio-66-Nh2 by Solvothermal Treatment Towards Enhanced Visible-Light-Driven Photocatalytic H2 Production. *Applied Catalysis B: Environmental* **2021,** 280, 119385.
55. Cavka, J. H.; Jakobsen, S.; Olsbye, U.; Guillou, N.; Lamberti, C.; Bordiga, S.; Lillerud, K. P., A New Zirconium Inorganic Building Brick Forming Metal Organic Frameworks with Exceptional Stability. *Journal of the American Chemical Society* **2008,** 130, 13850-13851.
56. Ahmad, B. I. Z.; Keasler, K. T.; Stacy, E. E.; Meng, S.; Hicks, T. J.; Milner, P. J., Mofganic Chemistry: Challenges and Opportunities for Metal–Organic Frameworks in Synthetic Organic Chemistry. *Chemistry of Materials* **2023,** 35, 4883-4896.
57. Kim, M.-K.; Kim, S. H.; Park, M.; Ryu, S. G.; Jung, H., Degradation of Chemical Warfare Agents over Cotton Fabric Functionalized with Uio-66-Nh2. *RSC Advances* **2018,** 8, 41633-41638.

58. Tan, S.; Li, D.; Zhang, Y.; Niu, Z.; Zhang, Z., Base Catalyzed Thiol–Ene Click Chemistry toward Inner Ch Cf Bonds for Controlled Functionalization of Poly(Vinylidene Fluoride). *Macromolecular Chemistry and Physics* **2018,** 219, 1700632.
59. Kardar, P.; Ebrahimi, M.; Bastani, S., Uv Curing Behavior and Mechanical Properties of Unpigmented and Pigmented Epoxy Acrylate/Sio2 Nanocomposites. *Journal of Thermal Analysis and Calorimetry* **2016,** 124, 1425-1430.
60. Jandt, K. D.; Mills, R. W., A Brief History of Led Photopolymerization. *Dental Materials* **2013,** 29, 605-617.
61. Hasegawa, S.; Horike, S.; Matsuda, R.; Furukawa, S.; Mochizuki, K.; Kinoshita, Y.; Kitagawa, S., Three-Dimensional Porous Coordination Polymer Functionalized with Amide Groups Based on Tridentate Ligand: Selective Sorption and Catalysis. *Journal of the American Chemical Society* **2007,** 129, 2607-2614.
62. Putra Hidayat, A. R.; Zulfa, L. L.; Widyanto, A. R.; Abdullah, R.; Kusumawati, Y.; Ediati, R., Selective Adsorption of Anionic and Cationic Dyes on Mesoporous Uio-66 Synthesized Using a Template-Free Sonochemistry Method: Kinetic, Isotherm and Thermodynamic Studies. *RSC Advances* **2023,** 13, 12320-12343.
63. Khan, N. A.; Hasan, Z.; Jhung, S. H., Adsorptive Removal of Hazardous Materials Using Metal-Organic Frameworks (Mofs): A Review. *Journal of Hazardous Materials* **2013,** 244-245, 444-456.
64. Hasan, Z.; Jhung, S. H., Removal of Hazardous Organics from Water Using Metal-Organic Frameworks (Mofs): Plausible Mechanisms for Selective Adsorptions. *Journal of Hazardous Materials* **2015,** 283, 329-339.
65. Jia, Y.; Ding, L.; Ren, P.; Zhong, M.; Ma, J.; Fan, X., Performances and Mechanism of Methyl Orange and Congo Red Adsorbed on the Magnetic Ion-Exchange Resin. *Journal of Chemical & Engineering Data* **2020,** 65, 725-736.
66. Qiu, J.; Feng, Y.; Zhang, X.; Jia, M.; Yao, J., Acid-Promoted Synthesis of Uio-66 for Highly Selective Adsorption of Anionic Dyes: Adsorption Performance and Mechanisms. *Journal of Colloid and Interface Science* **2017,** 499, 151-158.
67. Cheng, S.; Xie, P.; Yu, Z.; Gu, R.; Su, Y., Enhanced Adsorption Performance of Uio-66 Via Modification with Functional Groups and Integration into Hydrogels. *Environmental Research* **2022,** 212, 113354.
68. Li, X.; Li, Y.; Ye, Z., Preparation of Macroporous Bead Adsorbents Based on Poly(Vinyl Alcohol)/Chitosan and Their Adsorption Properties for Heavy Metals from Aqueous Solution. *Chemical Engineering Journal* **2011,** 178, 60-68.
69. Ali, R. M.; Hamad, H. A.; Hussein, M. M.; Malash, G. F., Potential of Using Green Adsorbent of Heavy Metal Removal from Aqueous Solutions: Adsorption Kinetics, Isotherm, Thermodynamic, Mechanism and Economic Analysis. *Ecological Engineering* **2016,** 91, 317-332.
70. Kalam, S.; Abu-Khamsin, S. A.; Kamal, M. S.; Patil, S., Surfactant Adsorption Isotherms: A Review. *ACS Omega* **2021,** 6, 32342-32348.
71. Li, B. N.; Zhang, X. L.; Bai, X. H.; Liang, Z. J.; Li, J.; Fan, X. Y., Electron-Rich Triazine-Conjugated Microporous Polymers for the Removal of Dyes from Wastewater. *Molecules* **2023,** 28.
72. Zhao, R.; Ma, T.; Zhao, S.; Rong, H.; Tian, Y.; Zhu, G., Uniform and Stable Immobilization of Metal-Organic Frameworks into Chitosan Matrix for Enhanced Tetracycline Removal from Water. *Chemical Engineering Journal* **2020,** 382, 122893.
73. Yang, D.; Qiu, L.; Yang, Y., Efficient Adsorption of Methyl Orange Using a Modified Chitosan Magnetic Composite Adsorbent. *Journal of Chemical & Engineering Data* **2016,** 61, 3933-3940.
74. Ahmadijokani, F.; Mohammadkhani, R.; Ahmadipouya, S.; Shokrgozar, A.; Rezakazemi, M.; Molavi, H.; Aminabhavi, T. M.; Arjmand, M., Superior Chemical Stability of Uio-66 Metal-Organic Frameworks (Mofs) for Selective Dye Adsorption. *Chemical Engineering Journal* **2020,** 399, 125346.
75. Abo El Naga, A. O.; Shaban, S. A.; El Kady, F. Y. A., Metal Organic Framework-Derived Nitrogen-Doped Nanoporous Carbon as an Efficient Adsorbent for Methyl Orange Removal from Aqueous Solution. *Journal of the Taiwan Institute of Chemical Engineers* **2018,** 93, 363-373.
76. Stillman, Z. S.; Jarai, B. M.; Raman, N.; Patel, P.; Fromen, C. A., Degradation Profiles of Poly(Ethylene Glycol) Diacrylate (Pegda)-Based Hydrogel Nanoparticles. *Polym Chem* **2020,** 11, 568-580.

4.9. Supporting information

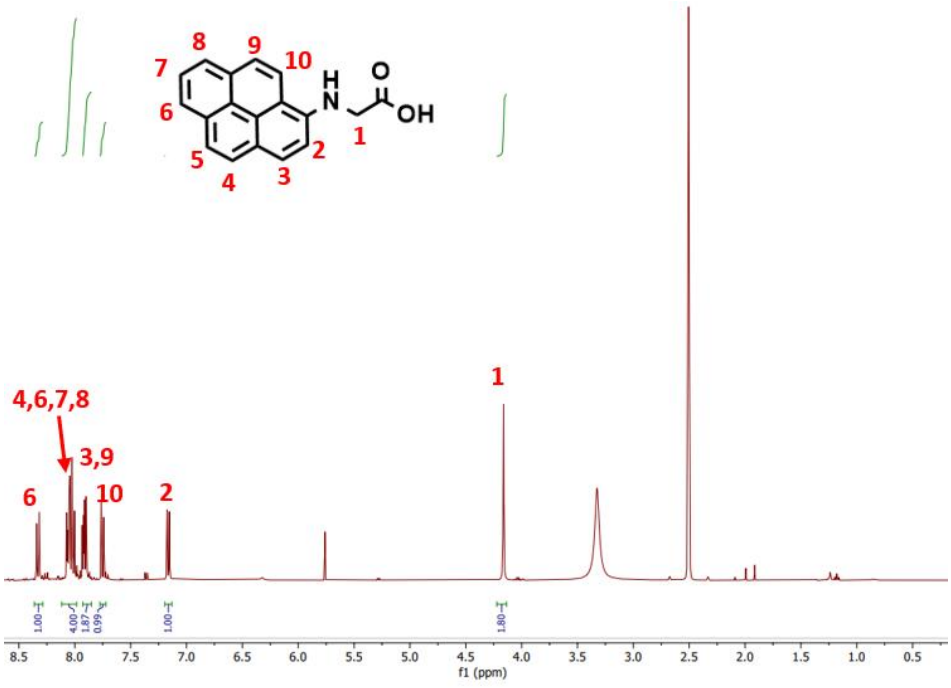

Figure S4. 1. ^{1}H NMR of *N*-(1-pyrenyl)glycine (NPYG) in d_6-DMSO (400 MHz).

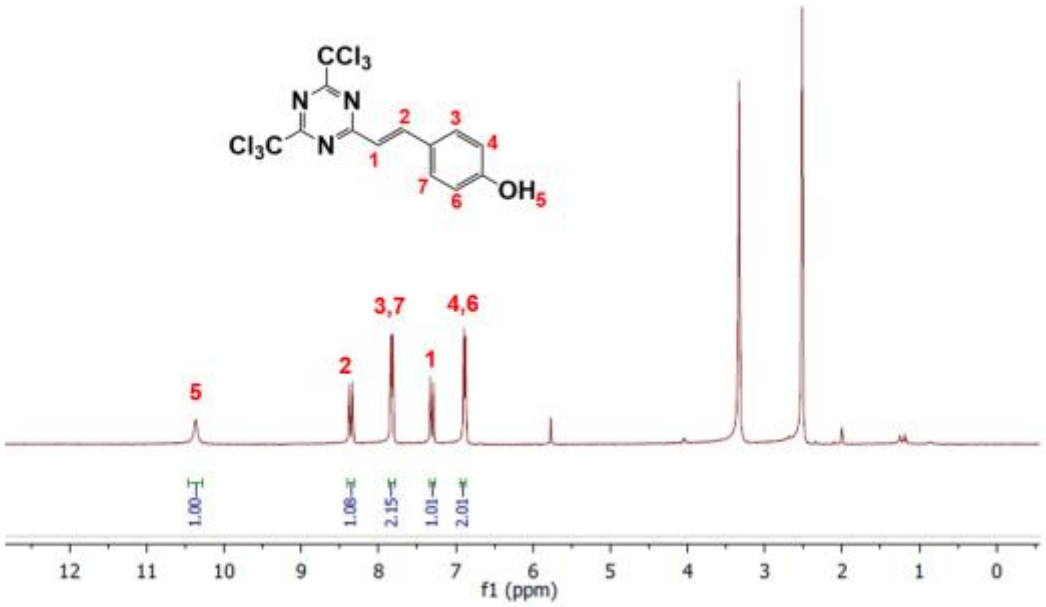

Figure S4. 2. ^{1}H NMR of 4-(2-(4,6-bis(trichloromethyl)-1,3,5-triazin-2-yl)vinyl)phenol (demethylated triazine) in d_6-DMSO (400 MHz).

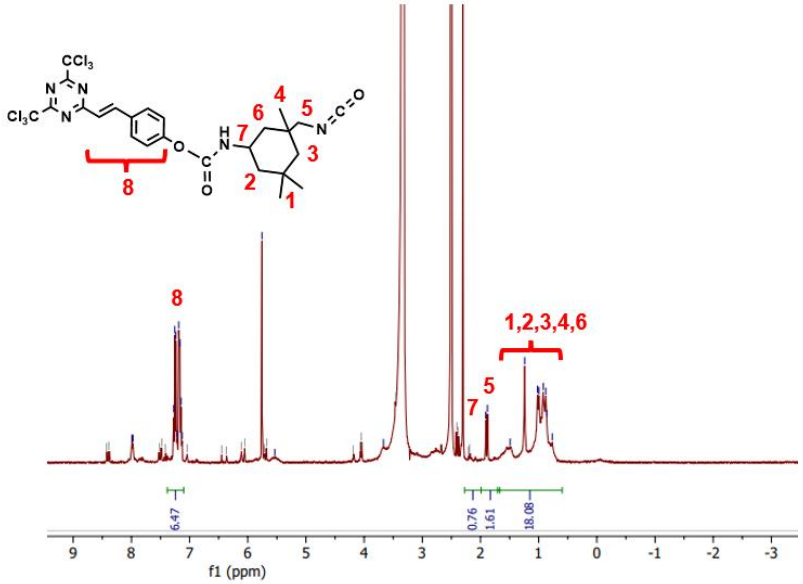

Figure S4. 3. ^{1}H NMR of 4-(2-(4,6-bis(trichloromethyl)-1,3,5-triazin-2-yl)vinyl)phenyl (3-(isocyanatomethyl)-3,5,5-trimethylcyclohexyl)carbamate (Tz-IPDI) in d_6-DMSO (400 MHz).

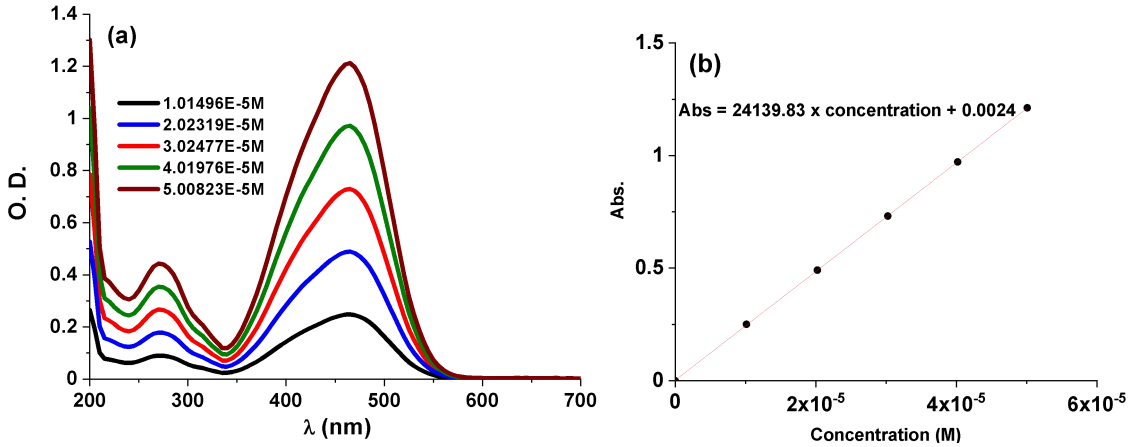

Figure S4. 4. (a) UV-vis spectra of different concentrations of methyl orange (MO) in water; (b) Calibration curve of methyl orange concentration vs absorbance in water.

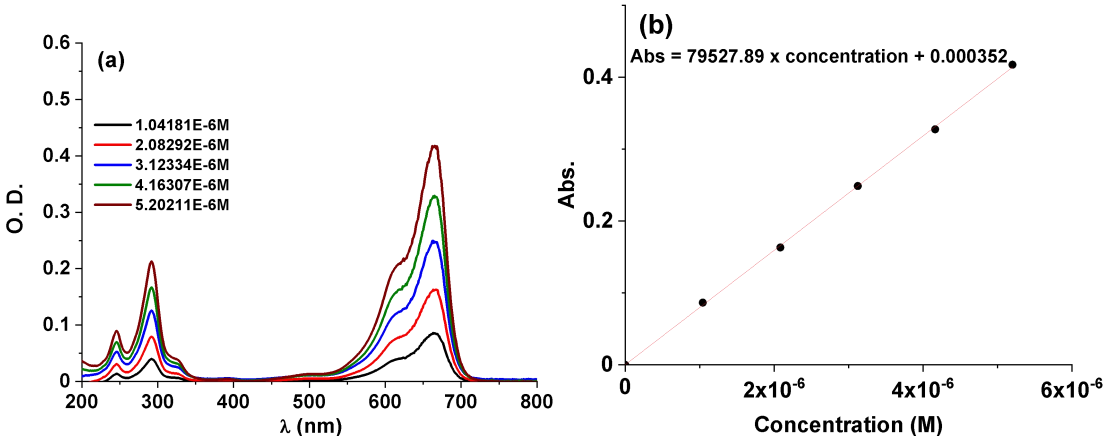

Figure S4. 5. (a) UV-vis spectra of different concentrations of methylene blue (MB) in water; (b) Calibration curve of methylene blue concentration vs absorbance in water.

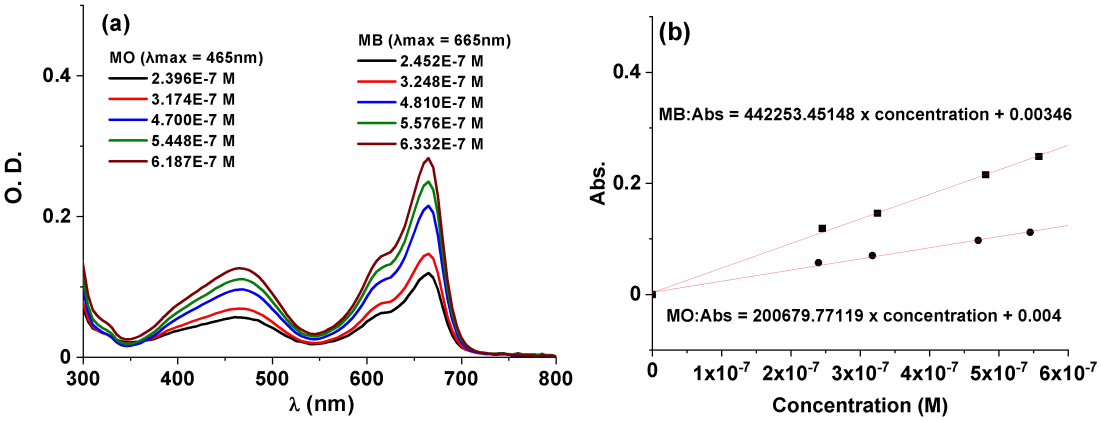

Figure S4. 6. (a) UV-vis spectra of different concentrations of mixed methyl orange and methylene in water; (b) Calibration curve of methyl orange/methylene blue concentration vs absorbance in water.

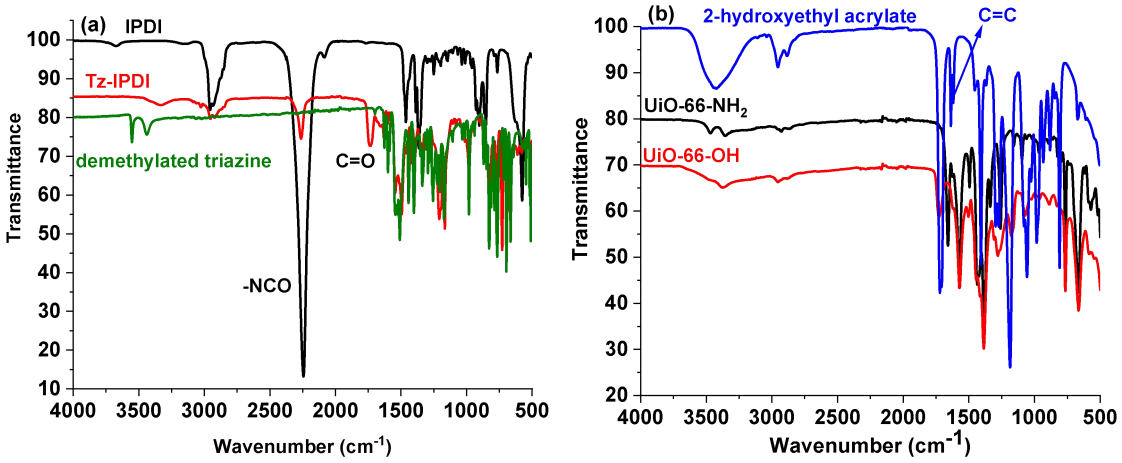

Figure S4. 7. FTIR spectra of (a) IPDI, Tz-IPDI, and demethylated triazine and (b) 2-hydroxyethyl acrylate, UiO-66-NH_2, and UiO-66-OH.

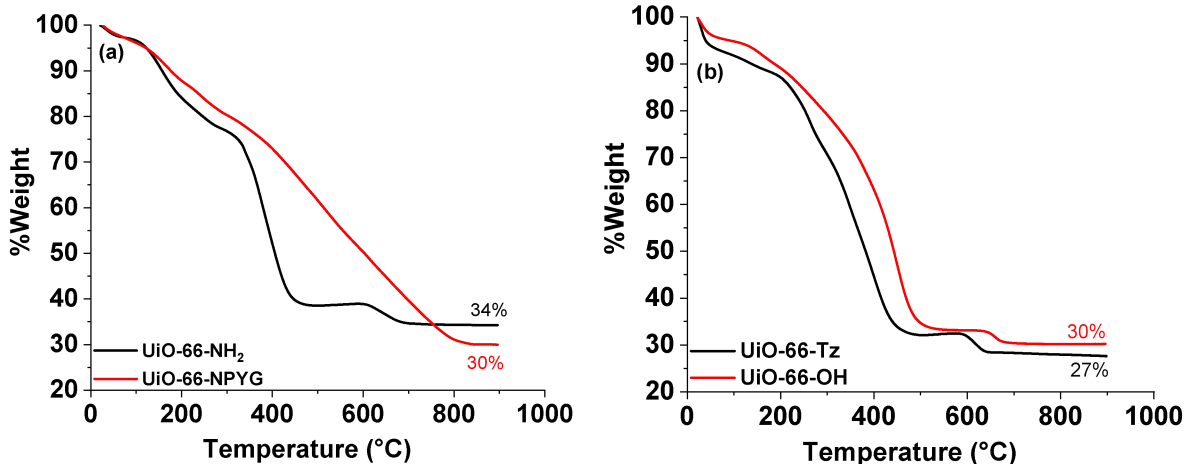

Figure S4. 8. TGA curves of (a) UiO-66-NH_2 and UiO-66-NPYG and (b) UiO-66-OH and UiO-66-Tz.

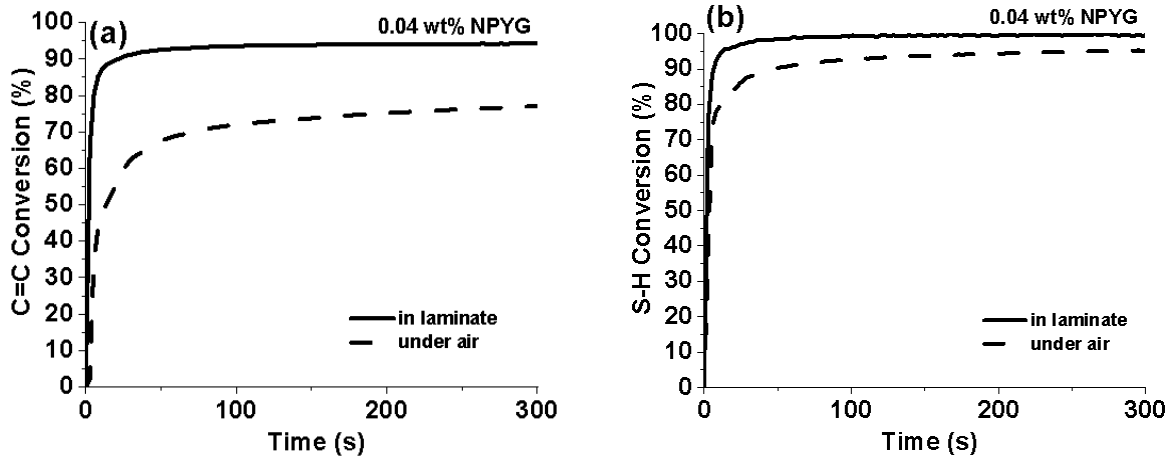

Figure S4. 9. Photopolymerization profiles of DVE-3/tetrathiol obtained in laminate/under air upon exposure to LED@410 in the presence of NPYG [NPYG: 0.04 wt %; ene/thiol = 1:1 in

functionality]. The diagram labelled (a) represents double bond conversions vs time and the diagram labelled (b) represents thiol bond conversions vs time.

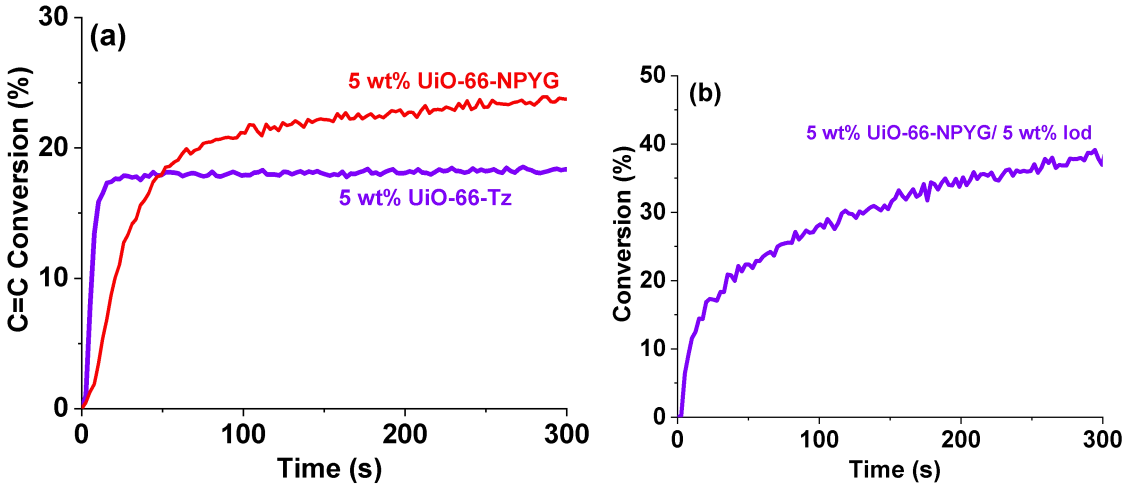

Figure S4. 10. Photopolymerization profiles of (a) PEGDA obtained in laminate upon exposure to LED@410 in the presence of UiO-66-NPYG or UiO-66-Tz [UiO-66-NPYG: 5 wt %; UiO-66-Tz: 5 wt %]; (b) EPOX obtained under air upon exposure to LED@410 in the presence of UiO-66-NPYG and Iod [UiO-66-NPYG: 5 wt %; Iod: 5 wt %]

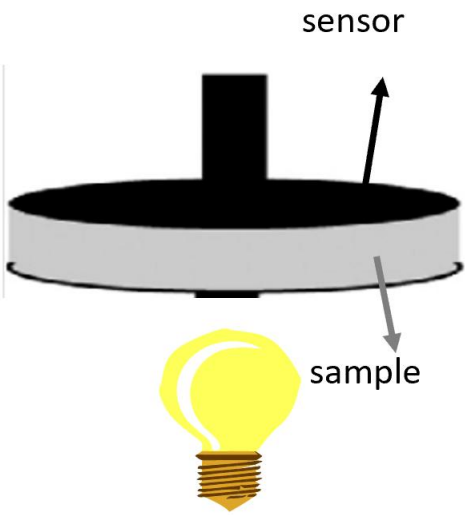

Figure S4. 11. Indication of photorheometer setup.

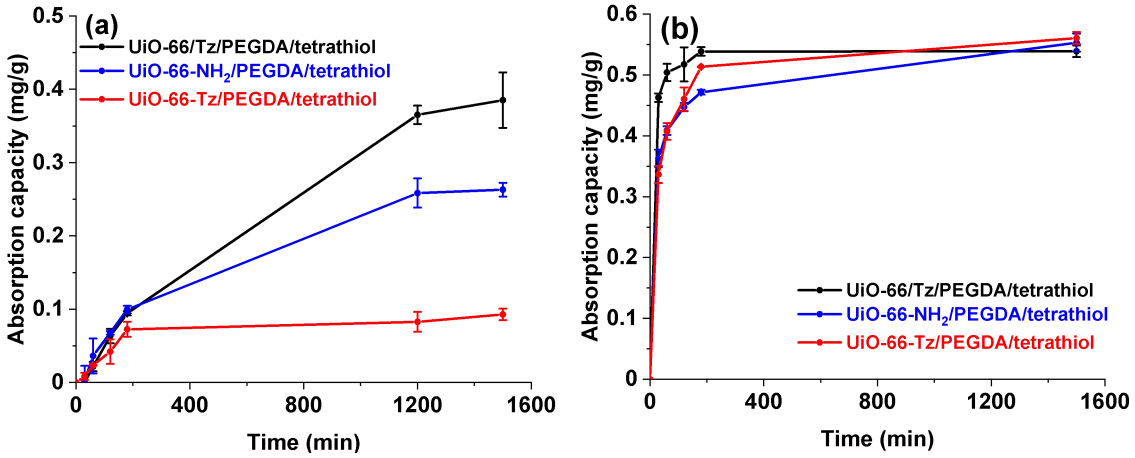

Figure S4. 12. Effect of (a) MO and (b) MB adsorption time on the absorption capacities of UiO-66/Tz/PEGDA/tetrathiol, UiO-66-NH_2/PEGDA/tetrathiol, and UiO-66-Tz/PEGDA/tetrathiol.

,

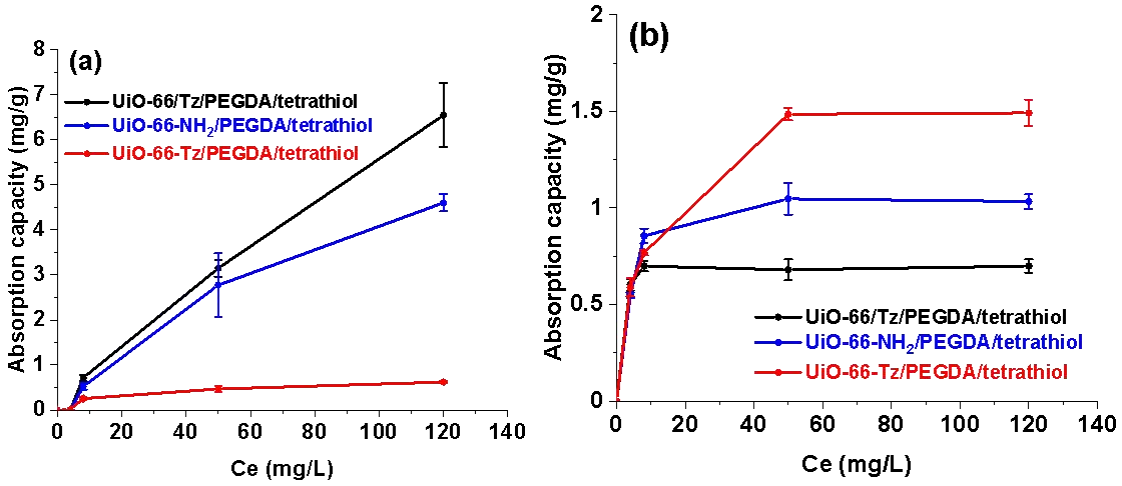

Figure S4. 13. Effect of initial concentrations of (a) MO and (b) MB on the absorption capacities of UiO-66/Tz/PEGDA/tetrathiol, UiO-66-NH_2/PEGDA/tetrathiol, and UiO-66-Tz/PEGDA/tetrathiol.

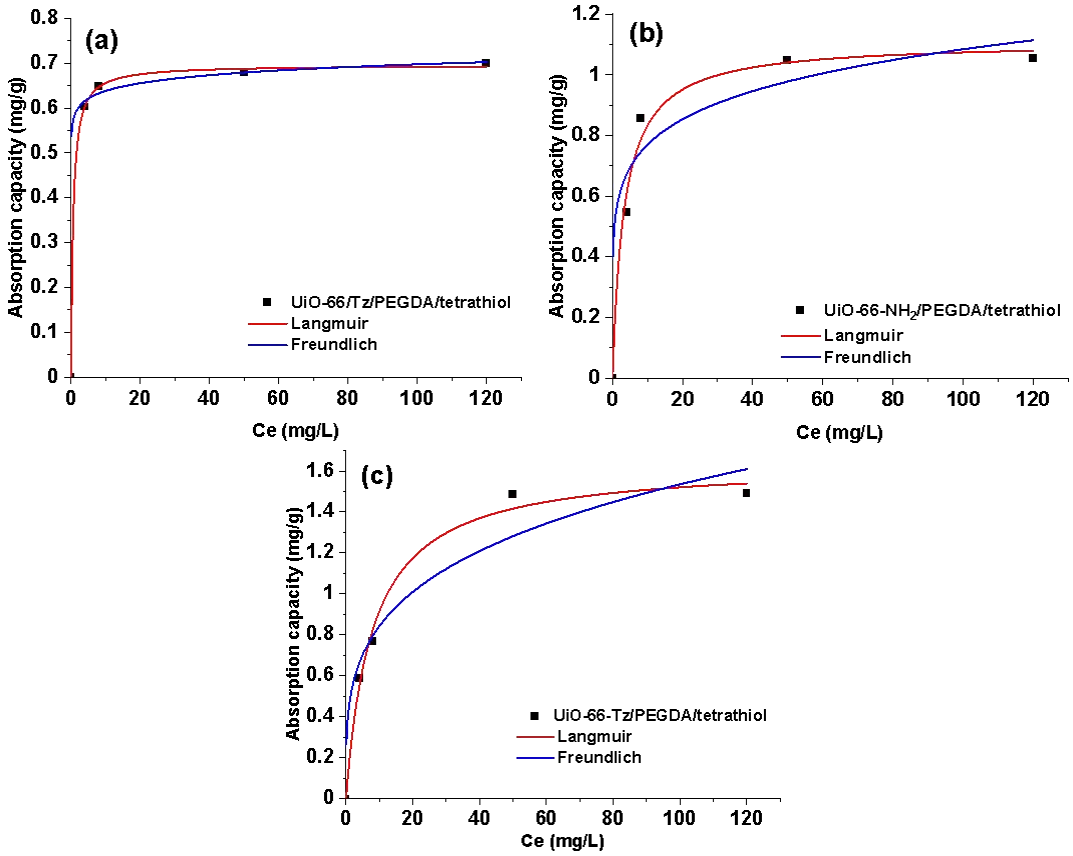

Figure S4. 14. Absorption isotherms of MB on (a) UiO-66/Tz/PEGDA/tetrathiol, (b) UiO-66-NH_2/PEGDA/tetrathiol, and (c) UiO-66-Tz/PEGDA/tetrathiol, fitted with Langmuir and Freundlich models.

Table S4. 1. MB adsorption isotherm model parameters of UiO-66/Tz/PEGDA/tetrathiol, UiO-66-NH_2/PEGDA/tetrathiol, and UiO-66-Tz/PEGDA/tetrathiol.

	Langmuir			Freundlich		
MOFs/polymer composites	Q_m (mg/g)	K_L (L/mg)	R^2	K_F (mg/g)	n	R^2
UiO-66/Tz/PEGDA/tetrathiol	0.7	1.63	0.99	0.58	0.039	0.91
UiO-66-NH_2/PEGDA/tetrathiol	1.11	0.3	0.99	0.55	0.15	0.78
UiO-66-Tz/PEGDA/tetrathiol	1.64	0.13	0.99	0.46	0.26	0.91

Chapter 5 Synergistic Nanodiamond/ TiO_2 Photopolymerization for Advanced Zwitterionic Nanocomposite Hydrogels

5.1. Preface

Whereas the previous chapters focused on incorporating individual modified nanomaterials to enhance polymer composite properties, this chapter explores a synergistic system combining TiO_2 and carboxylated nanodiamonds (NDs) to improve the mechanical and functional properties of zwitterionic hydrogels. Zwitterionic hydrogels, particularly those derived from 2-(N-3-Sulfopropyl-N,N-dimethyl ammonium)ethyl methacrylate (SBMA), are notable for their anti-fouling properties due to the formation of a robust hydration layer, making them ideal for biomedical applications such as biosensors.[1-3] However, their weak mechanical properties limit broader applications.

This chapter addresses these limitations by introducing a TiO_2/ carboxylated ND hybrid system into the SBMA hydrogel matrix, serving as both a photoinitiator and a reinforcing agent. This dual functionality enables rapid, precise, and solvent-free photopolymerization under visible-light LED (410 nm) irradiation. The chapter utilizes photorheometry to evaluate photoinitiation performance across different aqueous environments and employs electron paramagnetic resonance spin trapping (EPR-ST) to investigate the radical generation mechanisms within the hybrid system. Additionally, the swelling, mechanical, and electrical properties of the hydrogels are analyzed, demonstrating the composite's potential as a moisture sensor.

This chapter presents a sustainable and scalable approach for producing reinforced SBMA hydrogels, highlighting their versatility for applications in both industrial and biomedical fields and expanding the utility of photopolymerized nanocomposite systems.

5.2. Statement of contribution

I declare that the research findings presented in this chapter are the original work I conducted as part of my Ph.D. program at the Australian National University. As the primary author, I was responsible for developing the research concept, designing the experiments,

analyzing the data, creating the figures, and drafting the initial manuscript, under the guidance of my primary supervisor, Prof. Pu Xiao.

5.3. Abstract

This study explores a TiO_2/carboxylated nanodiamonds (NDs) hybrid system as a photoinitiating system and reinforcing agent in zwitterionic 2-(*N*-3-Sulfopropyl-*N,N*-dimethyl ammonium)ethyl methacrylate (SBMA) hydrogels, aiming to enhance the mechanical properties and functional versatility of photopolymerized hydrogels. Zwitterionic hydrogels, such as those derived from SBMA, possess unique structures that provide promising hydration properties and exhibit excellent responsiveness to external environmental conditions, making them suitable in biosensors. However, weak mechanical properties remain a limitation. In this work, the TiO_2/carboxylated NDs hybrid system addresses these issues by promoting strong interfacial bonding within the hydrogel matrix, minimizing electron-hole recombination, and improving the dispersion of nanomaterials. Photorheometry is used to evaluate the photoinitiation efficiency of the TiO_2/carboxylated NDs system in various aqueous environments, and EPR-ST analysis elucidates radical generation mechanisms. Mechanical and swelling properties are assessed for hydrogels with varying crosslinker concentrations. Additionally, electrical properties demonstrate the potential of hybrid system for moisture-sensing applications. Findings highlight the TiO_2/carboxylated NDs hybrid system as an effective photoinitiating and reinforcing agent, expanding the functional potential of SBMA hydrogels for biomedical and sensing applications.

5.4. Introduction

Photopolymerization is a process in which liquid monomers are irreversibly converted into stable solids through exposure to light, allowing for rapid and solvent-free curing with precise spatial and temporal control[1-3]. This method offers notable advantages for various industrial applications such as decorative and protective coatings[4, 5], printing[6], and biomedical fields[7]. In the biomedical domain, photopolymerization has expanded to enable applications such as photopolymerizable dental fillings and 3D printing of functional hydrogels and artificial organs, making it a valuable tool across disciplines[8, 9].Hydrogels have garnered considerable attention due to their unique properties, such as flexibility, softness, stretchability, transparency, and biocompatibility[10, 11]. These properties make hydrogels suitable for biomedical applications; however, their inherent low strength and weak adhesion limit their practical use in many fields[12]. Zwitterionic hydrogels derived from 2-(*N*-3-Sulfopropyl-*N,N*-dimethyl ammonium)ethyl methacrylate (SBMA) hold promise for overcoming some of these limitations. SBMA is a zwitterionic monomer featuring both cationic and anionic functional groups, which maintain an overall neutral charge[13]. The presence of opposite charges within the same repeating unit generates strong electrostatic interactions with water molecules, leading to the formation of a hydration layer on the surface of corresponding hydrogels.[14, 15] This robust hydration layer enhances the stability and biocompatibility of zwitterionic materials, making them highly suitable for biosensor development..[16] Specifically, SBMA can be efficiently photopolymerized with the commercially available water-soluble photoinitiator lithium phenyl-2,4,6-trimethylbenzoylphosphinate (LAP) under near-UV irradiation. However, the resulting photopolymerized hydrogel shares the common drawback of conventional ones, displaying weak mechanical properties.[17] To address this issue, strategies such as adjusting the crosslinker density, introducing polymers with rigid backbones, or adding nanomaterials to

create nanocomposites have been developed.[18] It is important to note, however, that introducing other polymers may alter the overall performance of the hydrogels, as the compatibility and interaction between different polymers can vary significantly..[17] Consequently, the incorporation of nanomaterials emerges as a promising alternative for enhancing the mechanical and functional properties of SBMA hydrogels while maintaining their desired characteristics. While nanocomposite hydrogels offer unique properties, their synthesis presents several significant challenges. One of the main issues is achieving a uniform distribution of nanoparticles within the continuous phase, as poor dispersion can lead to reduced mechanical strength.[19, 20] Therefore, the careful selection and surface modification of nanomaterials are crucial for enhancing both dispersion and interfacial interactions within the hydrogel matrix.[21, 22]

Among the nanomaterials, TiO_2 is the most extensively investigated candidate for membrane development, valued for its affordability, high stability, non-toxicity, hydrophilicity, and photocatalytic capabilities..[23] However, TiO_2 has a wide bandgap (3.2 eV) and thus requires UV light for activation, limiting its applicability in visible-light induced photopolymerization. To address this limitation, TiO_2 is often combined with noble metals like gold or silver, which enhance photocatalytic efficiency under visible light.[24, 25] However, the high cost of noble metals restricts large-scale applications. An alternative approach involves combining TiO_2 with low-cost carbon-based nanomaterials, which provide electron-hole separation and enhance photocatalytic performance. Nanodiamonds (NDs) are an attractive option among carbon-based nanomaterials due to their scalable synthesis, simple surface modification, and excellent biocompatibility.[26] Nevertheless, unmodified NDs tend to aggregate in aqueous solutions due to their high surface energy and small particle size, necessitating surface functionalization to improve dispersion.

In general, the use of a hybrid system combining TiO_2 and modified nanodiamonds (NDs) serves two main purposes: first, to minimize photo-generated electron−hole recombination,[27] and second, to enhance photodegradation properties.[28] Despite these promising photocatalytic features, hybrid systems have rarely been applied in photopolymerization. Building on pioneering work that explored photopolymerizing hydrogels with hybrid semiconductor-metal systems as photoinitiators,[29] this research investigates the potential of a TiO_2/modified ND hybrid system to function as both a photoinitiator and reinforcing filler in SBMA hydrogels. This study evaluates the photoinitiation ability of the TiO_2/modified ND hybrid system in SBMA hydrogel formulations under various aqueous conditions using photorheometry. Furthermore, the effects of different crosslinker concentrations on swelling behavior and mechanical properties are investigated. To clarify the photoinitiation mechanism, electron paramagnetic resonance spin trapping (EPR-ST) analysis is performed to detect radical formation within the hybrid system. Lastly, the photopolymerized TiO_2/modified ND/SBMA hydrogel composite is evaluated for its potential application as a moisture sensor, demonstrating the versatile functionalities enabled by this hybrid nanocomposite system.

5.5. Experimental

5.5.1. Materials

Titanium dioxide (21 nm), sodium hydroxide, 2-(*N*-3-Sulfopropyl-*N,N*-dimethyl ammonium)ethyl methacrylate (SBMA), poly(ethylene glycol) dimethacrylate (PEGDMA, Mn750), 2-(dimethylamino)ethyl methacrylate (DAEMA), bis(trifluoromethane)sulfonimide lithium salt (LiTFSI) and lithium phenyl-2,4,6-trimethylbenzoylphosphinate (LAP) were purchased from Sigma-Aldrich and used as received without further purification. Raw nanodiamonds (10 nm) and carboxylated nanodiamonds (60 nm and 190 nm) were

purchased from Adamas Nanotechnologies and used as received. The chemical structures of mentioned monomers, photoinitiator, and additive are summarized in Schemes 5.1.

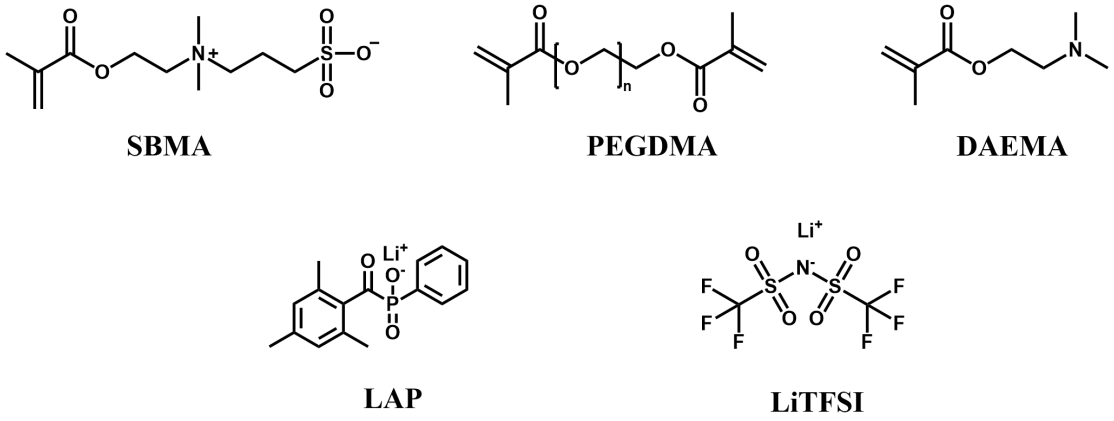

Scheme 5. 1. Chemical structures of investigated monomers (SBMA, PEGDMA, and DAEMA), photoinitiator (LAP), and additive (LiTFSI).

5.5.2. Irradiation Source

LED with emission wavelength centered at 410 nm (110 $mW \cdot cm^{-2}$) was used as irradiation sources.

5.5.3. Electron Paramagnetic Resonance Spin Trapping (EPR-ST) Experiments

EPR-ST experiments were performed using a Bruker E500 spectrometer equipped with a Bruker ER4122 SHQ resonator. Samples were loaded into standard X-band EPR tubes with an inner diameter of 2.8 mm. Radical generation was induced at room temperature under 410 nm LED irradiation in a nitrogen atmosphere, and radicals were trapped using phenyl-N-tert-butylnitrone (PBN), following the established procedure[30].

5.5.4. Photorheology Testing

Photorheology characterization was conducted using an Anton Paar MCR 702 multidrive rheometer at room temperature with a plate geometry of 25 mm diameter (PP25). Prepared samples were placed on a glass holder, and the plate sensor was lowered from above until

a 0.3 mm gap was achieved between the sensor and the holder. Irradiation was applied from the bottom of the sample holder, allowing light to pass through the sample from bottom to top. Measurements were taken at a constant angular frequency of 10 Hz with a shear strain of 0.1%. Changes in the storage and loss moduli of the formulations were recorded throughout the test.

5.5.5. Preparation of hydrogel nanocomposites

SBMA, DAEMA, and PEGDMA were dissolved in NaOH solutions, DI water, or HCl solutions at varying concentrations. TiO_2 and NDs (0.5 wt% each) were subsequently added, and the mixtures were sonicated for 5 minutes to achieve well-dispersed hydrogel precursor solutions. The monomer feeding ratios are provided in Table 5.1. The precursor solutions were then polymerized by exposure to 410 nm LED light for 10 minutes in dumbbell-shaped Teflon molds, prepared for swelling and mechanical property measurements.

5.5.6. Water content and swelling ratio

The water content of the hydrogels was measured gravimetrically by drying. The wet weight (W(w)) was recorded after gently removing surface moisture using lens cleaning paper. The hydrogels were subsequently dehydrated in a 45 °C oven for 24 hours, and the dehydrated weight (W(d)) was obtained. Water content was then calculated using the following formula (1):

$$Water\ content\ (\%) = \frac{W(w)-W(d)}{W(w)} * 100\% \qquad (1)$$

Measurements were performed 5 times for each hydrogel, and the results of water content were expressed as the mean ± standard deviation, which are shown in Table S5.1.

The swelling ratio was determined gravimetrically. Dehydrated hydrogels (S(d)) were immersed in DI water. At predetermined intervals, samples were removed, blotted gently with filter paper to eliminate surface moisture, and weighed (S(w)). Swelling was monitored until equilibrium was reached and calculated using the following formula (2):

$$Swelling\ ratio\ (\%) = \frac{S(w)-S(d)}{S(w)} * 100\% \qquad (2)$$

5.5.7. Mechanical Properties of the Hydrogels

The mechanical properties of different hydrogels were tested using a motorized test stand (EMX series, IMADA, Japan) with a 50 N force sensor at 25 °C. In the tensile tests, hydrogel specimens with a height, length, and width of 20 mm, 3.5 mm, and 1.3 mm, respectively were tightened on the metal clips. An initial stress corresponding to 5% of the initial length was applied to both sides of the sample to extend the hydrogel. The tensile speed was set at 10 mm/min for all tests. Each test was repeated at least three times to ensure reproducibility.

5.5.8. Electrical properties of the Hydrogels

The hydrogels were employed to fabricate moisture sensors. They were tested through the resistance measurements using AstroAI WH5000A multimeter. The investigated hydrogels with different water content were connected to electrical wires and the corresponding signals were recorded.

5.6. Result and discussion

5.6.1. The selection of nanodiamonds

In this work, three types of nanodiamonds (NDs), differing in size and surface functionality, were selected for incorporation with TiO_2: raw nanodiamonds (10 nm), carboxylated nanodiamonds (60 nm), and carboxylated nanodiamonds (190 nm). Raw nanodiamonds, with a zeta potential ranging from +20 mV to -20 mV, contain non-combustible impurities (primarily iron) and exhibit poor dispersion in aqueous solutions.[31] In contrast, surface modification with carboxylic acid groups and additional purification steps improved the dispersibility of the 190 nm carboxylated NDs in aqueous media, as indicated by their stable zeta potential of -45 mV.[31] Interestingly, the particle size of carboxylated NDs influenced the photoinitiation efficiency of the SBMA system. As shown in Figure S5.1, when precursor formulations (TiO_2/carboxylated NDs/SBMA/gelMA, with gelMA used as a crosslinker) were irradiated with 410 nm LED light, formulations containing 190 nm carboxylated NDs reached the gel point in a significantly shorter time (93 s) compared to those containing 60 nm carboxylated NDs (170 s). Based on these findings, the 190 nm carboxylated nanodiamonds were selected for incorporation with TiO_2 in this study.

5.6.2. Effect of various aqueous environment on the photopolymerization profile of the TiO_2/carboxylated NDs system

After identifying suitable NDs for the hybrid system, we evaluated the dispersibility of carboxylated NDs in various aqueous solutions. Dispersibility was significantly influenced by the aqueous environment (acidic, neutral, or alkaline) and the medium concentration. Notably, carboxylated NDs alone were capable of initiating the photopolymerization of SBMA under 410 nm LED irradiation, even in the absence of additional additives or crosslinkers. Figure 5.1(a) shows the photopolymerization profile of carboxylated NDs in

SBMA under different aqueous conditions. In alkaline conditions (1 mM NaOH), carboxylated NDs photopolymerized SBMA with a gel point of 104 s, which was significantly shorter than the time required in neutral (DI water, 166 s) and acidic conditions (1 mM HCl, 841 s). This difference was likely due to variations in carboxylated ND dispersibility in these environments. As illustrated in Figure S5.2, carboxylated ND agglomeration was observed in the as-photopolymerized SBMA hydrogel prepared in DI water and 1 mM HCl, while a clear hydrogel film was obtained under 1 mM NaOH conditions. In aqueous solution, the carboxylic groups on the NDs are dissociated[32], resulting in a negative zeta potential. Under acidic conditions, the increased presence of H^+ ions neutralized the negative surface charge of the carboxylated NDs, raising the zeta potential and disrupting colloidal stability, which led to agglomeration.[32, 33] We further examined the impact of NaOH concentration on the photopolymerization profile. As shown in Figure 5.1(b), while there was no significant difference in gel point between photopolymerizations conducted in 10 mM and 100 mM NaOH, a slight difference in the final modulus was observed. Additionally, Figure S5.2 indicates minor agglomeration in the hydrogel film prepared with 100 mM NaOH. Based on these findings, the optimal dispersibility of NDs in the SBMA solution was achieved under alkaline conditions, specifically with NaOH concentrations ranging from 1 mM to 10 mM.

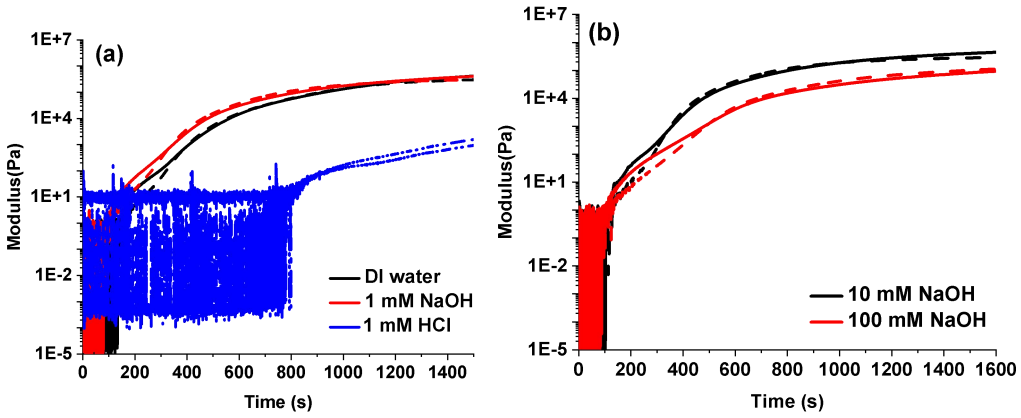

Figure 5. 1. Storage (G') and loss (G'') moduli of (a) carboxylated NDs/SBMA (carboxylated NDs: 0.5 wt%) system prepared in various aqueous solutions and (b) carboxylated NDs/SBMA (carboxylated NDs: 0.5 wt%) system prepared in NaOH solution with various

concentrations as a function of irradiation time. The samples were irradiated with LED@410 nm.

In addition to carboxylated NDs, the dispersibility of TiO_2 in various aqueous environments was also evaluated (Figure S5.3). Similar to NDs, TiO_2 alone can initiate the photopolymerization of SBMA under 410 nm LED irradiation without the addition of additives or crosslinkers. Overall, the photoinitiation ability of TiO_2 was relatively unaffected by the aqueous environment, as the gel points were nearly the same in neutral, acidic, and alkaline conditions (~120 s). However, the hydrogel films prepared in DI water and 10 mM HCl exhibited a higher final modulus compared to those prepared in 10 mM NaOH, indicating that TiO_2 achieved optimal dispersibility under neutral and acidic conditions. Given that carboxylated NDs were optimally dispersed in alkaline environments, the hybrid TiO_2/carboxylated ND system should therefore be prepared in a neutral or slightly alkaline environment.

5.6.3. Effect of the TiO_2/carboxylated NDs hybrid system on the photopolymerization of SBMA hydrogel

As previously mentioned, both TiO_2 and carboxylated nanodiamonds (NDs) can independently initiate the photopolymerization of SBMA hydrogels under 410 nm LED irradiation. As shown in Figure 5.3, when 4 wt% of GelMA is used as a crosslinker, TiO_2 and carboxylated NDs at 0.5 wt% each can induce gelation in SBMA hydrogels, with gel points of 163 s and 180 s, respectively. Upon irradiation, TiO_2 can facilitate the generation of hydroxyl radicals via electron excitation, as electrons can be promoted from the valence band (VB) to the conduction band (CB), resulting in radical formation.[34] However, rapid electron-hole recombination in TiO_2 [35, 36] limited radical availability, thereby reducing photoinitiation efficiency for SBMA hydrogels. In contrast, the TiO_2/carboxylated ND hybrid

system exhibited significantly enhanced photoinitiation efficiency, achieving a gel point of 93 s (Figure 5.2), nearly half the time required by TiO_2 or carboxylated NDs alone. This improvement can be attributed to the role of carboxylated NDs in mitigating electron-hole recombination.[27] Specifically, upon excitation, electrons in TiO_2 can transfer from the VB to the CB, creating holes in the VB. These photoexcited electrons subsequently migrated to the carboxylated NDs, effectively separating the electron-hole pairs. This separation markedly reduced recombination and enhanced radical generation, facilitating more efficient photopolymerization of SBMA hydrogels. [37, 38]

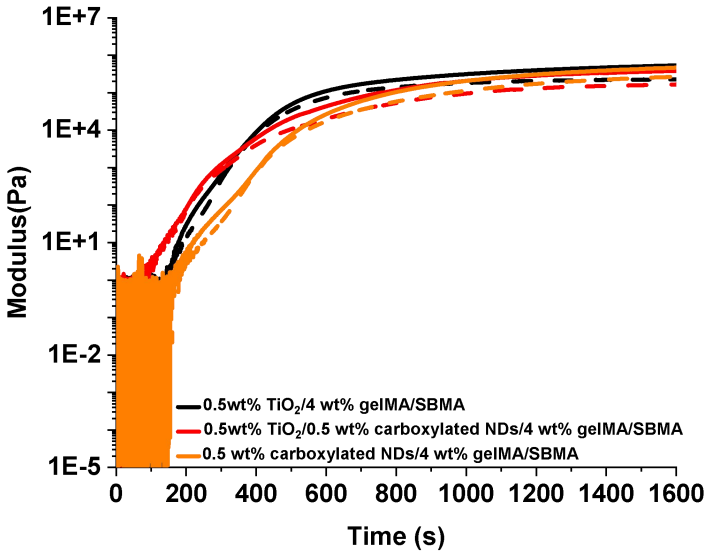

Figure 5. 2. Storage (G') and loss (G'') moduli of TiO_2/GelMA/SBMA, carboxylated NDs/GelMA/SBMA, and TiO_2-carboxylated NDs/GelMA/SBMA systems prepared in 1 mM NaOH (carboxylated NDs: 0.5 wt%, TiO_2: 0.5 wt% and GelMA: 4 wt%) as a function of irradiation time. The samples were irradiated with LED@410 nm.

5.6.4. EPR-ST analysis

To investigate hydroxyl radical generation in the TiO_2/carboxylated ND hybrid system under 410 nm light irradiation, the electron paramagnetic resonance (EPR-ST) technique was employed (Figure 5.3). Radicals generated upon irradiation were trapped using phenyl-N-tert-butylnitrone (PBN) and subsequently characterized. As shown in Figure 5.3(a), a weak

PBN/radical adduct signal with hyperfine splitting (HFS) constants αN = 15.5 G and αH = 2.7 G, indicative of hydroxyl radicals,[39] was observed after 20 minutes of irradiation. In contrast, the hybrid system in Figure 5.3(b) displayed a broad peak even in the absence of light irradiation, attributed to uncoupled spins localized on dangling bonds associated with structural defects in the ND core or metallic impurities (primarily iron).[40-42] Upon exposure to 410 nm LED light for just 2 minutes, a PBN/hydroxyl radical adduct signal emerged (Figure 5.3b). These findings aligned with the photorheology results, where TiO_2 alone underwent rapid electron-hole recombination after photoexcitation, leading to a delayed formation of the PBN/radical adduct. In contrast, the hybrid system benefited from improved electron-hole pair separation, resulting in the rapid formation of the PBN/radical adduct.

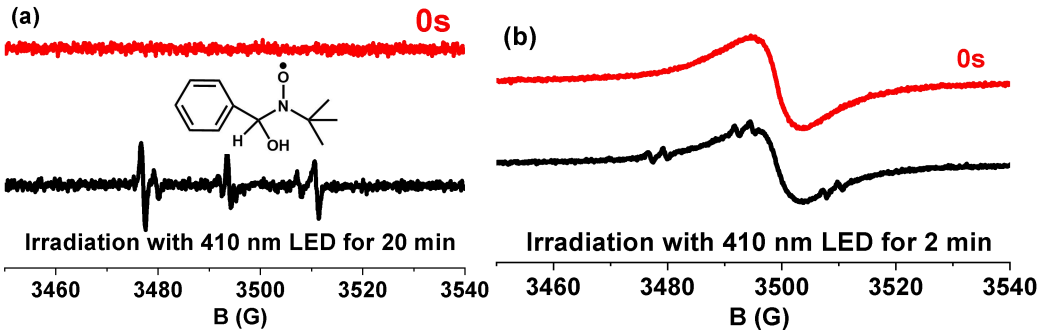

Figure 5. 3. EPR-ST spectra of the radicals generated in (a) TiO_2 and (b) TiO_2/carboxylated NDs hybrid system upon exposure to LED@410 nm and trapped by PBN in 1 mM NaOH solution.

5.6.5. Determination of prepolymer compositions for functional hydrogels

To broaden the potential applications of these hydrogels, careful optimization of the prepolymer composition is essential. Specifically, PEGDMA was used as a crosslinker to regulate the crosslinking density of the hydrogels, while DAEMA was incorporated to regulate their mechanical properties. The compositions of the hydrogels studied are detailed in Table 5.1. In each hydrogel formulation, the weight percentages of TiO_2 and

carboxylated NDs were kept constant at 0.5 wt%, while varying molar ratios of PEGDMA were evaluated. The photopolymerization profiles of the hydrogels were assessed using photorheometry. As shown in Figure S5.4(a), hydrogels 1, 2, 3, and 5 exhibited gel points of 52 s, 55 s, 19 s, and 76 s, respectively. A comparison between hydrogels 1 and 2, which shared the same molar ratio of PEGDMA, revealed that the addition of DAEMA in hydrogel 1 did not significantly alter the photopolymerization profile. This finding suggested excellent compatibility between DAEMA and the SBMA aqueous solution, which was critical for achieving hydrogels with enhanced properties. In hydrogels 2, 3, and 5, the PEGDMA: SBMA molar ratios are 1/60, 1/20, and 1/5, respectively. Interestingly, a PEGDMA: SBMA molar ratio of 1/20 yielded the fastest gelation time (19 s, Figure S5.4a), while increasing the ratio to 1/5 resulted in a marked delay in gelation (76 s, Figure S5.4a). At higher PEGDMA concentrations, the compatibility with the SBMA aqueous solution decreased, leading to phase separation after a few minutes without agitation. As the addition of PEGDMA may influence the photopolymerization system, further comparisons were made among hydrogels 3, 6, and 7 (Figure S5.5), which were prepared in different aqueous environments (NaOH, DI water, and HCl, respectively). The results confirmed that the TiO_2/carboxylated ND hybrid photoinitiating system exhibited superior photoinitiation efficiency under alkaline conditions compared to acidic conditions To further investigate the benefits of this hybrid photoinitiating system, we compared the photopolymerization profile of SBMA initiated by the commercially available water-soluble photoinitiator LAP (hydrogel 8). As shown in Figure S5.4(b), LAP-initiated polymerization achieved a gel point in 8 s; however, the resulting hydrogel film was extremely fragile. Additionally, to evaluate the multifunctional potential of these hydrogels, we examined the photopolymerization profile of a hydrogel containing LiTFSI (hydrogel 9), which can impart electrical properties. As

expected, the inclusion of LiTFSI significantly slowed photopolymerization, resulting in a gel point of 91 s.

Table 5. 1. Feeding ratio of the investigated hydrogels

Numbers	DAEMA (g)	SBMA (g)	TiO_2 (mg)	Carboxylated NDs (mg)	PEGDMA (g)	aq (ml)	LAP (mg)
1	0.148	0.804	10	10	0.0475	1(1mM NaOH)	0
2	0	0.804	8.4	8.4	0.036	0.84 (1mM NaOH)	0
3	0	0.804	9.1	9.1	0.108	0.912 (1mM NaOH)	0
4	0	0.804	6	6	0.036	0.36 (1mM NaOH)	0
5	0	0.804	12.4	12.4	0.432	1.236 (1mM NaOH)	0
6	0	0.804	9.1	9.1	0.108	0.912 (DI water)	0
7	0	0.804	9.1	9.1	0.108	0.912 (1 mM HCl)	0
8	0	0.804	0	0	0.108	0.912 (1 mM NaOH)	8.6
9 (Contain 9.1 mg LiTFSI)	0	0.804	9.1	9.1	0.108	0.912 (1 mM NaOH)	0

5.6.6. Swelling behaviour of the investigated hydrogels

The swelling behavior of hydrogels with varying additions of DAEMA, LiTFSI, and different molar ratios of PEGDMA was evaluated in DI water (Figure 5.4). Comparing hydrogels 2 and 3, with hydrogel 2 containing a lower molar ratio of PEGDMA, hydrogel 2 displayed a faster swelling rate and reached a higher swelling ratio than hydrogel 3. This outcome was consistent with expectations, as the reduced crosslinking density in hydrogel 2 resulted in larger mesh sizes in the polymer network, facilitating greater water absorption.[43] The addition of DAEMA in hydrogel 1 also led to a notable increase in both the swelling rate and final swelling ratio (250%). DAEMA interacted with SBMA, modifying the crosslinking

network and creating larger mesh sizes within the hydrogel, thereby enhancing its water uptake capacity.[44] In hydrogel 9, the swelling ratio exceeded that of hydrogel 3, likely due to the inclusion of LiTFSI, a hygroscopic salt that provided additional water absorption properties.[45]

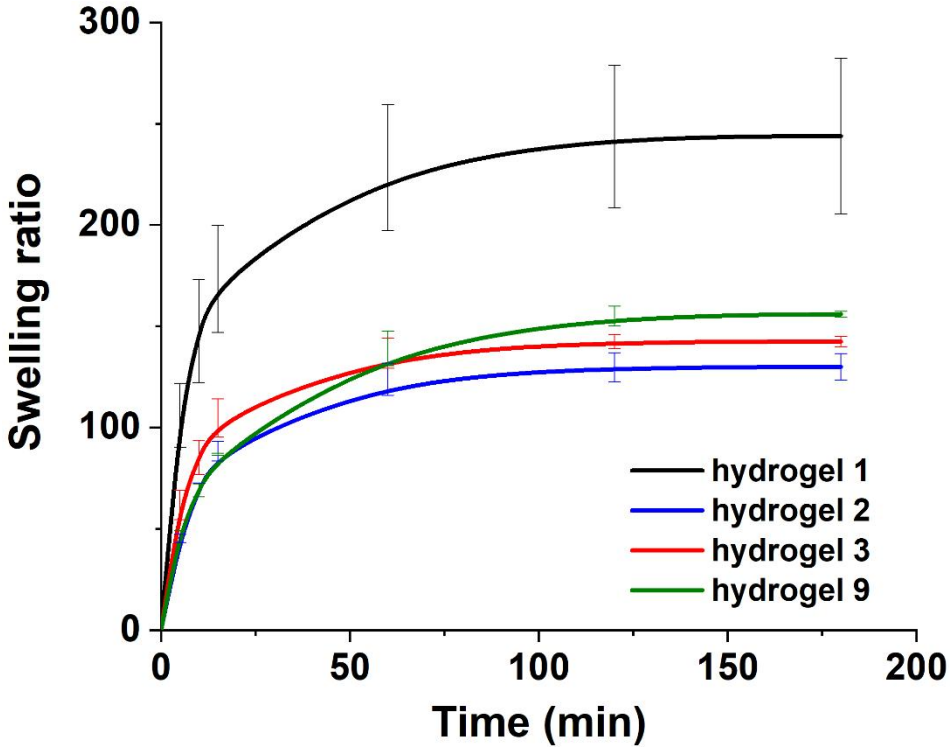

Figure 5. 4. Swelling ratio for photocured hydrogels prepared and swollen in DI water.

5.6.7. Mechanical properties of the investigated hydrogels

The mechanical properties of the photopolymerized hydrogels were assessed using tensile testing, with representative stress-strain curves shown in Figure 5.5 and Figure S5.6. Each sample displayed an initial linear region, from which Young's modulus, a measure of the material's elastic stiffness, was calculated. After reaching the maximum stress point, a sudden drop in stress signified material failure.

Hydrogels were tested in two states: 1. as-prepared state, where the hydrogels retained their natural water content (summarized in Table S5.1), and 2. dehydrated state, where samples were oven-dried for 24 hours, standardizing the water content at 30%.

As seen in Figure S5.6 and Table S5.1, the as-photopolymerized hydrogels showed varying mechanical properties influenced by their composition and preparation conditions. Hydrogel 1, containing DAEMA, exhibited the lowest tensile strength (0.06 MPa) due to its high-water content (42.7% ± 3.4%), which reduced crosslinking density. Despite this, it showed high elongation at break (120%), reflecting enhanced stretchability. In contrast, Hydrogel 2, which lacked DAEMA, had a higher crosslinking density, leading to a reduced water content (38.8% ± 6.3%) and an increased tensile strength of 0.14 MPa. Further analysis revealed that hydrogels prepared in different aqueous environments followed trends observed in photorheology investigation. Notably, Hydrogel 3, synthesized in an alkaline NaOH environment with the absence of DAEMA and an increased molar ratio of PEGDMA compared to Hydrogel 1 and 2, demonstrated the highest tensile strength (0.17 MPa) among the hydrogels. This improvement is likely due to the well-dispersed TiO_2/carboxylated NDs, which enhanced the mechanical properties. Conversely, Hydrogel 8, photopolymerized with the commercial photoinitiator LAP, was too fragile to be removed from the mold for tensile testing.

Upon dehydrating all hydrogels to a standardized 30% water content, their mechanical properties improved, and differences between samples became more pronounced (Figure 5.5 and Table 5.2). Among them, Hydrogel 1 retained the highest stretchability, with elongation at break reaching 160% and an increased tensile strength of 0.8 MPa. Comparing Hydrogels 2 and 3, the higher PEGDMA content in Hydrogel 3 resulted in increased crosslinking density, producing a stiffer structure with a Young's modulus of 17 MPa and a tensile strength of 2.6 MPa, whereas Hydrogel 2 had a tensile strength of 0.8

MPa and Young's modulus of 2.2 MPa. Consequently, Hydrogel 3 exhibited reduced stretchability due to its increased rigidity.

Hydrogels 6 and 7, prepared in DI water and HCl, respectively, displayed lower tensile strengths (1.9 MPa and 1.8 MPa) and Young's moduli (8.1 MPa and 13 MPa) compared to Hydrogel 3. This can be attributed to protonation of the carboxylated NDs under neutral and acidic conditions, which resulted in reduced surface charge, leading to filler agglomeration and a more inhomogeneous hydrogel structure .

A significant finding was the stark contrast in mechanical performance between Hydrogels 3 and 8. Hydrogel 3, photopolymerized with the TiO_2/carboxylated ND hybrid system, exhibited mechanical properties that were five-fold higher in tensile strength and 24-fold higher in Young's modulus than Hydrogel 8, which was polymerized using LAP (tensile strength of 0.5 MPa and Young's modulus of 0.7 MPa). The superior mechanical performance of Hydrogel 3 was likely due to the charged surface of carboxylated NDs, which enhanced interfacial bonding between the nanofillers and polymer matrix, facilitating efficient load transfer within the hydrogel network.

Finally, Hydrogel 9, incorporating LiTFSI, exhibited mechanical properties comparable to Hydrogel 3 (tensile strength of 2.7 MPa, Young's modulus of 13 MPa), despite undergoing a delayed photopolymerization process. This suggested that the addition of LiTFSI did not compromise structural integrity, further emphasizing the versatility and robustness of the developed TiO_2-carboxylated ND hybrid system.

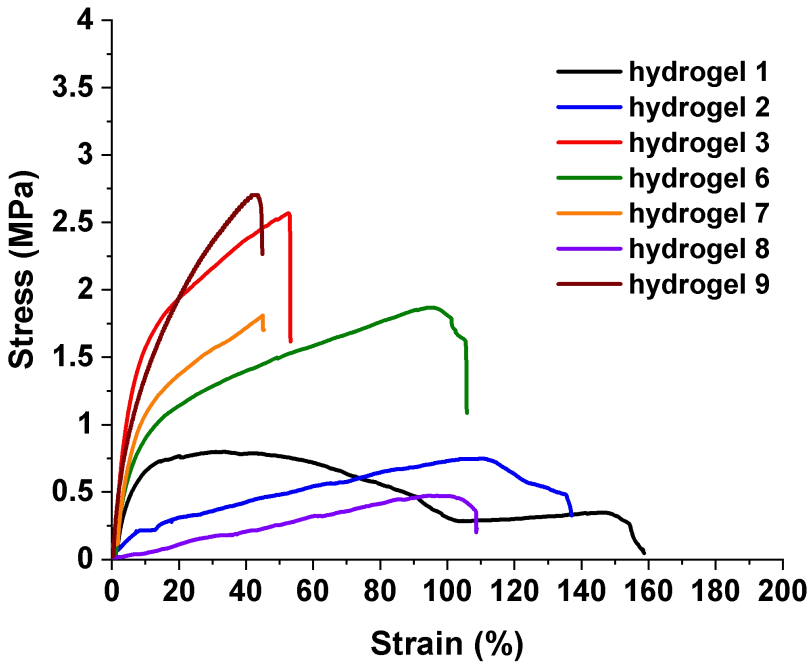

Figure 5. 5. Stress-strain curves in tensile test of the dehydrated photocured hydrogels with water content of 30%.

Table 5. 2. Mechanical properties of the investigated dehydrated photopolymerized hydrogels with water content of 30%.

Numbers	Tensile strength (MPa)	Elongation at break	Young's modulus (MPa)
1	0.8	160%	12
2	0.8	136%	2.2
3	2.6	53%	17
6	1.9	106%	8.1
7	1.8	45%	13
8	0.5	108%	0.7
9	2.7	45%	13

5.6.8. Electrical properties of hydrogels and their potential application

Generally, hydrogels exhibit low electrical conductivity due to the insulating nature of the commonly used hydrophilic polymer chains.[46] Conductivity can be achieved by incorporating conductive polymers into the hydrogel or by adding conductive materials.[47, 48] DAEMA, a cationic monomer, provides ionic conductivity,[49] while LiTFSI is a conductive salt. Therefore, we focused on evaluating the electrical properties of hydrogel 1 and hydrogel 9, which contained DAEMA and LiTFSI, respectively. To observe conductive

properties, a simple circuit was constructed by connecting a small LED and a 9V battery with copper wire. We confirmed that other hydrogels, even in their precursor stage, exhibited no electrical conductivity. Only hydrogels containing DAEMA or LiTFSI formed a closed circuit in both the precursor and photopolymerized states. Notably, electrical conductivity was found to vary with the water content of the hydrogels. In their dry state, both hydrogels 1 and 9 exhibited open circuits. However, upon rehydration, a closed circuit was re-established. Table 5.3 summarizes the relationship between water content and hydrogel resistance. For hydrogel 1, an 8% increase in water content led to approximately a 50% reduction in resistance. Similarly, in hydrogel 9, a 14% increase in water content resulted in a five-fold decrease in resistance compared to its dehydrated state. Overall, the electrical property analysis demonstrated that the resistance of the hydrogel was highly dependent on water content, making it a promising candidate for moisture and humidity sensors. Due to its zwitterionic nature, SBMA-based hydrogels can effectively retain and release moisture in response to environmental humidity fluctuations. This property is particularly beneficial in wearable electronics, environmental monitoring, and medical diagnostics, where real-time humidity detection is required.

Table 5. 3. Water content and electrical properties of photocured hydrogels.

Hydrogels	Initial water content (%)	Initial resistance (MΩ)	Final water content (%)	Final resistance (MΩ)
1	15%	26	24%	10
9	21%	9	35%	2

5.7. Conclusion

Based on the findings of this study, the TiO_2/carboxylated nanodiamond (ND) hybrid system emerges as an effective and versatile photoinitiating agent for zwitterionic SBMA-based hydrogels, demonstrating enhanced mechanical and conductive properties. The study

demonstrated the potential of the TiO_2/carboxylated NDs system to address limitations associated with conventional photopolymerization methods and single-component initiators. The TiO_2/carboxylated NDs hybrid system offered distinct advantages for photoinitiation, particularly in the formation of SBMA hydrogels. Under 410 nm LED light irradiation, both TiO_2 and carboxylated NDs independently initiated the photopolymerization of SBMA, with TiO_2 contributing photocatalytic capability and carboxylated NDs promoting electron-hole separation to mitigate recombination. The hybrid system outperformed individual components, achieving gelation of SBMA hydrogels in approximately half the time required by TiO_2 alone. This improvement was attributed to the enhanced electron-hole separation facilitated by carboxylated NDs, which promoted radical generation and thereby increased photopolymerization efficiency. Additionally, the findings emphasized the role of the aqueous environment on the dispersibility of both TiO_2 and carboxylated NDs, which directly affected photopolymerization efficiency. Carboxylated NDs exhibited optimal dispersibility in alkaline conditions (1 mM NaOH), enhancing photoinitiation performance, while TiO_2 displayed optimal dispersibility in neutral and acidic conditions. Consequently, a neutral or slightly alkaline environment was identified as the ideal condition to maximize the performance of TiO_2/carboxylated NDs hybrid system. EPR-ST analysis further verified the generation of hydroxyl radicals in the hybrid system, supporting the enhanced photoinitiation efficiency observed in photorheological data. Mechanical analysis reinforced the effectiveness of the TiO_2/carboxylated NDs system as reinforcing filler. The as-prepared hydrogels exhibited increased tensile strength and modulus in an alkaline environment compared to an acidic environment, which can be attributed to the stable dispersion and strong interfacial bonding between TiO_2-carboxylated ND fillers and the polymer matrix. Dehydrated hydrogels demonstrated even greater mechanical properties, highlighting the influence of water content on material performance. Notably, the TiO_2/carboxylated NDs

system imparted a five-fold increase in tensile strength and a 24-fold increase in Young's modulus compared to hydrogels photopolymerized with the conventional photoinitiator LAP. The inclusion of DAEMA and LiTFSI in the hydrogel formulations added further functional properties, such as ionic conductivity and potential for the moisture sensing application. Specifically, electrical properties of the hydrogels varied with water content, with a significant decrease in resistance upon rehydration, indicating potential for these hydrogels in moisture-sensing applications and expanding their utility beyond structural and mechanical enhancements. In summary, the TiO_2/carboxylated NDs hybrid system demonstrated substantial promise for the development of high-performance, multifunctional zwitterionic hydrogels. These findings can contribute to understanding the design and application of advanced photopolymerized hydrogels, highlighting the role of hybrid nanomaterials in overcoming traditional synthesis limitations. The versatility and efficiency of this system highlighted its potential across diverse applications, from biomedical devices to environmental sensors.

5.8. Reference

[1] C. Yu, J. Schimelman, P. Wang, K. L. Miller, X. Ma, S. You, J. Guan, B. Sun, W. Zhu, S. Chen, *Chemical reviews* 2020, *120*, 10695.
[2] N. Corrigan, J. Yeow, P. Judzewitsch, J. Xu, C. Boyer, *Angewandte Chemie International Edition* 2019, *58*, 5170.
[3] I. L. d. Camargo, M. M. Morais, C. A. Fortulan, M. C. Branciforti, *Ceramics International* 2021, *47*, 11906.
[4] F. Liu, A. Liu, W. Tao, Y. Yang, *Progress in Organic Coatings* 2020, *145*, 105685.
[5] M. Sangermano, I. Roppolo, M. Messori, *RSC Smart Materials* 2015, *2015*, 121.
[6] D. Chekkaramkodi, L. Jacob, M. S. C, R. Umer, H. Butt, *Additive Manufacturing* 2024, *86*, 104189.
[7] C. Yu, J. Schimelman, P. Wang, K. L. Miller, X. Ma, S. You, J. Guan, B. Sun, W. Zhu, S. Chen, *Chemical reviews* 2020, *120*, 10695.
[8] S. V. Murphy, A. Atala, *Nature Biotechnology* 2014, *32*, 773.
[9] Z. Guo, H. Zhang, W. Xie, A. Tang, W. Liu, *Additive Manufacturing* 2023, *77*, 103824.
[10] X. Chang, L. Chen, J. Chen, Y. Zhu, Z. Guo, *Advanced Composites and Hybrid Materials* 2021, *4*, 435.
[11] X. Wang, X. Liu, D. W. Schubert, *Nano-Micro Letters* 2021, *13*, 64.
[12] Y. S. Zhang, A. Khademhosseini, *Science* 2017, *356*, eaaf3627.

[13] I. Kamenova, M. Harrass, B. Lehmann, K. Friedrich, I. Ivanov, G. Georgiev, *Macromolecular Symposia* 2007, *254*, 122.
[14] S. Chen, J. Zheng, L. Li, S. Jiang, *Journal of the American Chemical Society* 2005, *127*, 14473.
[15] E. A. Vogler, *Advances in Colloid and Interface Science* 1998, *74*, 69.
[16] C. Diaz Blanco, A. Ortner, R. Dimitrov, A. Navarro, E. Mendoza, T. Tzanov, *ACS Applied Materials & Interfaces* 2014, *6*, 11385.
[17] H. He, X. Xuan, C. Zhang, Y. Song, S. Chen, X. Gong, B. Ren, J. Zheng, J. Wu, *Langmuir* 2019, *35*, 1828.
[18] R. Guo, D. Yu, S. Wang, L. Fu, Y. Lin, *Soft Matter* 2023, *19*, 1465.
[19] M. Rahmat, P. Hubert, *Composites Science and Technology* 2011, *72*, 72.
[20] S. Sinha Ray, M. Okamoto, *Progress in Polymer Science (Oxford)* 2003, *28*, 1539.
[21] D. M. Alshangiti, T. K. El-damhougy, A. Zaher, M. Madani, M. Mohamady ghobashy, *RSC Advances* 2023, *13*, 35251.
[22] C. Du, W. Huang, *Nanocomposites* 2022, *8*, 102.
[23] S. Leong, A. Razmjou, K. Wang, K. Hapgood, X. Zhang, H. Wang, *Journal of Membrane Science* 2014, *472*, 167.
[24] Y. Tian, T. Tatsuma, *Journal of the American Chemical Society* 2005, *127*, 7632.
[25] L. Liu, Z. Liu, H. Bai, D. D. Sun, *Water Research* 2012, *46*, 1101.
[26] V. N. Mochalin, O. Shenderova, D. Ho, Y. Gogotsi, *Nature Nanotechnology* 2012, *7*, 11.
[27] L. M. Pastrana-Martínez, S. Morales-Torres, S. A. C. Carabineiro, J. G. Buijnsters, J. L. Figueiredo, A. M. T. Silva, J. L. Faria, *Applied Surface Science* 2018, *458*, 839.
[28] K.-D. Kim, N. K. Dey, H. O. Seo, Y. D. Kim, D. C. Lim, M. Lee, *Applied Catalysis A: General* 2011, *408*, 148.
[29] A. A. Pawar, S. Halivni, N. Waiskopf, Y. Ben-Shahar, M. Soreni-Harari, S. Bergbreiter, U. Banin, S. Magdassi, *Nano Letters* 2017, *17*, 4497.
[30] J. Zhang, M. Frigoli, F. Dumur, P. Xiao, L. Ronchi, B. Graff, F. Morlet-Savary, J. P. Fouassier, D. Gigmes, J. Lalevée, *Macromolecules* 2014, *47*, 2811.
[31] A. Kumar, C. K. Dixit, "3 - Methods for characterization of nanoparticles", in *Advances in Nanomedicine for the Delivery of Therapeutic Nucleic Acids*, S. Nimesh, R. Chandra, and N. Gupta, Eds., Woodhead Publishing, 2017, p. 43.
[32] L. Ginés, S. Mandal, I. A. Ashek, C.-L. Cheng, M. Sow, O. A. Williams, *Nanoscale* 2017, *9*, 12549.
[33] M. J. Głowacki, P. Niedziałkowski, J. Ryl, M. Prześniak-Welenc, M. Sawczak, K. Prusik, M. Ficek, M. Janik, K. Pyrchla, M. Olewniczak, K. Bojarski, J. Czub, R. Bogdanowicz, *Journal of Colloid and Interface Science* 2024, *675*, 236.
[34] X. Chen, S. S. Mao, *ChemInform* 2007, *38*.
[35] J.-M. Herrmann, *Catalysis Today* 1999, *53*, 115.
[36] S. Anandan, T. Narasinga Rao, M. Sathish, D. Rangappa, I. Honma, M. Miyauchi, *ACS Applied Materials & Interfaces* 2013, *5*, 207.
[37] Z. Xu, T. Wu, J. Shi, K. Teng, W. Wang, M. Ma, J. Li, X. Qian, C. Li, J. Fan, *Journal of Membrane Science* 2016, *520*, 281.
[38] J. Yu, T. Ma, G. Liu, B. Cheng, *Dalton Transactions* 2011, *40*, 6635.
[39] G. R. Buettner, *Free Radical Biology and Medicine* 1987, *3*, 259.
[40] A. I. Shames, A. M. Panich, W. Kempiński, A. E. Alexenskii, M. V. Baidakova, A. T. Dideikin, V. Y. Osipov, V. I. Siklitski, E. Osawa, M. Ozawa, A. Y. Vul, *Journal of Physics and Chemistry of Solids* 2002, *63*, 1993.
[41] M. Dubois, K. Guérin, E. Petit, N. Batisse, A. Hamwi, N. Komatsu, J. Giraudet, P. Pirotte, F. Masin, *The Journal of Physical Chemistry C* 2009, *113*, 10371.

[42] X. Fang, J. Mao, E. M. Levin, K. Schmidt-Rohr, *Journal of the American Chemical Society* 2009, *131*, 1426.
[43] H. Chavda, C. Patel, *International journal of pharmaceutical investigation* 2011, *1*, 17.
[44] Y.-H. Wu, H. B. Park, T. Kai, B. D. Freeman, D. S. Kalika, *Journal of Membrane Science* 2010, *347*, 197.
[45] G. Graeber, C. D. Díaz-Marín, L. C. Gaugler, Y. Zhong, B. El Fil, X. Liu, E. N. Wang, *Advanced Materials* 2024, *36*, 2211783.
[46] G. Kougkolos, M. Golzio, L. Laudebat, Z. Valdez-Nava, E. Flahaut, *Journal of Materials Chemistry B* 2023, *11*, 2036.
[47] K. Liu, S. Wei, L. Song, H. Liu, T. Wang, *Journal of Agricultural and Food Chemistry* 2020, *68*, 7269.
[48] A. Malti, J. Edberg, H. Granberg, Z. U. Khan, J. W. Andreasen, X. Liu, D. Zhao, H. Zhang, Y. Yao, J. W. Brill, I. Engquist, M. Fahlman, L. Wågberg, X. Crispin, M. Berggren, *Advanced Science* 2016, *3*, 1500305.
[49] D. Stawski, *Royal Society open science* 2023, *10*, 230188.

5.9. Supporting information

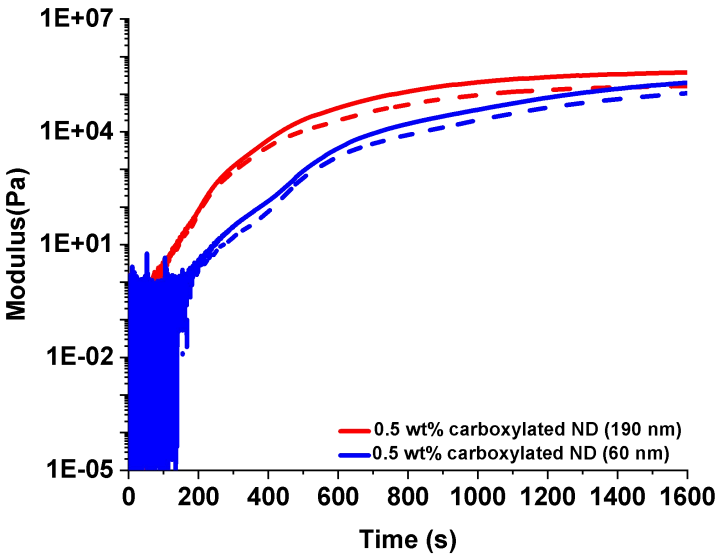

Figure S5. 1. Storage (G') and loss (G'') moduli of carboxylated NDs with various size/SBMA system prepared in 1 mM NaOH (carboxylated NDs: 0.5 wt%) as a function of irradiation time. The samples were irradiated with LED@410 nm.

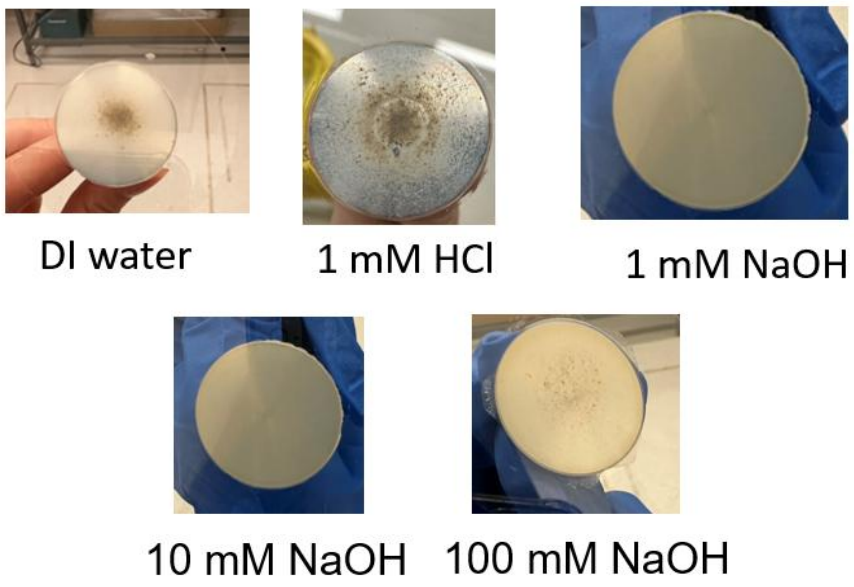

Figure S5. 2. Photopolymerized carboxylated NDs/SBMA hydrogel prepared in different aqueous environments irradiated with LED @410 nm.

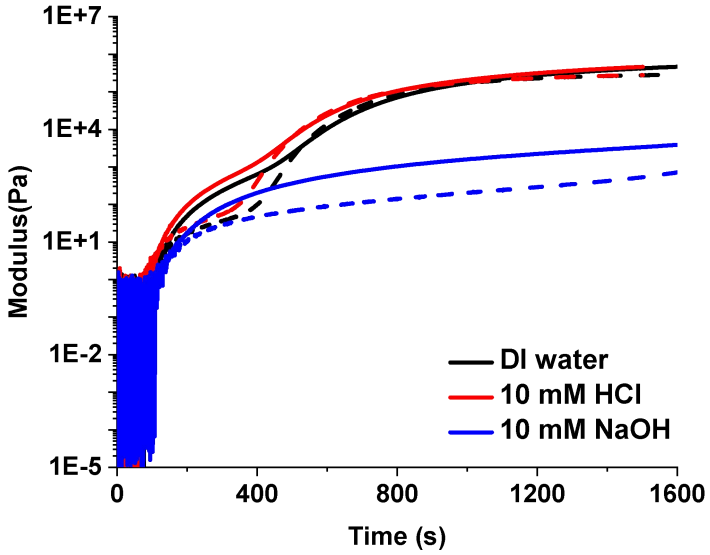

Figure S5. 3. Storage (G') and loss (G'') moduli of TiO_2/SBMA (TiO_2: 0.5 wt%) system prepared in various aqueous environments as a function of irradiation time. The sample was irradiated with LED@410 nm.

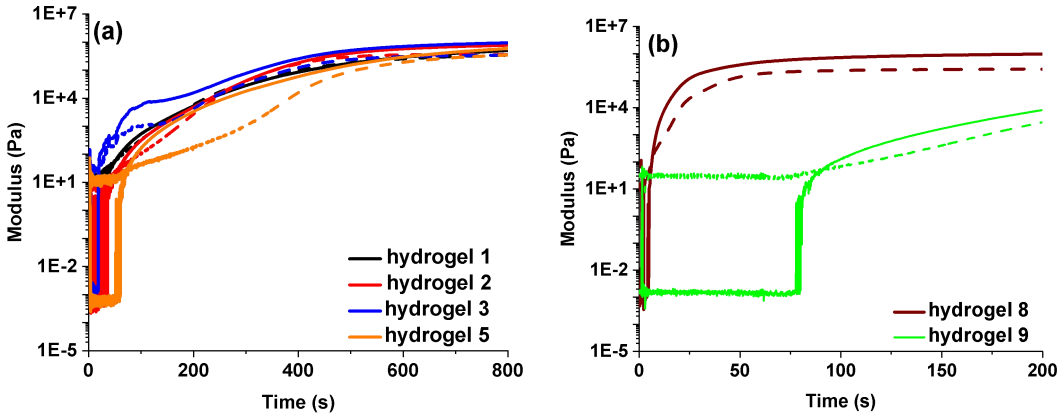

Figure S5. 4. Storage (G') and loss (G'') moduli of the investigated hydrogel precursors as a function of irradiation time. The investigated hydrogel precursors were irradiated with LED@410 nm.

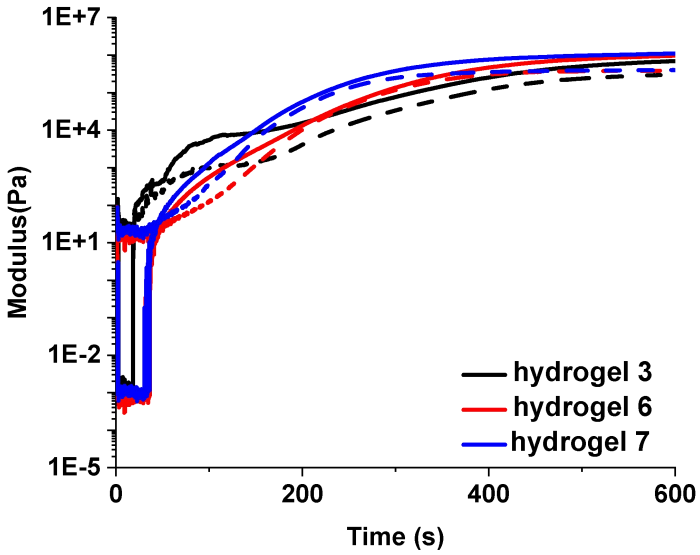

Figure S5. 5. Storage (G') and loss (G'') moduli of the investigated hydrogel precursors as a function of irradiation time. The investigated hydrogel precursors were irradiated with LED@410 nm.

Table S5. 1**.** Water content of investigated as-photopolymerized hydrogels.

Hydrogels	Water content (%)
1	42.7%± 3.4%
2	38.8%± 6.3%
3	35.7%± 6.9%
6	38.1%± 2.9%
7	34.8%±3.8%
11	35.1%±2.8%

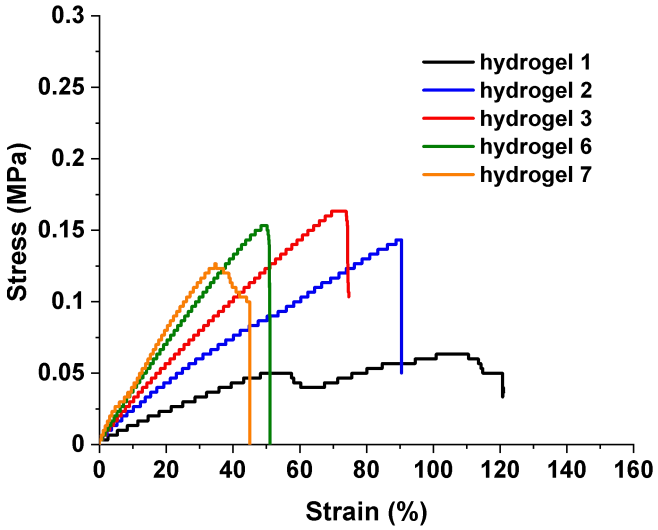

Figure S5. 6. Stress-strain curves in tensile test of the as photopolymerized hydrogels

Chapter 6. Conclusion

This thesis presents significant advancements in developing polymer nanocomposites through photopolymerization, demonstrating the potential of integrating functionalized nanomaterials as both photoinitiators and reinforcing agents. It comprises five chapters, beginning with a literature review in Chapter 1, followed by four chapters that each focus on the development of functional polymer nanocomposites using photopolymerization techniques with four different modified nanomaterials.

Chapter 1 provides a comprehensive review of recent advancements in functional polymer composites created using photopolymerization with nanofillers. It emphasizes the importance of nanofiller surface modification to improve compatibility and interfacial interaction with the polymer matrix, a factor crucial for achieving the desired mechanical, optical, and thermal properties. The chapter also discusses challenges, such as achieving

uniform dispersion and optimizing light penetration, suggesting potential solutions for expanding the practical applications of these materials.

In Chapter 2, a novel approach is introduced using triazine-coated silica nanoparticles (Si-triazine NPs) as visible light-sensitive photoinitiators and fillers. These modified nanoparticles successfully initiate free radical polymerization under LED light at 410 nm, achieving enhanced mechanical properties, reduced shrinkage, and improved migration stability of the nanocomposite. The study highlights the advantages of visible-light photopolymerization for applications in areas where UV exposure is restricted.

Chapter 3 investigates the use of cesium lead halide quantum dots ($CsPbBr_3$ QDs) as dual-role agents in nanocomposite materials, serving as both photoinitiators and emitters. The incorporation of additives, such as iodonium salt (Iod) and ethyl 4-(dimethylamino) benzoate (EDB), enhances the photoinitiation efficiency of these QDs. The resulting nanocomposites display exceptional photoluminescence and stability, indicating their suitability for applications in luminescent displays and lighting.

Chapter 4 explores the potential of visible-light-sensitive metal-organic frameworks (MOFs), specifically UiO-66 modified with *N*-(1-pyrenyl)glycine (NPYG) and 2-(4-methoxystyryl)-4,6-bis(trichloromethyl)-1,3,5-triazine (triazine), to serve as photoinitiators and fillers in photopolymerized nanocomposites. The modified UiO-66 MOFs exhibit strong photoinitiation capabilities, allowing for high-resolution 3D printing and selective dye absorption. These composites demonstrate the versatility of MOF-based photoinitiators, paving the way for their application in advanced manufacturing and environmental remediation.

Finally, Chapter 5 focuses on a hybrid system combining TiO_2 and carboxylated nanodiamonds (NDs) as a photoinitiator and reinforcing agent for zwitterionic SBMA hydrogels. This hybrid system enhances mechanical properties and provides conductivity, enabling the hydrogels to function as moisture sensors. The TiO_2-carboxylated NDs hybrid system demonstrates improved photoinitiation efficiency, enhanced radical generation, and optimal dispersibility, resulting in significant gains in tensile strength and Young's modulus compared to conventional photoinitiators.

Despite the promising advancements presented in this work, several challenges remain in the development of photopolymerized nanocomposites. One key limitation is achieving precise control over nanofiller dispersion and interfacial interactions within polymer matrices, as agglomeration or phase separation can compromise mechanical and optical properties. Further research is required to develop more efficient surface modification techniques and in situ polymerization strategies to enhance compatibility and uniform distribution of nanofillers.

Another critical challenge lies in optimizing photopolymerization efficiency under visible light. While this thesis demonstrates several successful strategies for utilizing visible-light-sensitive photoinitiators, many systems still require high-intensity light sources or co-initiators to achieve rapid curing and sufficient polymerization depth. Future studies could explore the development of highly efficient photoinitiators with broader absorption spectra, enabling faster polymerization under ambient or low-energy light sources.

Additionally, while this research highlights the potential functional applications of photopolymerized nanocomposites, further investigations are needed to evaluate their long-term stability, environmental durability, and biocompatibility. Stability concerns, such as photo-induced degradation, leaching of nanofillers, or mechanical fatigue, must be

addressed to ensure the practical viability of these materials in biomedical devices, coatings, and structural applications.

Furthermore, the expansion of 3D printing techniques for nanocomposite fabrication presents exciting opportunities but also demands improved control over print resolution, mechanical robustness, and post-processing methodologies. Exploring new photo-responsive materials and multi-material printing strategies could unlock new functionalities for applications in smart materials, tissue engineering, and flexible electronics.

Finally, integrating sustainable and environmentally friendly approaches into photopolymerization remains an important future direction. Developing biodegradable nanocomposites, solvent-free processing methods, and green photoinitiators could further expand the impact of these materials in eco-friendly packaging, water purification, and bioelectronics.

By addressing these challenges, future research can continue to push the boundaries of functional photopolymerized nanocomposites, enhancing their performance, scalability, and applicability across a wide range of fields.